19F MAGNETIC RESONANCE IMAGING OF LUNG VENTILATION DYNAMICS AND CELL TRACKING

Sang Hun Chung

A dissertation submitted to the faculty at the University of North Carolina at Chapel Hill in partial fulfillment of the requirements for the degree of Doctor of Philosophy in the department of biomedical engineering in the University of North Carolina Chapel Hill.

Chapel Hill
2023

Approved by:

Yueh Z. Lee

David S. Lalush

Jeffrey M. Macdonald

Jennifer L. Goralski

Gianmarco Pinton

ABSTRACT

Sang Hun Chung: 19F Magnetic Resonance Imaging of Lung Ventilation Dynamics and Cell Tracking
(Under the direction of Yueh Z. Lee)

The Fluorine isotope ^{19}F has great potential in the use of magnetic resonance imaging (MRI) for clinical applications. ^{19}F is inert, naturally abundant, has a close resonance frequency to proton (^{1}H) (allowing most modern MRI scanners to work with the addition of a tuned coil), has negligible presence in the mammalian body (allowing background signal free acquisitions), and the high gyromagnetic ratio provides sufficient magnetic resonance signal to be visible without hyperpolarization.

Uses for ^{19}F MRI includes functional lung imaging, diffusion imaging, cell tracking, and oxygenation sensing among others. Although not widely used in the clinical setting at the time of writing this dissertation. The potential improvements ^{19}F MRI could bring to healthcare are vast. ^{19}F lung imaging has been studied in animal and human models, and has shown to be capable of producing sensitive markers for lung diseases such as cystic fibrosis (CF) and chronic obstructive pulmonary disease (COPD) by providing spatially localized functional information. In cell tracking, ^{19}F has shown potential in drug delivery monitoring, inflammation imaging, immune cell tracking, and oxygenation measurement with the potential of spatial localization and cell quantification.

This dissertation presents my work on human in-vivo multi-breath wash-in/out ^{19}F lung imaging, and the processing of biomarkers more sensitive to CF disease progression

over the current gold standard (spirometry). 19F lung MRI was compared to hyperpolarized (HP) Xenon (^{129}Xe) ventilation defect percentage (VDP) analysis. The feasibility of free-breathing ^{19}F lung imaging was explored using a combination of spiral acquisition and denoising. The last two chapters present preliminary work on sequence programming for diffusion imaging and cell tracking at high magnetic fields (9.4T). Preliminary work on oxygen sensing at 9.4T is also explored.

To my parents, thank you for all your sacrifices

ACKNOWLEDGMENTS

I'm very grateful to my principal investigator Yueh Z. Lee for all the guidance, patience, and knowledge throughout my studies. Thank you to Jennifer L. Goralski for providing much needed clinical knowledge on cystic fibrosis. Thank you to my committee members, David Lalush, Jeffrey M. Macdonald, and Gianmarco Pinton for agreeing to be part of my committee. Thank you to Scott H. Donaldson for the insightful review of manuscripts. Thank you to Margret Z. Powell for recruiting and scheduling human imaging sessions. Thank you to Agathe S. Ceppe for performing and providing guidance on statistics.

Thank you to Eric Frederick from Bruker for helping set-up the 9.4T Bruker scanner for 19F. Thank you to Brian Dale from Siemens for teaching me about sequence programming and being there to answer questions.

Thank you to Rosa Tamara Branca for help with the 9.4T Bruker scanner and MR physics help. Thank you to Qiuhong He for help with MR physics and acquisition. Thank you to Michael Antonacci for helping me with performing scans with the 9.4T Bruker scanner. Thank you to Tzu-Wen Winnie Wang for helping with questions and scheduling.

Thank you to the Biomedical Research Imaging Center (BRIC) staff, Victor A. Pincay, Emily M. Hammer, and Amber A. Leinwand for running the human scans.

PREFACE

Chapter 3 includes excerpts from a previously published original article with the title "Dynamic perfluorinated gas MRI reveals abnormal ventilation despite normal FEV1 in cystic fibrosis." in the peer review journal JCI Insight in 2020 (JCI Insight. 2020 Jan 30; 5(2): e133400). As the second author, I was responsible for the data processing and results generation. This chapter is included because of its foundational nature in the rest of this dissertation and should be considered background information. Excerpts were reprinted with the permission of the publisher. It was co-authored by Jennifer L. Goralski, Sang Hun Chung, Tyler M. Glass, Agathe S. Ceppe, Esther O. Akinnagbe-Zusterzeel, Aaron T. Timble, Richard C. Boucher, Brian J. Soher, H. Cecil Charles, Scott H. Donaldson, and Yueh Z. Lee.

Chapter 4 was previously published in part as an original article with the titled "Comparison of single breath hyperpolarized 129 Xe MRI with dynamic 19 F MRI in cystic fibrosis lung disease." In the peer review journal Magnetic Resonance in Medicine in 2020 (https://doi.org/10.1002/mrm.28457). I'm the first co-author with Andrew McCallister. I was responsible for the 19F portion of the article. This article is reprinted with permission from the publisher. It was co-authored by Andre McCallister, San Hun Chung, Michael Antonacci, Margret Z. Powell, Agathe S. Ceppe, Scott H. Donaldson, Yueh Z .Lee, Rosa Tamara Branca, and Jennifer L. Goralski.

Chapter 5 was previously published as an original article titled "Feasibility of free-breathing 19 F MRI image acquisition to characterize ventilation defects in CF and healthy volunteers at wash-in" in the peer review journal Magnetic Resonance in Medicine in 2023

(https://doi.org/10.1002/mrm.29630). I'm the first co-author with Khoi Minh Huynh. I was responsible for study design, acquisition, processing, and writing. This article was reprinted with permission from the publisher. It was co-authored by Sang Hun Chung, Khoi Minh Huynh, Jennifer L. Goralski, Yong Chen, Pew-Thian Yap, Agathe S. Ceppe, Margret Z. Powell, Scott H. Donaldson, and Yueh Z. Lee.

Chapter 6 is a manuscript titled "19F dynamic analysis during free breathing, feasibility of spiral acquisition with denoising on patient with cystic fibrosis". This manuscript is in preparation for submission to a peer review journal with me as the first author.

For all chapters in this dissertation, I participated in data acquisition, data processing, writing, figure generation, table generation, drafting, editing, revisions, and result interpretation.

Brian J. Soher and H. Cecil Charles provided the software used to generate the results for chapter 3. Andrew McCallister performed the VDP analysis on the ^{129}Xe scans. Yong Chen did the sequence programming for the spiral sequence and guidance on reconstruction. Tyler M. Glass and Esther O. Akinnagbe-Zusterzeel coded the early version of the Matlab fitting code used in chapters 4-6.

Khoi Minh Huynh developed the denoising algorithm and performed denoising. Elena V. Batrakova, Yuling Zhao, and Mathew J. Haney did the macrophage loading and mice injections. Jeremy Meier did the CAR-T cell loading. Margret Z. Powell was the research coordinator for all human imaging, Agathe S. Ceppe was the statistician, Jennifer L. Goralski was the pulmonologist, study designer, and provided clinical expertise. Yueh Z. Lee was the principal investigator and provided guidance in all aspects of this dissertation.

TABLE OF CONTENTS

LIST OF TABLES

LIST OF FIGURES

LIST OF ABBREVIATIONS

ADC	Analog to digital converter, or Apparent diffusion coefficient
CDI	Convection-dependent inhomogeneity
CF	Cystic fibrosis
CFTR	Cystic fibrosis transmembrane conductance regulator
CFTR	Transmembrane conductance regulator
COPD	Chronic obstructive pulmonary disease
CT	Computed tomography
DCDI	Diffusion convection-interaction-dependent inhomogeneity
DFT	Discrete Fourier transform
ERV	Expiratory reserve volume
FEV1	Forced expiratory volume in 1 second
FFT	Fast Fourier transform
FID	Free induction decay
FLV	Fractional lung volume
FRC	Functional residual capacity
FT	Fourier transform
FVC	Forced vital capacity
GRE	Gradient echo

HSR	High spatial resolution
IC	Inspiratory capacity
IDFT	Inverse discrete Fourier transform
IFT	Inverse Fourier transform
IRT	Immunoreactive trypsinogen
IRV	Inspiratory reserve volume
ITGV	Intrathoracic gas volume
IVC	Inspiratory vital capacity
LCI	Lung clearance index
LSD	Least significant difference
LUS	Lung ultrasound
MBW	Multiple-breath washout
NM	Normal mixture
NUFFT	Non-uniform Fourier transform
PEF	Peak expiratory flow
RV	Residual volume
SNR	Signal to noise ratio
SNR	Signal to noise ratio
TE	Echo time

TLC	Total lung capacity
TR	Repetition time
TV	Tidal volume
UTE	Ultra short TE
VC	Vital capacity
VC	Vital capacity
VDP	Ventilation defect percentage

LIST OF SYMBOLS

$\vec{J}$	Angular momentum
Δ	Time between the 2 diffusion sensitizing gradient lobes
$\Delta x, \Delta y, \Delta z$	Voxel size
$\vec{\mu}$	Nuclear moment
B_0	Static magnetic field
$\vec{B}_{ext}$	External magnetic field
B_1	RF-pulse magnetic field
$B_1^e(\mathrm{t})$	Pulse envelop function
C	Curie constant
Cet_{start}	Concentration at end-tidal volume of the tracer gas at the start of wash-out
Cet_{end}	Concentration at end-tidal volume of the tracer gas at the end of wash-out
F_k	Frequency domain data, or Fourier transform
f_n	Spatial/time domain data, or inverse Fourier transform
I	Nuclear spin quantum number
l_s	Length of confining structure
l_d	Free diffusion length

l_g	Gradient dephasing length
N_{acq}	Number of acquisitions
N_y	Number of phase encodings
N_z	Number of slices
m_I	Magnetic quantum number
$\vec{M}$	Net magnetization
M_z	Longitudinal magnetization
$\vec{M}_{xy}$	Transverse magnetization
M_+	Transverse magnetization, complex
T	Tesla
T	Absolute temperature
T_{sADC}	Read time
T_T	Total acquisition time
T_1	Longitudinal decay time constant
T_2	Transverse decay time constant
T_2^*	Transverse decay time constant with field inhomogeneities and magnetic field fluctuations
T_2'	Transverse decay time constant with only field inhomogeneity accounted
V_{CE}	Cumulative net expired volume

$\hat{x}$	Unit vector along the x-axis
$\hat{y}$	Unit vector along the y-axis
$\hat{z}$	Unit vector along the z-axis
α	Flip angle
α_E	Ernst angle
γ	Gyromagnetic ratio
Υ	Efficiency
δ	Duration of the diffusion sensitizing gradients
τ_1	Wash-in time constant
τ_2	Wash-out time constant
ω_0	Larmor frequency
ω_{rf}	RF-pulse carrier frequency

CHAPTER 1: INTRODUCTION

Chapter 1 presents background information on the field of lung physiology, disease, imaging, and testing. The purpose of this chapter is to inform about the need for lung imaging, the current methods available, and where ^{19}F imaging is positioned among other imaging methods. This chapter was not intended to be an exhaustive review. Each methodology is under constant improvement and the information presented should be considered introductory.

1.1 PULMONARY PHYSIOLOGY

1.1.1 ANATOMY

The lungs function as the primary organ in the respiratory system and are the site of gas exchange. The lungs are divided into lobes, the right lung has three lobes (superior, middle, and inferior lobes) and the left lung has two lobes (superior and inferior lobes). The right lung is usually slightly larger than the left lung [1]. Air flows in through the respiratory tract mainly driven by a pressure differential created by the contraction of the diaphragm and relaxation of the intercostal muscles. Passive expiration happens from the elastic recoil of the lungs and ribcage. Active or forced expiration is driven, in addition to the passive expiration mechanics, by intercostal and abdominal muscles.

The respiratory tract, also known as airways, can be divided into upper and lower airways. The upper airway consists of the pharynx and larynx. The lower airway consists of the trachea, bronchi, bronchioles, and alveoli. The alveolus is the end point of the

respiratory system and main site of gas exchange. The alveolus are made of a single cell layer of pneumocytes [2] surrounded by capillaries and can be divided into alveolar ducts and sacs. The alveolar ducts are tubular structures from which clusters of alveolar sacs sprout.

The alveolar sacs in each cluster are connected through pores that permit pressure equalization between each other. The alveolar sacs and capillaries are termed the air-blood barrier where oxygen can be transported into the bloodstream and carbon dioxide extracted to the air stream.

The human lung surface area was measured in 2009 by Weibel et al [3] to be approximately 130 m^2 while other studies suggest roughly half the value at 70 m^2 [4,5].

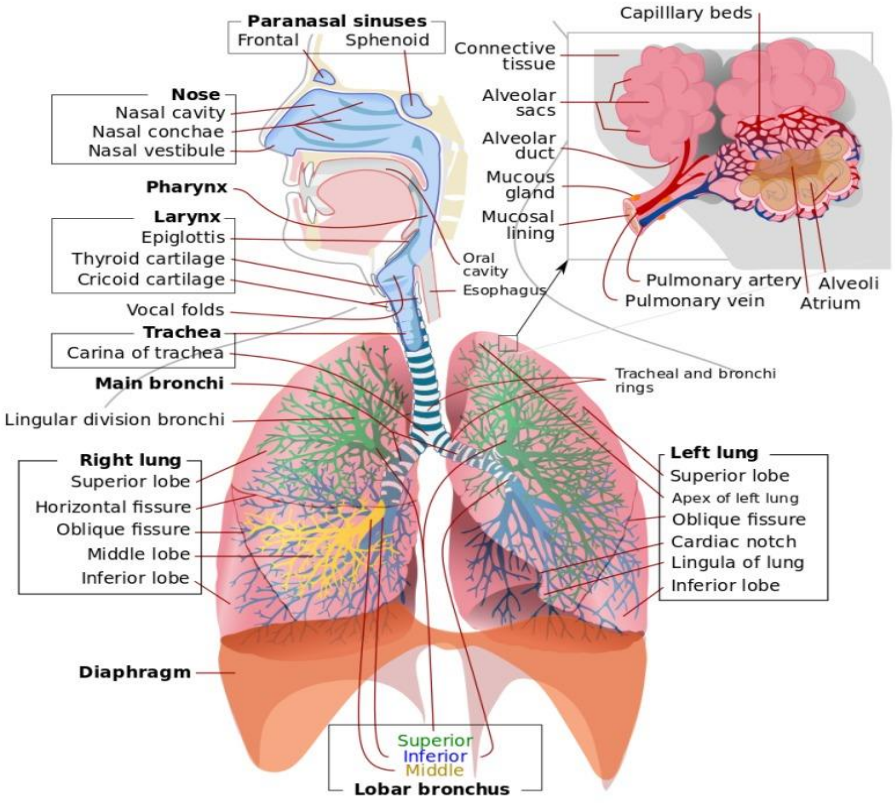

Figure 1.1. The anatomy of the human lung, figure reproduced from Ball et al[2] reprinted unaltered under license CC BY-NC-ND 4.0

1.1.2 LUNG FUNCTION

The total lung capacity (TLC) defined as the volume of the lungs at maximum inspiratory effort was reported to be 6 liters in average, though this value varies based on age, gender, body composition, and ethnicity [6].

Ventilation (V) is defined as the movement and gas exchange of air in and out the alveoli, and perfusion (Q) is defined as the flow of blood in the alveolar capillaries, which are both necessary for effective gas exchange [7]. The ratio of ventilation to perfusion (V/Q) is a commonly used clinical metric of whole, or global, lung function.

The lung air displacements and volumes have standardized names used in literature that include tidal volume (TV), residual volume (RV), inspiratory reserve volume (IRV), expiratory reserve volume (ERV), inspiratory capacity (IC), vital capacity (VC), functional residual capacity (FRC), and total lung capacity (TLC) [8]. These naming conventions facilitate efficient information exchange between clinicians and researchers and are extensively used in pulmonary literature. Lutfi et al [8] has an informative figure showing all the mentioned terms.

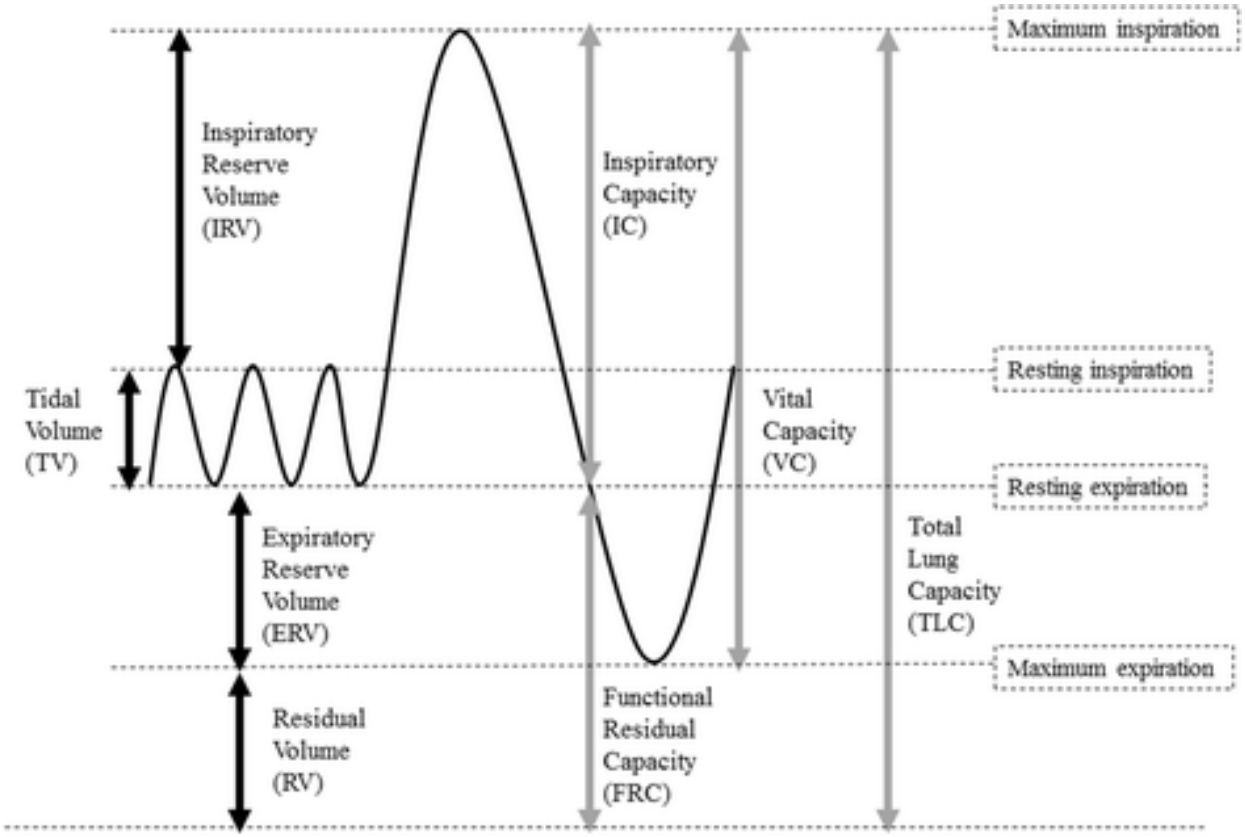

Figure 1.2. Lung volumes and capacities, reproduced from Lutfi et al[8] with permission from the publisher under license CC BY 4.0

1.1.3 LUNG MECHANICS

The study of lung mechanics goes as far back as the time of the ancient Greeks and include prominent figures like Leonardo da Vinci [9]. Quantitative research took off in the twentieth century, largely attributed to Jere Mead at the Harvard School of Public Health and his students.

Research into quantitative lung mechanics yielded several discoveries and greater understanding of the lung mechanics such as the roles of surface tension and surfactant [10], the pressure-volume (PV) curve [11], hysteresis [12], and collateral ventilation [13]. For a more in depth history on the study on lung mechanics refer to [14,15]

A simplified model of the lung by Fry et al in 1954 [16] shows the functional relationship between lung pressures; intrathoracic pressure (P_T), pressure caused by retractive forces of the lung (P_L), and the pressure between the alveoli and the oral cavity (P_p). The piston shown in Figure 1.3 represents the thoracic and diaphragm expansion/contraction.

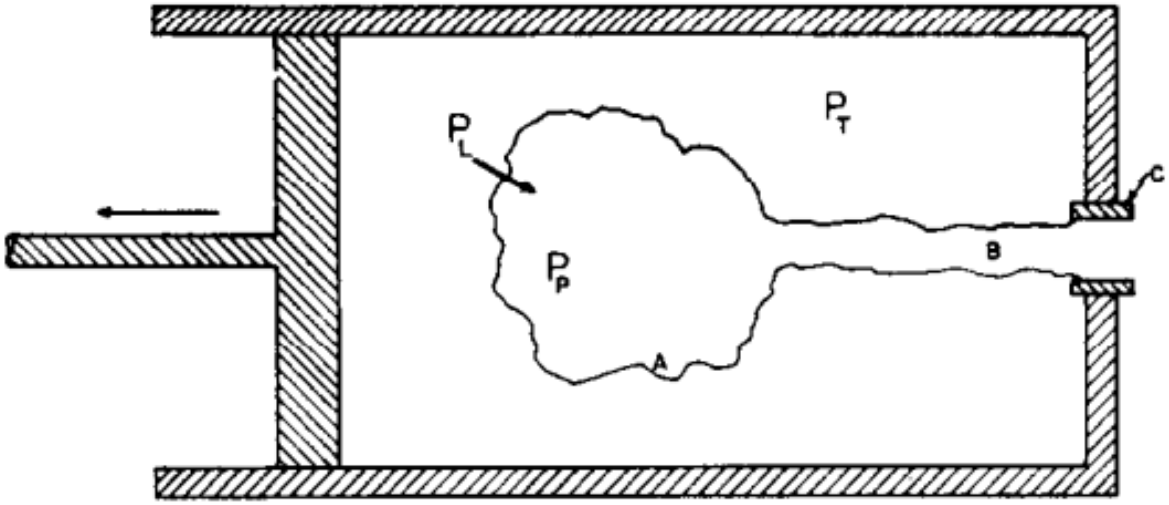

Figure 1.3. Basic Lung model from Fry et al [16], showing A, expansile elastic unit; B, unsupported bronchiole; C, rigid bronchus; P_T, pressure in cylinder; P_L, elastic pressure of expansile until; P_p, pressure in expansile unit. Reprinted with permission from the publisher

Fry et al. showed that by measuring repeated forced expirations at varying subject effort, it was possible to measure flows at different pressures and volumes. The measured data could then be visualized as a surface curve shown in Figure 1.4.

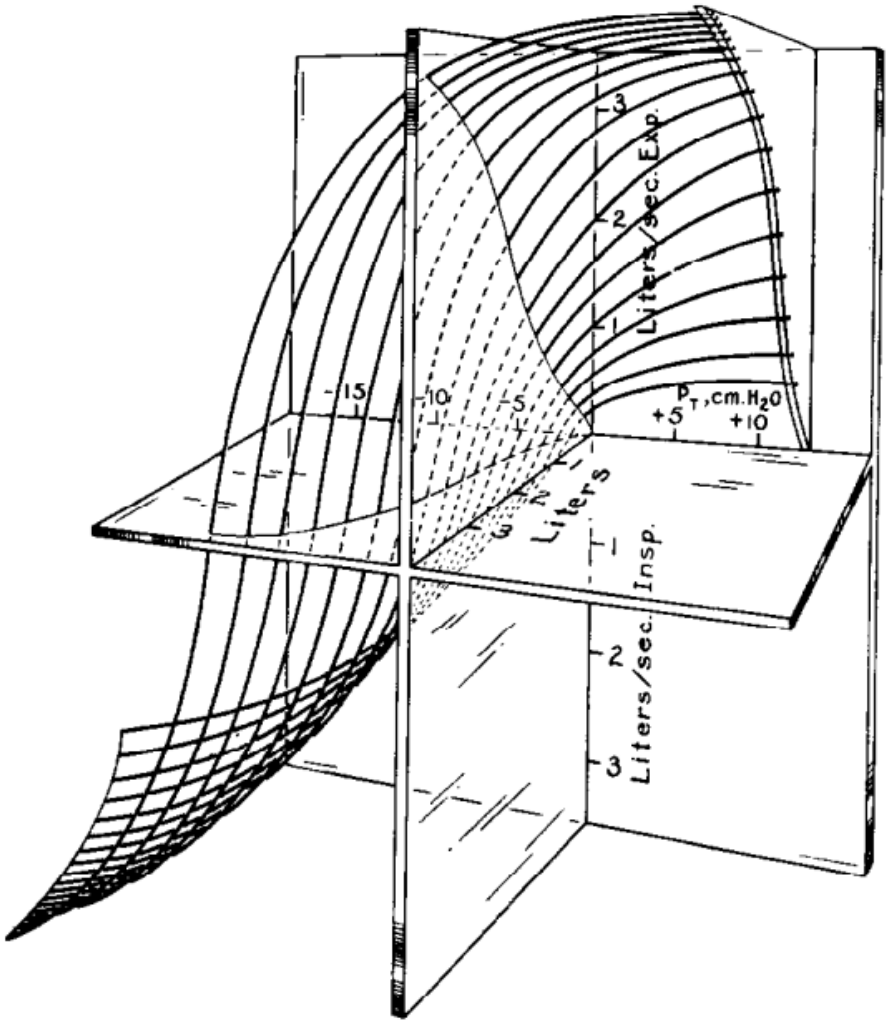

Figure 1.4. 3D graph showing the relationship between volume (liters), flow (liters/sec), and P_T (cm H_2O), in healthy adults. The vertical axis marks the separation between inspiration and expiration [16]. Reprinted with permission from the publisher.

The curves showed a flattening of the flow in regions of high pressures (in both positive and negative directions), i.e., the gain of flow with further effort was diminished. This effect was amplified in subjects with emphysema and present at lower airflow values. In addition, the flow-volume curve saw a marked change at expiration.

Fry et al concluded that emphysema alters the lung retractive force and increases the airflow resistance in the bronchiole which leads to positive intrathoracic pressure at low expiratory airflows, which in turn, forces the lung to maintain a higher inflation.

Through the years, new, more sophisticated lung mechanics models have been developed by using electrical circuit analogues. Among the first are the Otis' model [17], the Mead model [18], and the Mount model [19]. Starting from simpler resistance-capacitance (RC) models, the models have been developed in increased complexity resistance-inductance-capacitance (RIC) models such as the RIC [20], Viscoelastic [21], Dubois [22], Mead (upgraded) [23], and extended RIC models [24]. Note, capacitance (C) is often referred to as compliance and inductance (I) is often referred to as inertance to highlight that electrical components are treated as analogous to physical properties.

By the late 1990s and early 2000s, research into lung mechanics was generally understood to have peaked with new innovations coming instead from cell and molecular research [14]. However, new momentum into lung mechanics research is rising due to the emergence of medical imaging, which affords previously difficult or unpractical analysis. For example, medical imaging can provide high resolution anatomical information for the understanding of individual variance in airways or used as quantitative tools to measure mechanics such as ventilation and perfusion spatially.

1.2 PULMONARY PATHOLOGY

The scope of research presented in this dissertation is limited to Cystic fibrosis (CF). A short introduction to CF is presented in this subsection.

According to the Cystic Fibrosis Foundation (4550 Montgomery Ave. Suite 1100 N, Bethesda, MD 20814), 40,000 children and adults are living with cystic fibrosis in the United States. Approximately 1,000 cases are diagnosed every year. More than 75% are diagnosed by age 2 and more than half the current CF population is age 18 or older.

In 1954, the median survival age of patients with CF was estimated to be only 4-5 years. By 1978, the median survival age was 11 years[25]. Based on the Cystic Fibrosis Foundation Patient Registry (2006-2021), the median age of death in 2021 was 33.9 years. For patients that were born between 2015 and 2019, the median predicted survival is 46 years. Figure 1.5 shows the median age of death taken from the patient registry and plotted over time.

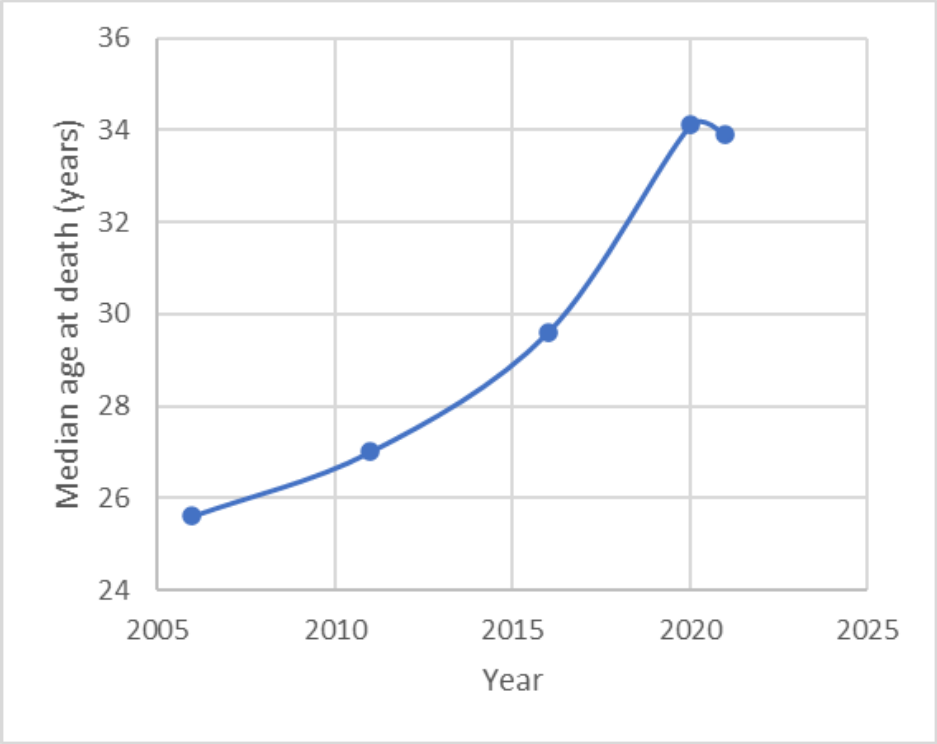

Figure 1.5. Median age of death from the Cystic Fibrosis Foundation patient registry (2006-2021)

CF was first recognized as a disease in 1938 by Dorothy H. Andersen[26], when the autopsy of infant bodies of then thought to be suffering from celiac disease revealed mucus plugging of the glandular ducts. Emphasis was also taken on the pancreas due to observable "cysts" formed by fibrous tissue which was referred to as cystic fibrosis of the pancreas. At this point, CF had no known cause other than a correlation with family history

and it was also described by other names such as mucoviscidosis[27] and generalized exocrinopathy[28]. In 1946, CF was recognized as a genetic disorder by Andersen et al[26]. In 1948, Paul di Sant'Agnese observed that infants with CF had consistent five-fold elevated sodium and chloride levels in their sweat[29].

In subsequent years, the sweat chloride test became the standard to diagnose CF due to its ease of application and specificity since few other diseases have a similar effect on sweat. The chloride sweat test was standardized as a diagnosis tool based on chloride concentration. The sweat test is currently considered the most reliable CF diagnosis tool by the Cystic Fibrosis foundation. The guidelines for CF diagnosis are shown in Figure 1.6

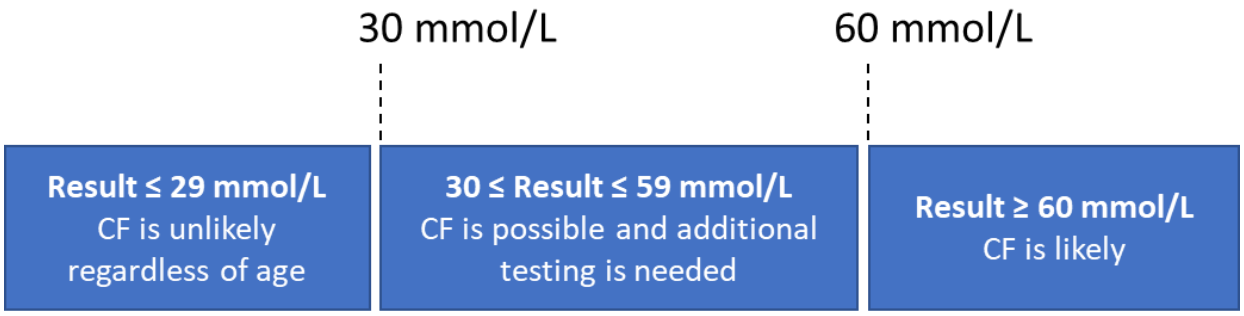

Figure 1.6. CF diagnosis criteria based on sweat chloride concentration

The CF diagnosis guidelines vary by age and are regularly updated, for further detail readers are directed to the Cystic Fibrosis Foundation guidelines(Farrell et al. 2017), and the Cystic Fibrosis Foundation website https://www.cff.org/.

In 1989, the CF gene was discovered and known as the CF transmembrane conductance regulator (CFTR) by researchers in collaboration from The Hospital for Sick Children (Toronto, Ontario, Canada), The University of Michigan (Ann Arbor, MI, USA), and the University of Pittsburg (Pittsburg, PA, USA) [30–32]. CFTR causes a defect in the cAMP-regulated chloride channels. CFTR expression is not localized to one organ, and

therefore can affect several organ functions throughout the body such as liver, pancreas, gall bladder, and the respiratory system.

Out of all the affected organs, disease of the lung is the major cause of morbidity and mortality in CF[28]. Patients with CF are more susceptible to lung infections, bronchitis, airway lung thickening, fibrosis, and mucus plugs. The Cystic Fibrosis Foundation Guidelines on lung transplantation is for patients with FEV1 < 50% predicted and rapidly declining or FEV1 < 40% predicted with markers of shortened survival or FEV1 < 30% predicted for patients 18 years old or older.

In 2019, the U.S. Food and Drug Administration approved the combination therapy Trikafta® for patients aged 12 and older, this therapy is a combination of CFTR modulators; elexacaftor, tezacaftor, and ivacaftor that works to increase the CFTR protein activity. The response to Trikafta® has been very positive[33,34] and in 2021, Trikafta® was extended to children of ages 6 to 11. As the writing of this dissertation, studies are being conducted on the effectiveness of Trikafta® on children ages 2-5.

With the introduction of effective CFTR modulators, CF patients are expected to have slower disease progression and longer expected survivability. The CF treatment guidelines are also expected to shift to earlier treatment and focus more on improving quality of life. Therefore, future CF care will be greatly aided by outcome measures that are repeatable, non-invasive, sensitive, safe, and suitable for children and babies.

There are several CF screening and monitoring methods such as the Immunoreactive trypsinogen (IRT) test, X-ray/computer tomography (CT) scans, lung cultures, and lung function tests, among others. ^{19}F MRI, and other X-Nuclei Lung MRI methods (such as those using hyperpolarized gases) can be thought of as belonging to the pulmonary function

test category due to its ability to measure lung ventilation. Pulmonary function tests are used for diagnosis and the measurement of disease severity, while the chloride sweat test is used for diagnosis.

Pulmonary function tests are methods to measure lung function via several different modalities. The methods can be categorized into two main categories, imaging based and non-imaging based methods. As the writing of this dissertation, non-imaging methods are widely used in clinics due to relatively lower cost and easier operation. Imaging methods are still in the domain of research.

1.3 NON-IMAGING PULMONARY FUNCTION TESTS

Non-imaging pulmonary function tests include spirometry, plethysmography, and lung clearance index (LCI). As we go into detail for each method in the following subsections, emphasis will be on the outcome measures and their physiological meanings that each method provides. In general, pulmonary function tests, measure airflow, ventilation, and volumes.

1.3.1 SPIROMETRY

Spirometry is the most popular and ubiquitous method currently in use in clinics around the world. It is compact, inexpensive, and requires relatively simple operator training. It measures inhalation volume, exhalation volume, and flowrates. Spirometry has been used to measure the severity of patients with asthma, chronic obstructive pulmonary disease (COPD), bronchitis, emphysema, cystic fibrosis, and pulmonary fibrosis.

During spirometry testing, patients are instructed to take a deep inhalation and then a quick, full expiration while the mouthpiece is tightly held in the mouth. This

maneuver creates the necessary data for the accompanying software to calculate the results.

Spirometry results include forced expiratory volume in 1 second (FEV_1), forced vital capacity (FVC), vital capacity (VC), FEV_1/FVC ratio, peak expiratory flow (PEF), forced expiratory flow, and inspiratory vital capacity (IVC).

FVC is the maximum amount of air that can be exhaled when blowing out as fast as possible.VC is the maximum amount of air that can be exhaled when blowing out at a steady rate after the deepest possible inspiration, PEF is the maximal flow that can be exhaled when blowing out as fast as possible, and IVC is the maximum amount of air that can be inhaled after a full expiration[35]. Note that some of these measures overlap with the lung function nomenclature discussed in section 1.1.2.

The obtained values can then be compared to expected normal values. These reference values come from population studies and take into account age, sex, height, and ethnicity. Out of all the measures, FEV_1 % predicted is the most commonly reported for obstructive lung disease. FEV_1 % predicted is the measured FEV_1 as a percentage of the FEV_1 regarded normal (healthy) for a given patient. Historically, 80% of the predicted FEV_1 has been considered normal[35].

A disadvantage of spirometry is that the measurement is a global measure of lung function, there is no spatial information of diseased areas. Users need to be able to follow directions and perform the required breathing maneuver. The result can be affected by Sub-maximal inhalation, cough, early termination, and variable effort, among other sources of error[36].

The collected spirometry data can be visualized in a flow volume loop graph that has been shown to provide indications of abnormality. Figure 1.7 shows common pulmonary abnormalities compared to a normal flow volume curve.

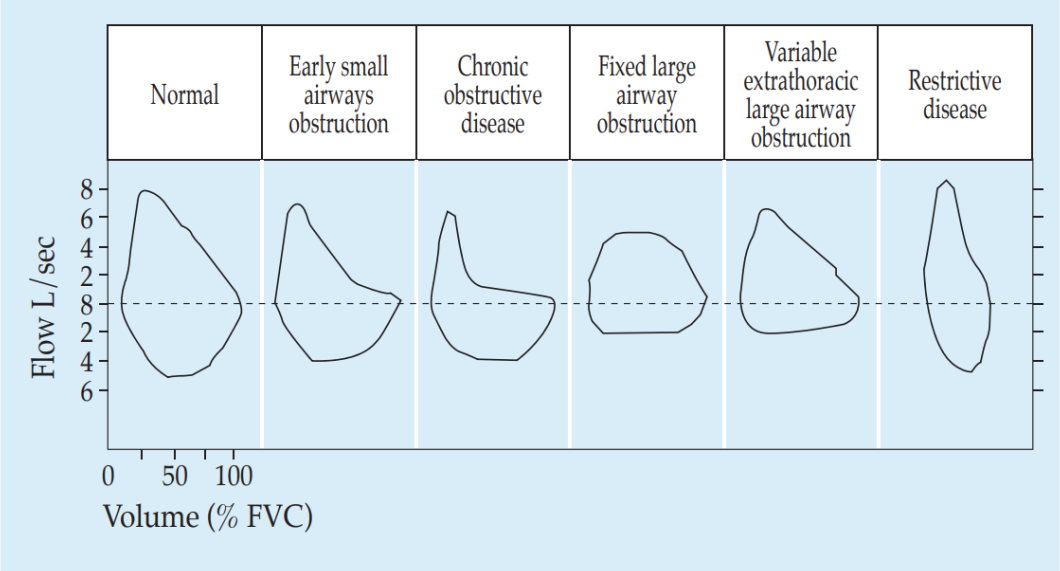

Figure 1.7. Flow volume curves indicating lung abnormalities compared to a healthy reference, reprinted from[37] under the creative commons attribution license

1.3.2 PLETHYSMOGRAPHY

Plethysmography is a technique that relies on the relationship between changes in volume and pressure measurements to measure different lung volumes and capacities.

Distinct from spirometry, plethysmography can be used to measure lung residual volume (RV), total lung capacity (TLC), airway resistance, and intrathoracic gas volume (ITGV)[38]. Another difference from spirometry is that plethysmography is performed while breathing at rest and not with forced maneuvers. A combination of spirometry and body plethysmography may be measured in tandem to complement each other.

Volume changes are calculated based on the Boyle-Mariotte's law that states the change in pressure is inversely proportional to the change in volume. Resistance can be calculated from the change in pressure and the flow rate. Further details about calculations and methodology may be found in[38].

1.3.3 LUNG CLEARANCE INDEX

The Lung clearance index (LCI) is a measure obtained from multiple-breath washout (MBW) testing and is related to lung ventilation turnover efficiency. Although not as popular as spirometry, LCI has garnered interest in the clinical and research community due to several advantages[39]. LCI has been shown to correlate to structural lung disease in CF patients detected via chest computed tomography (CT) [40,41], lung inflammation and infection[42], and ventilation inhomogeneity[43].

LCI measurement has also been shown to be feasible in children[44,45], which is a major unfulfilled area of pulmonary care outcome measures since spirometry maneuvers are difficult with young children. Furthermore, spirometry has been reported to have low sensitivity on early lung disease[46] compared to MBW[47–49] in CF. MBW has a test success rate of 72-99%, except for children below 3.5 years of age[50]. Another advantage of MBW is that it can be performed with only tidal breathing at rest, though attempts with volume controlled breathing has been performed with adults[51,52].

During MBW, patients breathe in an inert gas (ex. nitrogen, argon, sulfur hexafluoride, helium, or methane)[39] through a mouthpiece connected to flow and gas concentration sensors. The wash-in phase comprises of the patient breathing in the inert gas for 4 to 5 mins until a difference between inspiratory and expiratory gas concentration is below 0.004%[53]. Note that total wash-out time and the concentration difference is not

standardized and varies between study groups, age groups, and type of gas use. During the wash-out phase, the patients start breathing either room, medical air, or pure oxygen. Data is collected from the flow meter and gas sensors.

The primary outcome measures of MBW are LCI and FRC[54]. LCI is defined as the amount of ventilation required to wash out the tracer gas during oxygen breathing per liter of FRC down to a predetermined fraction of the original concentration, usually 1/40 or 2.5%[55]. i.e., LCI is a unitless measure the reflects the number of gas exchanges or volume turnovers needed to reach 1/40th of the starter gas concentration. An intuitive explanation is that LCI shows the number of FRCs required to clear the tracer gas[54]. FRC calculated from MBW is often termed FRC to highlight the method of acquisition (opposed to plethysmography) and is calculated from the wash-out data. FRC is calculated as shown in equation (1.1)[56]

$$FRC = \frac{net\ volume\ of\ inert\ gas\ exhaled}{Cet_{start} - Cet_{end}} \tag{1.1}$$

Where Cet_{start} is the concentration at end-tidal volume of the tracer gas at the start of wash-out, and Cet_{end} is the trace gas concentration at the end-tidal volume at the end of wash-out. LCI is then computed as shown in equation (1.2)[56]

$$LCI = \frac{V_{CE}}{FRC} \tag{1.2}$$

Where V_{CE} is the cumulative net expired volume.

The exact tidal breath from which to use Cet_{end} is not standardized[39], leading to difficulties in multicenter study comparisons.

Other outcome measures are ventilation inhomogeneity indices arising from diffusion convection-interaction-dependent inhomogeneity (DCDI) and convection-

dependent inhomogeneity (CDI) mechanisms (S_{acin} and S_{cond} respectively)[39]. S_{acin} reflects ventilation inhomogeneities in the acinar airway region and S_{cond} reflects ventilation inhomogeneities in the conductive airway region[57]. Figure 1.8 shows a depiction of conductive (conducting) and acinar airways. Further reading about S_{acin} and S_{cond} can be found in the original paper by Verbanck et al[52].

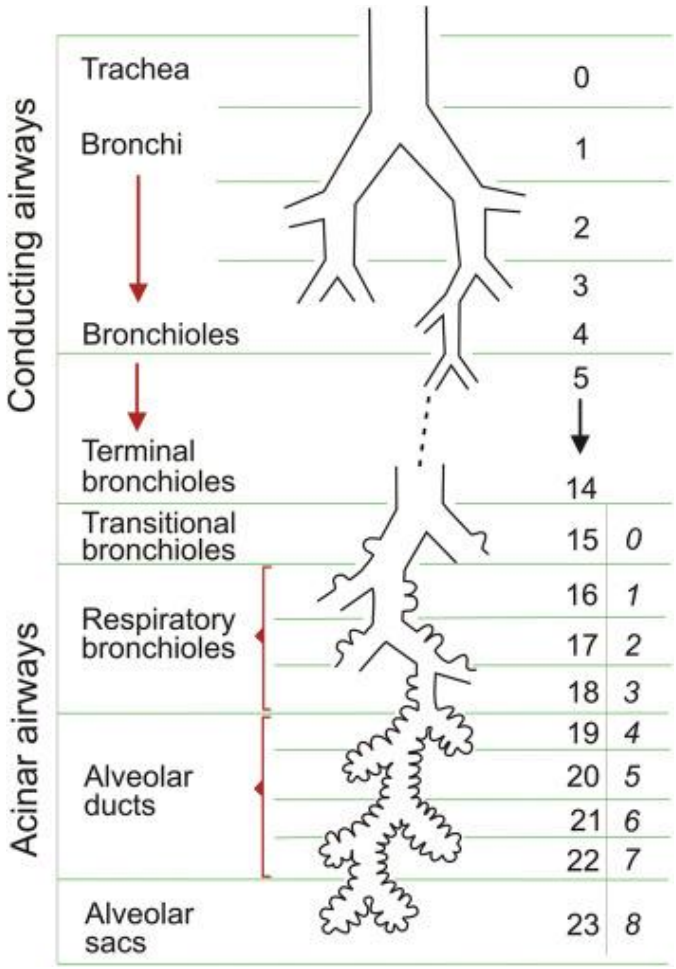

Figure 1.8. conducting and acinar airways in the human lung[58], reprinted with permission from Elsevier, Modified after Ochs, M., Weibel, E.R., 2008. Functional design of the human lung for gas exchange. In: Fishman, A.P., Elias, J.A., Fishman, J.A., Grippi, M.A., Senior, R.M., Pack, A.I. (Eds.), Fishman's Pulmonary Diseases and Disorders, fourth ed. McGrawHill, New York, pp. 23–69.

1.4 LUNG IMAGING

Section 1.4 summarizes lung imaging modalities: X-ray, computer tomography (CT), and MRI with ultrashort TE (UTE) sequences. These modalities provide images of the lungs from which trained clinicians can diagnose disease, often with standardized grading guidelines.

The methods discussed in 1.4 differ from those discussed in 1.5-1.7 in that the end result is an image arising from physical interactions with tissue. Therefore, their usage is generally limited to observable morphological changes.

1.4.1 CHEST X-RAY

X-ray imaging can be considered the most basic type of medical imaging. X-ray made possible for the first time, the non-invasive visualization of the in-vivo human anatomy. X-ray was discovered by Wilhelm Konrad Röntgen in 1895, (later translated to English in 1896)[59], where he noticed the exceptional ability of X-rays to penetrate mass. Röntgen further carried out his research on X-rays and was one of the authors of the first X-ray images. In 1901, Röntgen received the Nobel Prize in physics.

Clinical use of X-ray imaging soon followed and gave rise to a new subspecialty in medicine called Röntgenology[60] (known now as radiology). Today, modern X-ray is routinely carried out in hospitals.

The basic principle of X-ray imaging comes from the properties of X-rays when passing through matter. X-rays are absorbed at different rates by different types of tissue. Denser tissue (such as bone) absorbs more X-rays, the X-rays that pass through the imaging object are then collected to form an image. Earlier X-ray images were done by placing an X-ray sensitive plate (glass plates with a photosensitive emulsion) on the other

side of the generator. The plates were replaced with thin and flexible materials such as cellulose nitrate and cellulose triacetate to lower cost and improve handling[61]. Modern advances have made digital X-ray machines possible. The films are replaced with digital detectors that make possible digital image storing and sharing.

Modern X-ray imaging is relatively inexpensive and fast. However, a major drawback is that the patients are exposed to ionizing radiation. Ionizing radiation comes from high energy waves such as X-rays and Gamma rays that are capable of stripping electrons from living tissue. Overexposure to ionizing radiation causes tissue damage[62] and has been associated with multiple forms of cancer[63]. Lastly, another limitation of traditional X-ray imaging is that the resulting image is a form of projection from 3D to 2D. This causes localization in the axis of X-ray travel to be impossible. Figure 1.9 shows an example chest X-ray image.

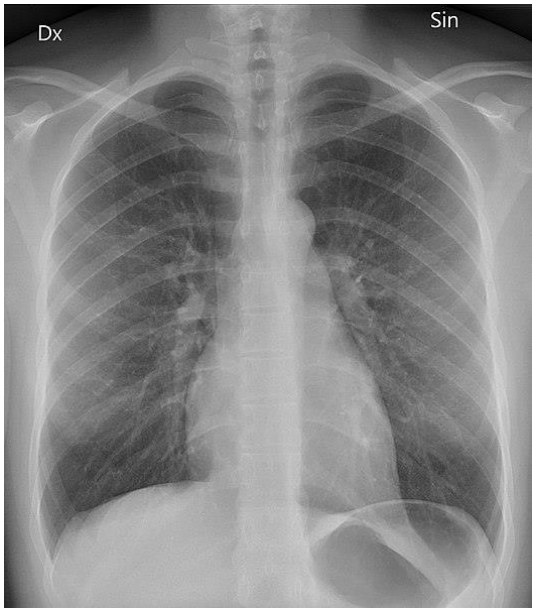

Figure 1.9. Chest X-Ray, with no alterations from the original, "Normal posteroanterior (PA) chest radiograph (X-ray) " by Mikael Häggström, licensed under the Creative Commons CC0 1.0 Universal Public Domain Dedication. Dx and Sin stand for "right" and "left" respectively

1.4.2 COMPUTED TOMOGRAPHY

Computed tomography (CT), also known as computerized tomography or computed axial tomography (CAT), is a technological extension of X-ray imaging where multiple X-rays are taken at different angles. CT was introduced in 1972[60]. The acquired data is digitally processed and is capable of producing tomographic data (the ability to focus on a single plane or slice) and therefore full 3D images. Figure 1.10 shows a Siemens single-photon emission CT machine.

Figure 1.10. CT Scanner at Narayana Multispecialty Hospital, Whitefield. General Electric Optima. Author Narenfox, reprinted without alterations under license CC-BY-SA-4.0

CT has a 1000-fold discrimination range of tissue density compared to X-ray[60]. CT can produce images with resolutions of 0.23-0.35 mm[64]. Newer advances, like the high spatial resolution CT (HSR-CT), can make images with a resolution of 0.15 mm at the cost

of higher radiation exposure[65]. These advances have made chest CT scans the current gold standard for lung disease imaging. However, pediatric and longitudinal research are uncommon due to radiation concerns.

1.4.3 LUNG ULTRASOUND

Ultrasound has been historically disregarded in the study of lung disease due to lungs being mostly air and sparse soft tissue[66]. Things changed in 1997 when Lichtenstein et al.[67] showed a correlation between lung ultrasound (LUS) and CT images for the presence of pulmonary interstitial edema and pulmonary fibrosis. Although not technically used for imaging in the sense of creating an image depiction of the lungs, the presence and number of artifacts called B-lines or comet tail artifacts[68] is understood to be a function of amount of air in the lungs. Figure 1.11 shows the presence of B-lines.

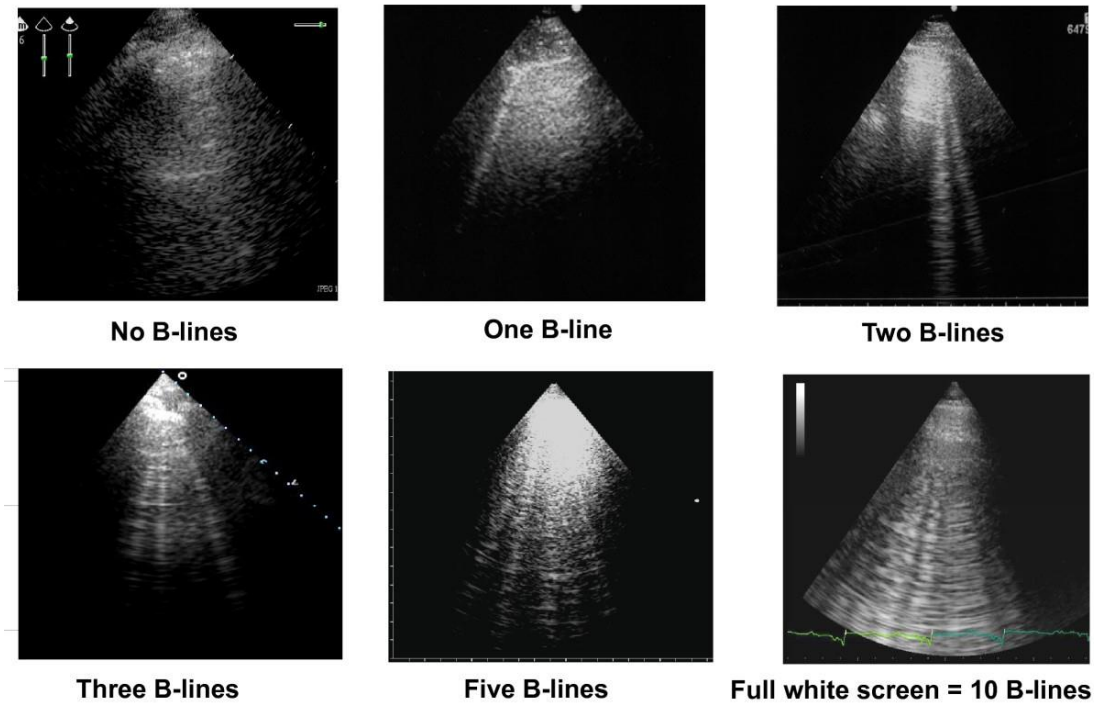

Figure 1.11. B-lines and how to enumerate them, unaltered from original[66], licensed under CC BY 2.0

The advantages of ultrasound are that it is generally safe, has no ionizing radiation, it is relatively inexpensive, and provides real time imaging. Ultrasound equipment is also portable making it the preferred choice in emergency care and mobile clinics. Some uses include rapid detection of pneumothorax and real time localization of pleural effusions for planned thoracentesis.

1.4.4 ULTRASHORT ECHO MRI

MRI of the lungs has lagged behind CT due to insufficient signal of the lung parenchyma. The biggest contributors to low signal of the lungs are the low proton density and fast signal decay due to the tissue/air interface[69] which results in large image voids inside the thoracic cavity.

Advances in scanner technology and sequence design have made MRI a possible alternative to CT lung imaging with the introduction of ultrashort echo (UTE) sequences. UTE lung imaging has been shown to have comparable efficacy for detecting lung disease to CT[70,71]. A major benefit is that UTE MRI made possible morphological scans without the risk of ionizing radiation[72]. Another advantage is that when UTE is paired with functional methods (discussed in 1.5 and 1.6), MRI provides the capability of morphological and functional acquisition in one single session without the need of other scan modalities.

UTE was first introduced by Bergin et al. in 1991[73] with a 3D radial sequence and an echo time (TE) of 0.05 ms, 2D slice selective methods were later introduced[74,75]. In general, UTE sequences have a non-cartesian acquisition with center out trajectories, which add the benefit of oversampling low frequencies and increasing signal to noise ratio (SNR). In general, TEs of less than 0.1 ms are required to capture signal before dephasing

occurs in the lung parenchyma. Spatial resolutions of $1mm^3$ have been reported at 3T[76]. Figure 1.12 shows a lung UTE image taken at breath hold of a healthy volunteer.

Figure 1.12. Lung UTE image of a healthy volunteer taken at breath hold (TE 0.05ms, 3T, resolution 2.1 x 2.1 x 2.5 mm, 18 second scan time)

1.5 NUCLEAR IMAGING

Nuclear imaging refers to the methods using radioactive contrast agents to measure various functional outcomes. These methods include scintigraphy, single photon emission computed tomography (SPECT), and positron emission tomography (PET). All three

methods use small amounts of radioactive material in either aerosol or injectable forms (called radiotracers). Exposure to ionizing radiation is therefore unavoidable. Nuclear imaging can be categorized as functional imaging since their goal is to measure function and not visualize morphology.

1.5.1 SCINTIGRAPHY AND SINGLE PHOTON EMISSION COMPUTED TOMOGRAPHY

Scintigraphy and SPECT have the same relationship as X-ray and CT, one is the tomographic (SPECT and CT) version of the other (Scintigraphy and X-ray). Scintigraphy and SPECT rely on the measurement of gamma ray radiation. Scintigraphy and SPECT can be traced back to the invention of the modern gamma camera by Hal Oscar Anger in 1957[77]. Gamma scintigraphy with inhaled aerosols for lung imaging was introduced in 1981[78] by three groups[79–81]. The beginning of modern SPECT is attributed to David E. Kuhl for his design innovation on probe systems in 1966[82].

In the context of lung imaging, the preferred tracers are technetium (^{99m}T) or technetium diethylenetriamine penta-acetic acid (^{99m}Tc-DTPA)[83]. Scintigraphy and SPECT for lungs may be used to measure ventilation, drug deposition, mucociliary clearance, epithelial permeability, and perfusion imaging[83,84]. For ventilation imaging, ^{99m}T in gas form, Technegas (Cyclopharm Ltd, Australia), is inhaled by patients and data is acquired[85]. For perfusion, ^{99m}T is loaded into macroaggregated albumin (MAA) and supplied to the patient as an aerosol[86,87]. The MAA particles then get trapped in the lung capillaries and the measured local concentration is related to perfusion.

Modern SPECT is often combined in the form of SPECT/CT machines where the functional information from SPECT can be complemented with the morphologic information

from CT. Typical resolutions for scintigraphy and SPECT are 10-14 mm. Figure 1.13 shows an example SPECT/CT scan of ventilation and perfusion.

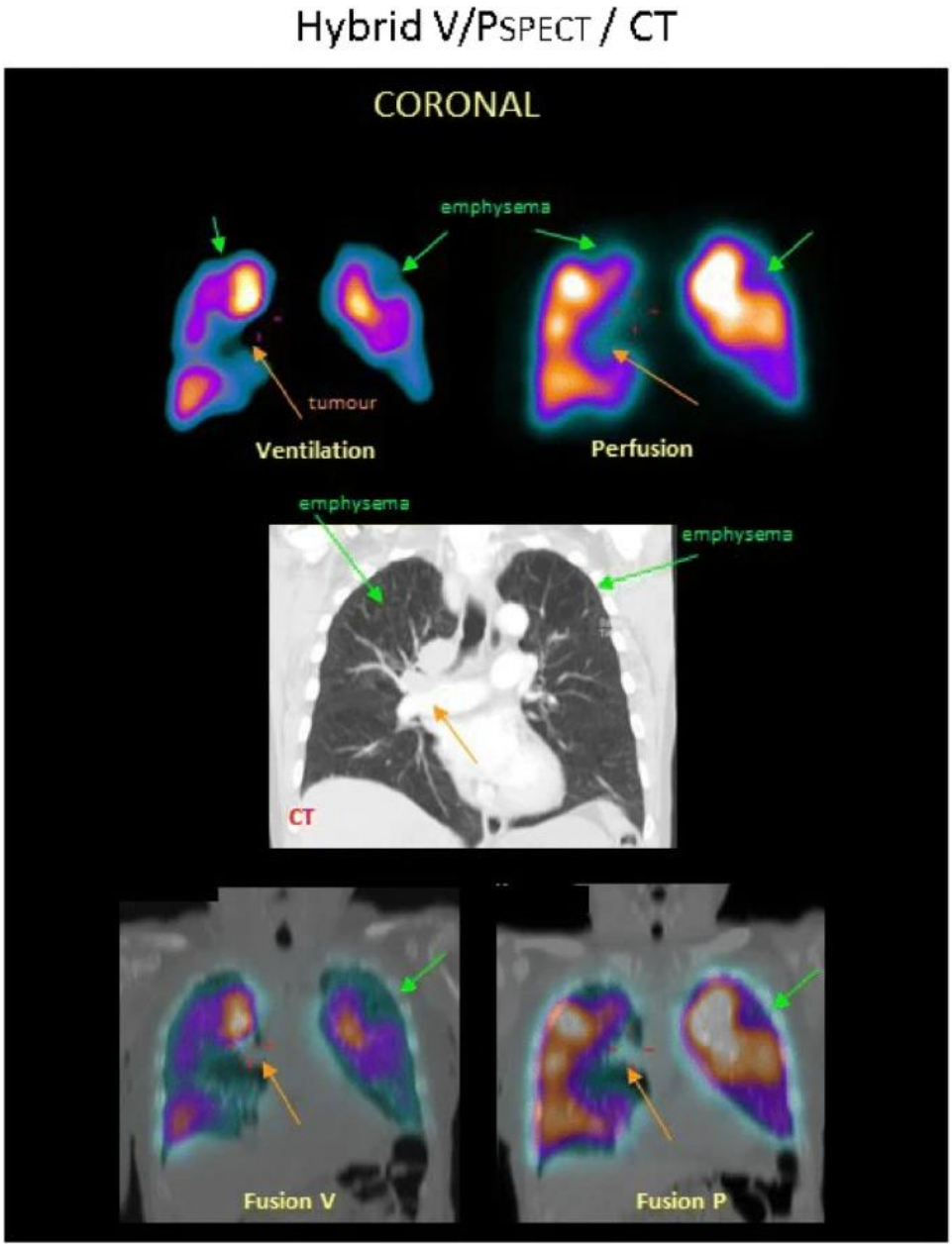

Figure 1.13. SPECT/CT of a patient with COPD, emphysema, and a tumor. The bottom fusion images are the SPECT and CT images overlaid. Figure taken from the EANM guideline[88] with no alterations under license CC BY 4.0

1.5.2 POSITRON EMISSION TOMOGRAPHY

PET is similar to SPECT but uses specific tracers such as ^{11}C and ^{18}F. The tracers used in PET produce positrons, the positrons interact with the surrounding electrons and produce 511 keV photons. The photons move in opposite directions and are then measured by the PET scanner. The first PET machine was built in 1974 by Michel M. Ter-Pogossian and colleagues (Michael E. Phelps, Jerry Cox, and Edward Hoffman among others) in Washington University St. Louis[89]. After a research period, PET became accepted in the clinical sector in the 1990s. Modern PET is usually incorporated into CT and MRI scanners.

^{18}F is the radioactive isotope of fluorine and is used as a radioactive tracer. The most commonly used form is ^{18}F-fluorodeoxyglucose (18F-FDG). 18F-FDG is a form of glucose and when injected can be used to measure abnormal sites of glucose metabolism and characterize many types of tumors. When scanned in conjunction with CT as in PET/CT scanners (or PET/MRI), anatomical data can be acquired in conjunction for precise localization[90].

PET for the lungs has been used to study inflammation[91], deposition[92,93], ventilation, and perfusion[94,95]. The typical PET resolution is 4-6 mm[83]. Compared to SPECT, PET gives better resolution but is higher in cost.

1.6 X-NUCLEI MRI

X-nuclei MRI refers to MRI acquisitions using nuclei other than the standard ^{1}H. This section provides an introduction on the most commonly used x-nuclei for lung MRI in the form of breathable gases.

Due to the imaged nuclei being part of the inhaled gas, the resulting signal comes from the air spaces in the lungs and not the parenchyma. The presence and absence of signal in a

given region of the lung, is therefore directly related to lung ventilation. The methods discussed in this section (and 1.6) are categorized as functional lung MRI methods.

The ability of MRI to isolate the signal of a target nuclei is due to different nuclei having a different resonance frequency (the Larmor frequency discussed in 2.1). Modern MRI scanners with multi-nuclear capable amplifiers and coils are suited for such scans. The excitation pulse is tuned to the Larmor frequency to only excite the target nuclei. Depending on the scanner, there are also frequency filters to minimize signal from unwanted sources.

The main advantage of X-nuclei lung imaging methods is their ability to measure functional information in a spatially localizable 3D manner without ionizing radiation. Table 1.1 shows common isotopes, their spin, abundance, and the magnetogyric ratio (gyromagnetic ratio).

Table 1.1 Isotopes, spin, abundance, and magnetogyric ratio, values from IUPAC recommendations 2001[96]

Isotope	Spin	Abundance	Magnetogyric ratio
		%	γ/10^7 rad s^(-1) T^(-1)
1H	1/2	99.9885	26.7522128
3He	1/2	0.0001	-20.3801587
13C	1/2	1.07	6.728287
15N	1/2	0.368	-2.71261804
19F	1/2	100	25.18148
23Na	3/2	100	7.0808493
31P	1/2	100	10.8394
129Xe	1/2	26.44	-7.452103

1.6.1 HYPERPOLARIZED GASES

Lung MRI with hyperpolarized gases is performed with noble gas isotopes of helium and xenon (^{3}He and ^{129}Xe respectively). Both are inert and non-toxic[97]. While hyperpolarized ^{3}He offers greater signal, ^{129}Xe has the advantage of perfusion measurements. This is due to ^{3}He being non-soluble in water or blood while ^{129}Xe is 10 times and 100 times more soluble in water and fatty tissue respectively. Both ^{3}He and ^{129}Xe have nuclear spin-1/2 (meaning two energy states, see 2.1).

Hyperpolarization is a process used to increase the measurable MR signal through optical pumping. Typical polarization levels used for MRI has been reported to be 25-60% for ^{3}He and 8-20% for ^{129}Xe[98]. 3He and 129Xe can be polarized using a method called spin-exchange optical pumping, where a laser is tuned to the excitation frequency of the valence electron in a transition metal vapor (typically rubidium). The valence electron then exchanges polarization with the imaging gas. For ^{3}He, hyperpolarization can also be achieved using a process called metastability exchange, in which the laser directly excites the He nucleus[98].

^{3}He is rare and costs about 150 US$/liter while ^{129}Xe costs ~30 US$/liter. However, enriched ^{129}Xe commonly used for hyperpolarization costs substantially more. ^{3}He is also a greenhouse gas and as such, has fallen out of favor.

Once polarized, the MR signal decays based on oxygen partial pressure. ^{129}Xe also undergoes change in processional frequency on top of depolarization. Therefore, the MR signal from hyperpolarized gases needs to be calibrated before image formation. Figure 1.14 shows example ^{129}Xe and ^{3}He lung images.

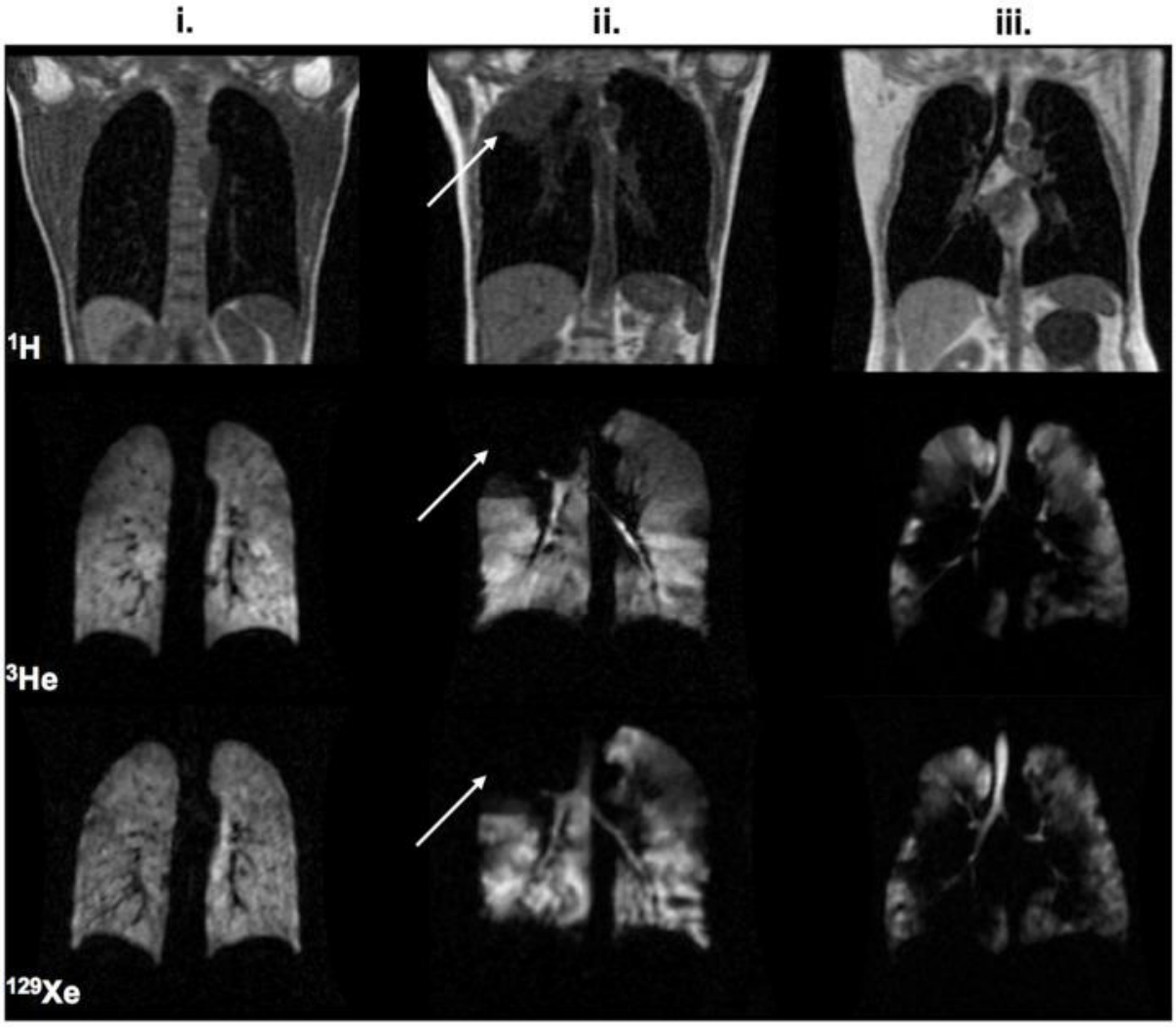

Figure 1.14. Comparison of 3He and 129Xe MR ventilation images of i. a healthy nonsmoker (group b), ii. a patient with NSCLC (white arrows indicate the location of a lesion), and iii. a patient with COPD. Adapted from [99] under the CC BY 4.0 license.

The depolarization effect of regional oxygen on ^{3}He has been used to measure alveolar PO_2 levels in human volunteers[100–102], The solubility of ^{129}Xe and the change in precession frequency based on the local surrounding has been used to measure lung perfusion, a measure not yet possible with ^{19}F. By selecting the imaging frequency with spectroscopy methods, the ^{129}Xe MR spectra has 3 distinct peaks caused by: the gas phase (the gas remaining inside the lung air space), and the dissolved phase. The gas dissolved in

the tissue and blood plasma (barrier) has one peak and the gas dissolved in the red blood cells has another. Figure 1.15 shows the ^{129}Xe spectra peaks in lung imaging.

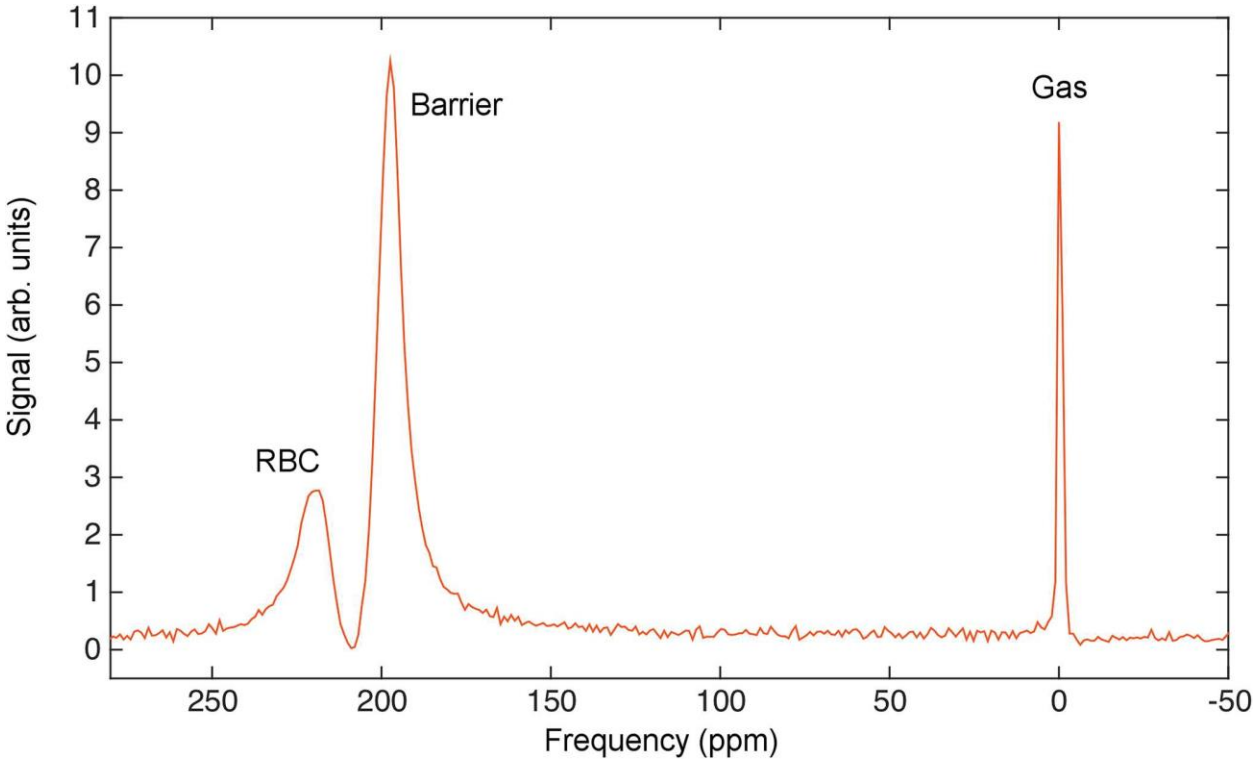

Figure 1.15. 129Xe spectra peaks at different phases in the lungs. Unmodified from[103] and reprinted under the open access CC BY 4.0 license.

1.6.2 FLUORINE

The fluorine isotope ^{19}F is an alternative to hyperpolarized gases in the magnetic imaging of the lungs. ^{19}F is abundant in nature, stable, non-toxic, odorless, colorless, and biologically inert. Due to these qualities, ^{19}F can be stored for long periods of time as a normoxic (21% O_2, 79% ^{19}F) pre-mixture. Which makes the transportation, storage, quality check, and application more practical in the clinical setting than hyperpolarized gases. ^{19}F is also substantially cheaper than hyperpolarized gases at ~15-20 US$/liter.

^{19}F does not need hyperpolarization for MRI, and ^{19}F compounds have 4 or 6 chemically equivalent fluorine atoms per molecule which create a detectable, narrow, spectral peak, using only thermal polarization. ^{19}F has been used in many forms for lung imaging such as SF_6[104], C_2F_6[105], and C_3F_8[106]. Magnetic resonance imaging with ^{19}F dates back to 1977[107], where Holland et al. proposed using perfluorotributylamine as a tracer agent for medical imaging.

Although ^{19}F signal is detectable without hyperpolarization, the signal is weaker than hyperpolarized ^{3}He or ^{129}Xe, therefore, ^{19}F has been historically imaged with larger voxel sizes (typically 6x6x15 mm). Figure 1.16 shows ^{19}F lung images compared to ^{3}He lung images.

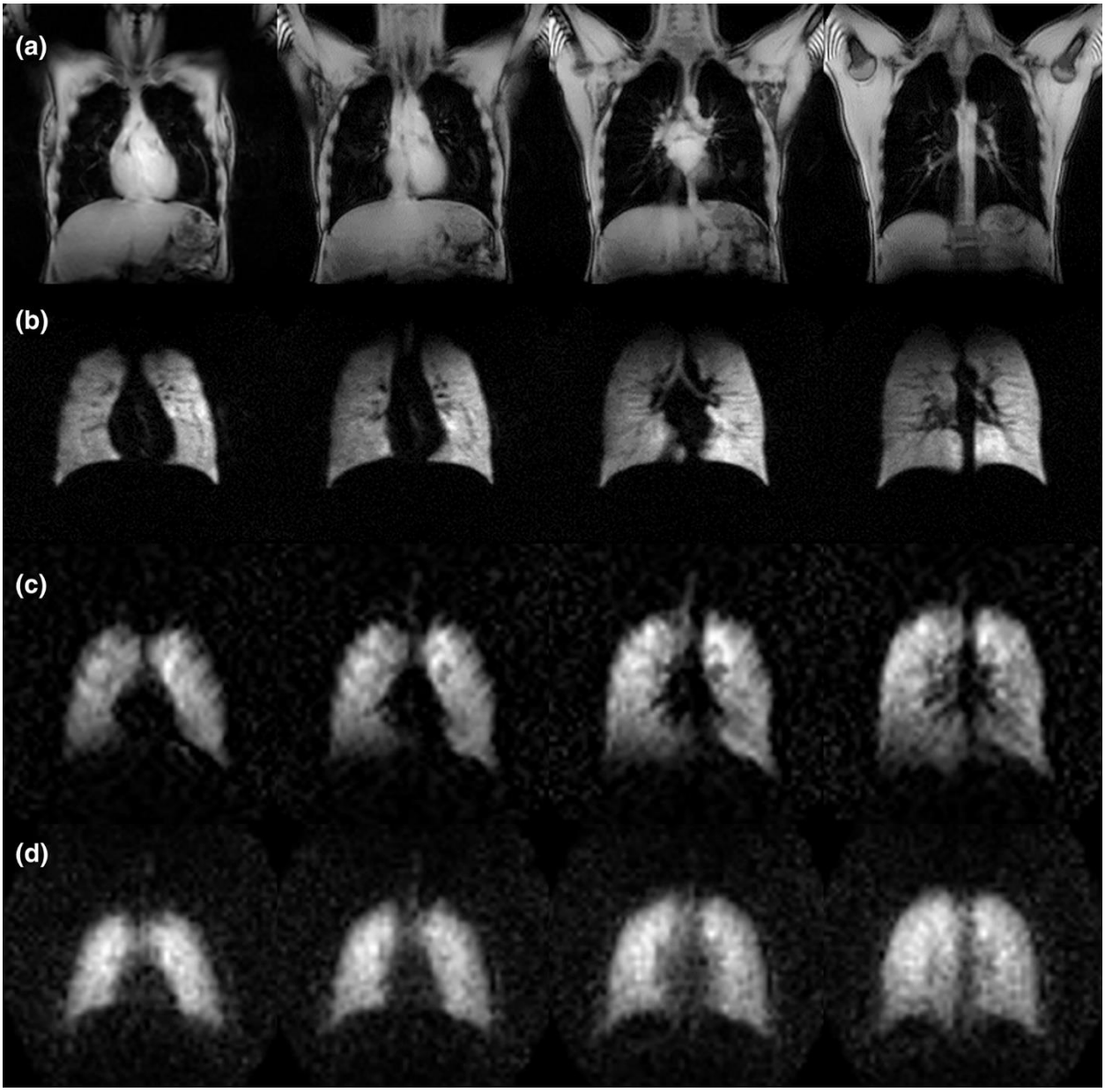

Figure 1.16. Comparison of (a) conventional ^{1}H, (b) HP ^{3}He 2D gradient echo, (c) ^{19}F 3D gradient echo, and (d) ^{19}F 3D UTE images acquired in the coronal plane from a healthy volunteer. Image reprinted unmodified from [108] with permission from the publisher.

^{19}F is stable in the presence of oxygen, therefore it is well suited for multi-breath wash-in wash-out studies without the need for additional flip angle and resonance calibrations. Multi-breath wash-in wash-out studies has been done by various groups with ^{19}F in the past[104,109,110]. While others have acquired data only during the mutli-breath wash-

out portion[105,111]. Multiple ^{19}F gas inhalations in humans has been shown to be generally safe[106,112,113] and have good repeatability in healthy and COPD participants[114].

1.7 ^{1}H BASED FUNCTIONAL MRI

^{1}H based functional MRI of the lungs are methods used to measure ventilation and perfusion with conventional ^{1}H scans. The advantages of these methods are that no additional hardware is needed for exciting and receiving signal. In the case of oxygen enhanced MRI, where 100% O_2 inhalation is used, the cost and availability of the used gas is negligible. Phase-resolved functional lung (PREFUL), a new method recently gaining popularity, uses no extra gas of any form other than regular room air.

1.7.1 PREFUL

PREFUL was introduced in 2019 by Voskrebenzev et al.[115] This method uses rapid ^{1}H scans at free breathing which are later used to sort and process the images for reconstructing a single breathing cycle. Depending on the goal of the processing, ventilation[115] or perfusion[116] data can be obtained from the images. Repeatability has been shown with healthy and COPD patients[117,118]. Figure 1.17 shows ventilation and perfusion maps of two scans of the same patient.

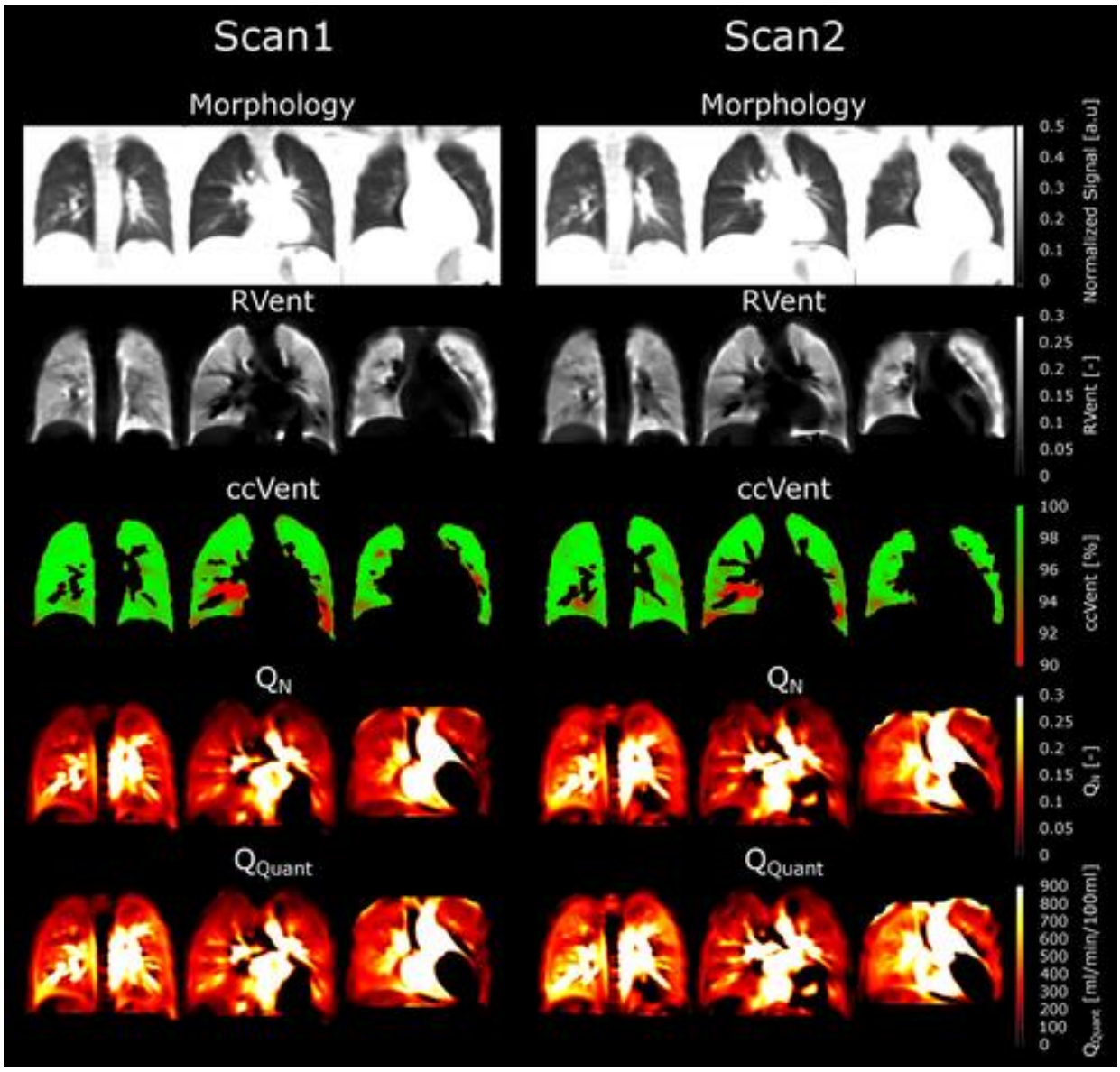

Figure 1.17. Exemplary regional ventilation (RVent), ventilation analyzed by cross-correlation metric (ccVent), normalized perfusion (QN) and quantified perfusion (QQuant) maps from a 30-year-old male healthy subject with a FEV1 predicted of 92%. Posterior, central, and anterior (left to right) coronal slices from scans 1 and 2. The red colored area in ccVent demonstrates where no ventilation is present. Therefore, the ccVent metric shows abnormal dynamics. Reprinted under the CC BY 4.0 license with no modifications from[118]

A limitation with PREFUL is that it is commonly done with one coronal slice (~15mm thickness) per acquisition, this coronal slice requires a clear view of the heart (for perfusion analysis) or the lung-diaphragm interface (for ventilation analysis). 3D

PREFUL[119] was proposed as an alternative method that scans the whole lung volume at higher resolution than 2D. However, perfusion analysis was found not feasible due to the non-selective hard RF pulse. The PREFUL processing limits the ventilation maps to one breathing cycle, which may miss longer temporal ventilation dynamic information such as distinction between slow (ventilated at timescales of multiple breaths) and unventilated areas, or collateral ventilation effects.

1.7.2 OXYGEN ENHANCED MRI

Oxygen enhanced (OE) MRI of the lungs was first proposed by Edelman et al. in 1996[120] as an alternative to noble gas contrast imaging. The underlying working principle of oxygen enhanced MRI works by the paramagnetic effect of oxygen in the lung parenchyma, effectively increasing the parenchyma MR signal in the presence of oxygen. Study participants inhale room air and 100% O_2 at different times and the changes in parenchyma MR signal is attributed to the presence of inhaled 100% O_2, this change in signal is therefore an indirect measure of ventilation. OE MRI has also been shown to be feasible on multi-breath wash-in wash-out dynamic acquisition[121]. Figure 1.18 shows oxygen enhanced MRI and the signal change from inhaling 100% O_2.

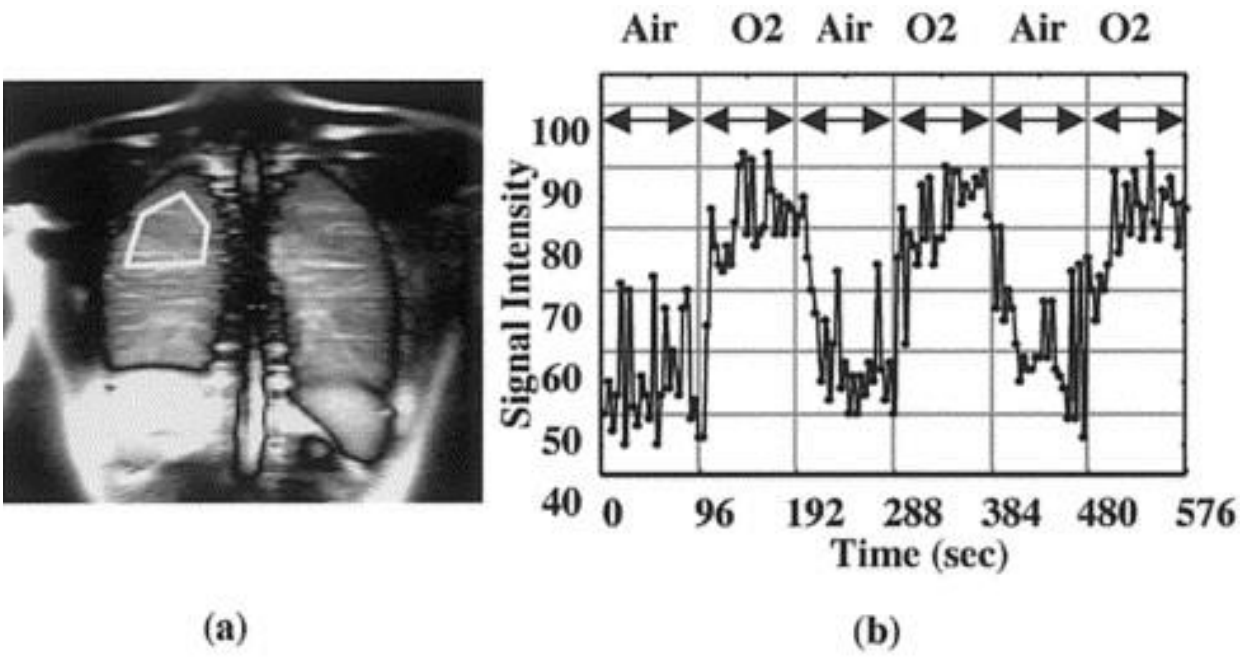

Figure 1.18. (a) T1-weighted anatomic image showing lung morphology. (b) Signal intensity of lung parenchyma versus time in a healthy subject (see RO1 in (a) during alternating inhalation of room air and 100% 02. One image was acquired every 4.8 s. Reprinted unmodified with permission from [122]

One advantage of OE MRI is the associated cost, oxygen is cheap and widely available. Another advantage is that OE does not require specialized equipment such as additional MR coils since the scans are done at ^{1}H frequencies. Lastly OE does not require hyperpolarizing equipment as those needed for ^{3}He and ^{129}Xe. Disadvantages include the low signal change from oxygen enhancing, and that the signal comes from the lung parenchyma instead of the gaseous medium. Table 1.2 shows an overview of logistical advantages and disadvantages of hyperpolarized gases (^{3}He and ^{129}Xe), OE MRI, and ^{19}F MRI.

Table 1.2. Strengths and Challenges of Different Gas Contrast Agents for Pulmonary Functional Imaging. Reprinted[123] with permission from publisher without alterations.

	HP He-3 MRI	HP Xe-129 MRI	OE MRI	F-19 MRI
SNR	High	Med-High	Low	Low
Breath-hold imaging	Yes	Yes	No	Yes*
Cost	~$800-1200/L	$170/L (enriched) $15/L (natural abundance)	<$1/L	$15-20/L
Hardware requirements	MNS T/R Polarizer	MNS T/R Polarizer	Conventional Clinical MRI	MNS T/R
IND required	Yes	Yes	No	Yes
Scan length	5-10 s	5-10 s	5-30 min	12-15 s
Typical spatial resolution	3 mm×3 mm×10 mm	3 mm×3 mm×10 mm	2 mm×2 mm×10 mm	6 mm×6 mm×15 mm
Most common quantitative measures	ADC, VDP, pO_2	ADC, VDP, pO2	MRSER, PSE, OTF	VDP
Repeatability established	Yes	Yes	No	No
Signal weightings	Ventilation, diffusion, oxygen mapping	Ventilation, diffusion, oxygen mapping, Gas exchange	Ventilation and perfusion	Ventilation and Oxygen mapping
Clinical research strengths	High spatial-temporal resolution regional measures of emphysema and gas trapping and airflow obstruction.	Regional measures of emphysema and gas trapping and airflow obstruction. Dissolved phases in tissue and blood are a measure of gas exchange.	Inexpensive, widely accessible method for ventilation weighted imaging. Potential for quantitative ventilation.	Less expensive method for ventilation weighted imaging. Potential for quantitative ventilation.

HP: hyperpolarized; OE: oxygen-enhanced; SNR: signal to noise ratio; IND: Investigational New Drug (FDA) application; ADC: apparent diffusion coefficient; VDP: ventilation defect percentage; pO2: oxygen partial pressure; MRSER: mean relative signal enhancement ratio; PSE: percent signal enhancement; OTF: oxygen transfer function; V/Q: ventilation-to-perfusion ratio. *After multiple breath-wash-in to approach steady-state.

CHAPTER 2: MAGNETIC RESONANCE IMAGING

2.1 NUCLEAR SPIN AND MAGNETIC MOMENT

At its core, magnetic resonance functions due to the phenomenon of nuclear spin behavior to magnetic fields. At the atomic level, all matter is composed of atoms, which are in turn composed of nuclei and electrons. Nuclei have a net electric charge and those that have odd atomic numbers or odd atomic weights have an angular momentum ($\vec{J}$) or spin.

Spins can be thought of as having a vector direction. A common depiction of nuclei with spin is that of a small magnet and its magnetic fields with the north pole corresponding to the positive direction of $\vec{J}$ as shown in Figure 2.1. Similar to a physical magnet, spinning nuclei also generate a magnetic field.

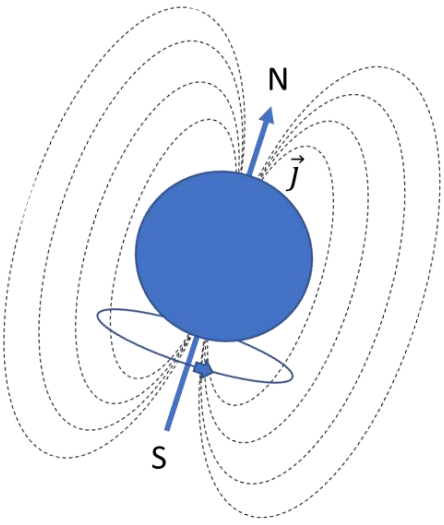

Figure 2.1: Nuclear spin, dashed lines illustrate magnetic fields

The magnetic field from nuclear spin is called the magnetic moment, represented as a vector quantity $\vec{\mu}$. $\vec{J}$ and $\vec{\mu}$ are related by the gyromagnetic ratio γ by

$$\vec{\mu} = \gamma\vec{J} \tag{1}$$

The gyromagnetic ratio is an intrinsic value dependent on the nuclei in units of rad/s/T or MHz/T. This value is important because it shows the spin frequency related to magnetic field strength influencing the spin. Common gyromagnetic ratios are: 42.58 MHz/T for ^{1}H, 10.71 MHz/T for ^{13}C, and 40.05 MHz/T for ^{19}F.

Spins can also be characterized by the nuclear spin quantum number (I) which is dependent on the type of particle. Most common NMR and MRI viable nuclei have I=1/2, although they can be of any value of n/2 where n is any non-negative integer. Nuclei with I not equal to 1/2 are out of the scope of this dissertation. Spin-1/2 systems under an external magnetic field B_0 have two possible discrete orientations that can be represented as the magnetic quantum number $m_I = \pm 1/2$. Each orientation varies in energy which makes one orientation slightly more favorable. In classical mechanics we simply refer to the nuclei orientation as parallel/antiparallel or positive/negative spins. Positive spins are usually assigned the lower energy state.

In practice, the nuclear magnetic resonance (NMR) and magnetic resonance imaging (MRI) signal is generated by an aggregate of multiple nuclei spins that generate a net magnetization $\vec{M}$ large enough to be detectable. A microscopic group of spins resulting in a net magnetization vector $\vec{M}$ is referred as isochromat.

$$\vec{M} = \sum \vec{\mu} \tag{2}$$

In the absence of an external magnetic field, the spins are oriented randomly in all directions resulting in zero net magnetic moment. The first step of signal generation is applying a strong external magnetic field B_0 and allowing the spins to align. This step is passive since it only involves placing the sample or scan object in the magnet bore. Figure 2.2 shows a depiction of the spin behavior under B_0.

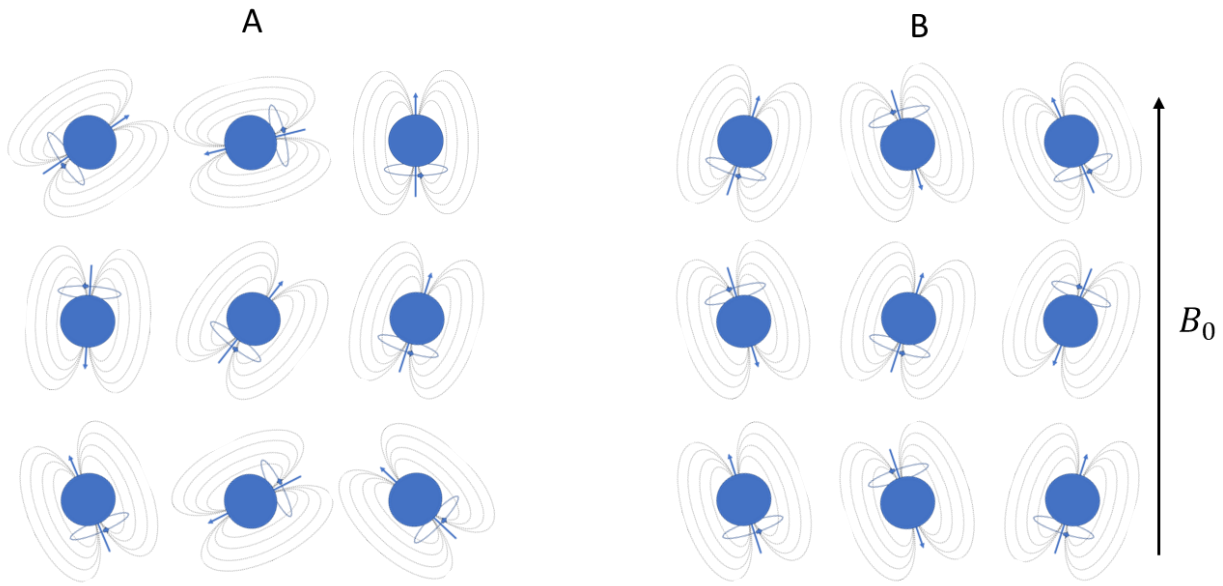

Figure 2.2. Random magnetic moment orientations in the absence of an external magnetic field (A), magnetic moments aligned to B_0 in parallel and antiparallel (B)

With random magnetic moment orientations, $\vec{M} = 0$. When B_0 is applied, there is slightly more parallel aligned nuclei due to it being a quantum state of lower energy. This discrepancy, called Zeeman splitting, is responsible for the detectable signal. In the presence of B_0, a non-zero $\vec{M}$ is induced along the B_0 direction. This state is thought of as being in equilibrium. If the temperature is the same throughout the system and B_0 is present, the spins are said to be in thermal equilibrium. The alignment of the spins is solely based on the thermal energy of the system and is governed by the Boltzman distribution.

In the classical mechanics interpretation, the nuclei dynamics can be interpreted as a spinning top. In addition to spin around its axis, there is also precession. Precession is analogous to the spinning top wobbling (i.e., movement of the spin axis around another axis) and follows the direction of the curl left-hand rule, depicted in Figure 2.3.

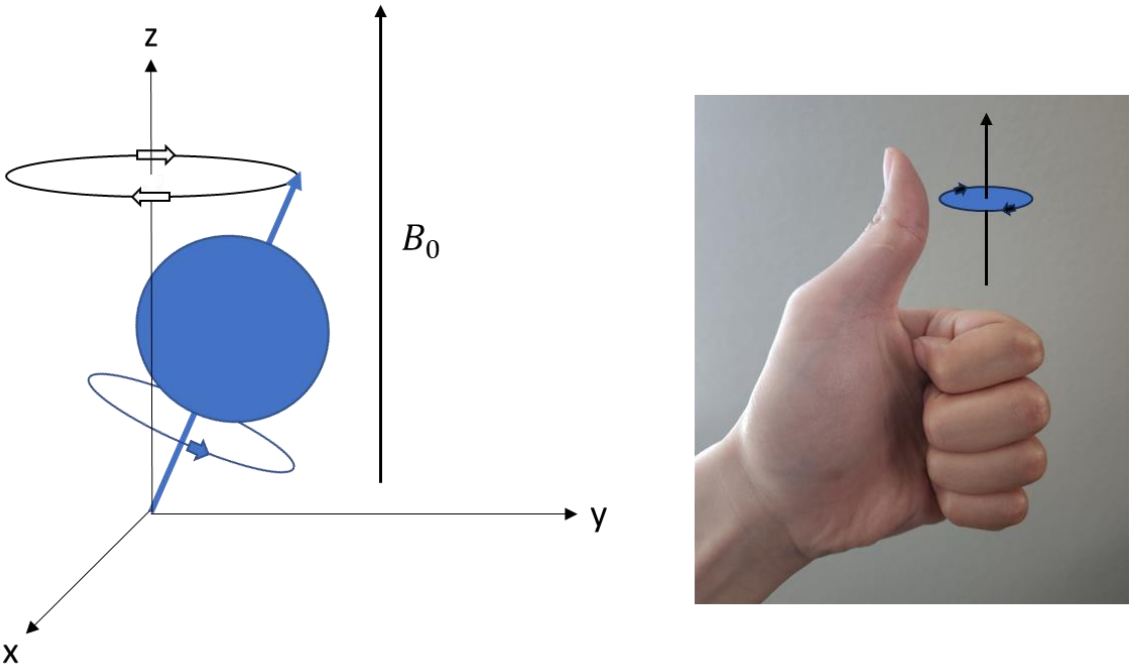

Figure 2.3. Precession around the z-axis

Precession of individual nuclei affects the net magnetization vector and has important repercussions for signal generation. The frequency of precession is dependent on the gyromagnetic ratio γ and external magnetic field B_0 by

$$\omega_0 = \gamma B_0 \tag{2.3}$$

ω_0 is called the Larmor frequency and is the resonance frequency. Note that B_0 is conventionally depicted as parallel and along the positive direction of the z-axis. The equation of motion (at equilibrium and static B_0) in the xy plane is:

$$\mu_{xy}(t) = \mu_{xy}(0)e^{-i\gamma B_0 t} \tag{2.4}$$

While in the z direction it is simply:

$$\mu_z(t) = \mu_z(0) \tag{2.5}$$

Where $\mu_{xy}(0)$ and $\mu_z(0)$ are the magnetic moments at initial conditions. It is useful to separate the magnetic moment between the xy plane (transverse) and z direction (longitudinal) because they relate to relaxation time constants T2 and T1 respectively. Separating relaxation in those two components also organizes magnetization between measurable (transverse) and unmeasurable (longitudinal).

As mentioned before, at equilibrium, the net magnetization $\vec{M}$ has a magnitude along the B_0 field. The xy component of $\vec{M}$ is zero. This happens because the precession phases of individual nuclei are random and end up canceling each other. The second step of signal generation is then to equalize the phases (referred to as phase coherence). Coherence will create a non-zero transverse component of $\vec{M}$ which is measurable.

Creating a measurable signal is accomplished with a radiofrequency (RF) pulse. The RF pulse is an oscillating magnetic field referred as the B_1 field with a carrier frequency ω_{rf}. When $\omega_{rf} = \omega_0$ (resonance), coherence is achieved, and transverse magnetization is created. The RF-pulse also inputs energy into the spin system, in turn reducing the number of spins in the low energy state (parallel). RF pulses usually last few milliseconds and have a much lower magnetic field strength compared to B_0. The resulting effect of an in-resonance RF-pulse is the 'tipping' of the net magnetization vector $\vec{M}$ away from the z-axis. The amount of tipping can be measured in degrees and is called the flip angle (FA) α given by

$$\alpha = \int_0^{\tau_p} \gamma B_1^e(t)dt \tag{2.6}$$

Where τ_p is the pulse duration and B_1^e(t) is an envelope function that controls the pulse shape with magnitude B_1. From equation (2.6) we can conclude that the flip angle is dependent on the pulse duration, pulse shape, and pulse magnitude.

2.2 RELAXATION

Relaxation occurs after the RF-pulse is applied and during the transition between excitation and equilibrium. To understand relaxation, it is easier to visualize the net magnetization vector $\vec{M}$ as the total summation of individual magnetic moments. In the longitudinal direction, the magnetization magnitude depends on the ratio between parallel and antiparallel spins, while transvers magnetization is dependent on precession phase coherence.

Following the longitudinal and transverse context, relaxation can be characterized as longitudinal relaxation (also referred to as spin-lattice or thermal relaxation) and transverse relaxation (also referred to as spin-spin relaxation). Both relaxations follow an exponential decay function with time constants T1 for longitudinal relaxation and T2 for transverse relaxation. T1 is the time it takes for the longitudinal magnetization to reach ~63% of the net magnetization at equilibrium. T2 is the time for the transverse magnetization to lose ~63% of its initial value (from excitation). T1 is always longer than T2. T1 and T2 values vary by type of nuclei and in the case of ^{1}H, by tissue types such as fatty tissue and muscle tissue.

This difference in T1 and T2 values by tissue type is the basis of contrast generation in clinical ^{1}H MRI images, giving rise to the widely used clinical T1 and T2 weighted

images. In practical use, the transverse relaxation time can be thought of as a combination of T2 and T2 prime (T2'). T2' is the dephasing due to external field inhomogeneities and the total observed transverse relaxation is called T2 star ($T2^*$).

$$\frac{1}{T_2^*} = \frac{1}{T_2} + \frac{1}{T\prime_2} \tag{2.7}$$

2.3 BLOCH EQUATION

In 1946, Felix Bloch published "Nuclear Induction"[124] which is the basis for the widely known Bloch equation. Further improvements, like adding the diffusion term, were done by Slichter[125] and Torrey[126]. The Bloch equation is a mathematical description of the net magnetization vector $\vec{M}$ as a function of time. This equation is particularly useful because it describes the change in magnetization given the relaxation time constants T1 and T2. It also has separate terms for the longitudinal and transverse magnetizations.

The net magnetization vector $\vec{M}$ can be written by its longitudinal component M_z and its transverse component $\vec{M}_{xy}$.

$$\vec{M} = M_x\hat{x} + M_y\hat{y} + M_z\hat{z} \tag{2.8}$$

$$\vec{M}_{xy} = M_x\hat{x} + M_y\hat{y} \tag{2.9}$$

The general form of the Bloch equation is:

$$\frac{d\vec{M}}{dt} = \gamma\vec{M} \times \vec{B}_{ext} + \frac{1}{T_1}(M_0 - M_z)\hat{z} - \frac{1}{T_2}\vec{M}_{xy} \tag{2.10}$$

Where M_0 is the longitudinal equilibrium value given by Curie's law:

$$M_0 = C\frac{B_0}{T} \tag{2.11}$$

Where C is the material's Curie constant in Kelvin and T is the absolute temperature in Kelvin. $\vec{B}_{ext}$ is the external magnetic field composed of the static field B_0 and the RF field B_1.

$$B_{ext} = \hat{x}B_1(t)cos\omega_{rf}t - \hat{y}B_1(t)sin\omega_{rf}t + \hat{z}B_0 \tag{2.12}$$

The Bloch equation in (2.10) is described in the *laboratory reference frame,* so called because the coordinate system is static and based on the scanner's position (x-axis horizontal, y-axis vertical, and z-axis parallel to the scanner bore lengthwise). A way to simplify and allow for further mathematical manipulation is by using the *rotating reference frame*. The rotating reference frame can be thought of as a coordinate frame that rotates along the z-axis at the Larmor frequency ω_0.

The laboratory reference frame and the rotating reference frame are simply related by a rotation with an angular frequency ω_0, assuming the z-axis stays the same:

$$x = x'xon(\omega_0 t) - y'\sin(\omega_0 t) \tag{2.13}$$

$$y = x'\sin(\omega_0 t) + y'\cos(\omega_0 t) \tag{2.14}$$

$$z = z' \tag{2.15}$$

Where x', y', z' are axis of the laboratory reference frame and x, y, z, are the axis of the rotating reference frame.

One of the most known and useful derivations of the Bloch equation is the transverse magnetic equation derived below[127].

Slichter[125] derived the relationship between the rate of changes of two reference frames:

$$\left(\frac{d\vec{M}}{dt}\right)_{lab} = \left(\frac{d\vec{M}}{dt}\right)_{rot} - \omega_o\hat{z} \times \vec{M} \tag{2.16}$$

Ignoring relaxation terms and combining equations (2.10) and (2.12) we get

$$\frac{d\vec{M}}{dt} = \gamma\vec{M} \times (\hat{x}B_1(t)cos\omega_{rf}t - \hat{y}B_1(t)sin\omega_{rf}t + \hat{z}B_0) \tag{2.17}$$

Then use equation (2.17) to convert equation (2.18) to the rotating reference frame

$$\left(\frac{d\vec{M}}{dt}\right)_{rot} = \gamma\vec{M} \times \left(\hat{x}B_1(t)cos\omega_{rf}t - \hat{y}B_1(t)sin\omega_{rf}t + \hat{z}B_0 - \frac{\omega_o\hat{z}}{\gamma}\right) \tag{2.18}$$

To convert $B_1(t)$ to the rotating reference frame, use a rotation matrix in the form of:

$$\begin{bmatrix} B_{1,x}(t) \\ B_{1,y}(t) \\ B_{1,z}(t) \end{bmatrix}_{rot} = \begin{bmatrix} cos\omega_0 t & -sin\omega_0 t & 0 \\ sin\omega_0 t & cos\omega_0 t & 0 \\ 0 & 0 & 1 \end{bmatrix} \begin{bmatrix} B_{1,x}(t) \\ B_{1,y}(t) \\ B_{1,z}(t) \end{bmatrix}_{lab} \tag{2.19}$$

$B_1(t)$ in the laboratory frame is given by

$$\vec{B}_1(t) = \hat{x}B_1(t)cos\omega_{rf}t - \hat{y}B_1(t)sin\omega_{rf}t \tag{2.20}$$

Combining (2.19) and (2.20)

$$\begin{bmatrix} B_{1,x}(t) \\ B_{1,y}(t) \\ B_{1,z}(t) \end{bmatrix}_{rot} = \begin{bmatrix} cos\omega_0 t & -sin\omega_0 t & 0 \\ sin\omega_0 t & cos\omega_0 t & 0 \\ 0 & 0 & 1 \end{bmatrix} \begin{bmatrix} B_1(t)cos\omega_{rf}t \\ B_1(t)sin\omega_{rf}t \\ 0 \end{bmatrix}_{lab} \tag{2.21}$$

Solve the matrix to get

$$B_{1,x,rot}(t) = B_1(t)\cos(\omega_0 - \omega_{rf})t \tag{2.22}$$

$$B_{1,y,rot}(t) = B_1(t)\sin(\omega_0 - \omega_{rf})t \tag{2.23}$$

$$B_{1,x,rot}(t) = 0 \tag{2.24}$$

Replace equations (2.22) and (2.23) into (2.18) to obtain the rotating reference frame Bloch equation

$$\left(\frac{d\vec{M}}{dt}\right)_{rot} = \gamma\vec{M} \times \left(B_1\left(\hat{x}\cos\left(\omega_{rf} - \omega_0\right)t - \hat{y}\sin\left(\omega_{rf} - \omega_0\right)\right) + \hat{z}B_0 - \frac{\omega_o\hat{z}}{\gamma}\right) \quad (2.25)$$

Solve the cross product to get

$$\frac{dM_{x,rot}}{dt} = \gamma M_y\left(B_0 - \frac{\omega_0}{\gamma}\right) + \gamma M_z B_1(t)\sin\left(\omega_{rf} - \omega_0\right)t \quad (2.26)$$

$$\frac{dM_{y,rot}}{dt} = -\gamma M_x\left(B_0 - \frac{\omega_0}{\gamma}\right) + \gamma M_z B_1(t)\cos\left(\omega_{rf} - \omega_0\right)t \quad (2.27)$$

The transverse magnetization vector $\vec{M}_{xy}$ can also be written as a complex value M_+:

$$M_+ = M_x + iM_y \quad (2.28)$$

Using equations (2.27) and (2.28) get the transverse magnetization equation:

$$\frac{dM_{+,rot}}{dt} = -i\gamma M_+\left(B_0 - \frac{\omega_0}{\gamma}\right) + i\gamma M_z B_1(t)e^{-i(\omega_{rf}-\omega_0)t} \quad (2.29)$$

Equation (2.29) describes the transverse magnetization after an RF pulse with angular frequency ω_{rf} in a rotating reference frame with angular frequency ω_0.

2.4 LOCALIZATION

In magnetic resonance imaging, localization refers to the techniques used to encode spatial information to the received signal. Localization is achieved by a combination of gradient switching and timing. This is a crucial part of sequence programming and k-space navigation. For basic modern sequences, localization can be divided into three main steps: slice selection, phase encoding, and frequency encoding. By convention, the slice selection gradient is on the z-axis, the phase encoding gradient is on the y-axis, and the frequency encoding gradient is on the x-axis. The z-axis runs from the front of the scanner to the back

parallel to the scanner bore, the y-axis and x-axis are along the vertical and horizontal directions respectively. The coordinate system follows the right-hand rule.

Gradients can be thought of as changes to the static magnetic field B_0 along each axis, usually with the units of milli Tesla over meter (mT/m). Another way to thinking about gradients is as a change of B_0 with the slope of the gradient amplitude (mT/m) in the direction of an axis. Figure 2.4 illustrates the effect of gradients along all three directions.

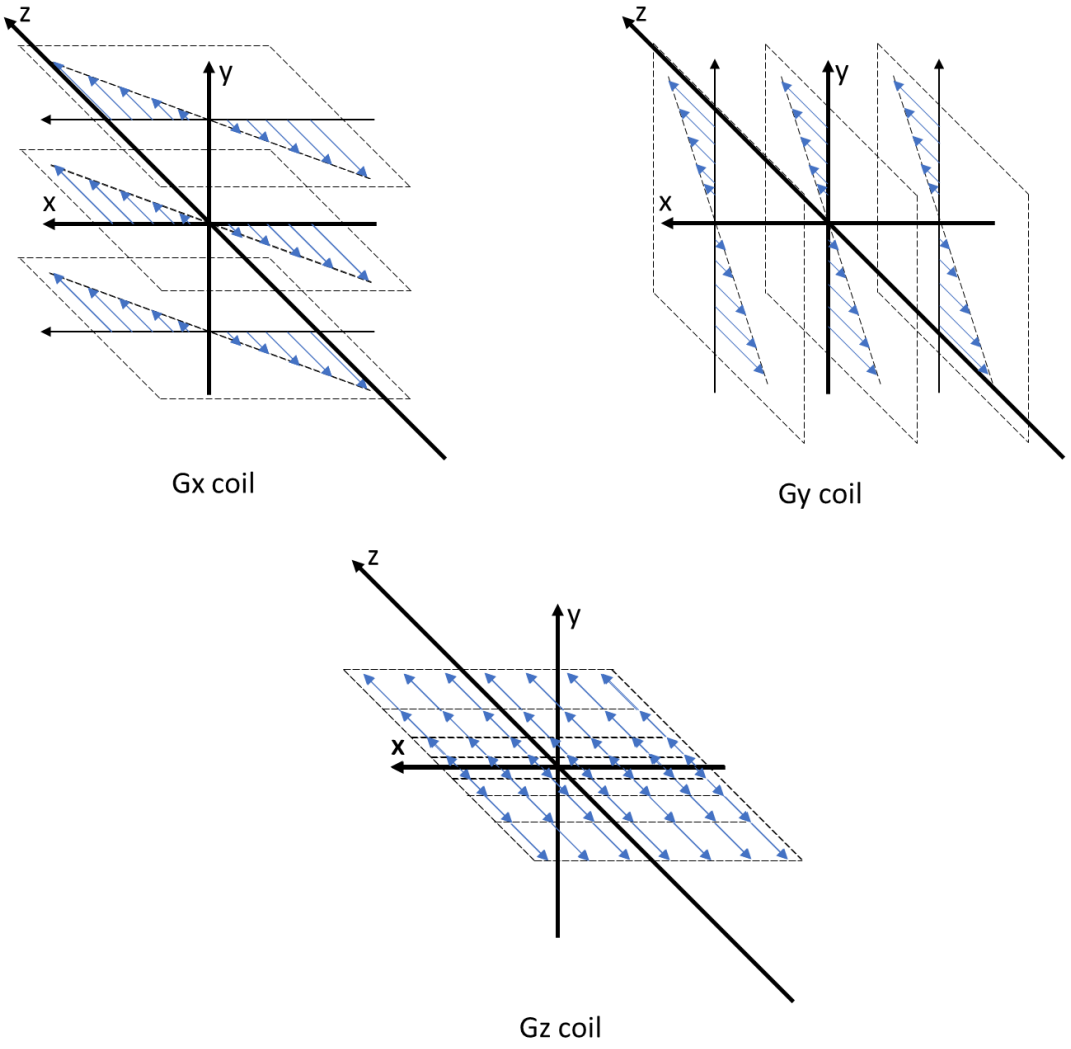

Figure 2.4. Depiction of active gradient coils in the coordinate system, blue arrows indicate direction and strength of gradients.

From figure 2.4, notice that the change in gradient strength (difference between each blue arrow) is along a set axis. Another observation is that there is no change in gradient magnitude along the other two axes. What is referred to as the gradient magnitude in mT/m is therefore the slope of the line connecting each blue arrow's head. Further explanation about gradients can be found in 'Foundations of medical imaging' by Zang-Hee Cho[60] Chapter 9.

2.4.1 SLICE SELECTION

Slice selection is the portion of an MRI sequence used to 'select' or activate a slice for imaging. It is usually performed with the Gz gradient. This selection occurs in the physical space and acts by sensitizing a slice to excitation.

From the Larmor frequency (2.3), we know that the resonance frequency depends on the active magnetic field. A RF excitation pulse will excite (or tip) only spins corresponding to matching frequencies. Therefore, if the RF pulse is activated in the presence of an active Gz gradient, only spins in a wanted x-y plane will be excited. This is the basis of slice selection and can be thought of as altering the spins along the z direction so that only those in a wanted x-y plane correspond (or resonates) to the RF pulse frequency.

2.4.2 PHASE ENCODING

Phase encoding, as the name suggests, uses the magnetization vector phase to encode for localization. A key difference between the phase encoding (and frequency encoding) step to the slice selection step is that this encoding is not on the physical space but can be thought of as a location in k-space. Further discussion on k-space can be found in subsection 2.6.

The underlying principle used for phase encoding is that in the presence of a gradient, the phases will change based on the active magnetic field. Higher fields will speed up the spins and lower ones will slow them down (this is sometimes called pre-frequency encoding, not to be confused with frequency encoding). If the gradient is switched on and off, the result is that the spins further from the center will have changed more in phase proportional to the gradient strength. Figure 2.5 shows the result of turning a gradient on and off.

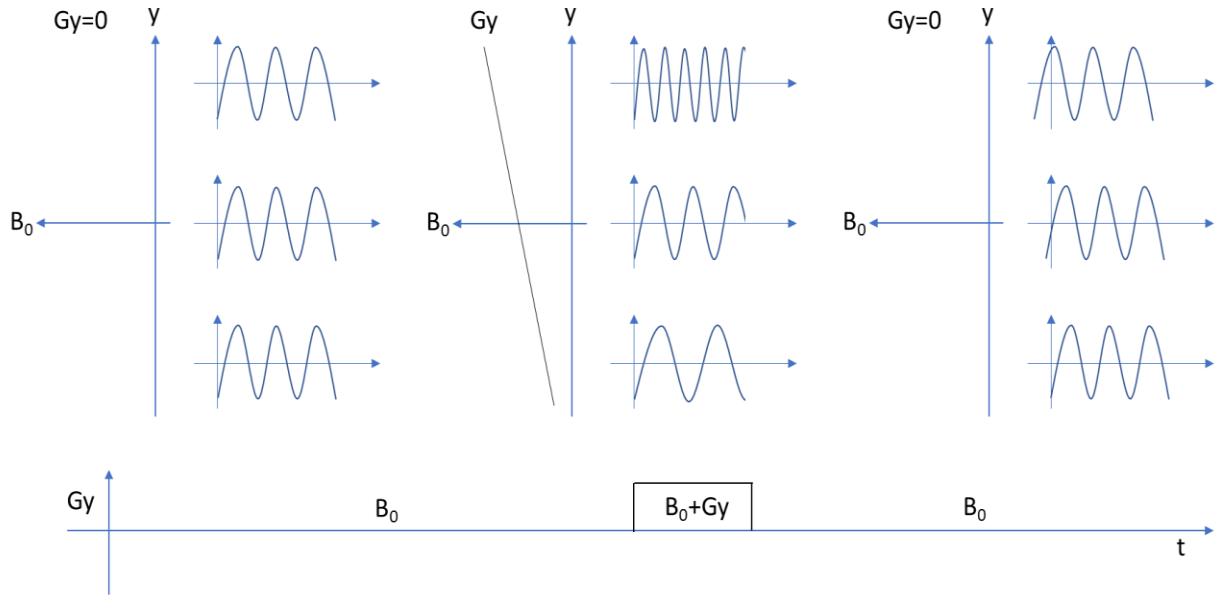

Figure 2.5. Phase encoding, showing the signal of tree spins along the y-axis.

The phase encoding step is usually used after the slice selection step and before the frequency encoding step. After the gradient is turned off, the spins end up with different phases along the direction of the gradient (last column in Figure 2.5).

2.4.3 FREQUENCY ENCODING

Frequency encoding is similar to phase encoding, with the difference that signal acquisition is performed while the frequency encoding gradient is active. Refer to Figure 2.5, in the intermediary step when the gradient is active, the change along the gradient axis is that of frequency and not phase.

As a summary, the slice selection step sensitizes an x-y plane of spins to the RF frequency, the phase encoding step changes the phase of the spins along the gradient, and the frequency encoding step changes the frequency along the gradient. Slice selection, phase encoding, and frequency encoding are usually done on the z, y, and x axes respectively.

2.5 SEQUENCES

Sequences are the set of instructions that the scanner follows to generate images. There are many types of sequences and improvements are an active area of research. Depending on the sequence design, the acquired signal can be sensitized to several different tissues and physical phenomena. This is the basis of the wide array of MRI functionality. Examples of MRI capabilities based on sequence design include water suppression, diffusion, angiography, fMRI, etc. Sequences are usually depicted as a graph over time of the instructions (referred to as chronogram) as shown in Figure 2.6.

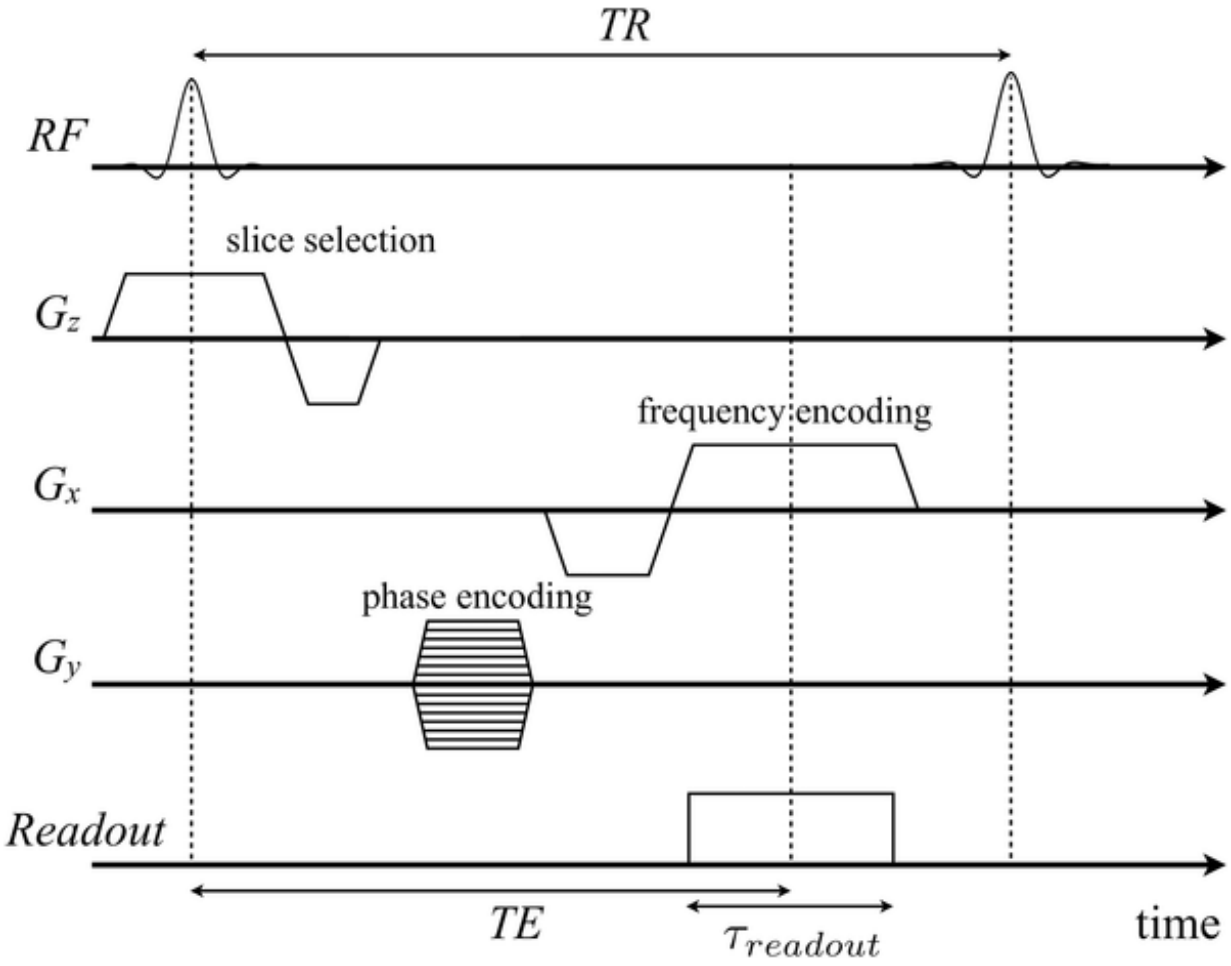

Figure 2.6. Diagram of a typical gradient echo pulse sequence with frequency and phase encoding gradients along x-axis and y-axis, and slice selection gradient along z-axis. Reprinted with no alterations Puiseux et al[128] with license CC BY 4.0.

Note the time parameters TR and TE depicting key timings. Repetition time (TR) is the time of a full sequence design (repeated multiple times at acquisition). Echo time (TE) is the time between the center of the RF pulse to the center of the ADC acquisition or signal echo. Also note the negative lobe in Gz, this is called the rephasing lobe and is used to revert spin dephasing caused by the slice selection gradient. Lastly, the multiple phase encoding lobes indicates that the Gy gradient is changed through repetitions in order to fill a k-space line.

2.5.1 GRADIENT ECHO

The gradient echo (GRE) sequence is one of the most basic sequences and widely available through all MRI system vendors. Depicted in Figure 2.6, the gradient echo is formed using the same gradient used for frequency encoding. Figure 2.7 shows the characteristic lobes of a gradient echo sequence and its effect on the free induction decay (FID) signal.

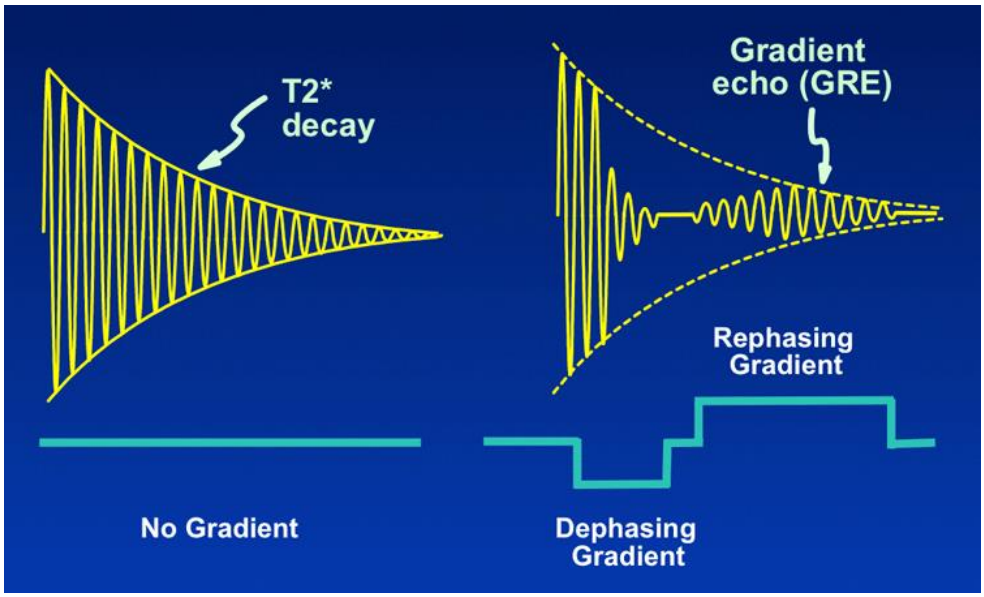

Figure 2.7. The formation of the gradient echo, Courtesy of Allen D. Elster, MRIquestions.com

The FID is dephased with the dephasing gradient, then rephased which creates an 'echo' that recovers the signal. Note that the echo can never the recovered outside of the T_2^* decay boundary (T_2 accounting for molecular interactions and field inhomogeneities). Given that any use of gradient other than 0 will dephase the spins (hence losing signal), the GRE design is a clever way to position the peak signal at the center of the readout without the dephasing effects of the required frequency encoding gradient. Further reading on the GRE sequence can be found in[129,130].

2.5.2 SPIN ECHO

The spin echo sequence is a technique that uses two RF pulses that create an echo of the FID. It was discovered by Erwin Hahn in 1950[131]. Although it was originally introduced with two 90° RF pulses, it is commonly used with a 90° and a 180° RF pulses. Figure 2.8 shows the chronogram of a basic spin echo.

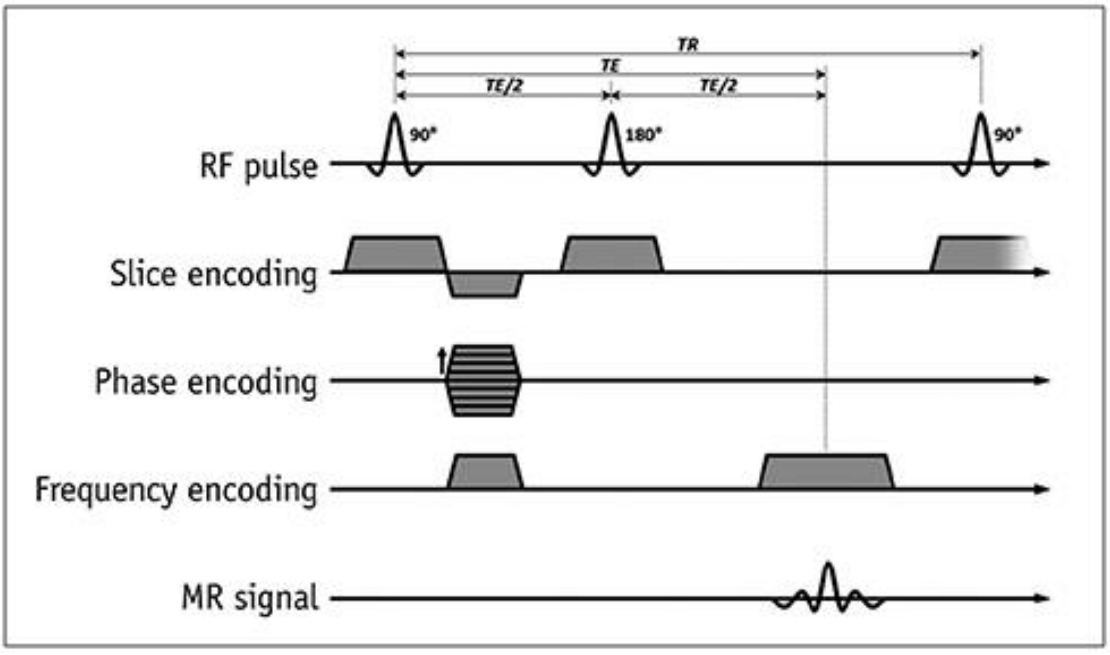

Figure 2.8. A basic spin echo pulse sequence. Reprinted without modification from Jo Y et al[132] under the CC BY-NC 4.0 license

In a spin echo, there are two RF pulses separated by half TE, after another TE/2, the echo forms for measurement. The main advantage of spin echoes is that part of the signal lost to field inhomogeneities can be recovered[133] (opposed to GRE). The recoverable signal is called T_2 prime (T_2'). Figure 2.9 shows the spin echo at the level of isochromats for both T_2' and T_2^*.

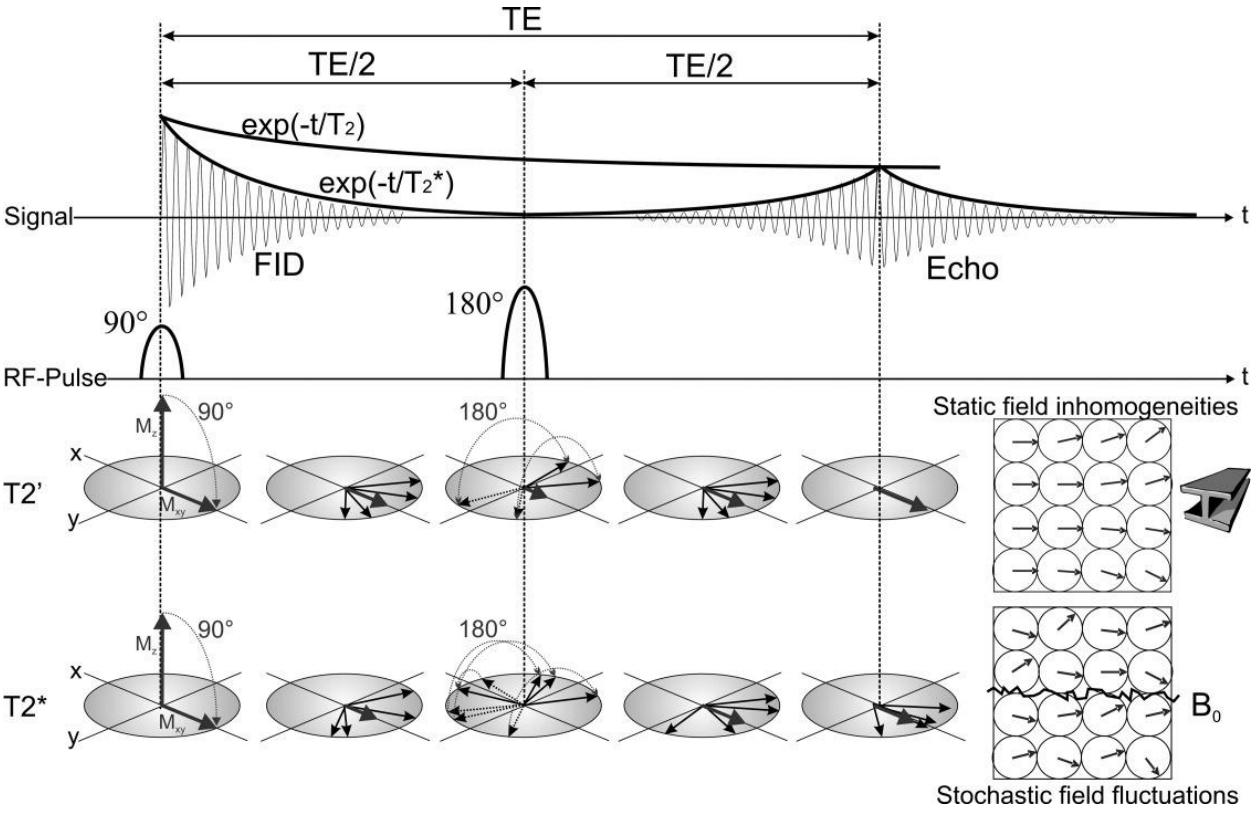

Figure 2.9. The spin echo and isochromats at T_2' and T_2^*. Reprinted with no alterations from Jung et al[134] with permission from the publisher

From Figure 2.9, it is evident that T_2' is fully recovered at the echo. However, even under perfect conditions, the echo cannot recover signal beyond the T_2 decay envelop. The 180° pulse flips the isochromats often described as flipping a pancake and reverts the dephasing. A helpful animation of this process can be found in https://en.wikipedia.org/wiki/Spin_echo.

2.5.3 K-SPACE

K-space is the result of an image Fourier transform. In MRI the acquired signal is in the form of k-space and the inverse Fourier transform is used to generate the resulting image (this process is also called reconstruction, see 2.6). Figure 2.10 shows the relationship between k-space (frequency domain) and the image (spatial domain).

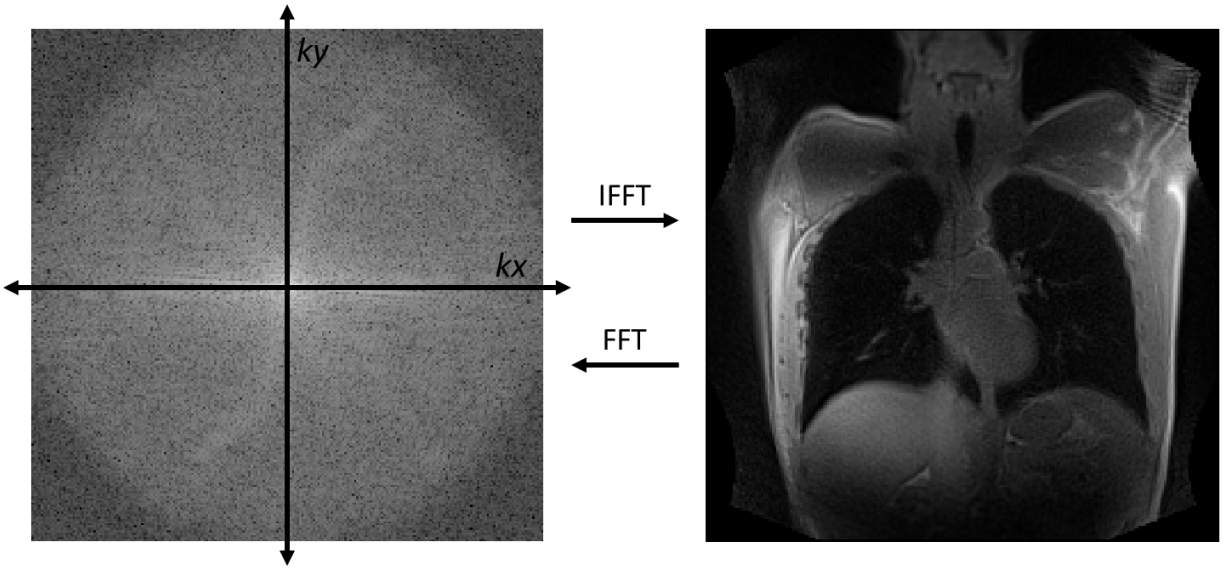

Figure 2.10. Relationship between k-space and image, IFFT is the inverse Fast Fourier transform and FFT is the Fast Fourier transform

Referring to 2.4, the phase and frequency encoding steps are responsible for creating k-space data. K-space is commonly depicted as a 2D image with axes (k_x, k_y) which correspond to scanner axes (x, y) and gradients (G_x, G_y). During a scan, the use of the gradients translates to movement in k-space. For a scan to finish, the k-space data has to be filled (measured discretely), which is often referred to as k-space navigation.

Most common sequences navigate k-space in a cartesian fashion. This means the k-space data or pixels (in k-space) are measured rectilinearly. For basic sequences, each sequence repetition TR measures one horizontal line in k-space. Figure 2.11 shows a GRE sequence and its related navigation in k-space.

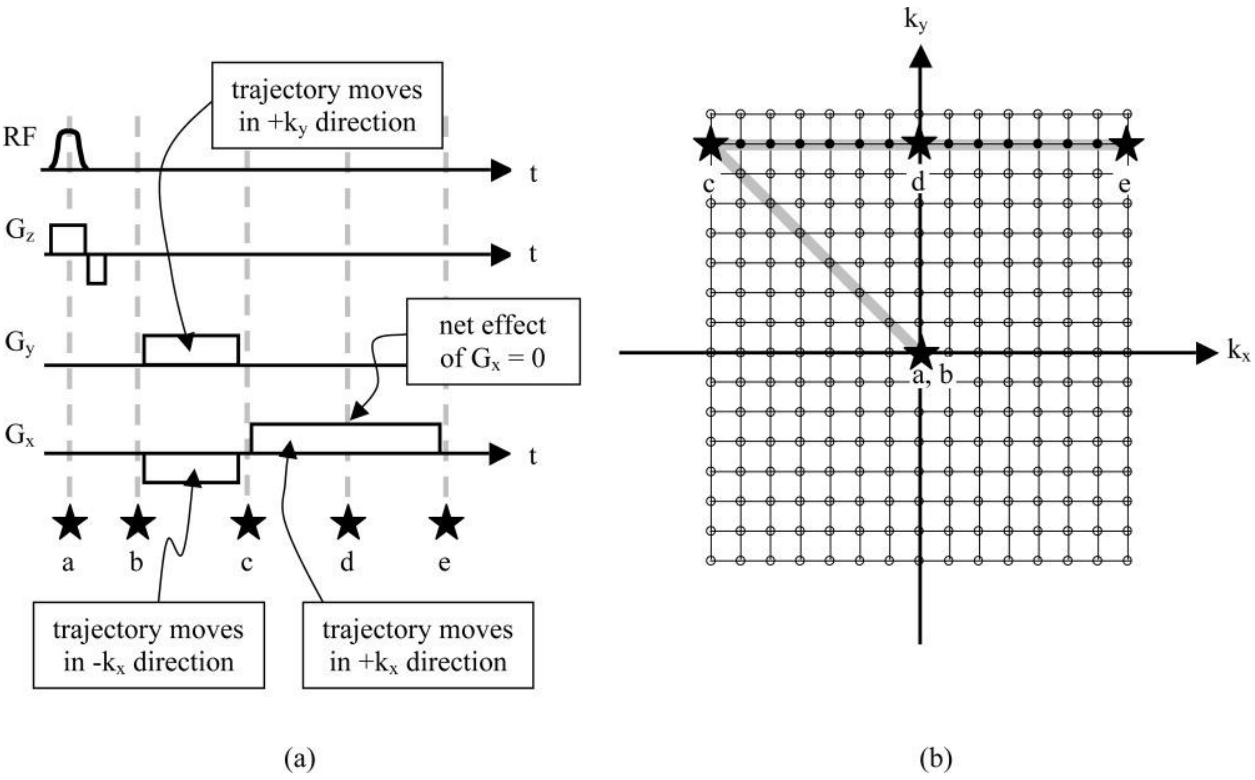

Figure 2.11. Gradient echo pulse sequence (a) and corresponding k-space trajectory (b). Reprinted without modification from Paschal et al[135] with permission from the publisher

By convention, positive Gy gradients move the location in k-space upwards and vice versa. Positive Gx gradients move the location in k-space to the right. The duration of the gradients corresponds to the distance moved in k-space. Therefore, gradient magnitudes correspond to direction in k-space and gradient duration corresponds to distance in k-space. During read-out (data collection between points c and d in Figure 2.11), the ADC collects data discretely, and the ADC sampling frequency is based on the matrix size. Sampling rates are limited by hardware performance limits. There are other trajectories such as radial and spiral trajectories, a good summary of trajectories used in the clinic is reviewed by Paschal et al.[135]

The k-space data can be regarded as complex since it has two components. A common signal detection method is the quadrature method where the detected signal

(voltage) is demodulated and split at a phase shift of 90° from each other. The demodulation split results in the real and imaginary components[136].

The data points in the frequency domain do not correspond to the data points (or pixels) in the spatial domain image. Instead, it is more appropriate to think of each data point in the frequency domain as representing individual images (also called base images) of which the combination creates the spatial domain image. Note that if one were to cut a base image perpendicular to its lines and plot the profile, the graph would have a sinusoidal shape. The center of k-space represents the low frequency, high contrast information. The outer edges represent the high frequency, detailed information (similar to sharpness). K-space figures are shown as the magnitude of the complex values. Figure 2.12 shows a k-space image with example base images. A very helpful Matlab demo is available for free in https://visiome.neuroinf.jp/database/item/6448 by Sasaki and Ohzawa.

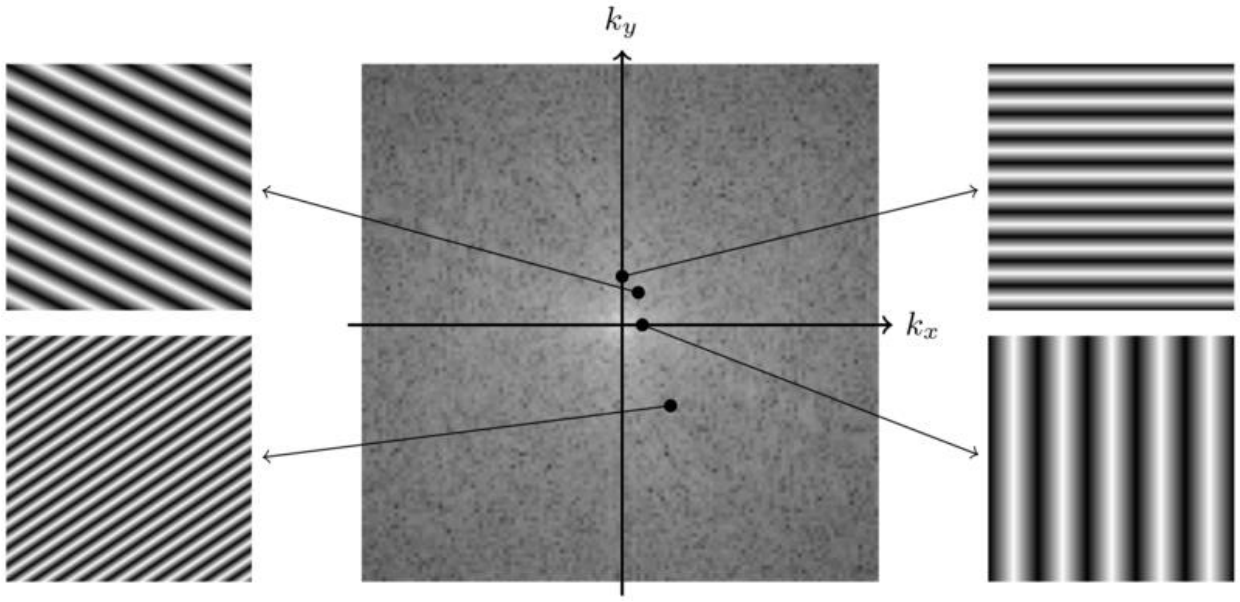

Figure 2.12. Example k-space and base images at different locations in k-space, reprinted unmodified from Maier et al[137] under license CC BY 4.0

To understand the relationship between sine waves, spatial image, and frequency domain better, imagine a 1D data set. We can construct a signal from an addition of several cosine waves (this is done to have individual and known frequency components). See Figure 2.13.

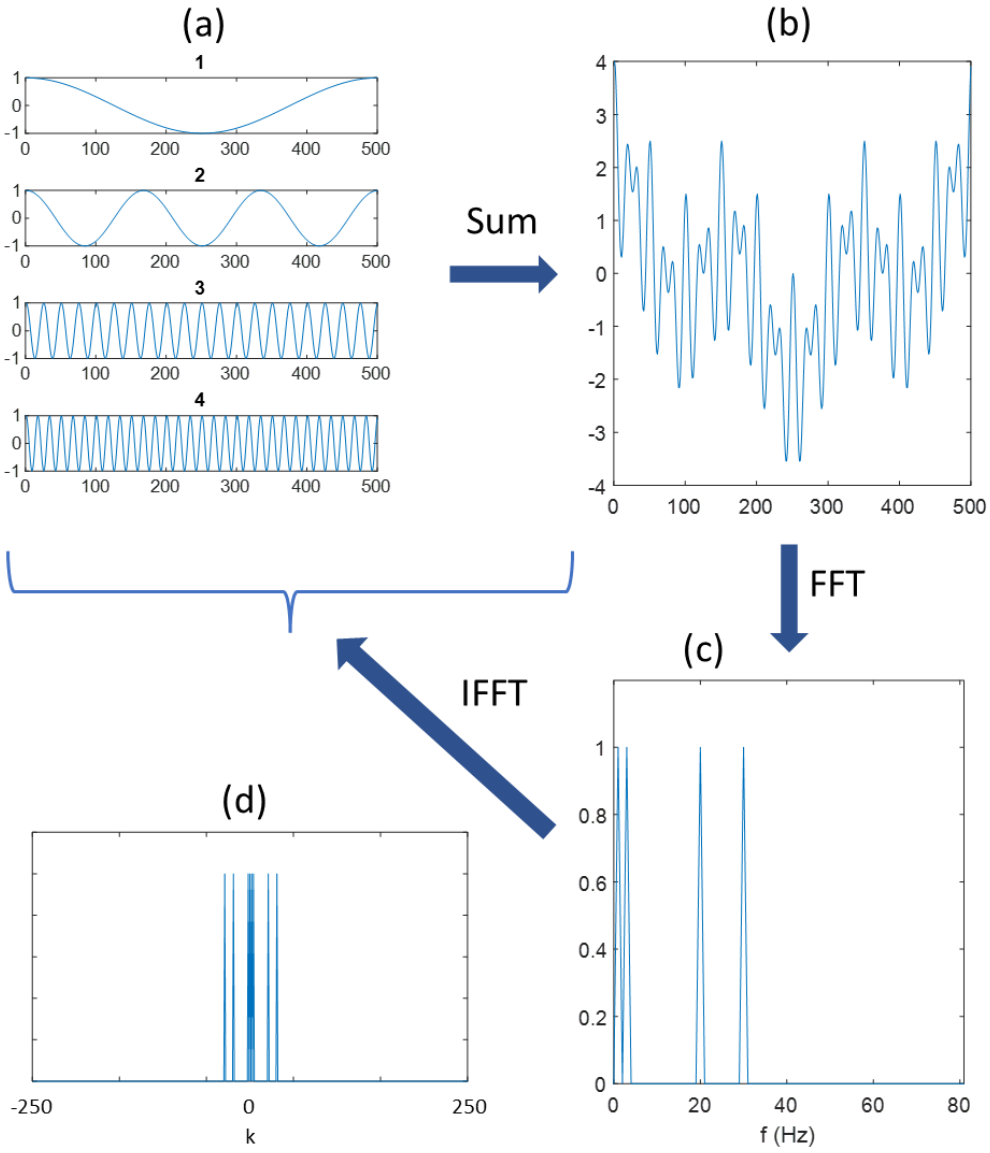

Figure 2.13. (a) frequency components of plotted in the time domain, (b) time domain signal, (c) frequency spectra, (d) spectra in k centered at 0

The spectra peaks in Figure 2.13 (c) match the frequencies of the individual components in Figure 2.13 (a) from the FFT. In this example, the individual components are analogous to the base images, of which the combination results in the time domain signal (Figure 2.13 (b)). Therefore, just as a single point in the spectra does not match a single point in the time domain signal, single points in k-space do not match a point in the spatial image of MRI.

The spectra in Figure 2.13 (c) can also be shown centered at zero by its k components (shown in Figure 2.13 (d)), this way of display is closer to the way k-space is usually shown. Notice that the spectra curve is symmetrical, which is a well-known characteristic of k-space.

2.5.4 ULTRASHORT ECHO TIME

The ultrashort echo time (UTE) sequence has gained popularity on the clinical setting due to it allowing TE times as short as 0.1 ms or lower[138]. In the field of lung imaging, CT is still considered the gold standard. However, recent studies have shown promising results for lung MRI with UTE[139–141], and as a radiation free alternative for children[142,143]

Historically, tissues with short T2s, such as the lung parenchyma, were not visible on MRI scans due to the signal decaying before the readout. The ability to reduce TE comes from altering the RF pulse and using non-cartesian k-space trajectories[144].

Non-cartesian trajectories have the advantage of not needing the initial move to the k-space edge before data collection since they commonly start acquisition from the center of k-space (this is called a center out design).

A potential advantage of center out design is that k-space density is higher at the center, making signal intensity higher. Figure 2.14 shows examples of cartesian, radial, and spiral trajectory sequences with their corresponding k-space trajectories.

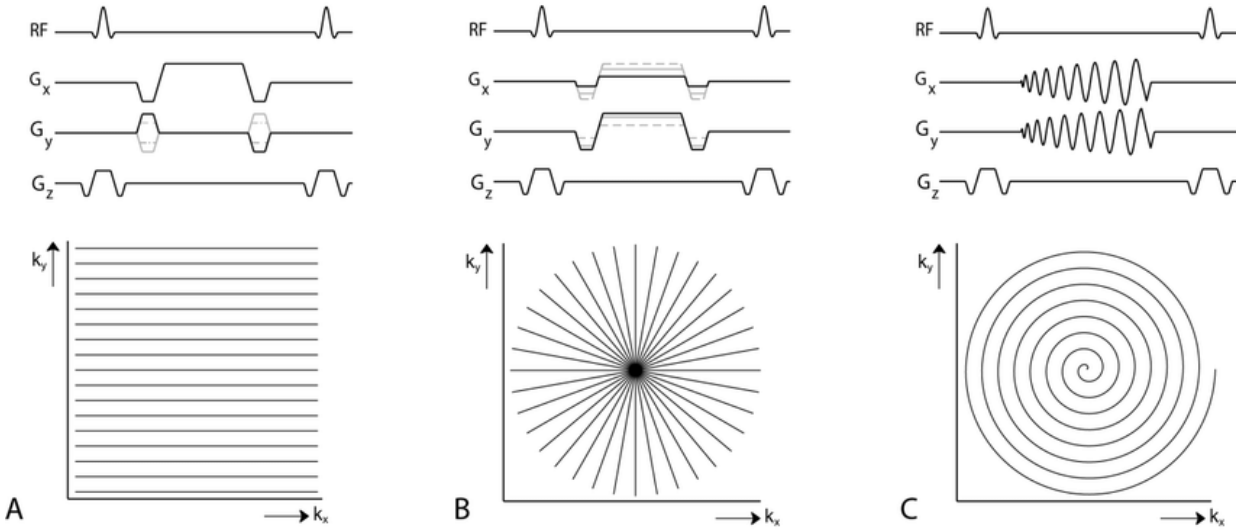

Figure 2.14. Cartesian (a), radial (b), and spiral(c) sequences and k-space trajectories. Reprinted without modification from Stemkens et al[145] under license CC BY 3.0

UTE sequences take advantage of non-cartesian trajectories in both 2D and 3D forms. 2D imaging refers to sequences with slice selective pulses, however they can still collect full 3D volumes by acquiring multiple slices. 3D scans are sequences where the k-space trajectory is 3d instead of a flat plane. Figure 2.15 shows 2D and 3D UTE sequences.

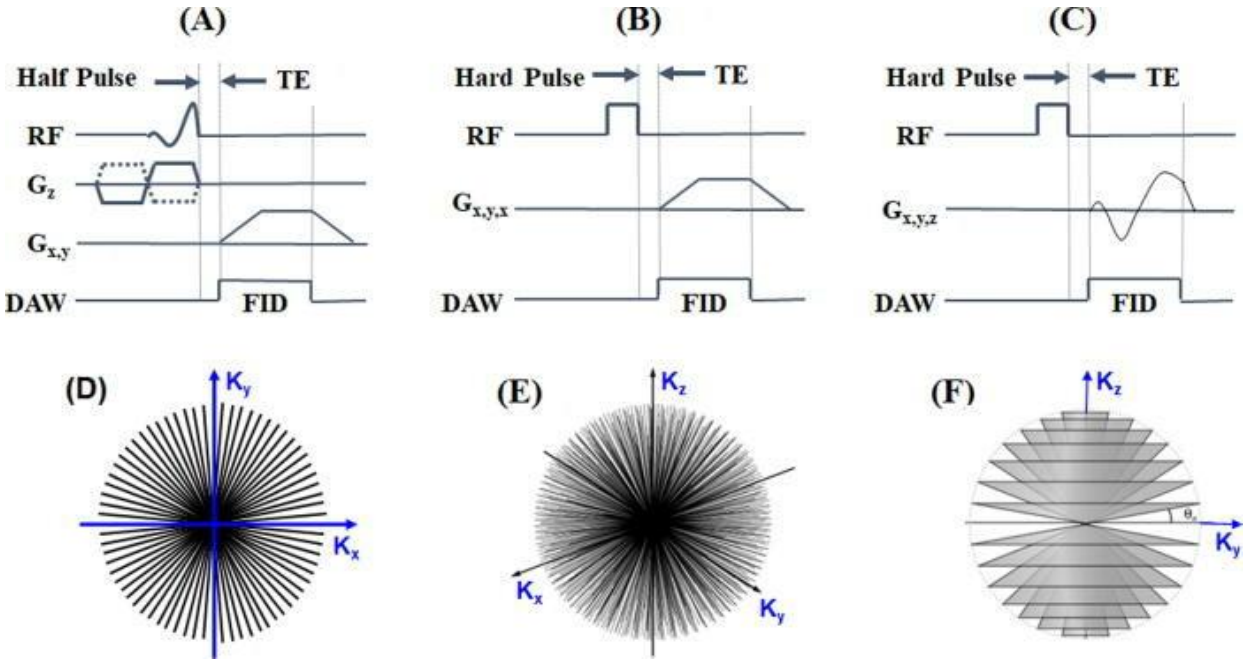

Figure 2.15. Diagrams of the 2D radial UTE sequence (a), the 3D radial UTE sequence (b), and the 3D spiral UTE sequence (c), as well as the corresponding k-space trajectories (d)–(f). Reprinted without modification from Ma et al[138] with permission from the publisher.

Notice that the 3D sequences in Figure 2.15 don't have slice selective Gz lobes. Instead, Gz is treated as another k-space navigation axis.

2.6 RECONSTRUCTION

Reconstruction is the process of taking the collected k-space data and getting the spatial domain image. This process can be done right at the scanner automatically or done post scan. The main step in reconstruction involves using the inverse Fourier transform (IFT) which is the reverse of the Fourier transform (FT). First introduced in 1821 by French mathematician Jean-Baptiste Joseph Fourier[146], the FT has had many versions and improvements. The most used form today for MRI reconstruction is the fast Fourier

transform (FFT), which is an efficient algorithm for computing the discrete Fourier transform (DFT).

The FFT reduces the number of operations required from O(N^2) in the DFT to $O(N\log_2 N)$ by separating the calculations. For more information on the FFT the reader is directed to the original paper by Cooley and Tukey[147].

The DFT is defined as:

$$F_k = \sum_{n=0}^{N-1} f_n \, e^{-(2\pi i n k)/N} \tag{2.30}$$

And the Inverse DFT (IDFT) is defined as:

$$f_n = \frac{1}{N} \sum_{k=0}^{N-1} F_k \, e^{(2\pi i n k)/N} \tag{2.31}$$

Where N is the number of data points, F_k is in the frequency domain and f_n is in the spatial domain. For 2D computations, the same computation in (30) and (31) can be run multiple times in composition once for each dimension.

Notice that (2.30) and (2.31) work in a rectilinear fashion, MRI data collected with cartesian trajectories thus can be reconstructed directly. However, non-cartesian trajectories require further processing.

For non-cartesian trajectories, reconstruction is done with the non-uniform fast Fourier transform (NUFFT). There are publicly available libraries for the computation of NUFFT such as the Michigan Image Reconstruction Toolbox (MIRT) https://web.eecs.umich.edu/~fessler/code/ and the Berkely Advanced Reconstruction Toolbox (BART) https://www.opensourceimaging.org/project/berkeley-advanced-reconstruction-toolbox-bart/.

At its core, NUFFT works by 'gridding', which means interpolating the non-cartesian data points to obtain uniformly gridded points in k-space[148,149]. A helpful review article by Pauly can be found in[150,151].

2.7 EFFICIENCY

In clinical imaging, and in-vivo imaging in general, the scan duration is an important aspect of the study design. In some cases, scan time has a hard limit. For example, breath hold scans are usually limited to be less than 20 seconds, and in-vivo scans (human or animal) are designed to be less than 1-hour scans. There is an incentive to maximize the signal to noise ratio (SNR) in the allotted time by optimizing the sequence parameters. A way to measure SNR per time is by measuring the efficiency[152]:

$$\Upsilon = \frac{(SNR/voxel)_{3D}}{\sqrt{T_T}} \alpha \frac{\Delta x \Delta y \Delta z \sqrt{N_{acq} N_y N_z T_s}}{\sqrt{N_{acq} N_y N_z}} \tag{2.32}$$

Where Υ is efficiency, $\Delta x, \Delta y, \Delta z$ are the voxel sizes, N_{acq} is the number of acquisitions, N_y is the number of phase encoding steps, N_z is the number of slices, T_s is the ADC read time, and T_T is the total time. (2.32) assumes a constant TE, TR, and bandwidth (BW) which should be set based on the material properties and sequence used. If the sequence is a GRE, the best flip angle is given by the Ernst angle α_E:

$$\alpha_E = \arccos\left(e^{-TR/T1}\right) \tag{2.33}$$

When developing new sequences or study designs, efficiency is a crucial component. Apart from patient comfort, achieving higher SNR in shorter time can also allow higher resolution or more averages depending on the purpose of the scan. In ^{19}F lung imaging, low SNRs and the fact that patient oxygenation might be at risk makes efficiency considerations imperative

CHAPTER 3: DYNAMIC 19F MRI VS SPIROMETRY IN CYSTIC FIBROSIS

3.1 INTRODUCTION

With the increase in CF care quality and longer expected survivability, there is a need for more sensitive and radiation free disease measuring methods. Methods such as spirometry and LCI only measure global parameters without the ability of spatial localization. CT, being the current gold standard, exposes the patients to ionizing radiation which is undesirable for long term monitoring or scanning with children.

MRI of the lungs has the potential to provide both morphological (with sequences such as UTE)[153] and functional (with contrast gases[45,48,123,154] such as ^{19}F, ^{129}Xe, or ^{3}He) information without ionizing radiation. The immediate advantage is that both morphological and functional scans can be done on the same MRI machine. 19F in particular, can be used with multiple breath scanning[104,108–111,155–158] that can provided functional time dynamic information. ^{19}F does not require additional polarization equipment and can be supplied in a normoxic mixture without regard to depolarization effect from oxygen. 19F, in the form of perfluoropropane (PFP) has been shown to be safe in healthy and diseased patients[106,110,112].

Part of this chapter has been published in part in <Goralski, Jennifer L., **Sang Hun Chung**, Agathe S. Ceppe, Margret Z. Powell, Muthu Sakthivel, Brian D. Handly, Yueh Z. Lee, and Scott H. Donaldson. "Dynamic perfluorinated gas mri shows improved lung ventilation in people with cystic fibrosis after elexacaftor/tezacaftor/ivacaftor: an observational study." Journal of Clinical Medicine 11, no. 20 (2022): 6160. >

This study was designed to assess the sensitivity of ^{19}F lung MRI specifically compared to FEV1 percent predicted (from spirometry) in the case where CF positive patients show normal FEV1 percent predicted (FEV1). 3 study groups; healthy control, mild (CF with FEV1 ≥ 80%), and moderate (FEV1 < 80%)

3.2 METHODS

20 healthy volunteers and 24 CF patients were recruited for this study, of which 13 healthy (3 male, ages 19-41) and 18 CF (5 males, ages 22-40) were used for data analysis. Exclusion of participants were due to withdrawal of consent (n=1), screen failure (n=1), abnormal spirometry (n=1), and image acquisition error (n=10). Figure 3.1 shows the study population grouping.

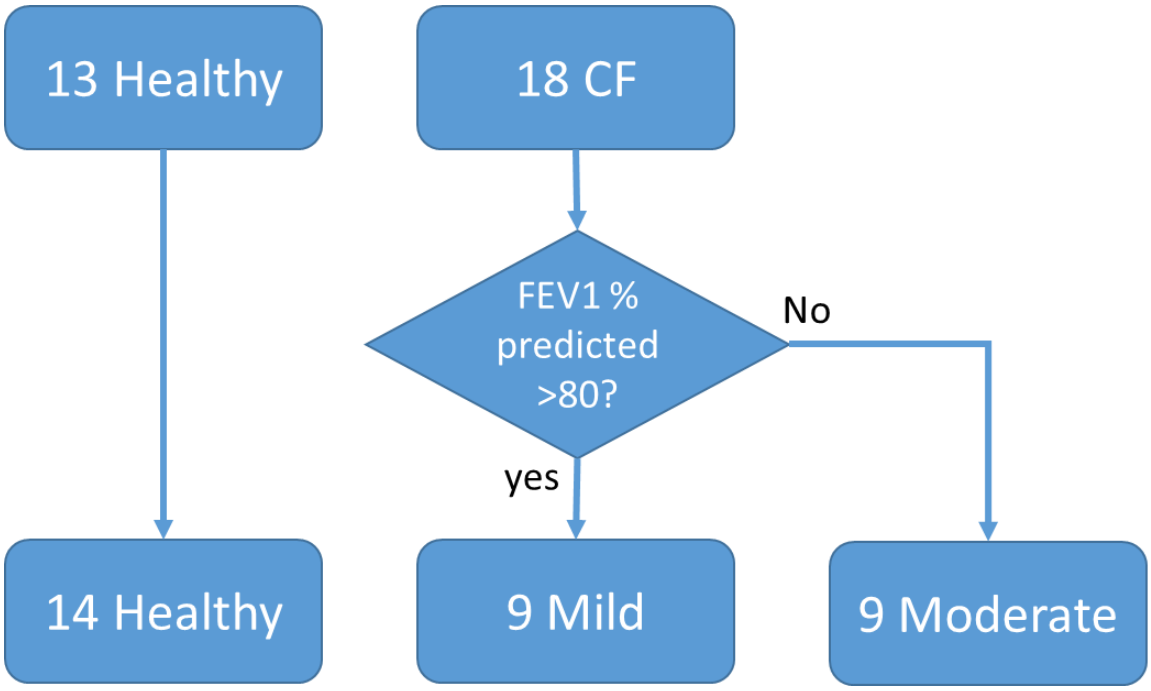

Figure 3.1. Study groups and assignment

Spirometry was performed using a KoKo spirometer (NSpire Health, Longmont, CO) according to American Thoracic Society guidelines[159]. ^{1}H MRI images were acquired during a 15 second breath-hold (3D fast low angle shot (FLASH), TE/TR, 0.05/2.42 ms; FA, 5°; resolution, 2.14 X 2.14 mm; slice thickness, 2.5 mm; number of slices, 103; acquisition matrix, 224 X 224, trajectory, spiral; interleaves, 130; spiral duration,1160 μs; slice partial Fourier, 6/8),, followed by ^{19}F MRI (3D Volumetric interpolated breath-hold examination (VIBE), TE/TR, 1.61/13 ms; FA, 74°; resolution of 6.25 X 6.25 mm; slice thickness, 15 mm; number of slices, 18; acquisition matrix, 64 X 64; bandwidth, 130 Hz/pixel; averages, 2; partial Fourier, 6/8) with inhaled PFP as the gaseous contrast agent (79% PFP; 21% O_2, pre-mixed medical grade gas; Air Liquide Healthcare, Plumsteadville, PA).

Scans were performed on a Siemens Prisma 3.0 Tesla MRI system (Siemens Medical Systems, Erlangen, Germany) with a custom 8-channel ^{19}F-tuned chest coil (ScanMed, Inc., Omaha NE). A customized gas delivery system using a mask/non-rebreathing circuit delivered PFP or room air during scans. Ventilation was monitored using a pneumotachometer, and gas-empty bag sensors automatically triggered a switch to room air if the PFP source was depleted during the study.

During gas wash-in cycles, subjects inhaled one tidal breath of PFP followed by a deep inspiration and 12-second breath-hold while images were obtained. Five imaging cycles were performed during PFP inhalation (wash-in). An identical breathing sequence and imaging was performed after switching to room air to characterize PFP wash-out. A minimum of five wash-out imaging cycles were performed, with additional room air cycles repeated if residual PFP signal was visible. Figure 3.2 shows the dynamic ^{19}F acquisition timeline.

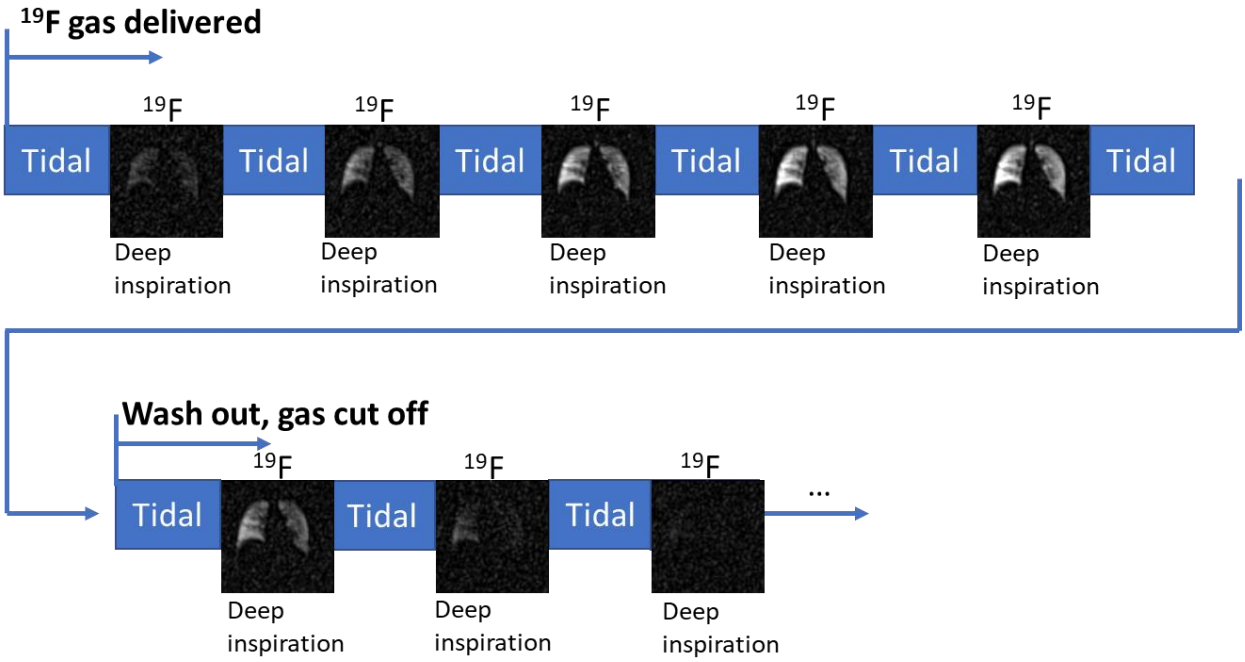

Figure 3.2. Dynamic ^{19}F acquisition timeline

^{19}F dynamic processing was performed with 3D Slicer (http://www.slicer.org, v4.8.1) for registration and segmentation, custom Python software (Python Software Foundation, Wilmington, DE) for biexponential fits and time constants, and Matlab (MATLAB version: 9.5 (R2018a), Natick, Massachusetts: The MathWorks Inc.; 2019) for calculation of time constant fractional lung volumes (FLV) and ventilation defect percentage (VDP). VDP was calculated as follows; the maximal signal intensity for each subject was defined as the 95th percentile of that individual subject's intensity distribution to exclude outlying voxels. After noise correction by subtracting mean background signal, VDP was defined as voxels not meeting a threshold of over 10% of the maximal signal intensity.

The signal-time curve for each voxel was fitted with a bi-exponential model (3.1, 3.2) to estimate the time constants that characterized the kinetics of gas wash-in (τ_1) and wash-out (τ_2).

$$d0 + peak\left(1 - e^{\frac{-(x-t0)}{\tau_1}}\right) \qquad x < t1 \tag{3.1}$$

$$d0 + peak\left(e^{\frac{-(x-t1)}{\tau_2}} - e^{\frac{-(x-t0)}{\tau_1}}\right) \qquad x \geq t1 \tag{3.2}$$

Where d0 is the base of curve, peak is the top of the curve, x is time, t_0 is the time the curve intersects the base, and t_1 is the time wash-in turns into wash-out as shown in Figure 3.3.

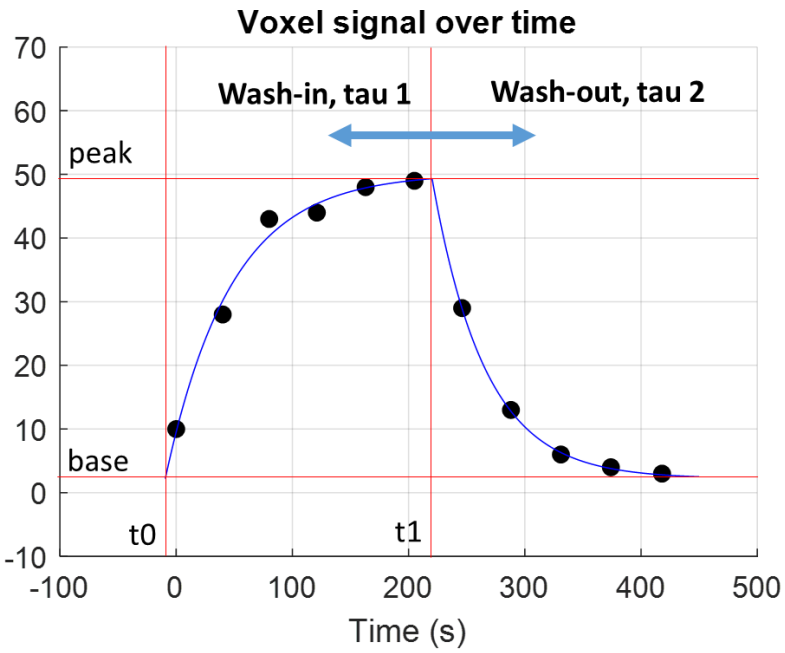

Figure 3.3. biexponential fit parameters

The frequency of each time constant in the whole ventilated lung was calculated and displayed via histograms.

Using normal mixture clustering (JMP®, Version *15*. SAS Institute Inc., Cary, NC, 1989–2021) of all τ_1 and τ_2 values in all participants (3 clusters, 2 limits), we defined two thresholds for each parameter (τ_1 and τ_2) based on the resulting cluster edges (Figure 3.4).

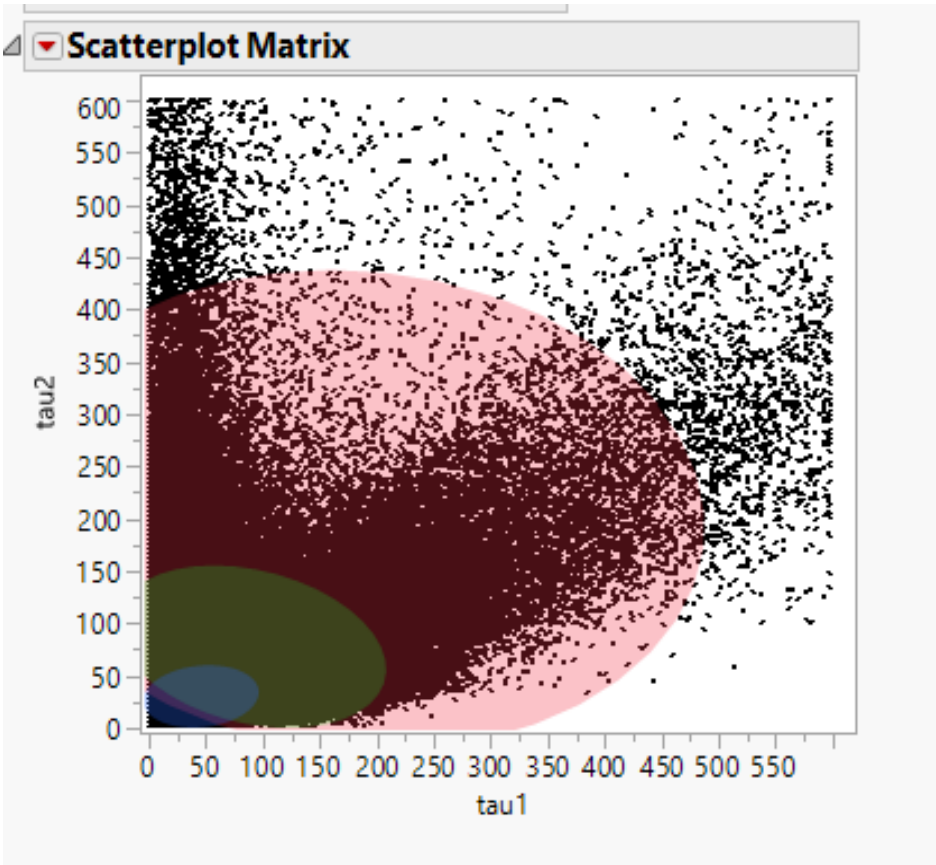

Figure 3.4. Normal mixture clusters with n=3

FLV was calculated as the percent of voxels with a time constant above or below the thresholds from the normal mixture clustering edges (3.3, 3.4).

$$FLV_{fast} = \frac{\#voxel_{\tau<fast\ threshold,i}\times 100}{\#voxel_{total,i}} \quad (3.3)$$

$$FLV_{slow} = \frac{\#voxel_{\tau>slow\ threshold,i}\times 100}{\#voxel_{total,i}} \quad (3.4)$$

Where i is the participant.

In total 4 FLVs were calculated: fast τ_1 and τ_2, and slow τ_1 and τ_2. Fast voxels were characterized as those with times constants < 64.44 and slow voxels were characterized as those with times constants >175.66.

3.3 RESULTS

Mean forced expiratory volume in the first second (FEV_1) percent predicted for healthy controls was 104.8% ± 9.6% (range 91–126), and mean FEV_1 percent predicted for all CF subjects was 76.8% ± 25.9% (range 37–117). Nine CF subjects in a "mild CF" cohort had an average FEV_1 of 98.2% ± 12.1%. In the remaining CF subjects, spirometry reflected moderate/severe disease severity (mean FEV_1, 55.4% ± 15.9%; n = 9). The frequency of each time constant within the ventilated lung is shown in Figure 3.5.

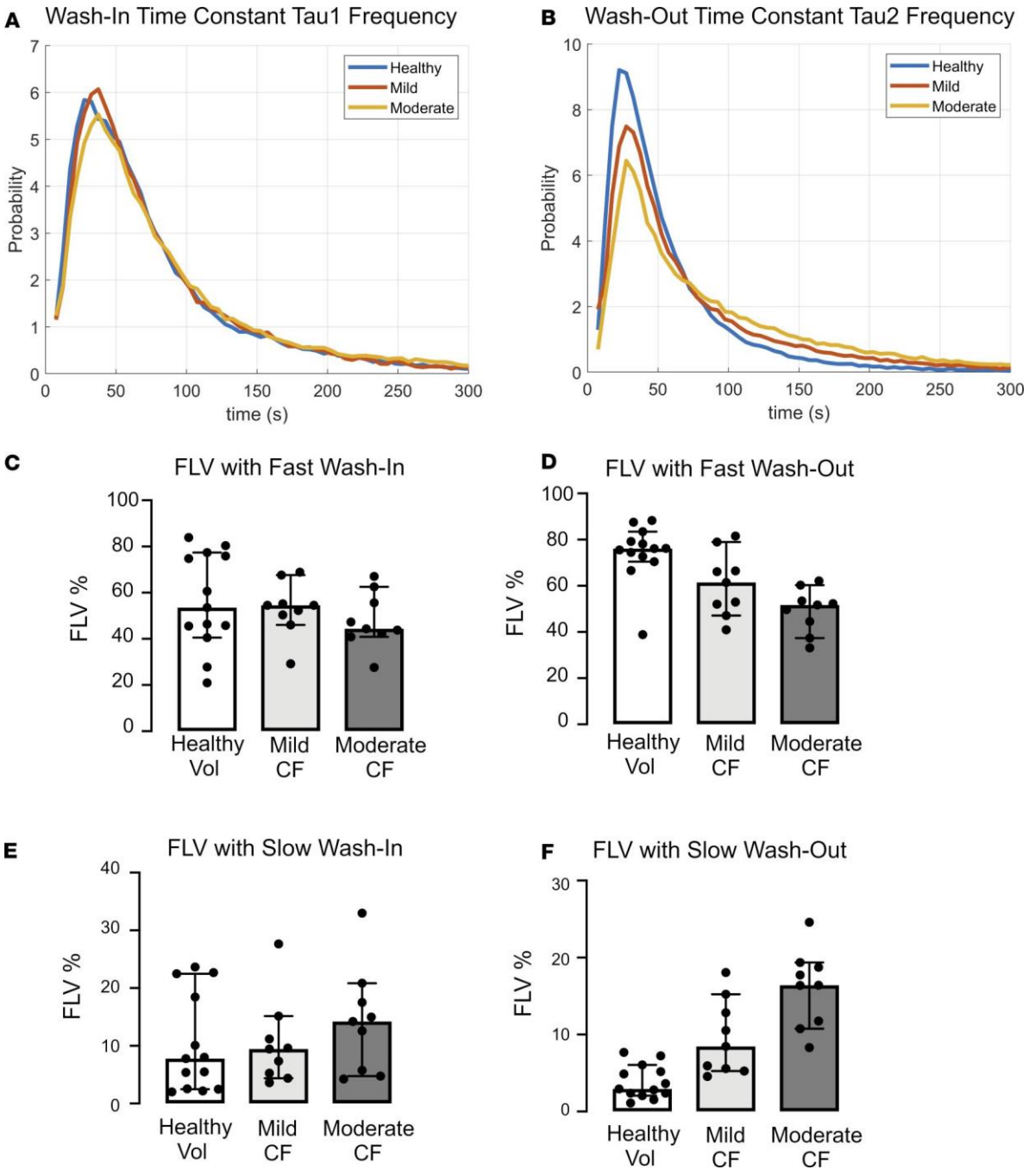

Figure 3.5. Ventilation Kinetics Analysis. (A and B) Histograms of wash-in (A) and wash-out (B) time constants for healthy controls, mild CF subjects, and moderate CF subjects. (C–F) Scatter and box plots (median ± 95% CI) demonstrating FLV of fast wash-in (C), fast wash-out (D), slow wash-in (E), and slow washout (F). ANOVA. Tukey's honest significance test (HSD) was performed for multiple between-group comparisons. Slow emptying fraction: healthy vs. mild CF, $P = 0.007$; mild CF vs. mod CF, $P = 0.006$. Fast emptying fraction: healthy vs. mild CF, $P = 0.04$; mild vs. moderate CF, $P = 0.13$)

Using clustering analysis as described in the method section, the thresholds describing abnormal τ_1 and τ_2 were 64.44 seconds or 175.66 seconds for fast and slow kinetics, respectively. These were applied to quantitate the FLV occupied by voxels with fast or slow filling (τ_1) or emptying (τ_2) in each subject. As shown in Figure 3.5 and Table 3.1, the FLV with slow wash-out (τ_2 > 175.66 seconds) and fast wash-out (τ_2 < 64.44 seconds) discriminated between each of the study groups, including between healthy volunteers and mild CF subjects (3.8% ± 2.2% vs. 9.6% ± 4.9%, P = 0.007 for slow wash-out; 74.4% ± 12.4% vs. 60.9% ± 13.9%, P = 0.04 for fast wash-out). No differences were observed in either fast or slow wash-in. Heatmaps of τ2 are shown in Figure 3.6. VDP was found significant between only healthy and moderate groups (p=0.001 with Tukey's HSD performed for multiple comparisons)

Table 3.1. Kinetics of 19F MRI ventilation wash-in/wash-out

	Variable	Healthy volunteers (n = 13)	All CF (n = 18)	Mild CF (n = 9)	Moderate/severe CF (n = 9)
FLV with fast τ_1	Mean (SD)	56.4 (20.8)	50.6 (11.8)	53.2 (11.7)	47.9 (12.1)
	Median (range)	53.6 (21.0–83.9)	50.38 (27.6–68.9)	54.5 (29.2–68.9)	44.4 (27.6–67.1)
FLV with slow τ_1	Mean (SD)	10.2 (8.5)	12.3 (8.3)	10.4 (7.4)	14.2 (9.2)
	Median (range)	7.8 (2.0–23.6)	5.8 (3.6–33.0)	9.5 (3.6–27.6)	14.2 (4.2–33.0)
FLV with fast τ_2[A]	Mean (SD)	74.4 (12.4)	55.1 (13.0)	60.9 (13.9)[B]	49.4 (9.6)[C]
	Median (range)	76.1 (38.8–88.3)	53.0 (41.0–81.6)	61.5 (41.0–81.6)	51.7 (33.1–62.1)
FLV with slow τ_2[A]	Mean (SD)	3.8 (2.2)	12.8 (5.8)	9.6 (4.9)[D]	16.0 (5.0)[E]
	Median (range)	3.0 (1.5–7.7)	11.8 (4.6–24.6)	8.5 (4.6–28.1)	16.4 (8.3–24.6)

Statistical gas kinetic results. Fractional lung volume (FLV) represents the percentage of lung with fast and slow wash-in and wash-out time constants. [A]P value via ANOVA < 0.0001 for FLV with fast and slow τ_2. Tukey's HSD performed for multiple comparisons. [B]Comparison between healthy and mild FLV with fast τ_2, P = 0.04. [C]Comparison between healthy and moderate FLV with fast τ_2, P < 0.0002. Comparison between mild and moderate FLV with fast τ_2, P = 0.13. [D]Comparison between healthy and mild FLV with slow τ_2, P = 0.007. [E]Comparison between healthy and moderate FLV with fast τ_2, P < 0.00001. Comparison between mild and moderate FLV with fast τ_2, P = 0.006.

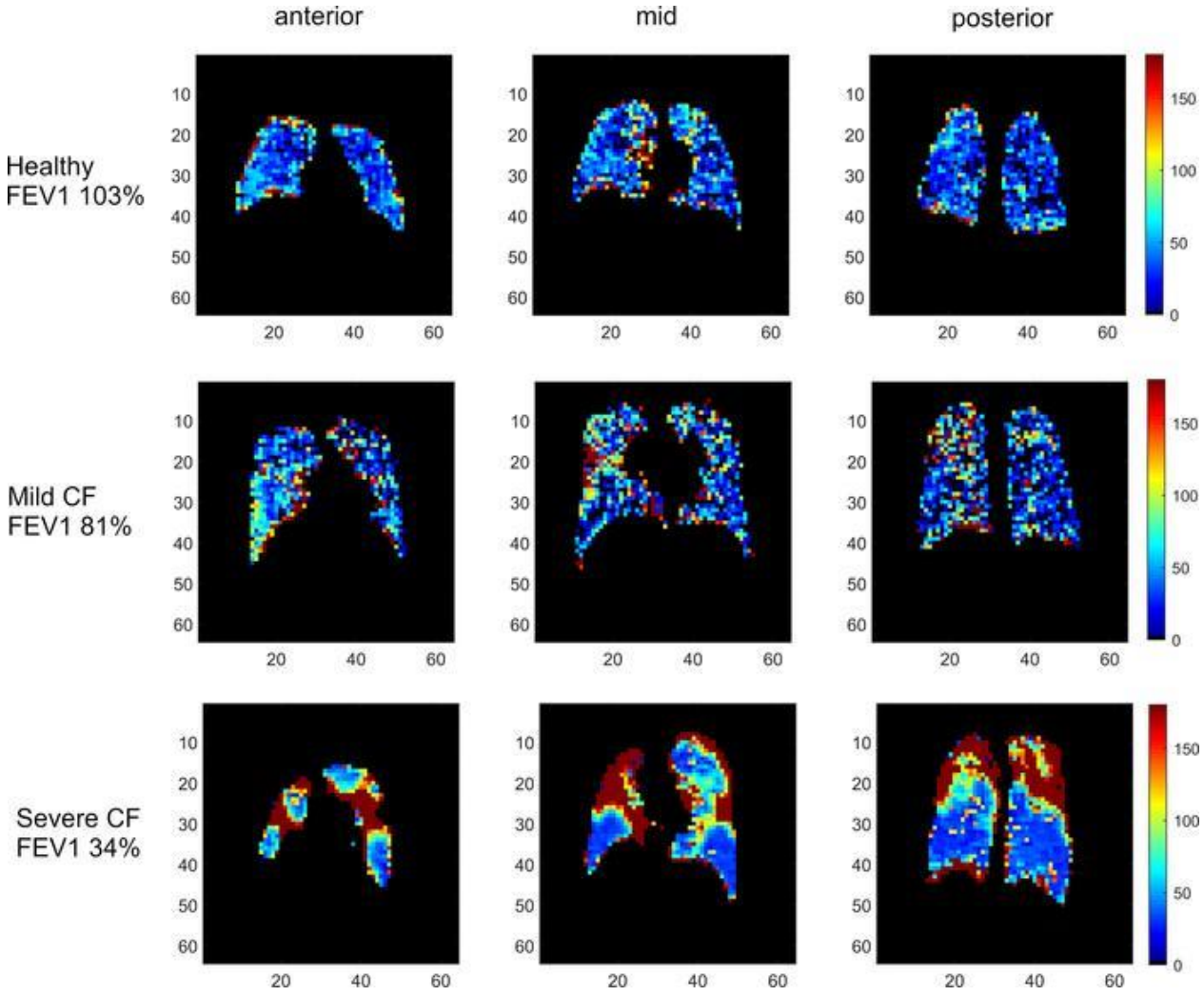

Figure 3.6. Coronal slice heatmaps of τ_2 from healthy, mild CF, and moderate CF participants

3.4 DISCUSSION AND CONCLUSION

Potential sources of error include breath size variability and chest coil positioning. Due to the analysis being on a voxel-by-voxel basis with the assumption that voxel position does not change in the time dimension, changes in lung inflation can introduce error by altering the wash-in/out curves.

Improvement to the presented methodology could include a breathing volume control either in the form of mechanically controlled valves or a visual feedback system for the participants.

VDP and τ_1 were not able to significantly discriminate between the healthy and mild groups. In the case of VDP, what breath scan during wash-in is used might play a role. τ_1 not being able to discriminate between healthy and mild is a surprise since τ_2 does. This might be due to flow physics in the lung and potential presence of flow blockages or dead space.

In conclusion, the results suggests that τ_2 is a disease marker more sensitive to FEV1 percent predicted and has the added advantage of spatial localization.

3.5 ACKNOWLEDGMENTS

This work was supported by NIH P30 DK065988, NIH 4 K12 HL 119998-4, CFF GORALS12L0, CFF PACE GORALS16AC0, and DONALD18Y7. We also acknowledge the regulatory assistance of the North Carolina Translational and Clinical Sciences (NC TraCS) Institute, which is supported by the National Center for Advancing Translational Sciences (NCATS), NIH, through grant award number UL1TR002489. Some of these results have been previously reported in the form of an abstract[160] (North American Cystic Fibrosis Conference, October 27–29, 2016, Orlando, Florida, USA

CHAPTER 4: 19F VS HYPERPOLARIZED 129XE VDP IN LUNG IMAGING

4.1 INTRODUCTION

Hyperpolarized (HP) ^{129}Xe is a popular gas used in lung MRI research[161–170]. It provides higher signal to noise ratio (SNR) than ^{19}F lung imaging and is capable of imaging resolutions roughly half than of ^{19}F[123]. HP ^{129}Xe has emerged as a cheaper and more accessible alternative to HP ^{3}He[171]. HP ^{129}Xe still requires a polarizer and has an anesthetic effect[172], however, it has been shows to be tolerable and safe in both adults and children[165,173].

^{19}F does not require a hyperpolarizer and can be stored pre-mixed as a normoxic (21% O_2, 79% ^{19}F) mixture, easing the logistics on scan day. Although 19F does not require hyperpolarization to see observable signal, the signal is often lower than HP ^{129}Xe[123] and therefore it is usually done at higher resolutions. A major advantage of ^{19}F is that there is no depolarization which makes multi breath acquisition viable. However, it is not clear how ventilation defect percentage (VDP) is affected by which breath in the wash-in sequence is chosen to calculate it, or how it compares to ^{129}Xe VDP.

Part of this content was published in part in <McCallister, Andrew, **Sang Hun Chung**, Michael Antonacci, Margret Z Powell, Agathe S. Ceppe, Scott H. Donaldson, Yueh Z. Lee, Rosa Tamara Branca, and Jennifer L. Goralski. "Comparison of single breath hyperpolarized 129Xe MRI with dynamic 19F MRI in cystic fibrosis lung disease." Magnetic Resonance in Medicine 85, no. 2 (2021): 1028-1038.>

This study compared ^{19}F VDPs computed from the first wash-in (early breath) scan and last wash-in (max-vent) scan with VDPs from high resolution ^{129}Xe and low resolution ^{129}Xe (resolution matched to ^{19}F) in participants with cystic fibrosis (CF).

4.2 METHODS

4.2.1 STUDY DESIGN AND PARTICIPANTS

This study was approved by the research ethics board at UNC-Chapel Hill (IRB 17-2569) and all participants provided written informed consent. Ten participants with stable CF lung disease, ≥ 18 y of age, non-smokers (<10 pack-year history and no active smoking in the past year), and a baseline FEV1 > 70% predicted were enrolled from May 2018 to March 2019.

Subject demographics are reported in Table 4.1. Subjects ranged in age from 21 to 44 years and had a mean FEV_1 of 81.7 ± 15.0% predicted. Each subject completed a single imaging session during which both ^{19}F and ^{129}Xe ventilation images were acquired in a random order. Prior to the imaging session, all subjects completed spirometry according to the American Thoracic Society standards.[159]

Table 4.1. Study population demographics

Gender	Age	FEV1 (%)	Genotype
F	20	73	F508del/F508del
F	27	72	W1282X/S341P
F	23	82	F508del/F508del
M	26	86	F508del/G551D
F	24	92	F508del/F508del
M	24	71	F508del/621 + 1G-->T
F	44	64*	R75X/R1066H
M	24	85	F508del/F508del
M	35	75	F508del/F508del
F	30	117	F508del/F508del

* Visit FEV_1 below baseline due to subject not performing their normal airway clearance procedure on the day of the study visit.

4.2.2 IMAGING

Imaging was performed on a Siemens PRISMA 3T MR scanner (Siemens AG) with multinuclear capabilities. Subjects were randomized to the order of ^{19}F and ^{129}Xe imaging; after the first scan, subjects exited the scanner and were allowed a 15-minute break, during which a single spirometric maneuver was completed to ensure no change in lung function as a result of either gas inhalation.

3D ^{1}H scans were completed before each ^{129}Xe and ^{19}F scan to facilitate co-registration of ^{129}Xe images with ^{19}F images. ^{1}H images acquired before ^{129}Xe scan were acquired during a breath hold of 1 L of medical air to improve matching of the lung volume at which ^{1}H and ^{129}Xe images were obtained and thus, image registration. All ^{1}H images were acquired by using a 3D stack of spiral VIBE sequence with 5° excitation flip angle, a TR of 2.42 ms,

echo time (TE) of 0.05 ms, 224 by 224 acquisition matrix, and a resolution of 2.1 mm × 2.1 mm × 2.5 mm.

For ^{19}F acquisitions, a PFP-filled dual-cylinder lung phantom was scanned prior to each participant for quality assurance and to establish the ^{19}F center frequency. Subjects were positioned supine in the scanner with a ^{19}F-tuned 8-channel chest coil (ScanMed LLC, NE) around the chest. Subjects inhaled a pre-mixed, medical grade gas mixture of 79% PFP:21% oxygen (IND 122,215) using a continuous-breathing custom gas delivery device.[106] PFP was administered with a full-face non-invasive ventilation mask and a non-rebreathing Douglas Bag system. Subjects inhaled and exhaled one tidal volume breath of the contrast gas followed by a maximal inhalation with a 12 second breath-hold, during which time images were obtained prior to exhalation. A total of five such imaging cycles during PFP inhalation (wash-in) were performed, followed by up to eight cycles of room air inhalation (wash-out) until no visible signal was present (for a total for 10 wash-in breaths and up to 16 wash-out breaths). Ventilation was coached with a pneumotachometer as a visual aid for the MRI technician, and safety was monitored via blood oxygenation saturation, exhaled CO_2 concentration, and heart rate. ^{19}F dynamic images were acquired using a coronal 2D gradient echo (GRE) sequence with a 74° flip angle, TE of 1.61 ms, a TR of 13 ms, 15 mm slice thickness, and a 64 by 64 acquisition matrix with a 130 Hz/pixel bandwidth and an in-plane resolution of 6.25 mm × 6.25 mm.

^{129}Xe imaging was performed using a flexible ^{129}Xe-tuned quadrature chest coil (Clinical MR Solutions, WI). For each subject, two images were acquired, each during a single 12 second breath-hold of 750 ml isotopically enriched ^{129}Xe, polarized up to ~14% with a Polarean 9800 ^{129}Xe Polarizer (Polarean, Inc, Durham, NC), mixed with 250 ml of N_2. During the first inhalation, the ^{129}Xe center frequency was determined right before the

acquisition of a low-resolution 2D multislice image data set. A high-resolution 2D multislice image data set was acquired during the second inhalation, approximately 30 minutes after the first inhalation using a second dose of hyperpolarized gas. Throughout the imaging session the subject's heart rate, blood pressure and oxygen saturation level were monitored every 5 min. After each xenon inhalation, subjects were also queried about symptoms associated with neurologic changes (i.e., euphoria, numbness, tingling, etc.). ^{129}Xe images were acquired using 2D GRE multislice sequences with a 10° excitation flip angle, a TR of 9 ms, an TE of 4 ms, a field of view of 280 × 350 (read × phase), and a matrix size of either 128 × 64 with a slice thickness of 21.0 mm, which resulted in an in-plane resolution of 2.2 mm × 6.4 mm (low resolution) with a total scan time of 7 s, or a matrix size of 128 × 80 with a slice thickness of 10.5 mm, which resulted in an in-plane resolution of 2.2 mm × 4.4 mm (high resolution) and a total scan time of 14 s.

4.2.3 IMAGE ANALYSIS

Registration and masking of images were performed using MIM Software (Cleveland, OH). The ^{1}H lung masks corresponding to the ^{129}Xe acquisitions were generated via a semi-automated segmentation of the ^{1}H lung-cavity images, using a simple region-growing algorithm. The ^{1}H lung masks corresponding to the ^{19}F acquisitions were generated through visual inspection using the threshold and manual region of interest (ROI) segmentation tools due to difference in lung inflation between the ^{1}H and ^{19}F in some subjects. The ^{1}H lung cavity images were used as lung masks to eliminate noise regions outside the lung ROI. Two sets of ^{19}F ventilation type images were created for each subject, an early-breath image and a maximum ventilation (max-vent) breath image. For the early-breath image, the first image to show ^{19}F signal was used[174]; for the max-vent image, the last wash-in image was used. ^{129}Xe low-resolution (low-res) and high-resolution (high-res)

were obtained as noted above. ^{129}Xe and ^{19}F images were then registered through a rigid registration transform on their respective ^{1}H images. The registered images and masks were then exported to MATLAB (version 2017b; MathWorks, Natick, MA) for further processing using in-house scripts.

The SNR was calculated as the ratio of the 90th percentile of the lung interior distribution to the noise signal SD (taken from an ROI outside the thorax). VDP was calculated with a threshold based system.[108] The VDP threshold was defined as the 95th percentile of the background noise distribution,[110] measured from an ROI drawn outside of the thoracic cavity, the threshold were individually calculated for ^{129}Xe, ^{19}F, and per participant. VDP was defined as the percent of total lung volume with signal lower than the threshold.

For comparison purposes, high resolution ^{129}Xe and max-vent ^{19}F images were registered using MIM with rigid translation only. ROIs were manually drawn to identify regions of mismatch. Mismatch regions are labeled as ^{129}Xe + ^{19}F- (regions where ^{129}Xe signal is above the VDP threshold and the ^{19}F signal is below the VDP threshold), ^{129}Xe- ^{19}F+ (regions where ^{129}Xe signal is below the VDP threshold and the ^{19}F signal is above the VDP threshold)

Wash-in time constants (τ_1) and wash-out time constants (τ_2) were calculated from the multi-breath ^{19}F data similar to Chapter 3. However, the bi-exponential fitting was done in Matlab using the non-linear least squares method and updated functions:

$$d0 + peak\left(1 - e^{\frac{-(x-t0)}{\tau_1}}\right) \qquad x < t1 \tag{4.1}$$

$$d0 + peak\left(1 - e^{\frac{-(t1-t0)}{\tau_1}}\right)e^{\frac{-(x-t1)}{\tau_2}} \qquad x \geq t1 \tag{4.2}$$

The time constants τ_1 and τ_2 were subdivided by ^{19}F and ^{129}Xe match/mismatch areas ^{129}Xe + ^{19}F-, ^{129}Xe- ^{19}F+, and ^{129}Xe+ ^{19}F+ (regions where both ^{129}Xe and ^{19}F have signal above the VDP threshold)

4.2.4 STATISTICAL ANALYSIS

Statistical analyses were performed using Matlab and SAS v9.4. Linear regressions and Pearson correlations were performed between VDP values measured by low and high-resolution ^{129}Xe and ^{19}F imaging. VDP mean differences are reported as [absolute] % difference and displayed in Bland-Altman plots. The goodness of fit between mean raw ^{19}F values in ROIs and fitted curves were assessed with R-square values. Repeated measures analysis of variance (ANOVA) was used to compare SNR, mean $\tau1$ and $\tau2$ values in the ^{129}Xe + ^{19}F+, ^{129}Xe + ^{19}F- and ^{129}Xe- ^{19}F + ROIs, and the peak ^{19}F signal in each ROI. Comparisons between all groups were corrected with the Tukey-Kramer adjustment. Results are reported as mean ± SD and displayed in Table 4.2. P-values < 0.05 were considered significant.

4.3 RESULTS

4.3.1 SIGNAL TO NOISE

Signal to noise values across the entire lung volume were determined in the early-breath ^{19}F, max-vent ^{19}F, low-resolution ^{129}Xe, and high-resolution ^{129}Xe images as shown in Figure 4.1 (early-breath ^{19}F: 18.36 ± 3.16; max-vent ^{19}F: 25.02 ± 4.02; low-res ^{129}Xe: 73.59 ± 53.82, high-res ^{129}Xe: 30.17 ± 20.82). Significant SNR differences were present between early-breath ^{19}F images vs. low-res ^{129}Xe images (P = .041) and between early-

breath ^{19}F vs. max-vent ^{19}F ($P < .001$). A nearly significant difference between low-res ^{129}Xe vs. High-res ^{129}Xe was observed ($P = .052$).

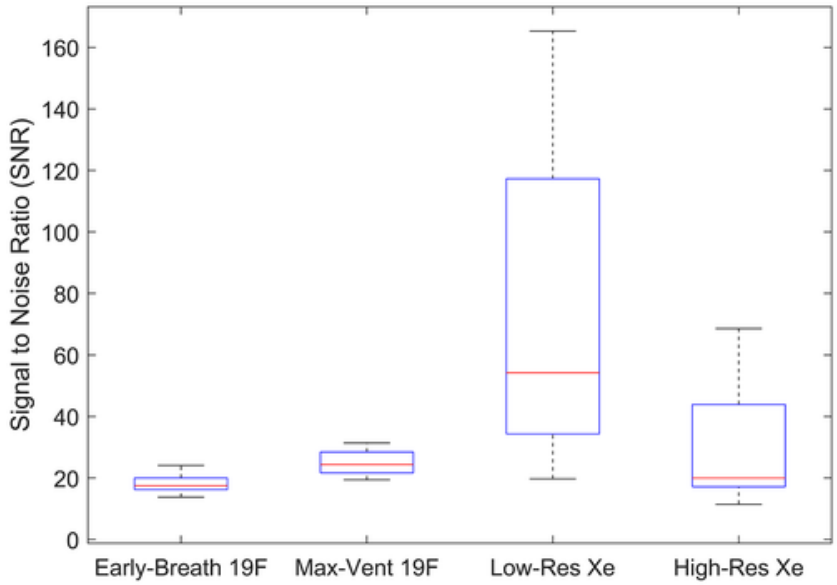

Figure 4.1. Boxplot showing distribution of ventilation images SNRs across all ten subjects, with the median (red line), 25th and 75th percentiles (blue box edges), and range (whiskers) displayed. Statistically significant differences were seen in early-breath ^{19}F vs. low-res ^{129}Xe ($P = .041$) and early-breath ^{19}F vs. max-vent ^{19}F ($P < .001$)

4.3.2 COMPARISION OF VENTILATION DEFECT PERCENTAGE ACROSS METHODS

Figure 4.2 provides examples of the variability of gas filling between methods. In Subject 1, the ventilation defect location and volume from the early-breath ^{19}F was similar to that of the high-resolution ^{129}Xe. In contrast, the max-vent ^{19}F showed eventual filling of a majority of these ventilation defects. In Subject 2, while neither ^{129}Xe images nor the max-vent ^{19}F images demonstrated significant ventilation defects, the early-breath ^{19}F images showed substantial defects that likely reflect inadequate SNR at this early time point.

In Subject 3, the early-breath ^{19}F image again shows large areas of ventilation defect in the right lung, thought to reflect inadequate gas uptake or signal at this early point of

the PFP wash-in cycle. The high-resolution ^{129}Xe image detected more ventilation defects than the low-resolution ^{129}Xe image, especially in the left upper lobe, for example, where volume averaging may be increasing the local mean value above the threshold.

Comparison of the max-vent ^{19}F and xenon images shows both matched ^{129}Xe- ^{19}F- and mismatched ^{129}Xe- ^{19}F + ventilation defects, suggesting that some lung regions never filled with PFP, whereas others demonstrated delayed filling.

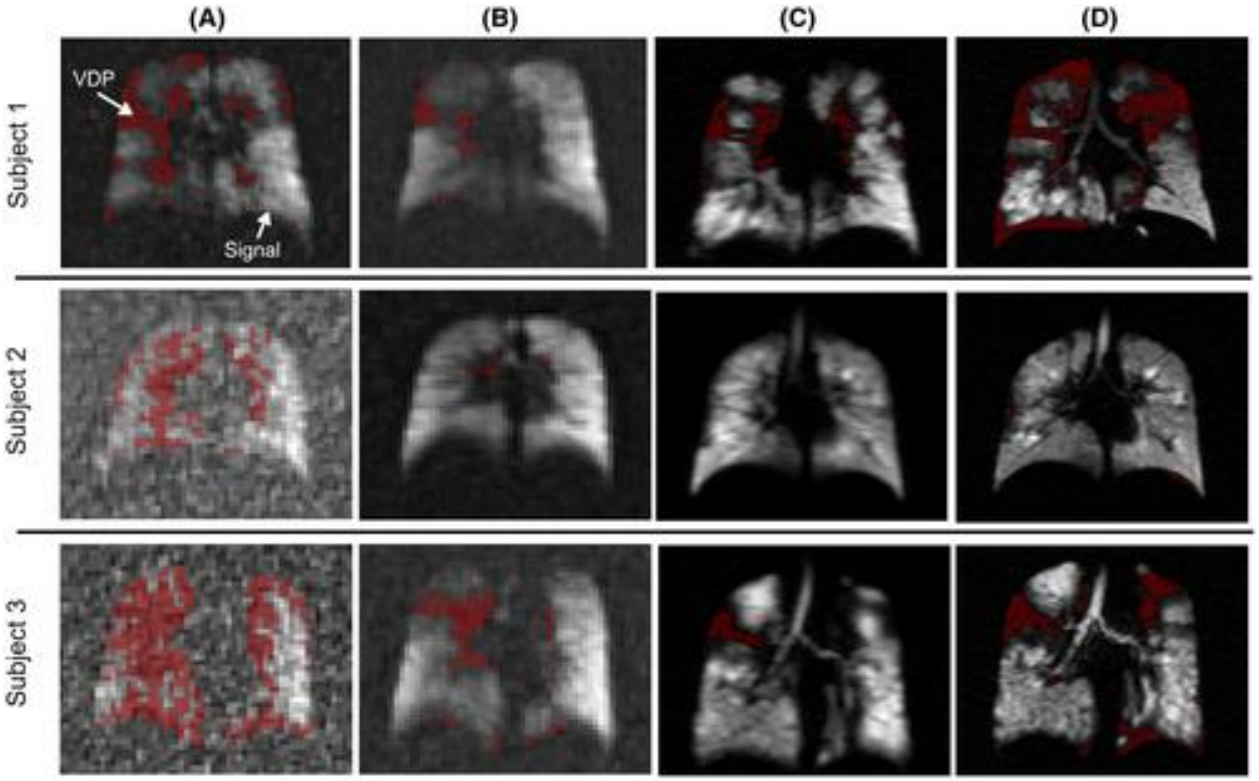

Figure 4.2 Representative images showing early-breath ^{19}F (A), max-vent ^{19}F (B), low-resolution ^{129}Xe (C), and high-resolution ^{129}Xe (D) images in three subjects. A threshold was applied to define regions of ventilation defects (red masks). VDPs were calculated as the percentage of lung with a ventilation defect compared with total lung volume calculated by the anatomic mask. VDPs in early-breath ^{19}F images were higher than in max-vent images, likely due to lack of sufficient signal. High-resolution ^{129}Xe images typically displayed higher VDPs than low-res images

Figure 4.3 shows correlations and Bland-Altman plots of VDPs calculated from each image type, referenced against the standard high-res ^{129}Xe VDP method. No correlation between early-breath ^{19}F VDP (r = 0.28, P = .43; Figure 4.3A) or max-vent ^{19}F VDP (r = 0.23, P = .52; Figure 4.3B) and high-res ^{129}Xe VDP values were observed.

The Bland-Altman plot shows a significant mean difference in VDP between max-vent ^{19}F and high-res ^{129}Xe (−10.6%, P = .007; Figure 4.3E). There was no significant difference in mean VDP values between early-breath ^{19}F and high-res ^{129}Xe (−0.5%, P = .87; Figure 4.3D). In contrast, low-res vs. high-res ^{129}Xe VDP display a significant correlation (r = 0.68, P = .03; Figure 4.3C), although a significant mean difference in VDP (−10.5%, P = .001; Figure 4.3F) indicated consistent underestimation of VDP values by low-res ^{129}Xe images.

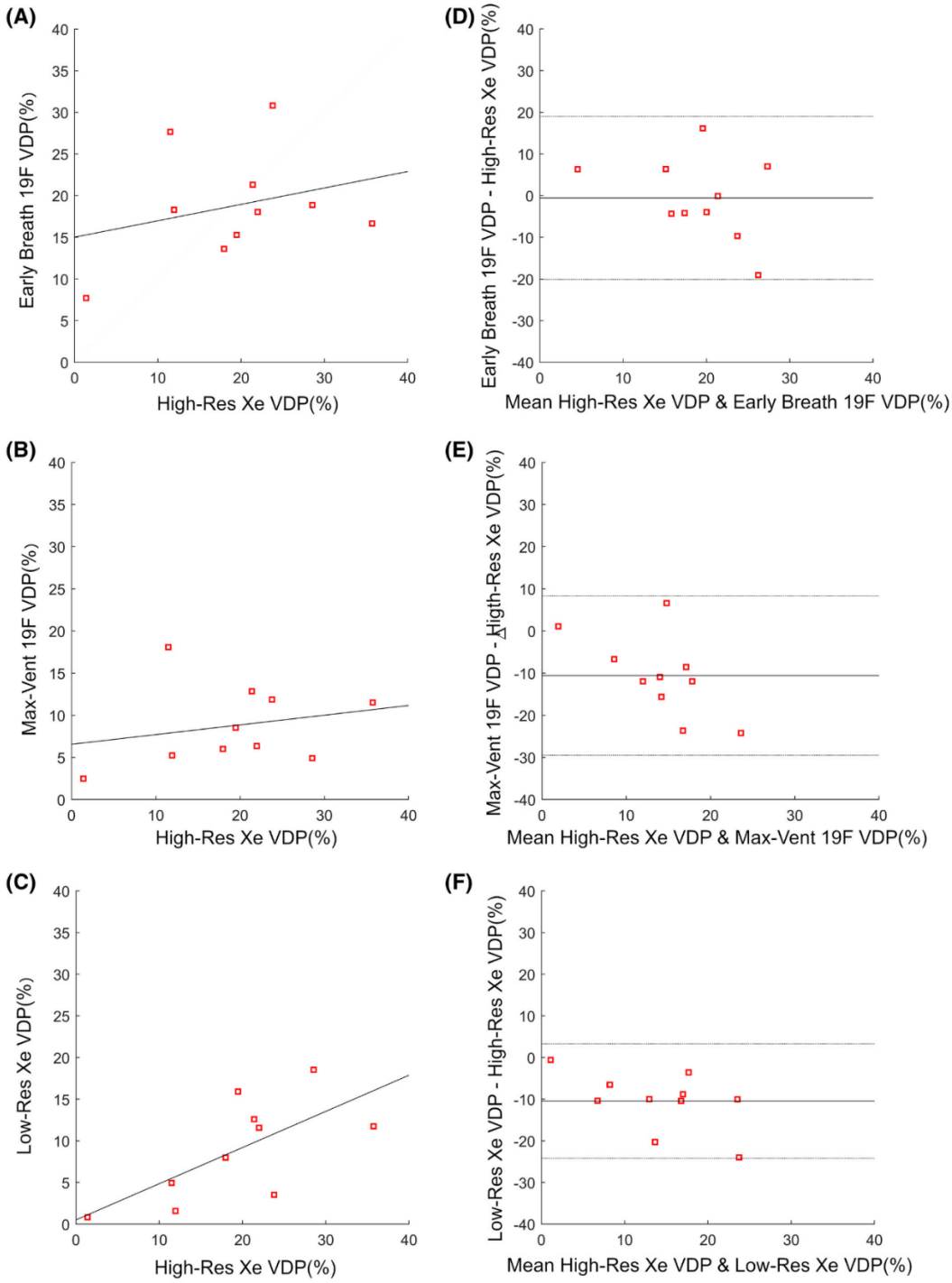

Figure 4.3 Scatter (A, B, C) and Bland-Altman (D, E, F) plots comparing VDP measurements. Regression line (dark gray) shown on scatter plots. Mean bias ± 95% lines of agreement shown on Bland-Altman plots. High-resolution ^{129}Xe is compared with: early-breath ^{19}F images (r = 0.28, P = .43. Estimated bias = −0.5 ± 19.6%, P = .87) (A,D); (B, E). max-vent ^{19}F images (r = 0.23, P = .52. Estimated bias = −10.6 ± 18.9%, P = .007) (B,E); low-resolution ^{129}Xe (r = 0.68, P = .03 (C,F). Estimated bias = −10.5% ± 13.8%, P = .001)

Figure 4.4 shows the comparison between max-vent ^{19}F VDP and early-breath ^{19}F VDP. There was significant correlation (r = 0.75, P= .012) and a significant mean difference (10.0%, P= 4.9e-5) indicating overestimation of VDP by early breath ^{19}F.

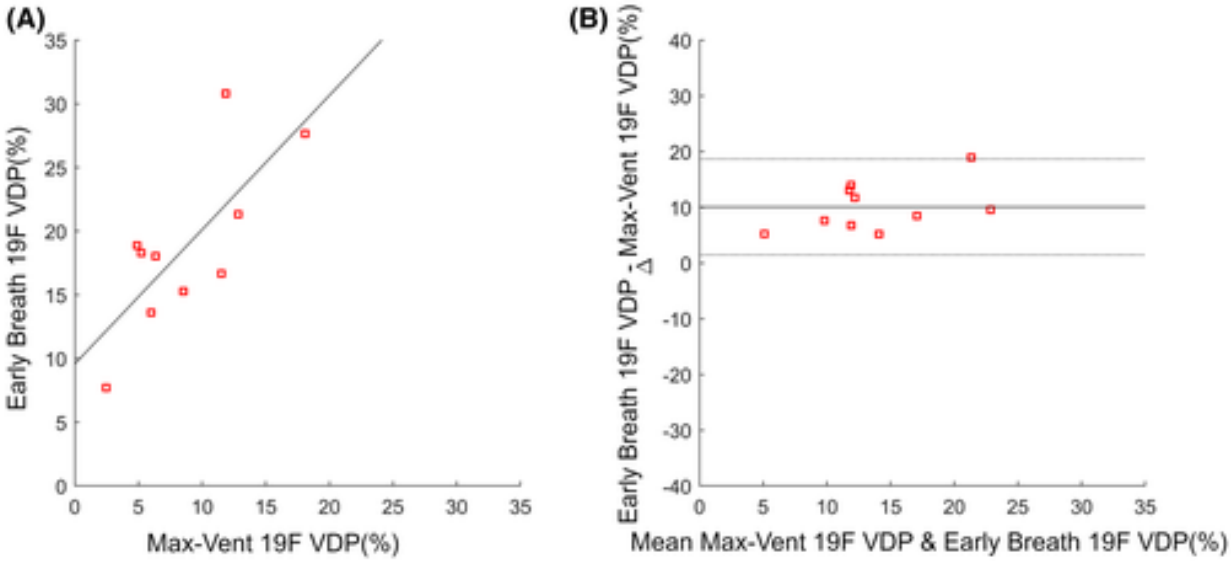

Figure 4.4 Scatter plot (A) and Bland-Altman plot (B) showing the comparison of VDP measurements from max-vent ^{19}F VDP and early-breath ^{19}F VDP. The correlation was r = 0.75, P= .01. The Bland-Altman plot shows estimated bias = 10.05 ± 8.6% with P= 4.9e-5

4.3.3 EVALUATING MISMATCHED ^{19}F AND ^{129}Xe VENTILATION DEFECTS

Comparison of low-resolution and high-resolution ^{129}Xe images did not reveal any region of non-congruency that could not be attributed to differences in resolution: high-resolution ventilation images consistently displayed sharper ventilation defects than the low-resolution images. In contrast, within the same subject, we observed differences in the location and volume of ventilation defects when comparing ^{129}Xe and ^{19}F images (Figure 4.5).

We sought to utilize the dynamic ventilation data afforded by ^{19}F imaging to further understand the nature of these mismatched regions. In Figure 4.6, representative mean ^{19}F

signal vs. time curves in matched and unmatched ROIs are shown. Mean ^{19}F wash-in ($\tau 1$) and wash-out ($\tau 2$) rate constants derived from these plots, along with the goodness of fit (r-square), from each ROI type (^{129}Xe + ^{19}F+, ^{129}Xe + ^{19}F-, and ^{129}Xe-^{19}F+) are shown with box plots in Figure 4.7. Wash-in and wash-out rate constants ($\tau 1$ and $\tau 2$, respectively) were higher in both types of mismatched ROIs (^{129}Xe- ^{19}F + and ^{129}Xe + ^{19}F-) when compared with matched ROI (^{129}Xe + ^{19}F+) regions, but only ^{129}Xe + ^{19}F+ vs. ^{129}Xe-^{19}F + $\tau 2$ showed significant difference ($P = .008$).

The mean maximum ^{19}F signal value derived from the modeled signal versus time plot was found to be statistically different between all three different regions (^{129}Xe- ^{19}F+, ^{129}Xe + ^{19}F-, and ^{129}Xe + ^{19}F+), as shown in Table 4.2. This demonstrates that lung regions with ^{19}F, but no ^{129}Xe, do indeed fill, but at a slower rate and to a lower peak signal (compared with defect-free ROIs). More surprising is the paradoxical finding of lung regions with ^{129}Xe signal after a single breath, but very low ^{19}F signal after multiple breaths. Examination of ^{19}F wash-in/out time constants and peak signals in these regions suggests that they also have abnormal ventilation kinetics, yet are not detected as abnormal by the ^{129}Xe method. Because poorly estimated $\tau 1$ and $\tau 2$ values could lead to misinterpretation of our data, we calculated the goodness of fit for ^{19}F signal in each type of ROI to assess the quality of the data. Importantly.

The r-square values between raw data and calculated exponential curves were very high in each type of ROI, including those with low ^{19}F signal, providing confidence in these observations ($R^2 = 0.89 \pm 0.18$ for ^{129}Xe + ^{19}F-, 0.99 ± 0.003 for ^{129}Xe + ^{19}F+, and 0.99 ± 0.01 for ^{129}Xe- ^{19}F+).

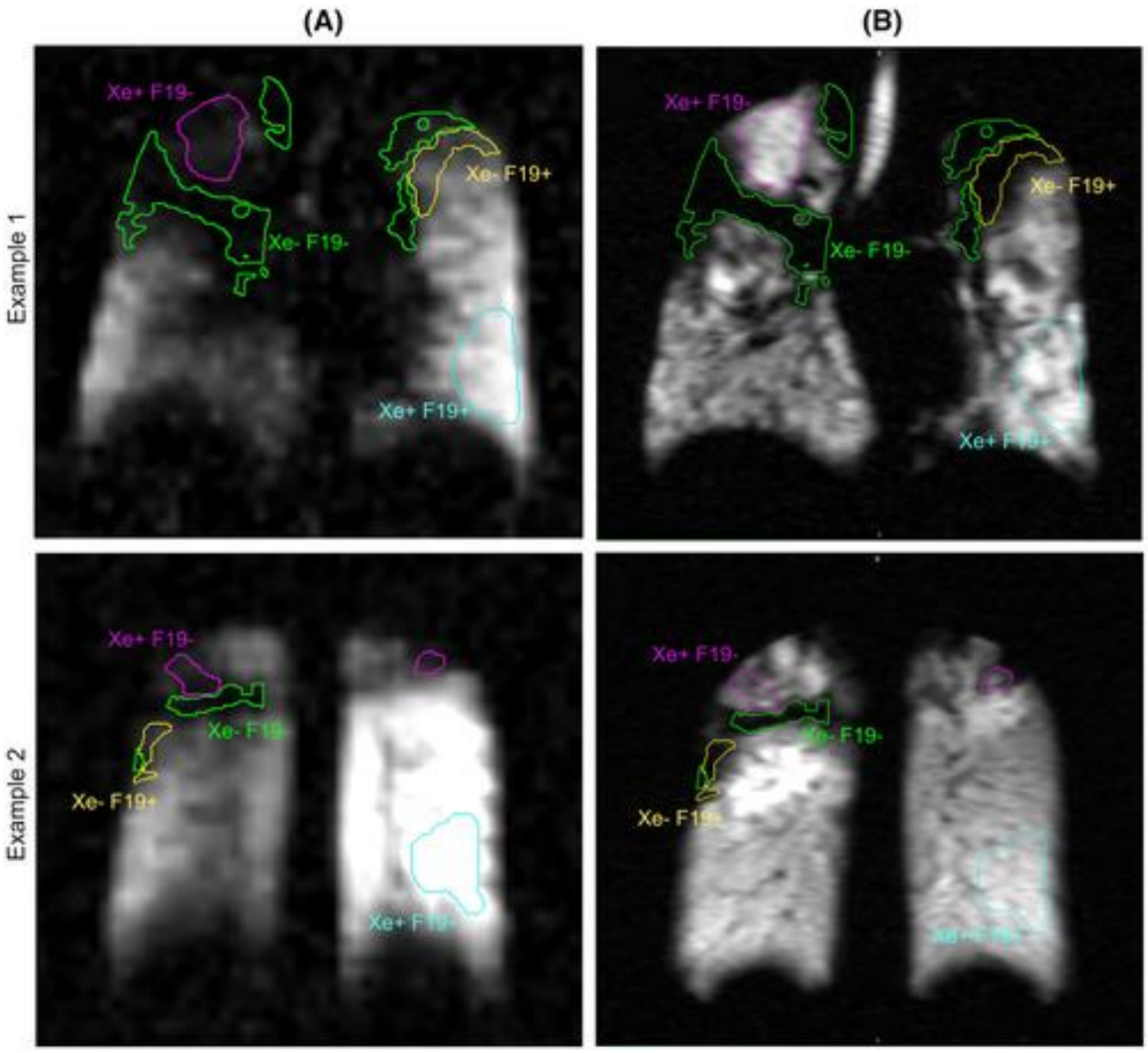

Figure 4.5 Examples of mismatched ventilation signal from two subjects. A. max-vent ^{19}F and B. high-resolution ^{123}Xe images. The purple ROI outlines ^{129}Xe + ^{19}F- regions; the yellow ROI outlines ^{129}Xe-^{19}F + regions; the cyan ROI outlines a matched ^{129}Xe + ^{19}F+ region used for comparison. The green ROI outlines a matched ^{129}Xe-^{19}F- for additional comparison

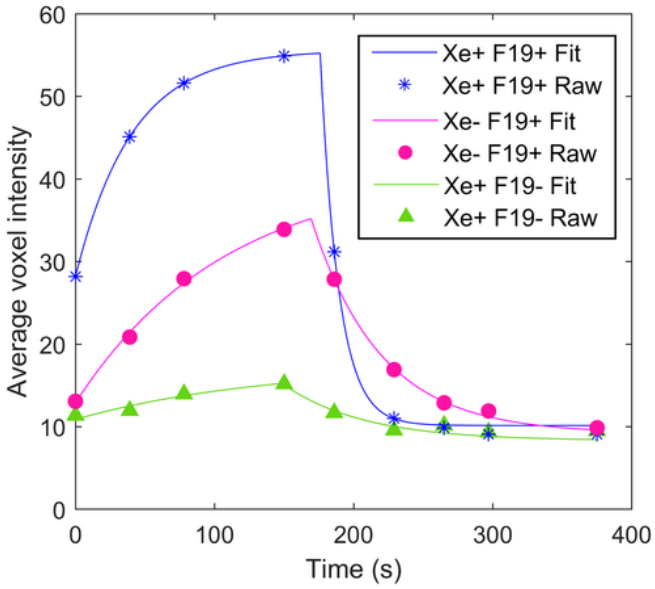

Figure 4.6 Plots of the raw (symbols) and modeled (lines) ^{19}F signal time course in matched (^{129}Xe + ^{19}F+; blue) and unmatched (^{129}Xe-^{19}F + and ^{129}Xe + ^{19}F-; red and green, respectively) ROIs from a single representative subject. In all subjects with mismatched ROIs, a consistent rank order of maximum gas ^{19}F signal of ^{129}Xe + ^{19}F+> ^{129}Xe-^{19}F+> ^{129}Xe + ^{19}F- was observed despite accentuated ^{129}Xe signal (i.e., higher than mean lung signal) in some of the ^{129}Xe + ^{19}F- ROIs.

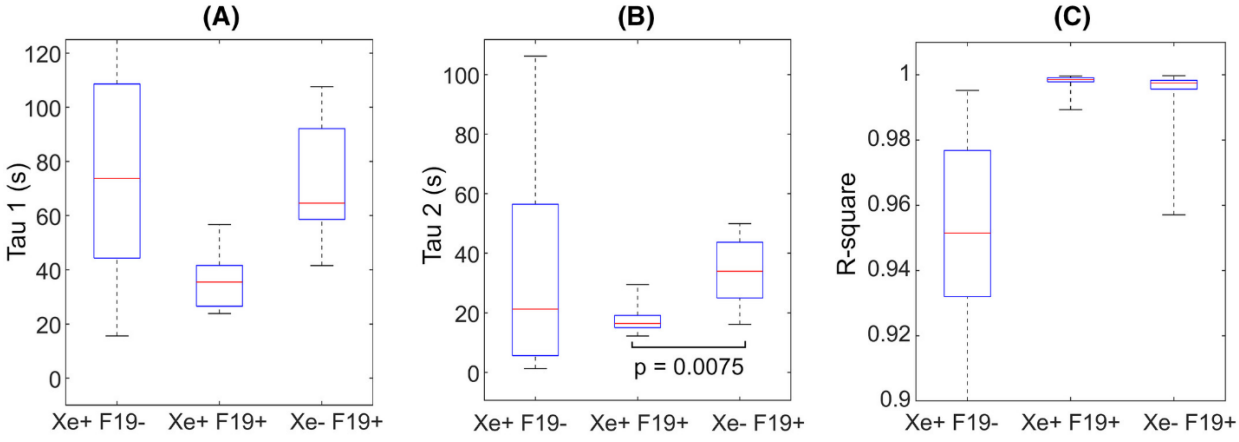

Figure 4.7 Box plots of wash-in (τ1) (A) and wash-out (τ2) (B) time constants from the ^{19}F bi-exponential fit. c. R-square indicates the goodness of the fit between raw data and modeled curves. The horizontal brackets indicate statistical significance with corresponding P-values

4.4 DISCUSSION

This study reports a first comparison of regional lung ventilation as assessed by dynamic ^{19}F and HP ^{129}Xe MRI imaging in CF subjects. The sequential performance of ^{19}F and ^{129}Xe MRI scans within the same day in subjects with mild CF lung disease provided a powerful platform to make comparisons between these modalities.

As expected, ^{19}F images were characterized by a markedly lower SNR, which prevented direct comparison of single breath ^{129}Xe ventilation images to single breath ^{19}F images. Therefore, we compared early-breath ^{19}F images (i.e., after first appearance of signal during the multiple breath wash-in procedure) to single breath ^{129}Xe images. However, when assessed after multiple PFP breaths, SNR increased as expected, and a portion of ventilation defects disappeared, indicating that many ventilation defects detected by single breath ^{129}Xe MRI ultimately do fill during the multiple breath wash-in cycle. What is unclear from this data, however, is whether the filling was due to direct versus collateral ventilation.

When measuring VDP values, image resolution also played a role. In our study, direct comparison of VDP values from high-resolution ^{129}Xe and low-resolution ^{129}Xe ventilation images allowed for the isolation of the effect of resolution on VDP. As expected, relative to the high-res ^{129}Xe scans, the low-res ^{129}Xe scans were more prone to partial volume effects and consistently underestimated VDP. This underestimation is larger at higher VDPs, with the trend showing low-res scans underestimate VDP by about 50%. It is important to note that the size of the VDP underestimation in the low-resolution ^{129}Xe images is a function of the specific signal intensity threshold used. In particular, by using a

less conservative signal threshold, some additional ventilation defects could be captured in the low-resolution ^{129}Xe images, resulting into higher VDP values.

Our data also suggests that VDP may be overestimated by single breath approaches (early-breath ^{19}F, low-res ^{129}Xe, high-res ^{129}Xe), which consistently measured higher VDPs than those determined via max-vent ^{19}F images. Since slow filling regions appear as regions of ventilation defects in single-breath hold images, they cannot be differentiated from regions of true ventilation defects. To this end, the multiple breath protocol employed for ^{19}F imaging provides the ability to differentiate between true ventilation defects and slow filling regions, by providing wash-in and wash-out gas kinetics. In particular, in areas of congruence (^{129}Xe + ^{19}F+ or ^{129}Xe-^{19}F-), ventilation kinetics were as expected, with either rapid or absent ventilation, respectively. In regions that were ^{129}Xe-^{19}F+, on the contrary, the multiple breath PFP protocol was able to demonstrate that these regions were not truly unventilated, but, rather, slow to filling. Because HP ^{129}Xe images are acquired using a single breath technique, these slowly filling regions could not be differentiated from true non-filling regions. As such, dynamic imaging using ^{19}F provides additional resolution to characterize these abnormal regions.

The observation of lung regions with a ^{129}Xe + ^{19}F- pattern was unexpected, as multiple breaths of PFP is not expected to be less likely to fill a partially obstructed region than a single breath of ^{129}Xe. The presence of ^{129}Xe gas suggests that these areas must be receiving some ventilation, despite the paucity of ^{19}F signal. The reduced ^{19}F signal in these regions may be explained by the low SNR and diffusivity of the gas, when compared with ^{129}Xe, coupled with an increase in airway resistance in the region, similarly to what has already been observed in ^{129}Xe/^{3}He comparison studies in COPD patients.[163] The

analysis of τ1 and τ2 rate constants, which we were able to characterize with a high degree of confidence despite the relatively low ^{19}F signal, confirmed that in these lung regions, not only was peak ^{19}F signal low, but also the rates of both gas wash-in and wash-out were markedly slowed.

The presence of ^{129}Xe signal (in some cases, even an accentuated ^{129}Xe signal) in these regions could be explained by a reduced concentration of molecular oxygen in these poorly ventilated regions. This could theoretically be encountered in areas of gas trapping, where some contrast gas is able to enter the region, perhaps by collateral ventilation, but encounters an environment that is relatively devoid of oxygen. This would thereby reduce the rate of HP ^{129}Xe depolarization and, in turn, cause a paradoxically higher ^{129}Xe signal. If this is the case, ^{129}Xe MRI may at times under-report true ventilation defects, as the result of the complex relationship between ^{129}Xe polarization and the local lung oxygen tension. While further testing is required to fully assess gas trapping effects on ^{129}Xe MRI images, our results show that the addition of dynamic ^{19}F imaging in registration with HP ^{129}Xe has provided important additional insights into lung ventilation dynamics.

The peak ^{19}F value at the end of the inhalation sequences was also able to differentiate these three different filling patterns, suggesting that the delayed phase filling with PFP as a single parameter may be the most informative of the ventilation status. Further work in other disease states could better inform the clinical utility of the dynamic ^{19}F approaches. Although we did not perform repeatability scans as a part of this study, others have shown that dynamic ^{19}F ventilation imaging, albeit with a different scanning protocol, has good repeatability in normal subjects and subjects with chronic obstructive pulmonary diseases.[114]

Several technical factors impacted our data, including challenges related to co-registration of ^{19}F, ^{129}Xe, and ^{1}H images. Proton images of the thoracic cavity and gas ventilation images were obtained during separate maximal inhalation breath-holds, making it likely that the same inspiratory capacity might not be reached consistently. As a result, differences in lung inflation volumes can be expected to cause co-registration errors, both in ^{19}F and ^{1}H images. This problem is avoided with the ^{129}Xe-MRI method, as a fixed inhalation volume can be achieved simply through the use of a fixed volume gas delivery bag.

Differences in lung inflation may have led to additional ventilation defects around the lung edges. Thus, the ability to simultaneously acquire anatomical and ventilation images within a single breath-hold, as done for HP ventilation imaging, would likely benefit the ^{19}F method.[175,176] Recent work to accelerate ^{19}F ventilation imaging, which could allow for acquisition of $^{19}F/^{1}H$ images in a single breath hold, would accomplish this goal.[177178] A related minor limitation for the study was the need to reposition the patient between the two inhaled gas studies.

Finally, the use of a multi-channel ^{19}F lung coil led to B_1 inhomogeneities that were subject and coil position dependent and could not be corrected. B_1 inhomogeneities made ventilation thresholds position dependent, preventing the application of typical linear binning techniques that delineate regions of high, medium and low intensity areas based on universal thresholds.[179] Moreover, retrospective bias-field estimation techniques, often used to reduce subject-dependent B_1 effects in ^{129}Xe studies,[179] created spurious gas-filled regions from noise level intensity in low SNR ^{19}F images. This is not surprising as these techniques have been developed for high-SNR images and, in ^{19}F images, where SNR is on the order of the bias-field correction, they artificially change image intensities by a factor of 2 or 3.[179,180]

4.5 CONCLUSIONS

In CF subjects, ventilation abnormalities are identified by both ^{19}F and HP ^{129}Xe imaging but are not entirely congruent across all areas of ventilation. The use of both modalities in this study allowed us to identify an "imaging phenotype" that resulted from normally ventilated, slowly ventilated, and non-ventilated regions. Although further work is needed to evaluate these techniques in other patient populations, these data strongly suggest the complimentary nature of ^{19}F and HP ^{129}Xe imaging; however, VDPs obtained from each method should not be considered equivalent. These data also highlight the utility of ventilation kinetic analyses with ^{19}F MRI and the inherent limitations of relying on a single breath VDP assessment for the characterization of airway function.

4.6 ACKNOWLEDGMENTS

This work was supported by the Cystic Fibrosis Foundation (DONALD14XX0 and GORALS19Y5) and the NIDDK (P30 DK 065988 and DK 108231). We gratefully acknowledge the regulatory assistance of the North Carolina Translational and Clinical Sciences (NC TraCS) Institute, which is supported by the National Center for Advancing Translational Sciences (NCATS), National Institute of Health, through Grant Award Number UL1TR002489. Dr Goralski also acknowledges support from the Doris Duke Charitable Foundation (Grant 2015213)

CHAPTER 5: FEASIBILITY OF FREE-BREATHING 19F MRI IMAGE ACQUISITION TO CHARACTERIZE VENTILATION DEFECTS IN CF AND HEALTHY VOLUNTEERS AT WASH-IN

5.1 INTRODUCTION

^{19}F pulmonary MRI with fluorinated gases has been used to characterize ventilation abnormalities such as unventilated areas (ventilation defect percentages) and poorly ventilated regions (fractional lung volume with prolonged gas washout time in both cystic fibrosis (CF) and chronic obstructive pulmonary disease (COPD)[110,112,181–184]. The ^{19}F gases, including C_3F_8 and SF_6 can be mixed with oxygen to create normoxic gas mixtures. ^{19}F MRI has the potential to spatially measure lung function[112] at multi-slice acquisitions encapsulating the full 3D lung cavity without the need for ionizing radiation. Although hyperpolarized (HP) gas MRI approaches using ^{3}He [185–190] and ^{129}Xe [103,162,163,165,166,191,192] offer greater absolute signal, no hyperpolarizer is needed for ^{19}F imaging, and the signal does not decay with time. ^{19}F gases also make multi-breath wash-in/out studies possible due to being chemically inert and mixable with oxygen without losing its magnetic resonance behavior[110]. Multiple ^{19}F gas inhalations has been shown to be generally safe[106,112,113].

Part of this content was published in part in <**Chung, Sang Hun**, Khoi Minh Huynh, Jennifer L. Goralski, Yong Chen, Pew-Thian Yap, Agathe S. Ceppe, Margret Z. Powell, Scott H. Donaldson, and Yueh Z. Lee. "Feasibility of free-breathing 19F MRI image acquisition to characterize ventilation defects in CF and healthy volunteers at wash-in." Magnetic Resonance in Medicine 90, no. 1 (2023): 79-89. >

One major limitation of ^{19}F MRI with conventional sequences is the scan time required to achieve adequate signal-to-noise ratio (SNR), as most ^{19}F lung acquisitions are performed at breath-holds with an acquisition time of 5.62 to 18 seconds [110,184,193]. This limitation constrains ^{19}F lung imaging to patients able to follow commands and who are comfortable holding their breath for this duration. A much shorter acquisition time could greatly increase patient comfort and allow free breathing scans, making possible the application of ^{19}F MRI to participants unable to reliably hold their breath during image acquisition. The importance of facilitating the development of novel ventilatory biomarkers that can be used in young children cannot be understated. In the case of CF, early detection and treatment is important to prevent irreversible damage in the lungs and to allow us to study the effect of early disease interventions. However, research and development of novel therapies for children has historically been stymied by outcome measures that are impractical or impossible in young children[194–196].

Free breathing functional MRI with x-nuclei has been studied with mice lung models using hyperpolarized ^{129}Xe respiration-gated phase encoding[197] and using SF_6 with 5 minute acquisitions[108], both of which are not suitable for gas dynamics analysis. ^{19}F free breathing human lung MRI with temporal resolutions as short as 0.544 seconds[198], 0.98 seconds[114], and 2.1 seconds[110] have been achieved by Gutberlet et al. However, free breathing was applied to only the wash-out portion resulting in wash-out dynamic metrics such as time to wash-out, number of breaths to wash-out and fraction ventilation (FV), while ventilation defect percentage (VDP) was omitted[198] or measured from the static breath-hold acquisitions[110].

Analysis of VDP during multi-breath wash-in protocols has the potential to discriminate between completely unventilated lung, slowly ventilated regions, and regions

with gas trapping in a way that is not feasible with single breath contrast imaging[199] . VDP has been shown to be affected by the number of contrast agent breaths, partially due to slow or collateral ventilation[191]. Hyperpolarized methods have been traditionally performed using a single breath of tracer gas[161,199] due to difficulty to hyperpolarize large gas volumes. Oxygen (O_2) delivery with hyperpolarized gases is also a challenge due to the depolarization effect of O_2[200]. HP multi-breath wash-in lung imaging has been achieved[190] but require additional hardware for accurate on-site mixing of gas volumes and T_1 change correction. In contrast, ^{19}F gases are commercially available as pre-mixed normoxic (21% O_2) mixture that can be obtained and stored in large quantities and delivered directly to patients, making multi-breath wash-in studies logistically simpler.

This paper explores the feasibility of using a fast spiral acquisition sequence(0.45 second temporal resolution) combined with post-acquisition denoising[201] to reduce scan time while maintaining adequate SNR for the analysis of VDP during wash-in. The free-breathing acquisition method was compared to a previously published ^{19}F MRI acquisition method[184,191] where images were obtained during breath-holds. We examined the correlation of VDP determined by each approach at varying timepoints of gas intake.

5.2 METHODS

5.2.1 MATERIALS

MRI acquisitions were performed on a multi-nuclear capable Siemens Prisma 3.0T scanner (Siemens Medical Systems, Erlangen, Germany) and a custom, commercially available 8-channel transmit/receive ^{19}F-tuned chest coil (ScanMed, Inc., Omaha NE, model: 668SI3001). Figure 5.1 shows the gas delivery set-up[202], comprised of a gas reservoir and valves attached to an MR-compatible frame. The air-flow direction is controlled with

one-way valves and a tight-fitting non-rebreathing mask to separate inhalation and exhalation flows. Flow-rate sensors are used to monitor inhalation/exhalation states at scan time.

Figure 5.1. Experimental set-up and gas apparatus[202,203]

8 adults with CF (ages 20-37, 6 female) and 5 healthy volunteers (ages 22-27, 3 female) contributed data to this study. Written informed consent was obtained from all participants. The study was approved by the University of North Carolina Institutional Review Board.

5.2.2 ACQUISITION

^{1}H UTE MRI images were acquired with the embedded scanner body coil during a 17 second maximal inspiration breath-hold while the participant was breathing room air. Using the 3D fast low angle shot (FLASH) sequence (TE/TR, 0.05/2.42 ms; FA, 5°;

resolution, 2.14 X 2.14 mm; slice thickness, 2.5 mm; number of slices, 103; acquisition matrix, 224 X 224, trajectory, spiral; interleaves, 130; spiral duration,1160 μs; slice partial Fourier, 6/8), breath-hold images were acquired at full inspiratory capacity. For the gas inhalation portion of the scan, participants breathed a mixture of 79% PFP and 21% O2 (Airgas Healthcare, Radnor, PA; used under IND 122,215). During gas wash-in, participants inhaled the PFP mixture starting with a tidal volume inspiration/expiration cycle followed by a maximal inspiration and 18 second breath-hold, as illustrated in Figure 5.2.

During the breath hold, a 3D Volumetric interpolated breath-hold examination (VIBE) sequence (TE/TR, 1.61/13 ms; FA, 74°; resolution of 6.25 X 6.25 mm; slice thickness, 15 mm; number of slices, 18; acquisition matrix, 64 X 64; bandwidth, 130 Hz/pixel; averages, 2; partial Fourier, 6/8) was performed; once the acquisition ended, the patient was instructed to exhale and then began next respiratory cycle (tidal inspiration/expiration then maximal inspiration with breath hold). 5 cycles were performed for the wash-in portion resulting in 5 breath-hold acquisitions (gas inhalation total: 5 deep inspirations and 5 tidal inspirations,15-20 L). The wash-out portion was collected similarly but with the participant breathing room air (not used for analysis in this study). Wash-out cycles were repeated until no ^{19}F signal was visible. More details of the approach were previously reported[184,191].

In between the breath-hold scans, a multi-shot (4 arms), 3D stack-of-spirals sequence tuned to ^{19}F was applied while the participant performed their tidal volume breath. A uniform spiral trajectory was designed and the readout time for each spiral interleaf was ~3.6 ms. A total of 12 repetitions were acquired and each repetition lasted 0.45 seconds. The participants were instructed to end breath-hold and start free breathing

after 0.5 seconds had passed from the start of spiral acquisition to maintain lung inflation between VIBE and spiral acquisitions. Spatial resolution, position, and the number of slices were identical to the breath-hold VIBE acquisition. Other imaging parameters included: TE/TR, 0.48/11 ms; FA 74°; partial Fourier along the partition-encoding direction, 6/8. Similar to the VIBE acquisition, a 0.4-ms hard pulse was used in this study for volumetric excitation.

The first gas intake scans are referred as VIBE_Wi2 and Spiral_Wi2 (taken after a tidal inspiration and during a deep inhalation breath-hold), the last wash-in scans are referred as VIBE_Wi10 and Spiral_Wi10 to refer to the scan time point based on the total number of wash-in inhalations (both deep and tidal).

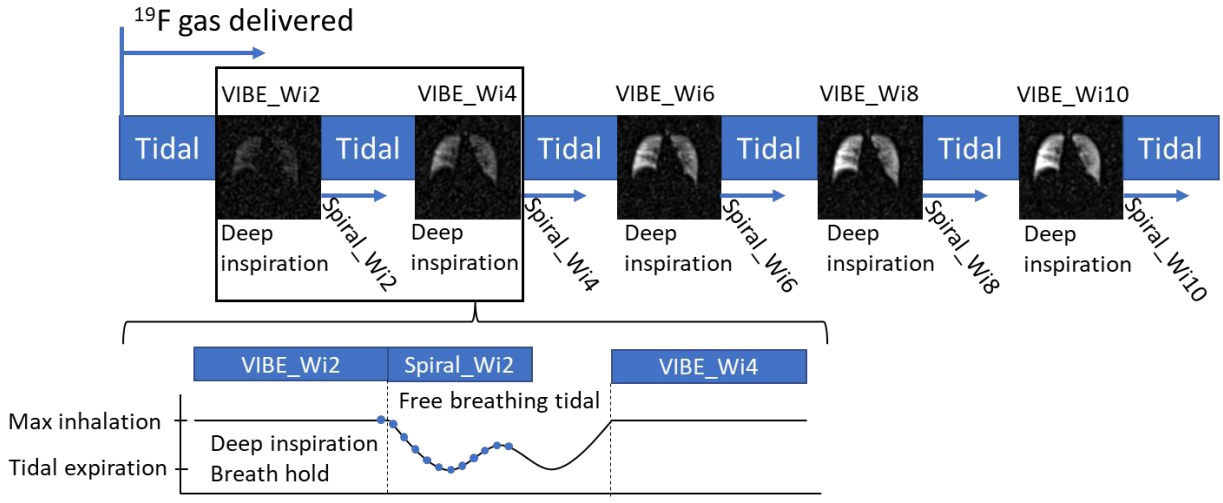

Figure 5.2. Acquisition method showing 5 deep inspiration breath holds, 5 tidal inspirations, and spiral timing at wash-in, Acquisitions taken from the second and 10th inhalations (first and 5th deep inspiration breath holds) were used in the analysis of VDP. The 12 spiral repetitions are illustrated as solid circle markers, with the first spiral repetition being taken while the participant was still in breath-hold.

The ^{19}F VIBE scans and ^{1}H FL3D scans were saved as DICOM images and imported to MIM (MIM 6.9.2, MIM Software, inc. Cleveland, OH) to define the whole thoracic lung cavity mask. The masks were drawn from a fusion of ^{1}H and ^{19}F VIBE, by hand and with

bias towards the ^{19}F outline if inflation difference was present. The spiral scan data was exported as RAW files and reconstructed in MATLAB (MATLAB R2019b, The MathWorks, inc.) using the Michigan Image reconstruction toolbox (MIRT)[204] .

5.2.3 DENOISING

The data was denoised using low-rank matrix recovery with optimal shrinkage of singular value[205], an idea akin to Principal Component Analysis (PCA) denoising. Specifically, for each voxel, we selected a 3-by-3-by-3 block of neighboring voxels, forming a vector of voxel measurements. We then stacked the respective vectors of voxel measurements from all channels, repetitions, and timepoints to form a signal tensor, which can be reshaped to a 2-D matrix. This matrix is inherently low-rank due to signal similarity across neighboring voxels, channels, repetitions, and timepoints, as the same lung region is studied from multiple vantage points. However, the random noise obscures this low-rank structure, making the matrix full-rank. Therefore, with proper low-rank matrix recovery, we can remove the noise and reveal the underlying signal.

This approach has been proven to be effective in diffusion MRI context [201]. Note that to satisfy the random Gaussian noise assumption of the low-rank matrix recovery technique, we performed denoising for the real and imaginary part of the complex data separately. The resulting multi-coil spiral data was then combined using the adaptive reconstruction method[206]. Lastly, the spiral scans were registered to the VIBE scans using the MATLAB functions imregtform and imtranslate rigidly using only translation.

The spiral F19 data was acquired and processed as follow:

1. Acquire 12 repetitions for 4-arm spiral data and reconstruct it using non-uniform fast Fourier transform, yielding a 5D Cartesian complex-valued data of 3 spatial dimensions (x, y, and z), channels, and repetitions.
2. Perform Mahalanobis whitening transformation for cross-channel de-correlation to ensure independent and identically distributed Gaussian noise across channels.
3. Using an overlapping sliding-block approach, a tensor of 3x3x3 voxels block across 8 channels and 12 repetitions was reshaped into a 17x96 Casorati 2D matrix for denoising. While the noisy matrix is full-rank due to noise, the actual noise-free matrix is low-rank due to correlated measurements from all channels, repetitions, and voxels in the block. We reveal this low-rank structure by mapping the matrix's singular values using an optimal shrinking function in[201,205]

   Specifically, for a noisy $M \times N$ 2D matrix S, perform singular value decomposition

$$S = \sqrt{N} U \Sigma V^T \tag{5.1}$$

   Where U and V are the unitary matrices containing the left and right singular vectors of S and Σ is the diagonal matrix of which diagonal elements are singular values $s_1 \geq s_2 \geq s_3 \geq \cdots \geq s_M$.

   The singular values are then mapped using

$$f(s) = \begin{cases} \frac{1}{z^2(y)y}\left(z^4(y) - \delta - \sqrt{\delta} yz(y)\right), \ if\ z^4(y) \geq \delta + \sqrt{\delta} yz(y) \\ 0\ ,\ otherwise \end{cases} \tag{5.2}$$

   Where $y = s/\sigma$ with noise level σ, $\delta = \frac{M}{N}$, and

$$z(y) = \frac{1}{\sqrt{2}}\sqrt{y^2 - \delta - 1 + \sqrt{(y^2 - \delta - 1)^2 - 4\delta}} \tag{5.3}$$

   The estimated noise-free matrix is then

$$\hat{S} = \sqrt{N}U\hat{\Sigma}V^T \tag{5.4}$$

Where the diagonal matrix $\hat{\Sigma}$ has diagonal elements of $f(s_1), f(s_2), f(s_3), \ldots, f(s_M)$.

The noise level σ is estimated during denoising as

$$\sigma = \frac{s_{0.5}}{\sqrt{N\delta_{0.5}}} \tag{5.6}$$

Where $s_{0.5}$ is the median of all $s_1 \geq s_2 \geq s_3 \geq \cdots \geq s_M$ and $\delta_{0.5}$ is the median of the Marcenko-Pastur distribution, determined by solving

$$\int_{\delta_-}^{\delta_{0.5}} \frac{\sqrt{(\delta_+ - x)(x - \delta_-)}}{2\pi x} dx = 0.5 \tag{5.6}$$

With $\delta_\pm = \left(1 \pm \sqrt{\delta}\right)^2$.

This shrinkage step was done for the real and the imaginary parts of the complex-valued data separately.

4. Perform adaptive channel combination giving a complex 4D data of 3 spatial dimensions and the fourth for repetitions.
5. Compute the magnitude of the complex-valued data.
6. Select the spiral first repetition for VDP and SNR calculations.

5.2.4 VENTILATION DEFECT PERCENTAGE AND SNR

Regions in the lung with signal lower than the 95th percentile signal intensity[110,207] of the most posterior slice (outside the lung, representing a noise-only region) were characterized as VDP. The VIBE SNR was calculated as the ratio between the mean signal (inside the whole lung ROI, excluding VDP) over the standard deviation (taken from the most posterior slice, outside the lung).

The Spiral SNR for both pre and post denoising was calculated spatially by diving voxel magnitudes by the noise standard deviation calculated by the Marchenko Pastur (MP-PCA) method[208,209,210]. The spiral SNR values are reported from the average voxel wise SNR inside the lung cavity excluding VDP regions. The VDP processing workflow is shown in Figure 5.3. For comparison, VDP values are taken from the first single repetition spiral scans immediately following the VIBE scans. SNR values are calculated from the last wash-in scans (Wi10).

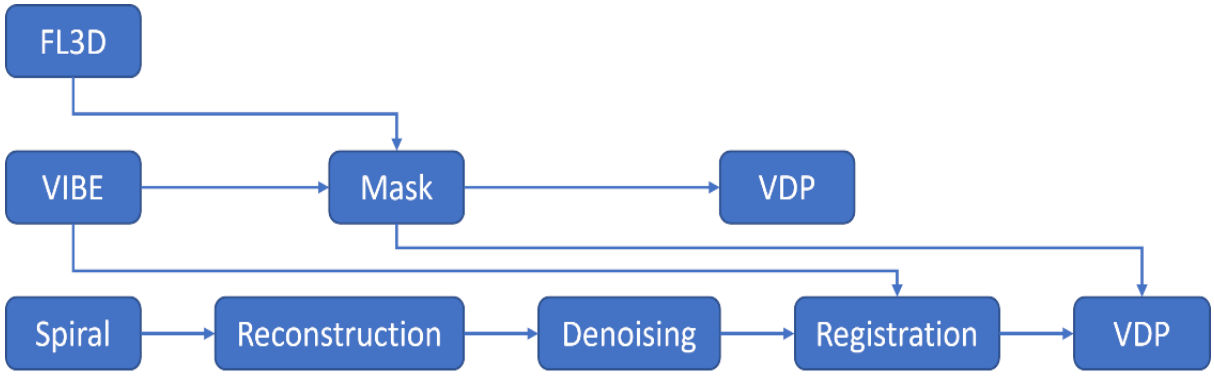

Figure 5.3. Processing workflow, arrows show the inputs for each processing step. A single mask is used to calculate VDP for VIBE and Spiral acquisitions

5.2.5 STATISTICAL ANALYSIS

Analysis of variance was performed on all measured VDPs using 2-way repeated measure ANOVA and multiple comparisons were corrected with Tukey (SAS 9.4, SAS Institute Inc., Cary, NC, USA). Bland-Altman plots were generated to show difference in means. Pearson Correlation coefficients (r) were calculated using the MATLAB corrplot function (MATLAB R2019b, The MathWorks, inc.).

5.3 RESULTS

5.3.1 FEV1 % PREDICTED AND SNR

FEV1 % predicted was measured for each participant prior to MRI scanning. Table 5.1 shows the CF/Healthy groups with the measured FEV1 % predicted and SNR values.

Table 5.1. Study Population FEV1 % predicted and SNR values

CF		SNR			Healthy		SNR		
Patient	FEV1 % predicted	VIBE	Spiral not denoised	Spiral denoised	Patient	FEV1 % predicted	VIBE	Spiral not denoised	Spiral denoised
1	106	16.86	2.54	36.14	9	98	17.92	2.71	41.44
2	99	17.72	2.52	35.06	10	88	19.21	2.63	40.62
3	92	17.72	2.54	38.49	11	92	19.82	2.63	36.22
4	94	14.95	2.26	26.79	12	110	20.68	2.74	41.53
5	74	13.73	2.18	25.20	13	116	14.68	2.27	28.23
6	103	19.28	2.61	36.62					
7	106	18.27	2.17	26.24					
8	64	16.93	2.24	28.28					
mean	92.25	16.93	2.38	31.60	mean	100.8	18.46	2.60	37.61
st. dev	15.46	1.80	0.19	5.47	st. dev	11.88	2.34	0.19	5.68

The ^{19}F VIBE scans yielded an average SNR of 16.93±1.80 for CF and 18.46±2.34 for the healthy group. Before the denoising procedure, 19F spiral scans had an average SNR of 2.38±0.19 for CF and 2.60±0.19 for the healthy group. The denoised ^{19}F spiral scans had an average SNR of 31.60±5.47 for CF and 37.61±5.68 for the healthy group. Figure 5.4 shows example slices from a VIBE acquisition (breath hold), and from spiral acquisitions before and after denoising was performed, the last bottom line shows the corresponding spiral SNR maps.

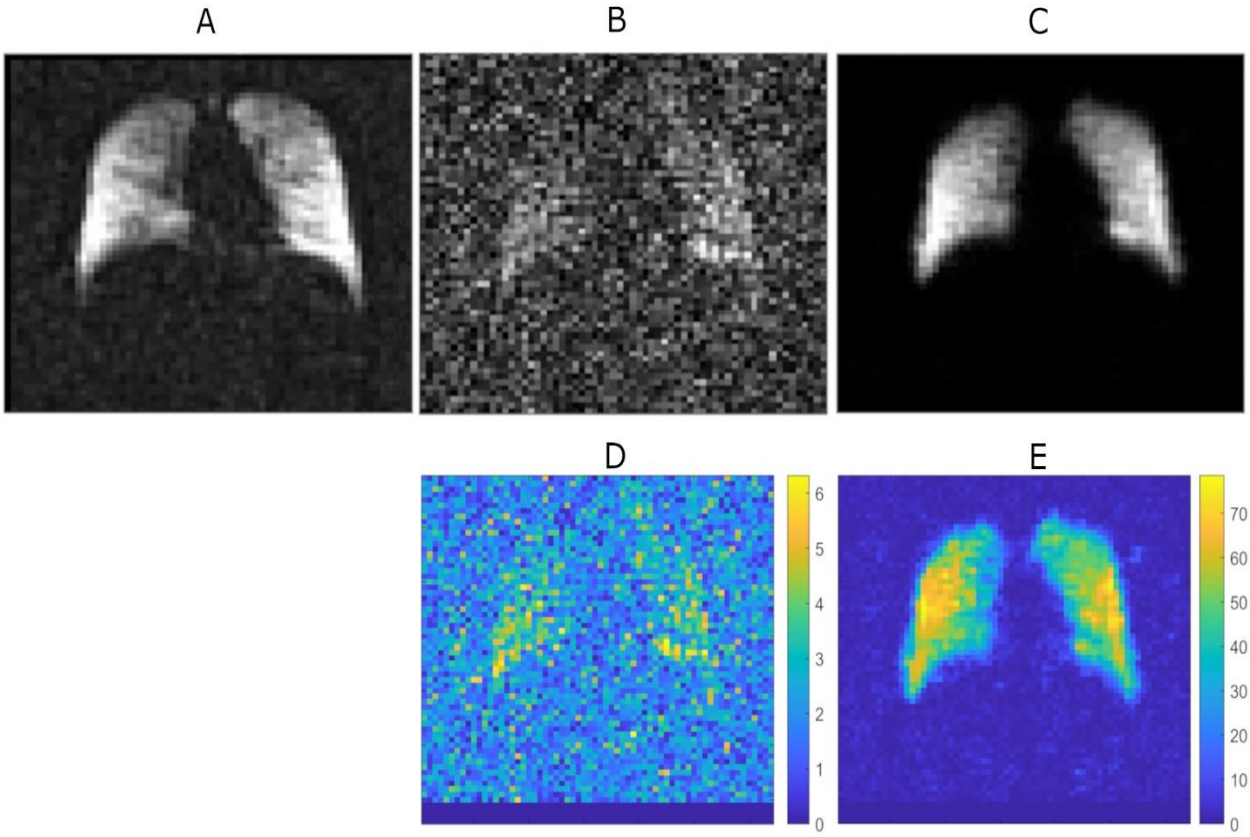

Figure 5.4. Coronal slices of a healthy participant at the last wash-in scans, (A) VIBE_Wi10 at breath hold, (B) Spiral_Wi10 not denoised, (C) Spiral_Wi10 denoised, (D) Spiral_Wi10 SNR not denoised, (E) Spiral_Wi10 SNR denoised

5.3.2 VENTILATION DEFECT PERCENTAGE

VDP values were calculated at each breath cycle, with emphasis placed on the first scans (VIBE_Wi2, Spiral_Wi2) and after the 5th breathing cycle when the lung likely neared gas saturation (VIBE_Wi10, Spiral_Wi10). Figure 5.5 shows coronal slice images with VDP maps as green areas for a representative CF and healthy volunteer.

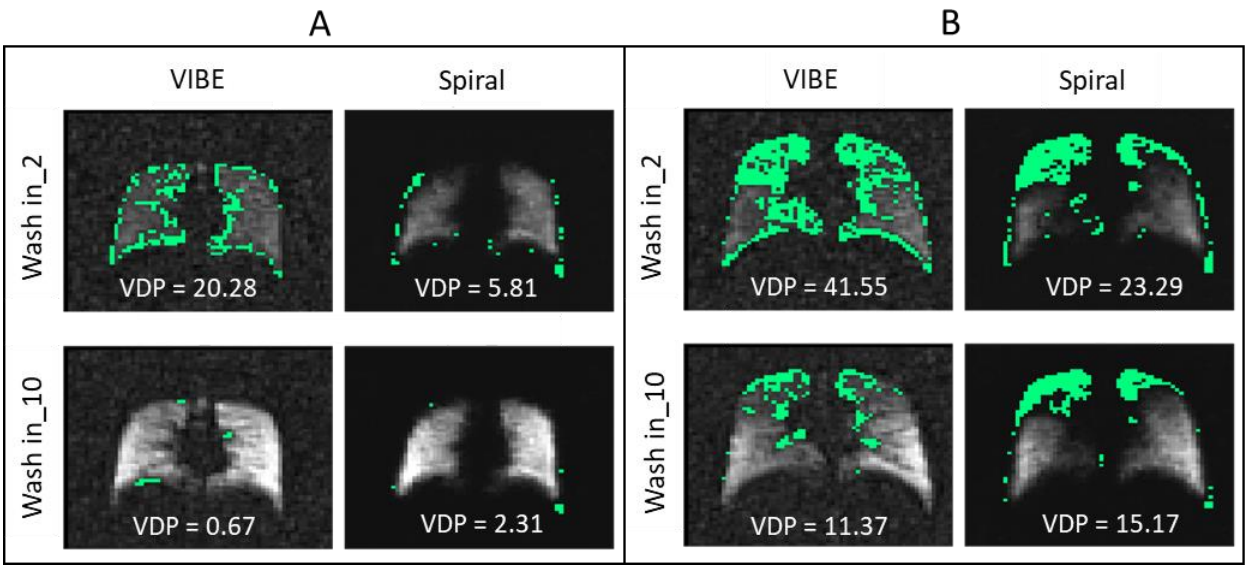

Figure 5.5. (A) Healthy participant, (B) patient with CF. VDPs are shown at the bottom of each image

5.3.3 STATISTICAL ANALYSIS

The Pearson correlation coefficient relating the VDP from VIBE_Wi10 was highly correlated to the spiral_Wi10 VDP (r=0.84). The VDP from spiral_Wi2 was also highly correlated with both the VDPs from VIBE_Wi2 (r=0.88) and spiral_Wi10 (r=0.88). FEV1 % predicted was not strongly correlated to any measured VDP, with the highest correlations from VIBE_Wi10 (r=-0.52) and VIBE_Wi2 breath (r=-0.52).

The VDPs also showed a difference in mean values between the approaches, with the mean VDP of spiral_ Wi2 higher by 5.3 % than the mean VDP from spiral_Wi10. The mean VDP of VIBE_Wi2 was higher by 19 % over the mean VDP of VIBE_Wi10. The mean VDP of VIBE_Wi10 was lower by 1.8 % compared to the mean VDP from spiral_Wi10. The mean VDP of VIBE_Wi2 was higher by 12 % over the mean VDP of spiral_ Wi2. The differences in mean values are shown as Bland-Altman plots in Figure 5.6. With the

exception of VIBE_Wi10 vs. spiral_Wi10 ($p = 0.074$), all other comparisons were found to be statistically significant with $p \leq 0.001$.

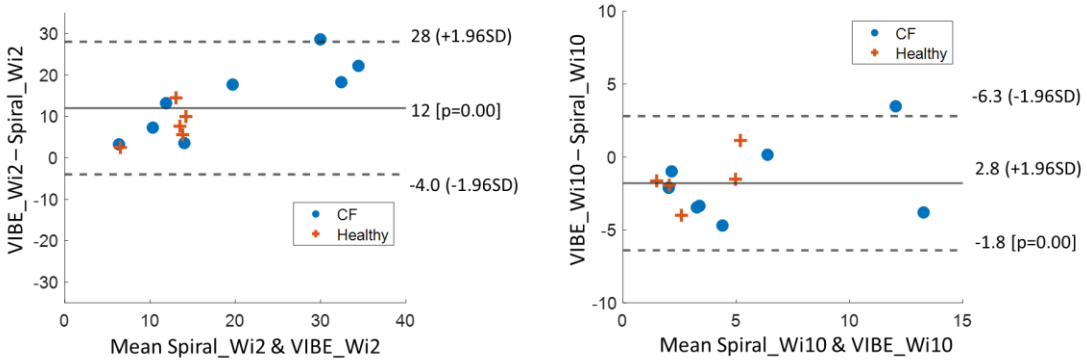

Figure 5.6. Bland-Altman plots between VDPs of VIBE_Wi2 & Spiral_Wi2 and VIBE_Wi10 & Spiral_Wi10, makers show CF status (solid circles: CF, orange +: Healthy)

VDPs at Wi2 breath were greater when compared to VDPs at the last wash-in. However, the VIBE VDPs at Wi2 were generally much higher. In Figure 5.7 VIBE VDPs start proportionally high before plateauing at Wi10. This effect is reduced in the spiral VDPs.

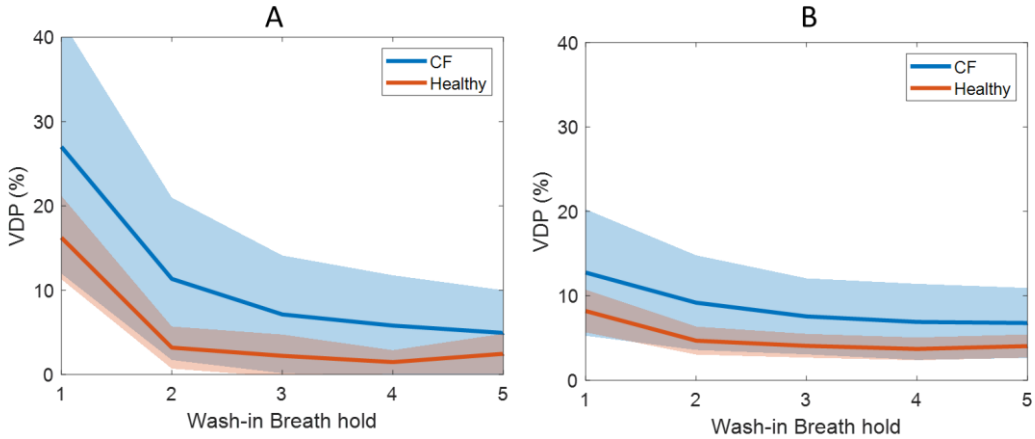

Figure 5.7. Graphs showing the relationship between average VDP and scanned breath for all patients. In the x-axis; 1 represents Wi2 and 5 represents Wi10. (A) VIBE scans, (B) first repetition spiral scans for CF and healthy groups. Shaded areas show ± 1 standard deviation

5.4 DISCUSSION AND CONCLUSION

5.4.1 FUTURE IMPLICATIONS

Evaluating ventilation with MRI based free-breathing approaches has been of significant interest to a number of research groups, especially given the applicability across a range of ages, and potential to eliminate sedation requirements for younger children. Though free-breathing ^{19}F studies have also been reported by other groups[108,110,114,158,197,198], our 0.45 second temporal resolution spiral ^{19}F acquisition with denoising allows free-breathing ventilation acquisition with substantial SNR improvement capable of VDP measurement. Our results suggest that ^{19}F free breathing acquisition with denoising for measuring VDP is comparable to those results obtained via cartesian VIBE breath-hold acquisitions. The significance of these results indicates that breath-hold acquisitions could be replaced by free breathing acquisition on wash-in while maintain the ability to measure regional VDP.

With free breathing scans, participant fatigue from repeated breath holds would no longer be a limiting factor for ventilation studies; instead, the test would be constrained by the amount of gas available. Bag volumes are readily customizable, and our studies are currently performed with a 30L bag. Longer wash-in/out sessions with ^{19}F might enable the further characterization of VDP in various disease states. For example, a computed tomography (CT) study using xenon gas as contrast agent showed that in the presence of complete bronchial obstruction, unventilated areas will eventually reach signal saturation through collateral flow in 72 tidal breaths using a canine model[207]. A longer wash-in cycle might allow for additional characterization of slow-ventilating regions due to local bronchial obstruction, as compared to complete defects resulting from alveolar obstruction.

In a prior study comparing ^{19}F MRI to ^{129}Xe HP-MRI[191] in CF patients, we established that ventilation defects calculated after single breath-holds of hyperpolarized xenon were not equivalent to those assessed after multiple breaths of a perfluorinated gas. The proposed explanation is that longer exposure to a contrast gas allows for regional filling due to collateral ventilation to a partially or completely obstructed area. Thus, one might expect that additional wash-in breaths could reveal a more complete picture of the dynamic ventilatory capacity of the lung.

Removing the need for breath holds in an acquisition is anticipated to improve patient comfort, possibly improving breath size stability and compliance. We expect it will also facilitate ^{19}F scans for the pediatric population and for those unable to perform breath holds. Other MRI free breathing lung ventilation assessment methods have been recently published such as Phase-Resolved Functional Lung (PREFUL)[115,167,211,212] and a Deep Convolutional Neural Network (DCNN) based method[213]. Both methods only require ^{1}H based scans with no contrast enhancing agents. PREFUL has the added advantage of calculating perfusion and has been applied to younger CF patients in the age range of 11-16 years old[212]. However, ^{1}H MRI ventilation methods operate in the scope of single breath changes, lacking the multi-breath dynamic ventilation assessment that ^{19}F provides.

In our results, VDPs at Wi2 from the VIBE scans were higher than the first scan spiral VDPs (spiral_Wi2) by 5.3% difference in mean, which might reflect systematic 19F gas diffusion or collateral ventilation towards slow ventilated areas during the time length of the VIBE scan breath hold. Other possible causes of the lower overall VDP values from the spiral might be due to the relative decrease of noise level to the signal level due to denoising especially at voxels affected by partial volume. The spiral sequence (being sparser

at the boundaries of k-space) also causes blurring which might partially explain the offset in measured VDP.

A current observation with our denoising method is that Spiral_Wi2 breath VDP values were lower compared to VIBE_Wi2. Although average signal intensity seems to be linear between the two methods, the change between signal and background noise distributions due to denoising might be causing a discrepancy between VDP values that requires further adjustments in either denoising or VDP calculation methods.

5.4.2 LIMITATIONS

One limitation of this study is that our goal was to compare the two acquisition modalities while not exposing the participant to additional gas inhalation beyond what we have already studied. Therefore, we chose to run the spiral sequences in bursts of 12 repetitions in between each breath-hold acquisition. In future studies, we plan to conduct the scan with continuous spiral repetitions over multiple breaths with no interruption.

The spiral acquisition, while shortening the scan time, also introduces susceptibility to B0 inhomogeneities, Eddy currents, and gradient delay errors resulting in distortions. Many correction methods have been published [214–219] but have not yet been adapted widely by scanner manufacturers. It might be possible to achieve similar scan times using radial acquisition or acceleration methods such as GRAPPA, SENSE, or compressed sensing.

Another limitation is that SNR was calculated based on regions of interest (ROI) analysis of a ROI outside the thoracic cavity and a ROI with signal for the VIBE scans due to our group having access to only magnitude DICOM images. This approach does not provide information of spatially varying noise throughout the acquisition volume and makes it difficult for direct comparison with comparable denoising methods. The spiral

SNR was calculated using the noise standard deviation from the Marchenko Pastur (MP-PCA)[209,210] denoising method. This method was used due to its ability to calculate noise standard deviation from channel combined complex MRI data without additional scans. However, the MP method assumes a Gaussian noise distribution which might lead to inaccurate SNR values if the noise is not Gaussian.

An alternative to the ROI based SNR calculation is the pseudo multiple replica approach proposed by Robson et al.[220], which is capable of in-vivo spatial noise calculations suitable for acquisitions where patient motion or physiological noise might be an issue. Future work will use a more complete and objectively comparable SNR calculation method needed specially when comparing or optimizing denoising methods in-vivo.

5.4.3 DENOISING

The denoising process appears to decrease the difference in VDPs between Wi2 and Wi10 values (VIBE_Wi2 – VIBE_Wi10 = 19%, spiral_Wi2 – spiral_Wi10 = 5.3%). This might be due to denoising bringing the low ventilated areas above the noise threshold. The denoising process also changes the signal and noise distributions in the images. For the VIBE data, the intensity distribution in the background follows a Chi distribution while the distribution in the lung follows a non-central Chi distribution as the data was reconstructed using the sum-of-square method[206,221]. For the spiral noise data, both before and after denoising, the intensity distributions are Rayleighian because the data was reconstructed using adaptive channel combination[206]. Note that after denoising, the noise standard deviation was significantly lower and the distributions in the background and the lung (assumed to be purely signal of interest) are distinguishable, while before denoising, there is no significant difference between them.

Low-rank matrix recovery denoising has been widely used to remove random additive noise in MR images[208,222]. Here, with the available multi-channel k-space data, our implementation [201] utilizes the similarity in multiple measurements across channels and repetitions to further improve denoising power. In case the multi-channel data is not available, a simple solution is to use variance-stabilizing-transform (VST) to Gaussianize the Rician noise in the channel-combined data prior to low-rank matrix recovery[223]. One assumption of denoising across all channels and repetitions is that the misalignment between images is not significant. In cases where misalignment is prominent, one could perform registration prior to denoising or non-local block-matching to stack spatial blocks with similar structural features for denoising together[224].

5.4.4 CONCLUSION

In conclusion, this study shows the feasibility of VDP calculation with multi-breath wash-in taken during free breathing. The VDP from free-breathing acquisition was highly correlated to the VDP with breath-hold acquisition at the first wash-in scanned time point Wi2 (R=0.88) and at the last scanned wash-in time point Wi10 (R=0.84).

5.5 ACKNOWLEDGMENTS

This work was supported by the Cystic Fibrosis Foundation (PROMISE-MCC18K0; GORALS19Y5) and the National Institute of Health (K23-HL138257-01A1; P30 DK065988)

CHAPTER 6: 19F DYNAMIC ANALYSIS DURING FREE BREATHING, FEASIBILITY OF SPIRAL ACQUISITION WITH DENOISING ON PATIENTS WITH CYSTIC FIBROSIS

6.1 INTRODUCTION

^{19}F pulmonary MRI with fluorinated gases has been used to characterize ventilation abnormalities such as unventilated areas (VDP) and poorly ventilated regions in cystic fibrosis (CF) and chronic obstructive pulmonary disease (COPD)[110,112,181–184].

The ^{19}F gases, including C_3F_8 and SF_6 can be mixed with oxygen to create a stable normoxic gas mixture, making the clinical logistics of supply and storage easy. ^{19}F MRI has the potential to spatially measure lung function[112] at multi-slice acquisitions encapsulating the full 3D lung cavity without the need for ionizing radiation. Multiple ^{19}F gas inhalations with C_3F_8 (PFP) has been shown to be generally safe[106,112,113]. No hyperpolarizer is needed for ^{19}F imaging like in those used for hyperpolarized (HP) gas MRI approaches using ^{3}He [185–190] and ^{129}Xe [103,162,163,165,166,191,192].

Most ^{19}F lung acquisitions are performed at 5.62 to 18 seconds long breath-holds [110,184,193]. This constrains ^{19}F lung imaging to relatively healthy and grown patients. In the case of CF, early detection and treatment is important to prevent irreversible damage in the lungs. ^{19}F has the potential to study the effect of early disease interventions[225], making the ability to scan <5 years old patients consequential. Widely available lung outcome measures such as spirometry are impractical or impossible in young children[194–196].

^{19}F free breathing human lung MRI with temporal resolutions as short as 0.544 seconds[198], 0.98 seconds[114], and 2.1 seconds[110] have been achieved by Gutberlet et al. However, free breathing was applied to only the wash-out portion and ventilation defect percentage (VDP) was omitted[198] or measured from the static breath-hold acquisitions[110].

^{19}F gases also make multi-breath wash-in/out studies possible due to being chemically inert and mixable with oxygen without losing its magnetic resonance behavior[110]. In a previous study by our group, ^{19}F dynamic lung analysis has been shown to be discriminative between healthy controls and CF patients when FEV1% predicted and VDP are not[184]. We also showed that VDP can be measured with a sub 0.5 seconds scan time spiral sequence combined with denoising with good correlation to longer breath hold scans ($R = 0.84$)[225].

This chapter explores the feasibility of using a fast spiral acquisition sequence (0.45 second temporal resolution) combined with post-acquisition denoising[201] to compute dynamic wash-in/out time constants in-vivo. The in-vivo dynamic time constants and VDPs from the denoised spiral was compared to a previously published ^{19}F MRI breath-hold acquisition[184,191].

In-vivo participants were grouped in 3 groups (Healthy, Mild, Moderate), where healthy participants were treated as control, mild participants were those with CF and FEV1% predicted $\geq$ 80%, and moderates were those with CF and FEV1% predicted < 80%.

6.2 METHODS

6.2.1 MATERIALS

MRI acquisitions were performed on a multi-nuclear capable Siemens Prisma 3.0T scanner (Siemens Medical Systems, Erlangen, Germany) and a custom, commercially available 8-channel transmit/receive ^{19}F-tuned chest coil (ScanMed, Inc., Omaha NE, model: 668SI3001).

A gas delivery set-up[202,203], comprised of a gas reservoir and valves attached to an MR-compatible frame was used.

The air-flow direction was controlled with one-way valves and a tight-fitting non-rebreathing mask to separate inhalation and exhalation flows. Flow-rate sensors were used to monitor inhalation/exhalation states at scan time. (See Figure 5.1 in Chapter 5). Cylindrical phantoms filled with the same ^{19}F normoxic mixture used to supply in-vivo participants was used for frequency centering.

20 adults with CF (ages 23-46, 12 female) and 5 healthy volunteers (ages 22-27, 3 female) contributed data to this study.

Written informed consent was obtained from all participants. The study was approved by the University of North Carolina Institutional Review Board. The participants were grouped into Healthy, Mild, Moderate groups as shown in Figure 6.1.

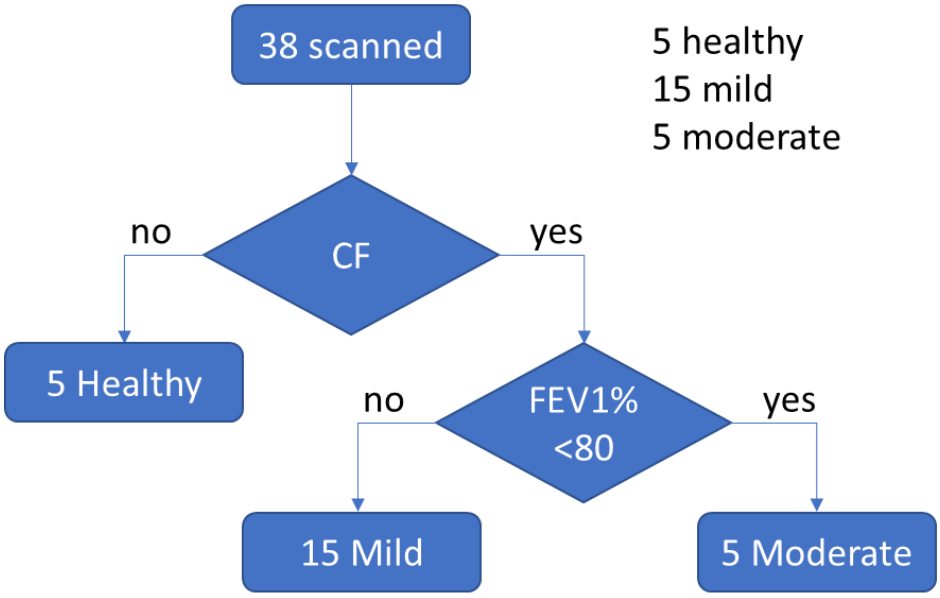

Figure 6.1. Study group design

6.2.2 ACQUISITION

Image acquisition was identical to that described in Chapter 5. Anatomical ^{1}H ultra short echo time (UTE) 3D fast low angle shot (FL3D), (TE/TR, 0.05/2.42 ms; FA, 5°; resolution, 2.14 X 2.14 mm; slice thickness, 2.5 mm; number of slices, 103; acquisition matrix, 224 X 224, trajectory, spiral; interleaves, 130; spiral duration,1160 µs; slice partial Fourier, 6/8).

For ^{19}F, a Breath-hold 3D Volumetric interpolated breath-hold examination (VIBE) sequence (TE/TR, 1.61/13 ms; FA, 74°; resolution of 6.25 X 6.25 mm; slice thickness, 15 mm; number of slices, 18; acquisition matrix, 64 X 64; bandwidth, 130 Hz/pixel; averages, 2; partial Fourier, 6/8), and a 4-arm spiral (TE/TR, 0.48/11 ms; FA 74°; partial Fourier along the partition-encoding direction, 6/8; repetitions, 12; averages, 0) with identical resolution to the VIBE were taken in alternating order. 5 breath-hold VIBEs and 5 spiral were taken during wash-in while the participant breathed in the ^{19}F gas mixture. Wash-out scans were

performed until no visible signal was present in the VIBE scans. Further detail in acquisition design is in Chapter 5.

6.2.3 PROCESSING

The ^{19}F VIBE scans and ^{1}H UTE scans were saved as DICOM images and imported to MIM (MIM 6.9.2, MIM Software, inc. Cleveland, OH) to define the whole thoracic lung cavity mask. The masks were drawn from a fusion of ^{1}H and ^{19}F VIBE, by hand and with bias towards the ^{19}F outline if inflation difference was present. The spiral scan data was exported as RAW files and reconstructed in MATLAB (MATLAB R2019b, The MathWorks, inc.) using the non-uniform Fourier transform (NUFFT) function in the Fessler Michigan Image reconstruction toolbox (MIRT)[204]. After reconstruction, the spiral data was denoised (See 5.3.3), and registered to the VIBE (rigid translation only) using the MATLAB imregister() function. The work-flow for preparing the data for fitting is shown in Figure 6.2.

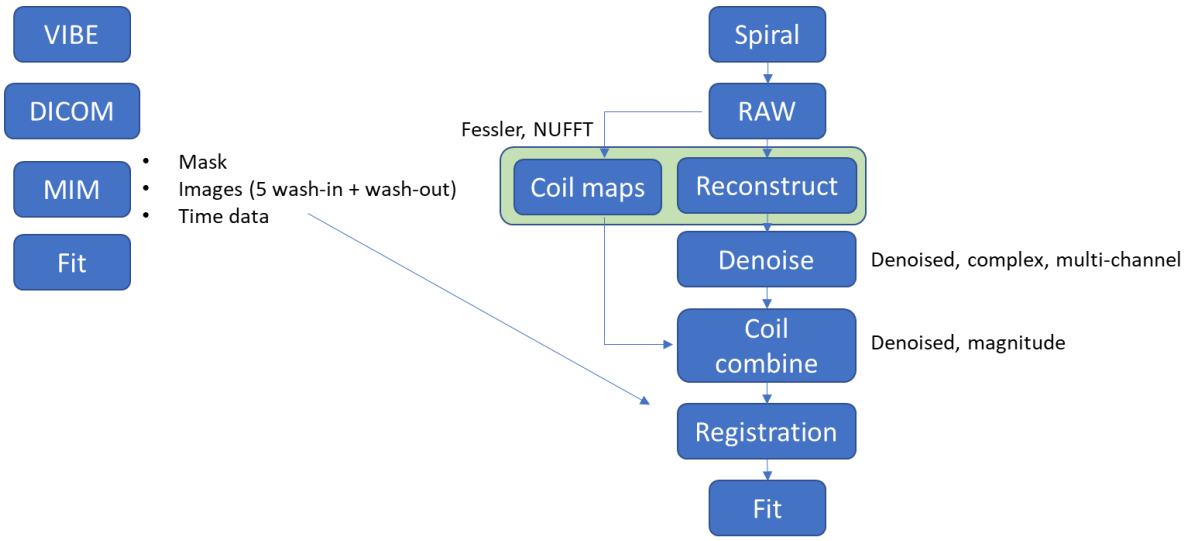

Figure 6.2. processing steps including registration, segmentation, reconstruction, and denoising in preparation for fitting.

The prepared data from both VIBE and spiral images were then fitted using the MATLAB function fit() using the nonlinear least squares option. The fit also used a weight vector with bias to the last wash-in and first wash-out scans. The used fit equations are:

$$d0 + peak\left(1 - e^{\frac{-(x-t0)}{\tau_1}}\right) \qquad x < t1 \tag{6.1}$$

$$d0 + peak\left(1 - e^{\frac{-(t1-t0)}{\tau_1}}\right)e^{\frac{-(x-t1)}{\tau_2}} \qquad x \geq t1 \tag{6.2}$$

Where τ_1 is the wash-in constant,τ_2 is the wash-out constant, d0 is the base of curve, peak is the top of the curve, x is time, t_0 is the time the curve intersects the base, and t_1 is the time wash-in turns into wash-out.

The parameters resulting from the fit were then used to calculate fractional lung volume (FLV) as shown:

$$FLV_{fast} = \frac{\#voxel_{\tau<fast\ threshold,i}\times 100}{\#voxel_{total,i}} \tag{6.3}$$

$$FLV_{slow} = \frac{\#voxel_{\tau>slow\ threshold,i}\times 100}{\#voxel_{total,i}} \tag{6.4}$$

Where *i* is the participant. The FLV thresholds were calculated from clustering using the normal mixture cluster (NM) method in JMP (JMP®, Version *15*. SAS Institute Inc., Cary, NC, 1989–2021) with τ_1 and τ_2 as the axes. The previous NM analysis with the fitting equations used in Chapter 3 (3.1)(3.2) yielded FLV thresholds 64.44 (fast) 175.66 (slow)[184]. The FLV thresholds using equations (6.1) and (6.2) on the current data were calculated for both VIBE and spiral with the current data set.

Ventilation defect percentage (VDP) was computed as the percent of the lung volume with signal below the 95th percentile of noise. Noise was obtained from voxels outside the lung cavity. An additional step was done on the denoised spiral before fitting by using Z-score normalization, and multiple FLV thresholds were tested (39-195 slow and 30-95 fast)

A combination score (comb) was computed as a summation of VDP and FLV τ_2 slow, where voxels that were categorized as both VDP and FLV τ_2 slow were counted only once.

The results are shown as correlation coefficients (R) and Bland-Altman plots. Statistical analysis was done using Fisher's least significant difference (LSD) multiple comparison with MATLAB multicompare() function.

6.3 RESULTS

The collected FEV1% predicted values for each test group are shown in Figure 6.3.

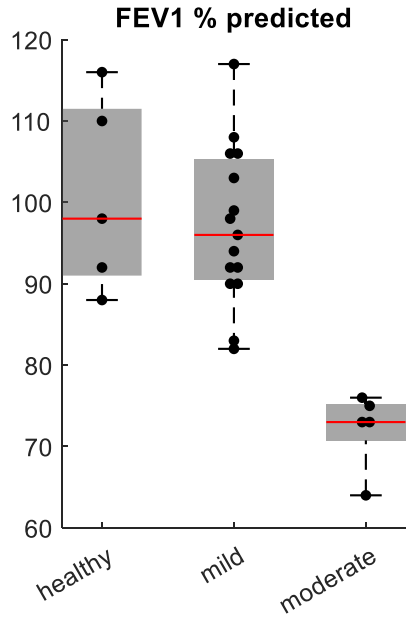

Figure 6.3. FEV1 % predicted values for each group

The NM clustering gave new FLV thresholds 57 (fast), 157 (slow) for VIBE and 40 (fast), 70 (slow) for spiral. Figure 6.4 shows the resulting clusters and the resulting FLV thresholds.

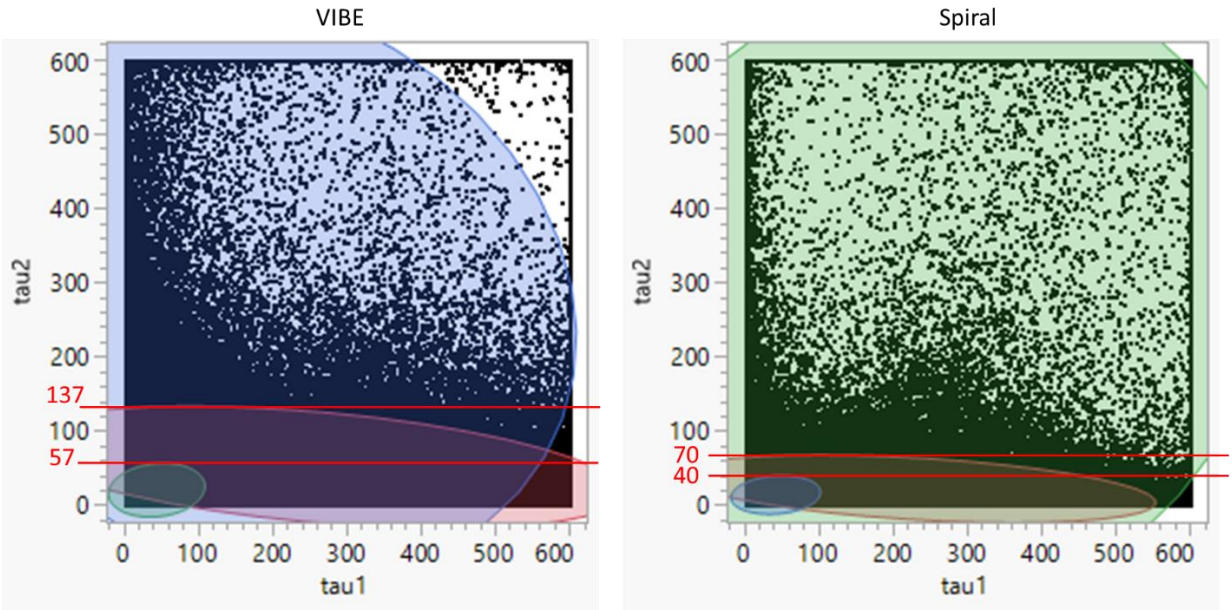

Figure 6.4. Normal mixture clusters on VIBE and Spiral, red lines show the FLV thresholds.

The FLV results with FLV thresholds (57, 157) VIBE and (40, 70) Spiral, VDP, and comb are shown in Figure 6.5. Table 6.2 shows the multiple comparison p-values at a range of FLV thresholds.

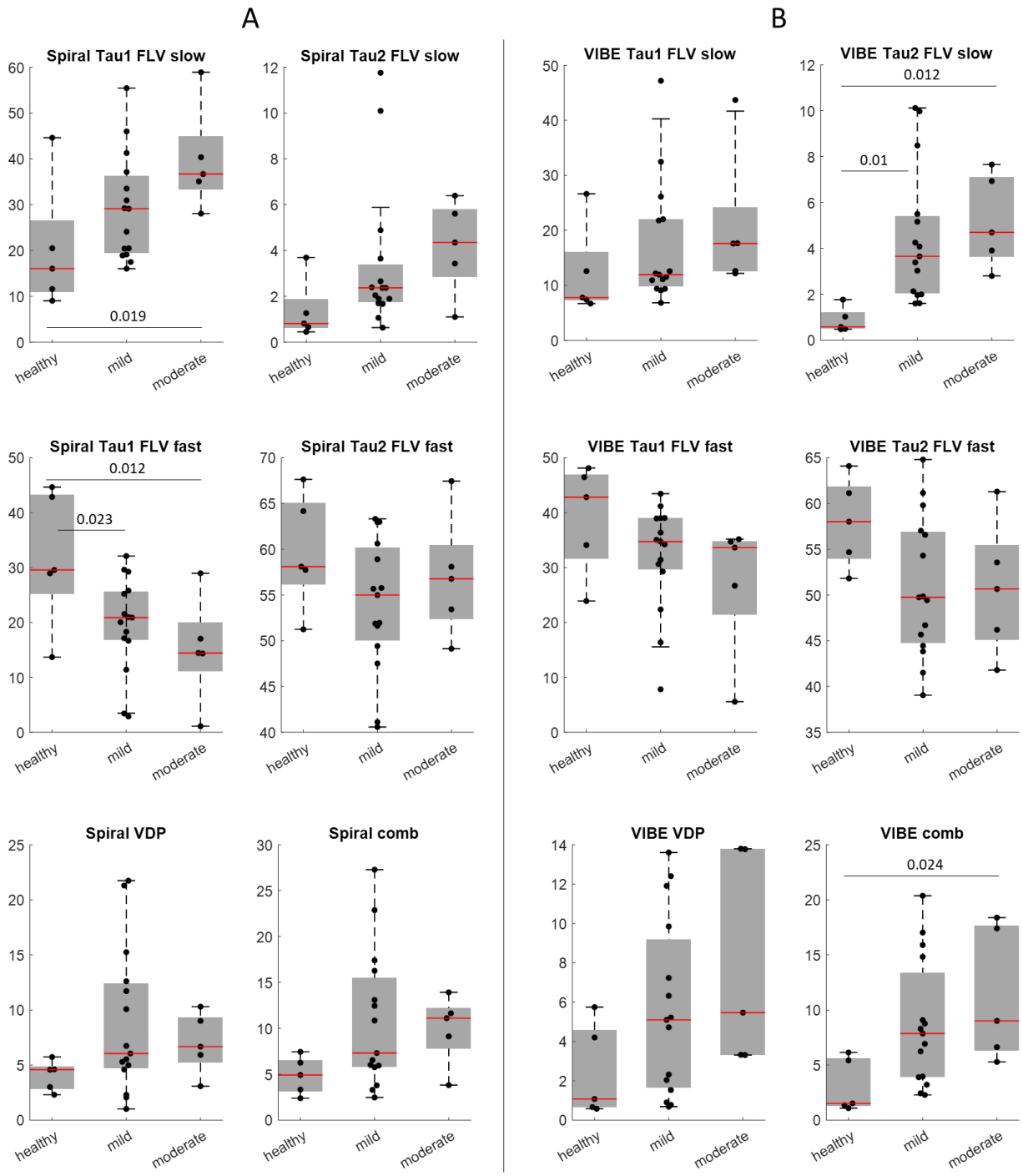

Figure 6.5. FLV, VDP, and comb results by study groups, (A) VIBE (FLV thresholds 57, 137), (B) Spiral (FLV thresholds 40, 70)

The Bland-Altman plots between VIBE and Spiral FLVs, VDPs, and Combs are shown in Figures 6.6 and 6.7.

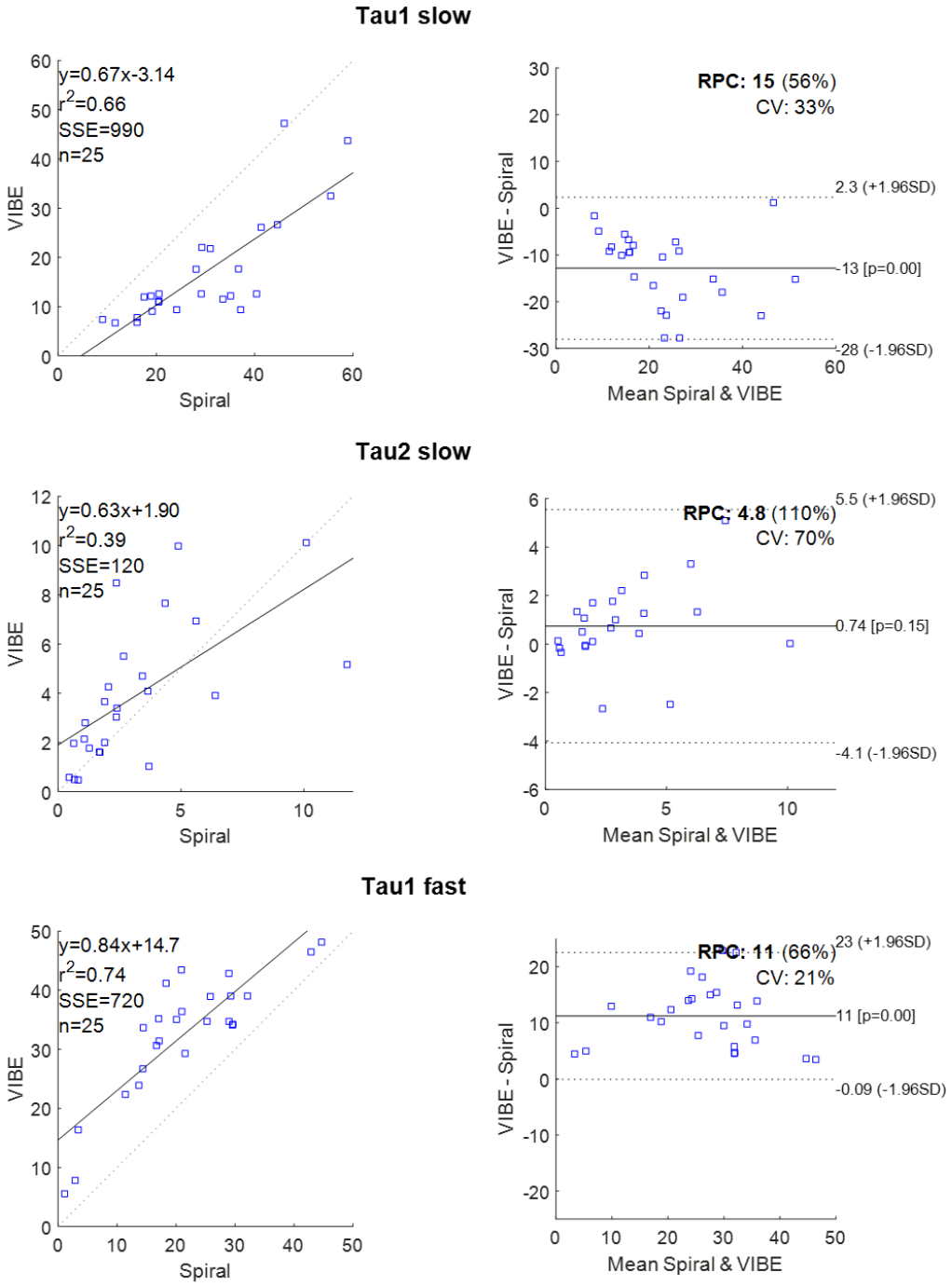

Figure 6.6. FLV Bland-Altman plots for FLV τ_1 slow, FLV τ_2 slow, and FLV τ_1 fast

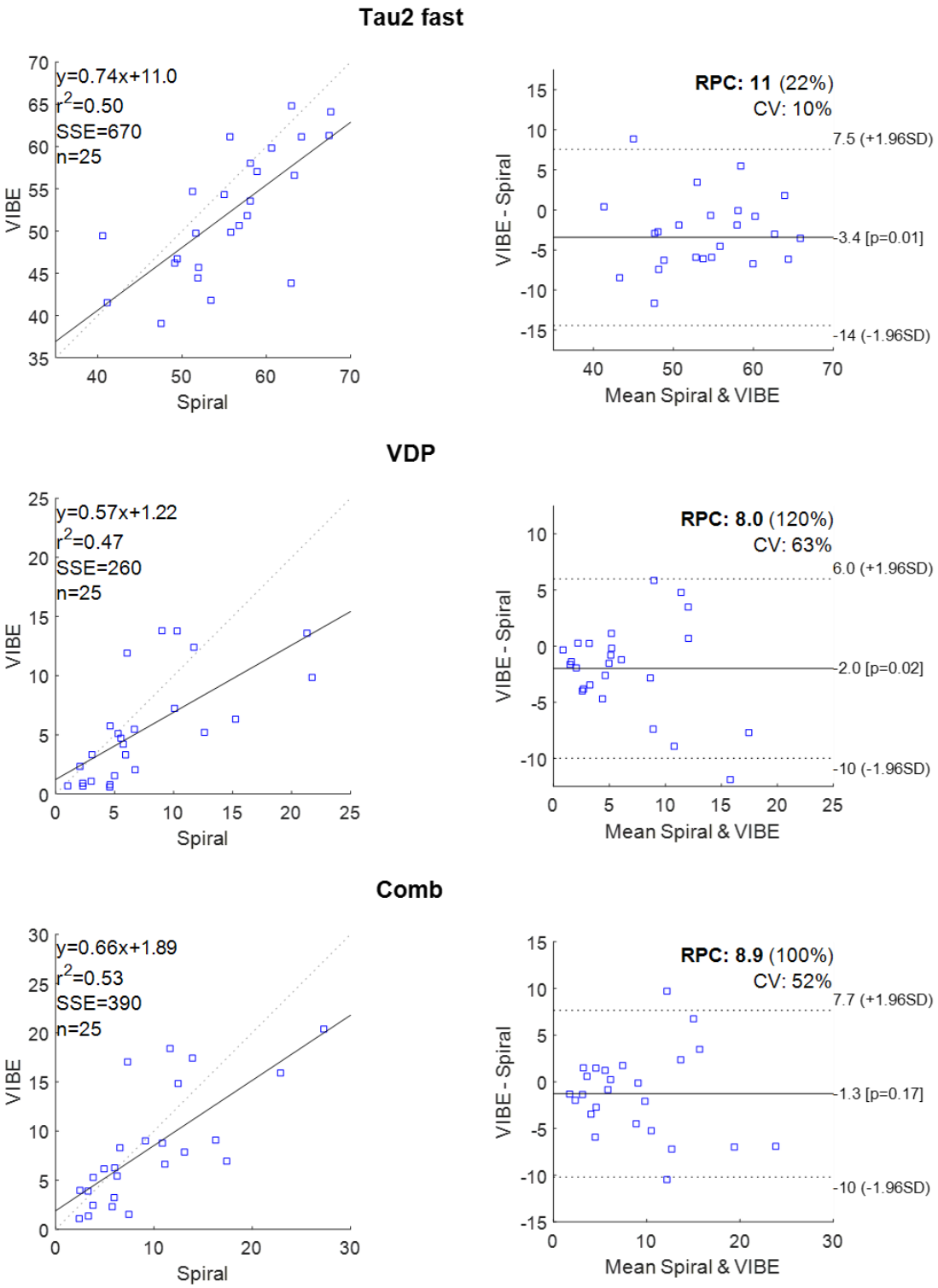

Figure 6.7. Bland-Altman plots for FLV τ_2 fast, VDP, and Comb

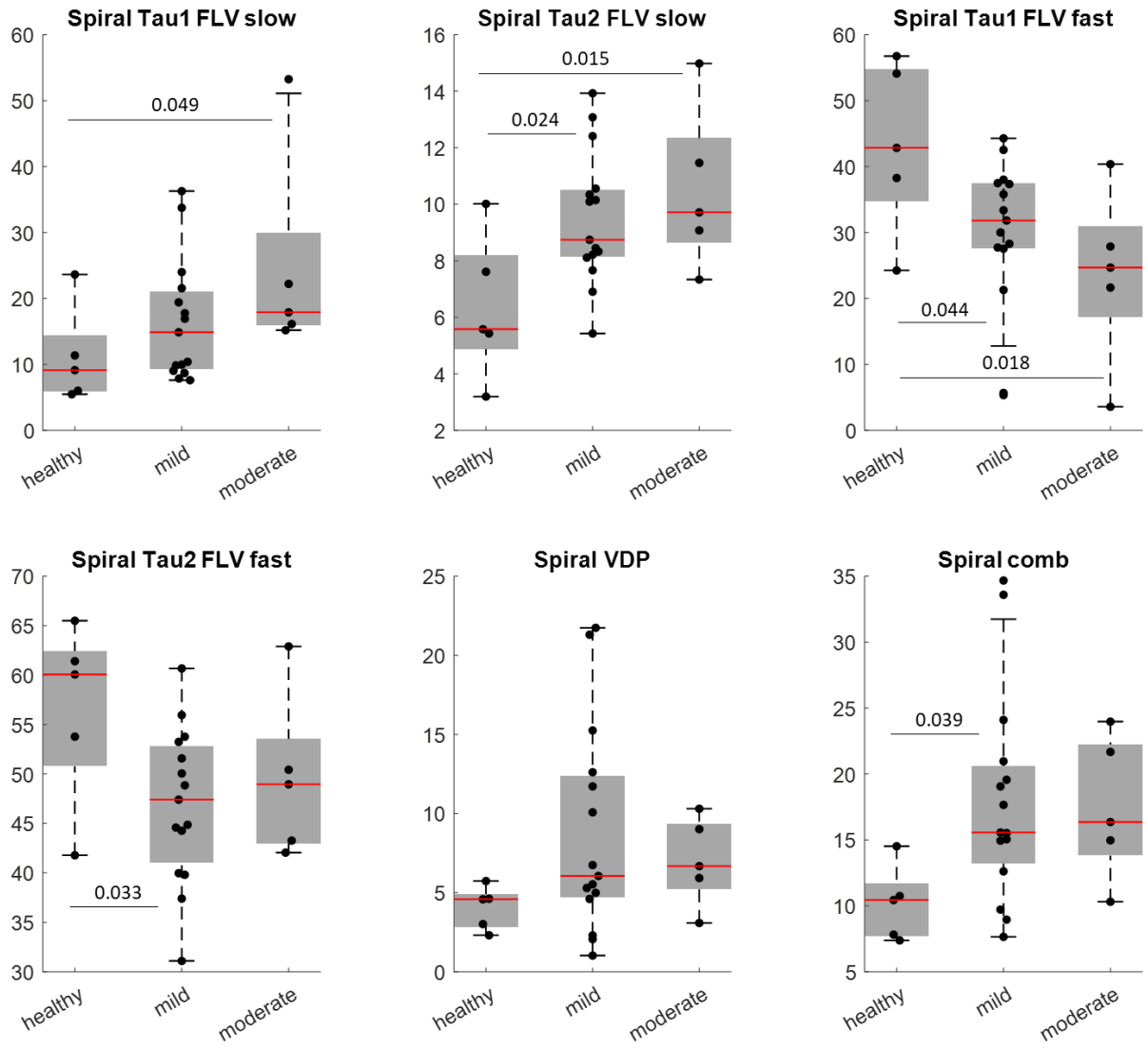

Figure 6.8. Z-score normalized FLV, VDP, and comb results by study groups at FLV thresholds [101,50]

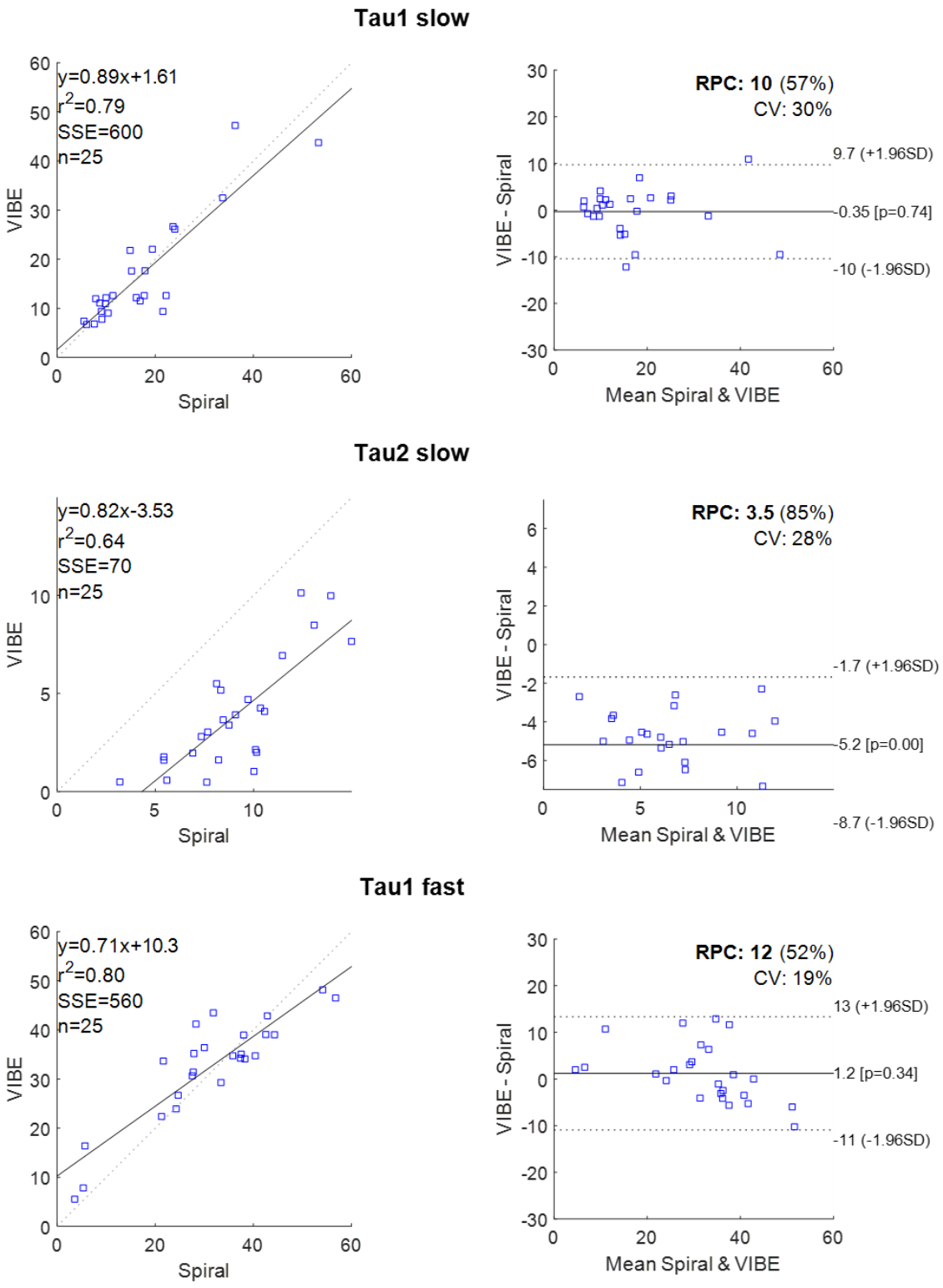

Figure 6.9. FLV Bland-Altman plots for FLV τ1 slow, FLV τ2 slow, and FLV τ1 fast

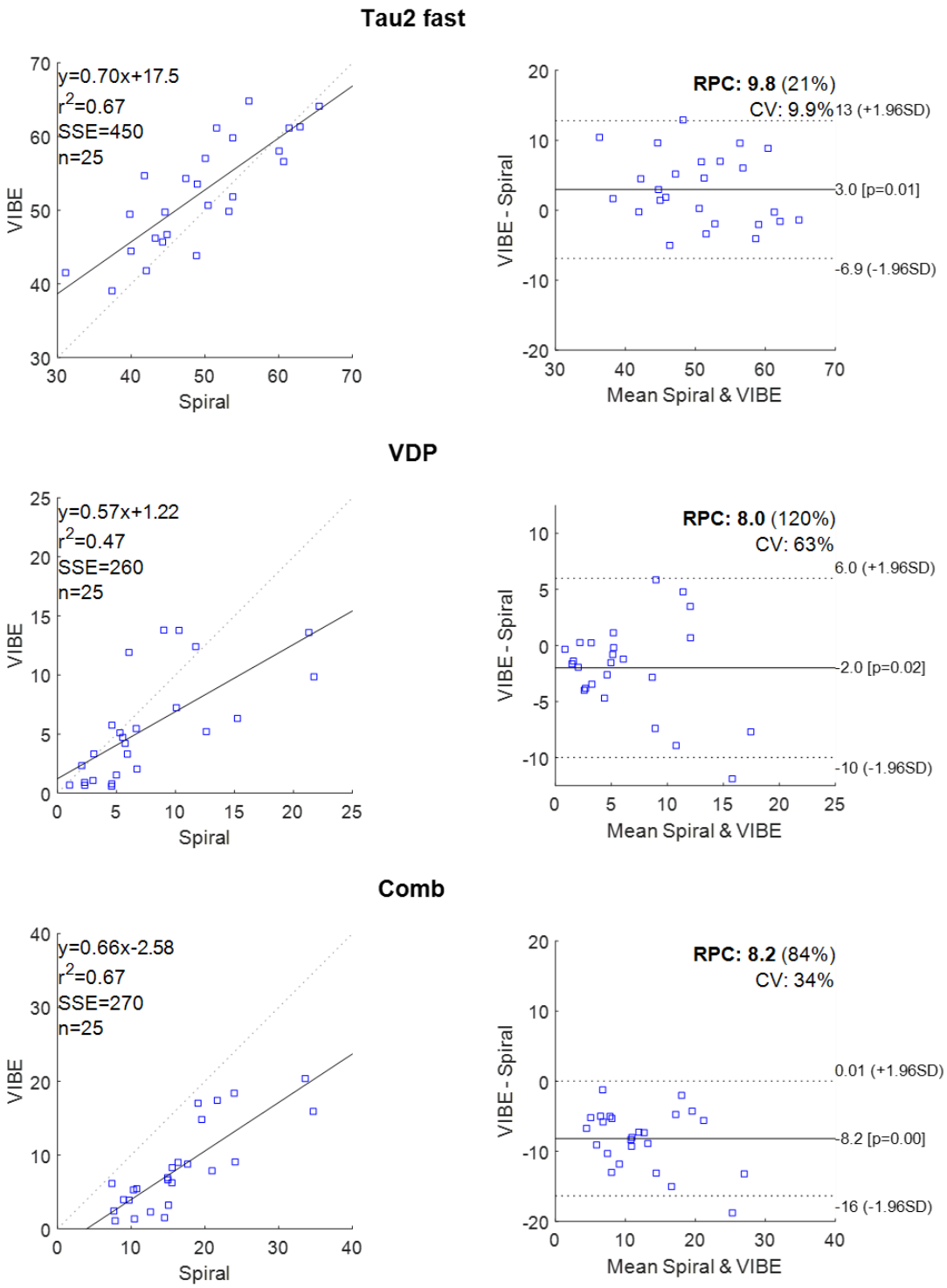

Figure 6.10. Bland-Altman plots for FLV τ_2 fast, VDP, and Comb

Table 6.1 shows the correlation coefficients R between VIBE and Spiral parameters.

Table 6.1 Correlation coefficient R

VIBE & Spiral denoised						
	FLV slow		FLV fast		VDP	Comb
	Tau1	Tau2	Tau1	Tau2		
R	0.86	0.71	0.81	0.63	0.69	0.82

VIBE & Spiral denoised Z-score normalized						
	FLV slow		FLV fast		VDP	Comb
	Tau1	Tau2	Tau1	Tau2		
R	0.89	0.80	0.90	0.82	0.69	0.82

Table 6.2. Multiple comparison p-values, significance ($p<0.05$) is highlighted in red

	VIBE								
	FLV thresholds		115,35	120,40	125,45	130,50	137,57	143,60	156,66	163,70
	Group1	Group2	p	p	p	p	p	p	p	p
VDP	Healthy	Mild	0.173	0.173	0.173	0.173	0.173	0.173	0.173	0.173
	Healthy	Mod	0.060	0.060	0.060	0.060	0.060	0.060	0.060	0.060
	Mild	Mod	0.321	0.321	0.321	0.321	0.321	0.321	0.321	0.321
Tau1 slow	Healthy	Mild	0.431	0.432	0.425	0.423	0.416	0.418	0.402	0.402
	Healthy	Mod	0.248	0.245	0.242	0.236	0.237	0.237	0.230	0.230
	Mild	Mod	0.523	0.514	0.516	0.506	0.516	0.515	0.517	0.517
Tau2 slow	Healthy	Mild	0.008	0.008	0.008	0.009	0.010	0.012	0.014	0.015
	Healthy	Mod	0.013	0.012	0.011	0.011	0.012	0.011	0.010	0.009
	Mild	Mod	0.690	0.677	0.627	0.591	0.573	0.510	0.438	0.397
Tau1 fast	Healthy	Mild	0.168	0.157	0.163	0.179	0.199	0.208	0.225	0.240
	Healthy	Mod	0.055	0.063	0.067	0.072	0.083	0.086	0.086	0.094
	Mild	Mod	0.305	0.358	0.367	0.363	0.377	0.377	0.352	0.361
Tau2 fast	Healthy	Mild	0.177	0.134	0.108	0.083	0.073	0.072	0.073	0.070
	Healthy	Mod	0.419	0.310	0.234	0.166	0.126	0.114	0.097	0.084
	Mild	Mod	0.702	0.780	0.862	0.953	0.952	0.905	0.813	0.758
comb	Healthy	Mild	0.039	0.041	0.044	0.049	0.055	0.060	0.070	0.075
	Healthy	Mod	0.021	0.021	0.021	0.022	0.024	0.025	0.026	0.027
	Mild	Mod	0.399	0.392	0.372	0.364	0.359	0.340	0.324	0.314
	Spiral denoised									
	FLV thresholds		39,30	70,40	101,50	132,60	163,70	170,80	190,90	195,95
	Group1	Group2	p	p	p	p	p	p	p	p
VDP	Healthy	Mild	0.106	0.106	0.106	0.106	0.106	0.106	0.106	0.106
	Healthy	Mod	0.398	0.398	0.398	0.398	0.398	0.398	0.398	0.398
	Mild	Mod	0.537	0.537	0.537	0.537	0.537	0.537	0.537	0.537
Tau1 slow	Healthy	Mild	0.310	0.169	0.181	0.196	0.183	0.184	0.183	0.182
	Healthy	Mod	0.078	0.019	0.017	0.023	0.030	0.031	0.034	0.035
	Mild	Mod	0.235	0.107	0.087	0.110	0.157	0.162	0.177	0.183
Tau2 slow	Healthy	Mild	0.890	0.172	0.125	0.108	0.098	0.091	0.071	0.071
	Healthy	Mod	0.801	0.126	0.065	0.081	0.089	0.094	0.093	0.090
	Mild	Mod	0.865	0.596	0.442	0.579	0.654	0.708	0.800	0.790
Tau1 fast	Healthy	Mild	0.027	0.023	0.034	0.050	0.061	0.071	0.085	0.093
	Healthy	Mod	0.014	0.012	0.016	0.022	0.027	0.031	0.038	0.041
	Mild	Mod	0.388	0.379	0.362	0.356	0.361	0.362	0.377	0.378
Tau2 fast	Healthy	Mild	0.317	0.124	0.082	0.109	0.155	0.188	0.212	0.222
	Healthy	Mod	0.672	0.535	0.421	0.454	0.526	0.580	0.626	0.647
	Mild	Mod	0.623	0.416	0.420	0.469	0.501	0.509	0.503	0.499
comb	Healthy	Mild	0.469	0.080	0.093	0.097	0.100	0.100	0.101	0.101
	Healthy	Mod	0.599	0.212	0.272	0.326	0.351	0.355	0.361	0.363
	Mild	Mod	0.934	0.797	0.708	0.622	0.589	0.583	0.575	0.573
	Spiral Z-normalized									
	FLV thresholds		39,30 Z	70,40 Z	101,50 Z	132,60 Z	163,70 Z	170,80 Z	190,90 Z	195,95 Z
	Group1	Group2	p	p	p	p	p	p	p	p
VDP	Healthy	Mild	0.106	0.106	0.106	0.106	0.106	0.106	0.106	0.106
	Healthy	Mod	0.398	0.398	0.398	0.398	0.398	0.398	0.398	0.398
	Mild	Mod	0.537	0.537	0.537	0.537	0.537	0.537	0.537	0.537
Tau1 slow	Healthy	Mild	0.472	0.315	0.330	0.363	0.370	0.381	0.371	0.373
	Healthy	Mod	0.145	0.051	0.049	0.066	0.087	0.092	0.107	0.110
	Mild	Mod	0.275	0.148	0.136	0.165	0.214	0.219	0.264	0.271
Tau2 slow	Healthy	Mild	0.728	0.122	0.024	0.029	0.036	0.037	0.040	0.041
	Healthy	Mod	0.862	0.154	0.015	0.015	0.019	0.019	0.021	0.019
	Mild	Mod	0.892	0.844	0.437	0.392	0.394	0.394	0.402	0.366
Tau1 fast	Healthy	Mild	0.043	0.035	0.044	0.059	0.075	0.085	0.096	0.102
	Healthy	Mod	0.018	0.015	0.018	0.025	0.031	0.038	0.044	0.049
	Mild	Mod	0.342	0.335	0.340	0.352	0.356	0.377	0.393	0.404
Tau2 fast	Healthy	Mild	0.119	0.055	0.033	0.024	0.024	0.030	0.041	0.045
	Healthy	Mod	0.350	0.266	0.190	0.129	0.111	0.114	0.130	0.138
	Mild	Mod	0.657	0.533	0.541	0.630	0.698	0.768	0.807	0.816
comb	Healthy	Mild	0.289	0.041	0.039	0.050	0.059	0.061	0.065	0.067
	Healthy	Mod	0.569	0.139	0.108	0.134	0.162	0.167	0.183	0.184
	Mild	Mod	0.710	0.769	0.885	0.868	0.831	0.824	0.800	0.805

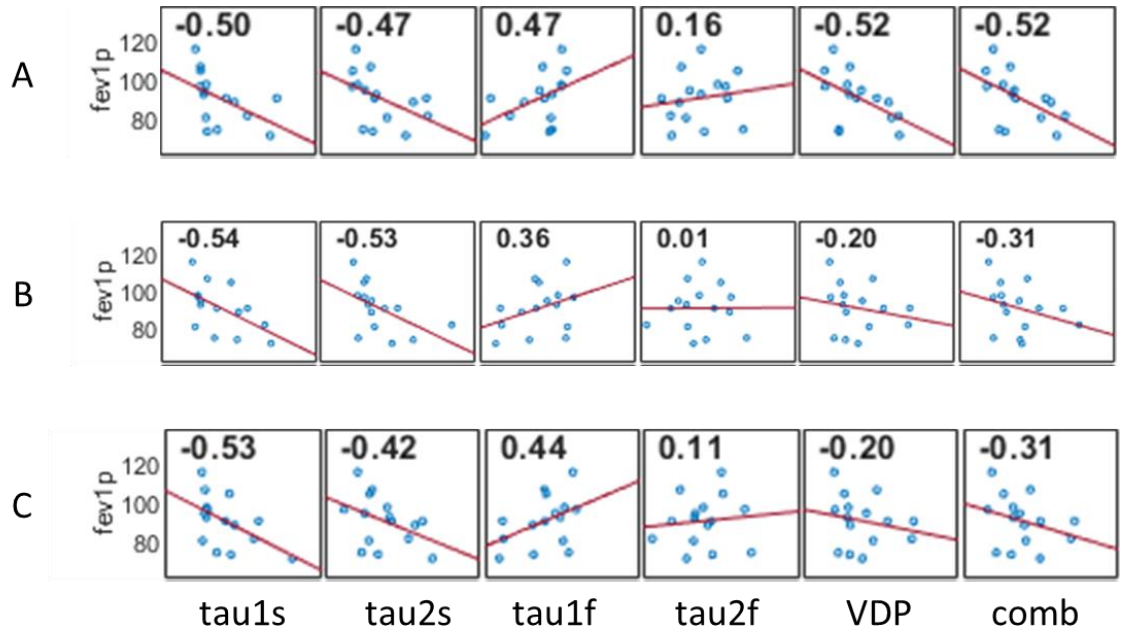

Figure 6.11. FEV1 % predicted (fev1p) scatter plot and correlation coefficient (R) with VIBE (A), Spiral (B) and Spiral Z-normalized (C) with parameters FLV τ_1 slow (tau1s), FLV τ_2 slow (tau2s), FLV τ_1 slow (tau1f), FLV τ_2 slow (tau2f), VDP, and Comb

6.4 DISCUSSION AND CONCLUSION

Spiral and VIBE dynamic time constant and VDP values had good correlations with R values > 0.7 (spiral denoised) and R > 0.8 (spiral denoised and z-score normalized). Z-score normalization of the spiral denoised increased R values across all FLV values, most visible in FLV τ_2 slow (R=0.71 to R=0.80) and FLV τ_2 fast (R=0.63 to R=0.82). From the Bland-Altman plots, visual examination seems to show proportional bias for all tested parameters (FLV τ_1 slow, FLV τ_2 slow, VDP, Comb) except for FLV τ_1 and FLV τ_2 fast. Z-score normalization decreased the bias across all FLV values. These trends likely indicate that VIBE and Spiral parameters differ more as the magnitude of said parameters grows larger. In the context of disease and physiology, it is the amount of unventilated or low ventilated (i.e., low signal) regions that dictate the magnitudes. A possible explanation is

that the sensitivity of VIBE and Spiral differ due to the change in sequence programs, different collected k-space locations, and TE/TR values. Further differences in sensitivity could also be due to the Spiral sequence having extra processing steps in reconstruction with the NUFFT algorithm and the denoising step.

FLV τ_2 slow was expected to show significance in means between healthy and mild groups based on our own previous study[184]. VIBE FLV τ_2 slow showed significance with all tested FLV thresholds ($p < 0.015$). While spiral denoised showed significance with FLV τ_1 fast ($p < 0.034$ with FLV thresholds [39-101, 30-50]). Using Z-score normalization on the spiral denoised, FLV τ_2 slow showed significance ($p = 0.024$-0.041 with FLV thresholds [101-195, 50-95]). The Z-score normalized spiral also showed significance in FLV τ_1 fast ($p = 0.035$-0.044 FLV thresholds [39-100, 30-50]) and FLV τ_2 fast ($p = 0.033$-0.045 FLV thresholds [101-195, 50-95]). The difference in discriminating availability between the VIBE of this chapter with those reported in Chapter 3 are likely due to the small number of participants in the healthy group (n=5) and the moderate group (n=5). The Spiral (both with and without Z-score normalization) finding significance in FLV τ_1 fast was unexpected and requires further analysis.

In Chapter 3, the FLV thresholds from the normal mixture cluster yielded [175.66 (slow), 64.44 (fast)] with time constants fitted with equations (3.1,3.2). Using the data set from chapter 3 and the updated equations (6.1, 6.2) yielded FLV thresholds [163 (slow), 70 (fast)]. Therefore, FLV thresholds [175.66 (slow), 64.44 (fast)] were not evaluated. Previous data sets did not collect spiral scans, therefore spiral FLV thresholds were not computed for the data set from Chapter 3. The newly computed FLV thresholds with the recent data (Chapter 6) have an overrepresentation in the mild group. This might have resulted in lower FLV thresholds from the normal mixture clusters.

Possible sources of error in this study come from the low number of data points and differences in breath sizes through the wash-in/out scans for each participant. Another possible source of error is that the healthy scans were collected first before any CF scans.

In conclusion, VIBE and Spiral dynamic parameters showed good agreement with correlation coefficient ($R > 0.7$ without Z-score normalization and $R > 0.80$ with Z-score normalization). Both VIBE and Spiral showed significance between healthy and mild groups but with different FLV times constants (VIBE; FLV τ_2 slow, Spiral; FLV τ_1 fast, and Z-score normalized spiral; FLV τ_2 slow, FLV τ_1 fast, and FLV τ_2 fast). Our results show that ^{19}F sub second spiral acquisitions with denoising and z-score normalization performs comparatively to breath-hold ^{19}F for dynamic analysis of CF lung disease.

CHAPTER 7: 19F LUNG DIFFUSION IMAGING

This chapter presents exploratory work on the feasibility of ^{19}F lung diffusion imaging. In-vivo data was not collected due to various technical and unforeseen external interruptions.

7.1 INTRODUCTION

^{19}F diffusion weighted imaging (DWI) has not been widely established as with hyperpolarized gases[99,226–229]. However there has been many feasibility studies done on rats[230,231], excised lungs[232], and more recently in-vivo human participants[181,233]. The apparent diffusion coefficient (ADC) is related to the gas confining structure. Therefore, the ADC is a measure of alveolar size or microstructure[99,181,228,234]. The ADC has been shown to be sensitive to lung disease such as emphysema[226], fibrosis[235,236], and chronic obstructive pulmonary disease (COPD)[237,238].

Due to low SNR, MRI safety (specific absorption rate (SAR), nerve stimulation), time constraints (breath hold duration), and the need to measure multiple diffusion weightings, human in-vivo DWI imaging with ^{19}F is a very restricted endeavor.

We hypothesize that lung microstructure can be measured with a simple GRE sequence and diffusion sensitization in one direction. This exploratory work shows the sequence programming, parameter selection, and phantom scan results.

Diffusion weighted imaging was introduced in 1965 by Stejskal and Tanner[239], the modern method was introduced by Le Bihan et al. in 1986[240]. In Le Bihan's paper, they showed the use of diffusion sensitizing gradient lobes in a spin echo sequence. Figure 7.1 shows diffusion sensitizing gradients in one direction.

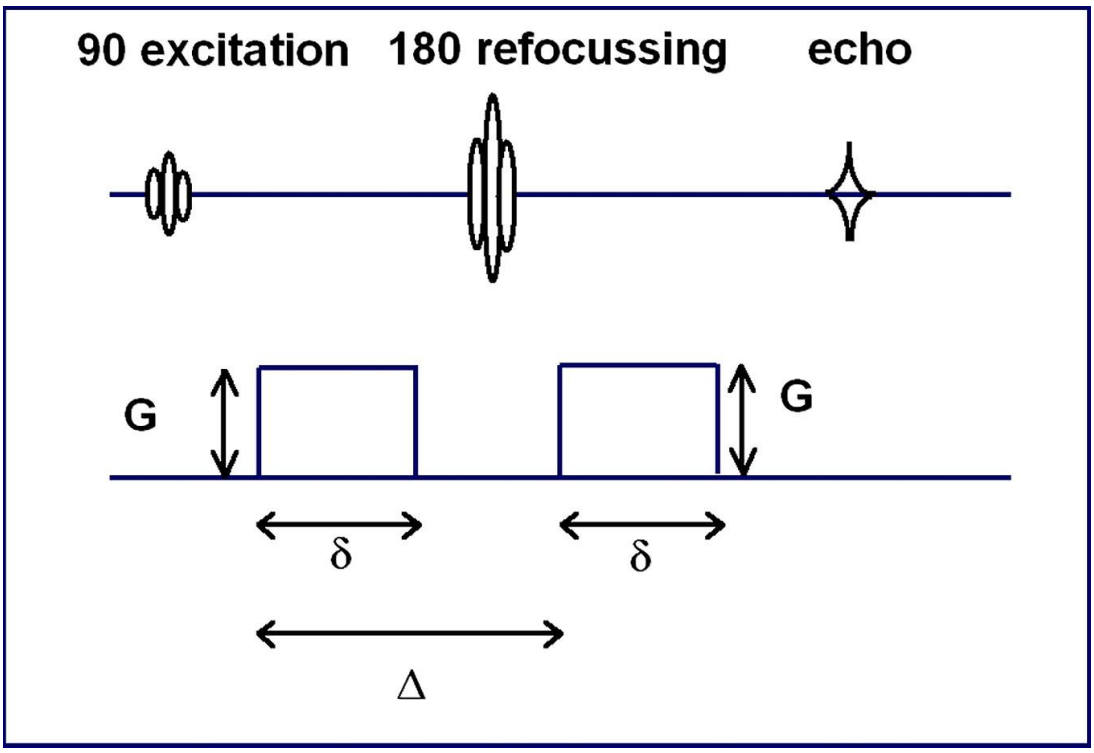

Figure 7.1. Stejskal-Tanner Scheme: 2 diffusion-sensitizing gradients inserted before and after 180° RF refocusing pulse using precisely controlled duration and distance. G, amplitude; δ, duration of the sensitizing gradient; Δ, time between the 2 sensitizing gradient lobes. Image printed unmodified from[241] with permission from the publisher.

The operating principle is that when the diffusion sensitizing lobes are activated, spatially fixed spins will be affected by the first diffusion sensitizing lobe but be corrected by the second of equal magnitude diffusion sensitizing lobe, resulting in no observable change in signal. Moving spins on the other hand, will receive the effect of the first sensitizing lobe but by the time the second diffusion sensitizing lobe is activated, they will

have moved and therefore be affected by a different gradient strength. This will result in dephasing and a reduction of signal.

The amplitude (G), duration of the sensitizing gradient (δ), and the time between the 2 sensitizing gradient lobes (Δ) should be selected carefully depending on the type of matter and confining structure shape and size. Note that in the presence of a 180° pulse as shown in Figure 7.1, the first and second diffusion sensitizing lobes are both positive due to the 180° pulse effectively flipping the spins. In the absence of a 180° pulse, it is sufficient to use a positive and negative pair of diffusion sensitizing lobes where order is not important. Another consideration is in how many directions is diffusion sensitizing required.

The diffusion weighting factor (b-value) is a helpful way to compute the effects of G, δ, and Δ, and is conveniently in units of s/mm^2 given by:

$$b = \gamma^2 \times G^2 \times \delta^2(\Delta - \delta/3) \tag{7.1}$$

Where γ is the gyromagnetic ratio.

7.2 METHOD

MRI acquisitions were performed on a multi-nuclear capable Siemens Prisma 3.0T scanner (Siemens Medical Systems, Erlangen, Germany) and a custom, commercially available 8-channel transmit/receive ^{19}F-tuned chest coil (ScanMed, Inc., Omaha NE, model: 668SI3001). ^{19}F gas perfluoropropane (PFP) in a normoxic mixture (21% O_2, 79% PFP) was used for imaging.

7.2.1 SEQUENCE PROGRAMING

The sequence was programed by modifying a base GRE Siemens sequence shown in Figure 7.2.

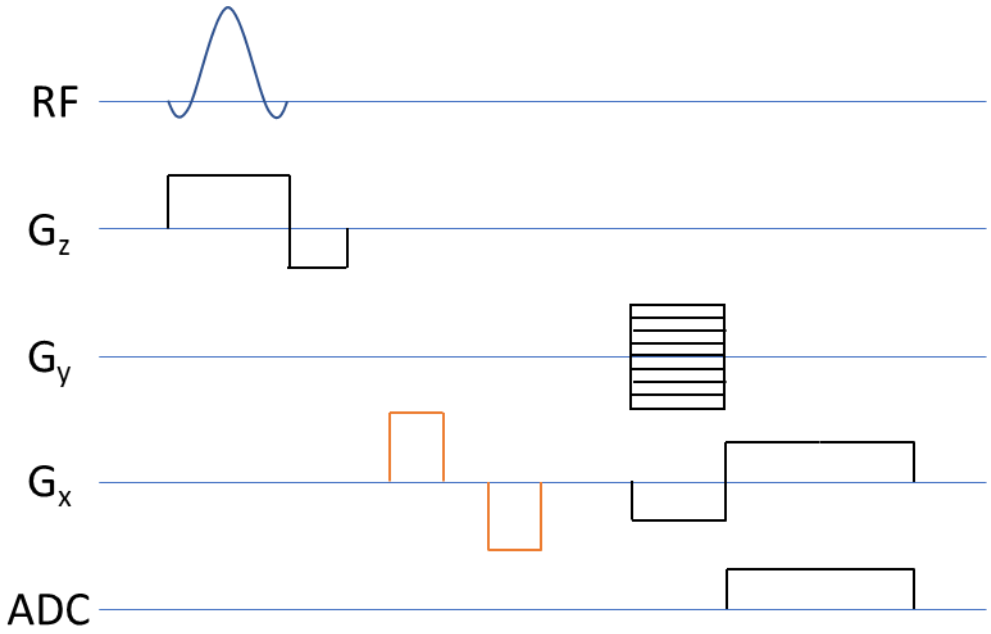

Figure 7.2. GRE sequence with diffusion sensitizing lobes shown in orange

The inclusion of the diffusion sensitizing lobes necessitates higher TE and TR values. The T_2* of PFP in-vivo lungs has been shown to be in the range of ~2-3 ms[112,242] at 3T. Therefore, it is crucial to minimize the time between the 2 diffusion sensitizing lobes (Δ).

For this experiment, the slew rate which is the rate of change of the gradients was set to the maximum allowed (188.679 mT/(m*ms)). It was found experimentally that the maximum gradient amplitude (G) allowed without nerve stimulation error to be 30 mT/m. The b-value was chosen to be 0.18 s/mm^2 based on previous literature[232,233]

Given G=30 mT/m and b=0.18 s/mm^2, the time between diffusion sensitizing lobes (Δ) and the diffusion sensitizing lobe duration (δ) was minimized using (1). Figure 7.3 shows Δ and δ versus the total time (start of lobe 1 to end of lobe 2) over a range of values.

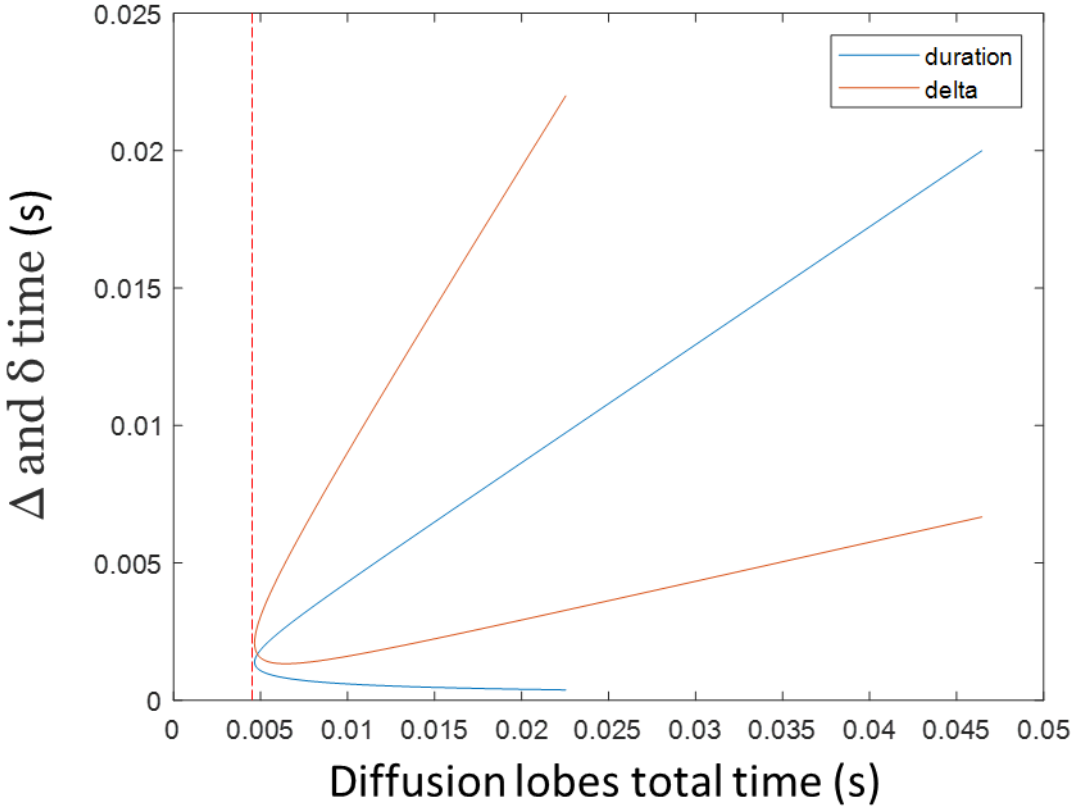

Figure 7.3. duration of the sensitizing gradient (δ) and the time between the 2 sensitizing gradient lobes (Δ) versus total time at several values.

The ADC can be calculated with:

$$ADC = -\frac{\ln(S_1/S_0)}{b_1 - b_0} \quad (2)$$

Where b_0 and b_1 are the b-values of the scan without diffusion sensitization and with diffusion sensitization respectively. S_0 and S_1 are the signal of the scan without diffusion sensitization and with diffusion sensitization respectively.

7.3 RESULTS

The optimization yielded Δ = 1712 μs, δ=1689 μs. The other sequence parameters were set at TE 6.7ms, TR 9.8ms, flip angle 62°, resolution 13.3X13.3X30 mm, matrix 30X30X7, FOV 400X400, bandwidth 340 Hz/px, 3 averages, and GRAPPA (acceleration factor 2, reference lines 15). This setup allowed scanning both b=0 and b=0.18 s/mm^2 scan with 3 averages each. Figure 7.4 shows the acquired images and SNR values, Figure 7.5 shows the resulting ADC heat map in mm^2/s. Figure 7.6 shows the histogram of the ADC values inside the phantom.

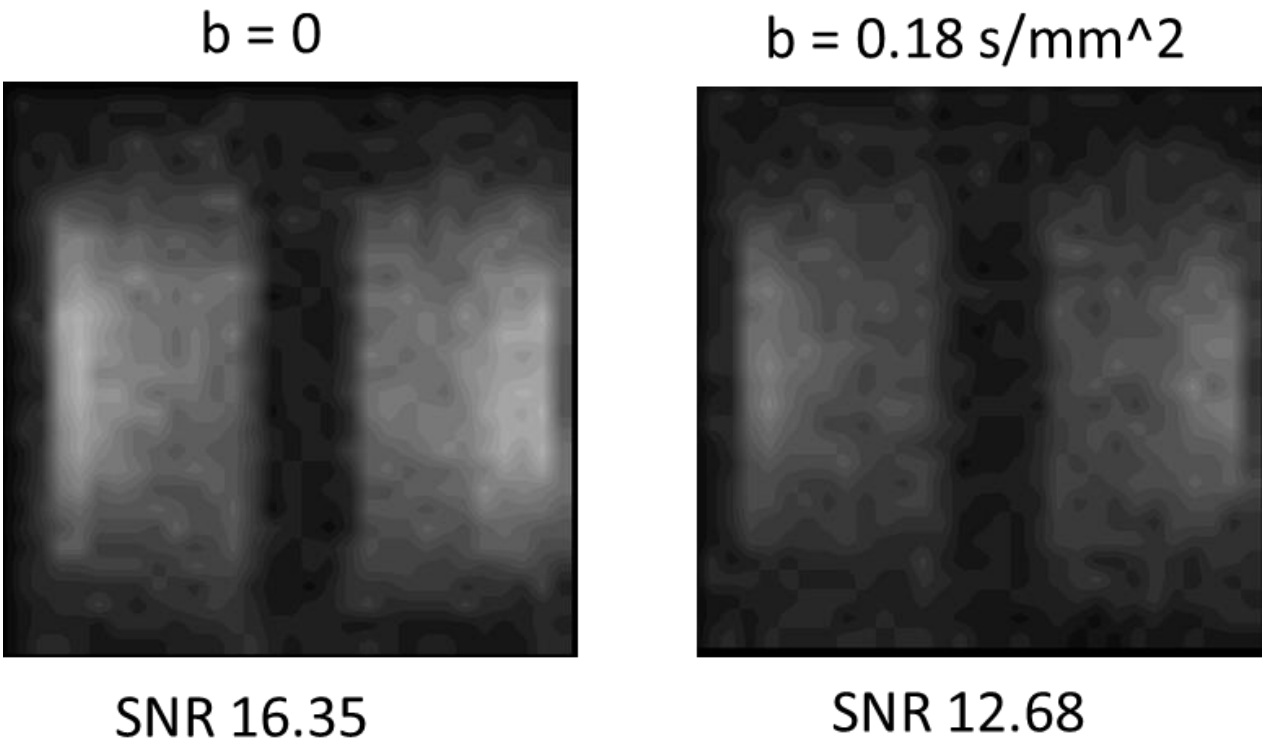

Figure 7.4. 19F Phantom scans with b=0 and b=0.18 s/mm^2, SNR is shown at the bottom of each scan.

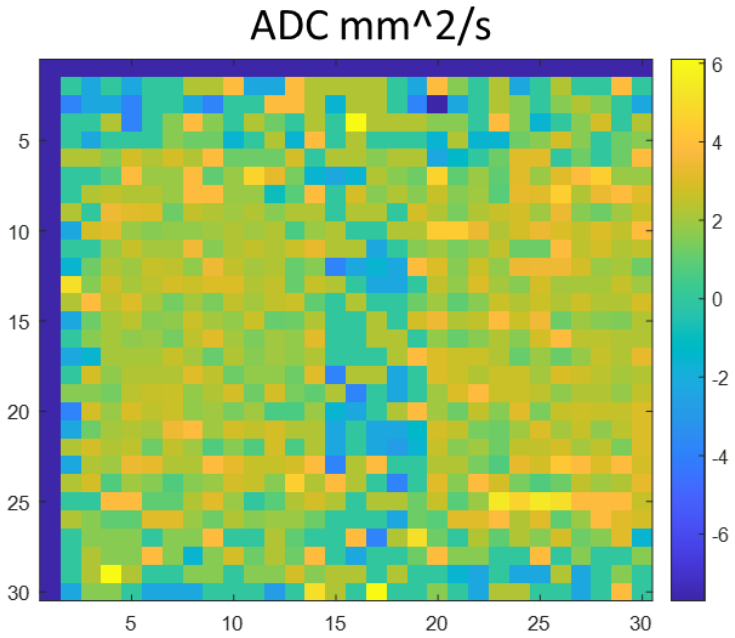

Figure 7.5. ADC heatmap in units of mm^2/s

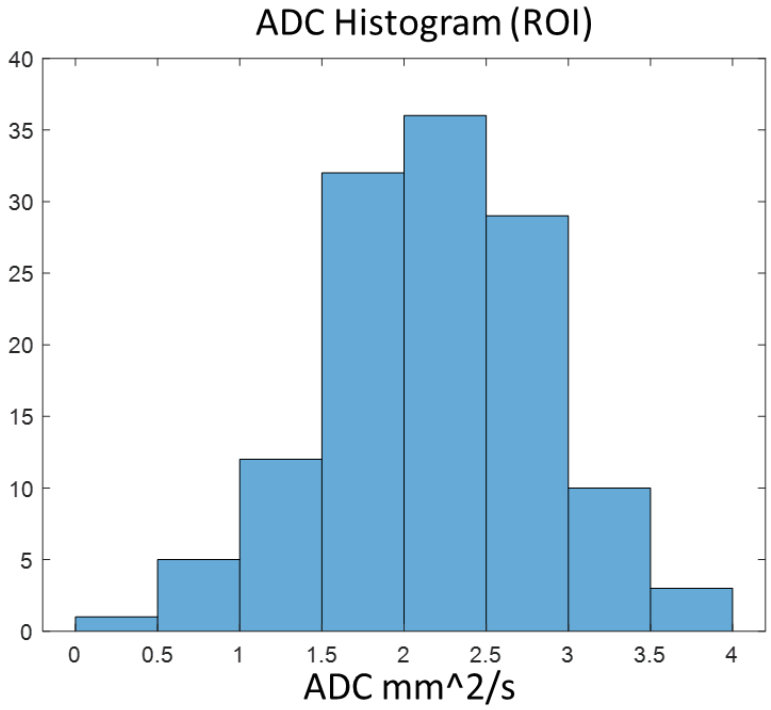

Figure 7.6. ADC histogram of ADC values inside the phantom region of interest

7.4 DISCUSSION AND CONCLUSION

The results show adequate SNR at 3 averages per b values. The scan time was below the max limit of 18 seconds making it suitable for in-vivo breath hold scans. There is room to add a third b-value for increased ADC accuracy using exponential fitting[241,243,244].

Another aspect of diffusion is the diffusion regimes[233,245–247]. For effective DWI, the length of the confining structure (l_s) must be the same magnitude as the free diffusion length (l_d) or the gradient dephasing length (l_g):

$$l_d = \sqrt{2D_0\Delta} \tag{7.3}$$

$$l_g = (D_0/\gamma G)^{1/3} \tag{7.4}$$

Where D_0 is the free diffusion coefficient.

There are three characteristic diffusion regimes; the free diffusion region where $l_d << l_s$, l_g and the ADC = D_0, the restricted diffusion region where $l_s << l_d$, l_g and the ADC depends on the geometry and dimension of the confining structure, and the localized diffusion region where $l_g << l_s$, l_d and the ADC acts as an edge detector[247]. Figure 7 possible locations in the regimes space where ^{19}F is possible with very loose limits.

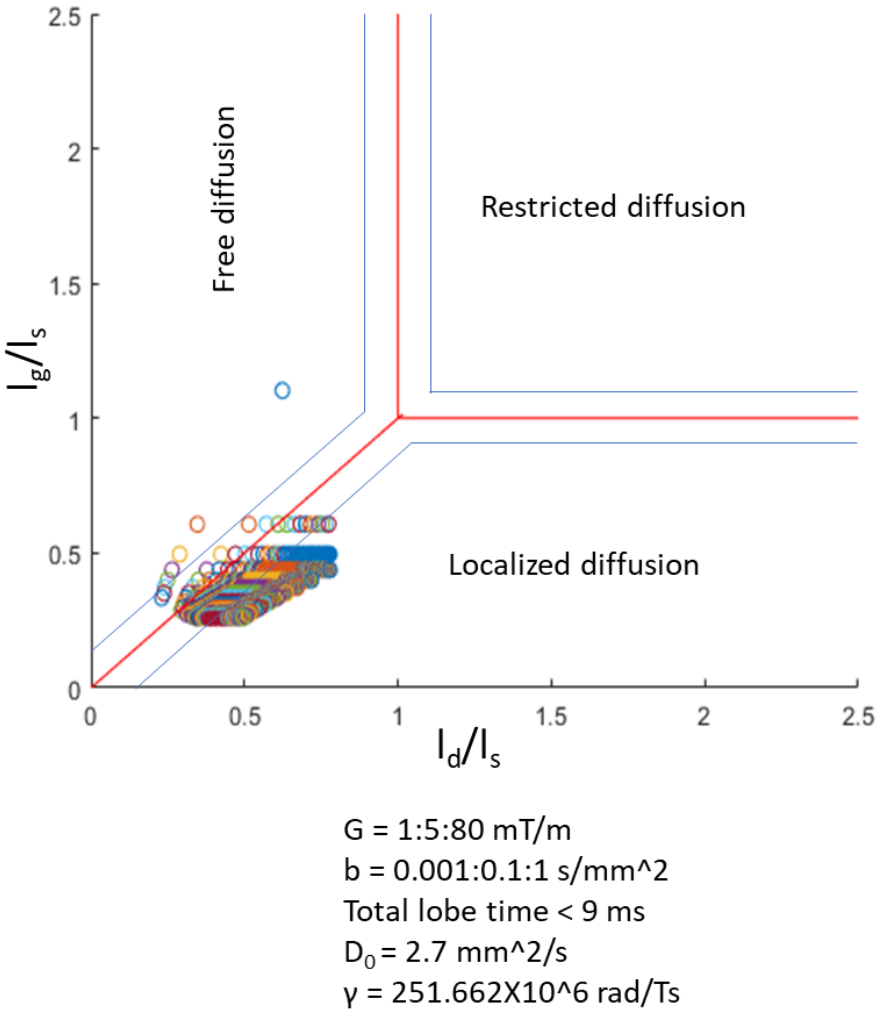

Figure 7.7. Shows achievable locations in the diffusion regimes space with PFP, the conditions and limits are shown at the bottom of the graph. The blue lines indicate transition between regimes where a single regime is not dominant.

Figure 7.7 shows that ^{19}F is not capable of reaching the restricted diffusion region. Hyperpolarized gases are known to be able to reach the restricted diffusion region[233], nevertheless, ^{19}F has been shown to be sensitive to lung microstructure[181,233].

In conclusion ^{19}F lung diffusion MRI with a basic GRE sequence shows promise for in-vivo breath hold measurement. Feasibility should be verified with in-vivo human trials.

CHAPTER 8: CELL TRACKING AND OXYGEN SENSING

Chapter 8 presents exploratory work on ^{19}F cell tracking. Cell loading lab work was done by our contributors; Dr. Elena V. Batrakova, Matthew J. Haney, and Yuling Zhao for macrophages, and Dr. Jeremy Meir for CAR-T cells.

8.1 INTRODUCTION

The ^{19}F fluorine isotope is non-toxic, non-reactive, and stable in biological systems. Furthermore, ^{19}F although naturally abundant in nature, is not present in the mammalian body at MR detectable levels. ^{19}F MRI provides background-free in-vivo imaging capable of localization without ionizing radiation[248]. Cell quantification is possible from the image[249]. These qualities make ^{19}F and ideal contrast and labeling agent for tracking the migration of cells in-vivo with magnetic resonance imaging.

^{19}F MRI has been previously studied for immunotherapy tracking[250–252], inflammation imaging[253–255], and oxygenation measurements[256–260]. The in-vivo half life has been reported to be up to 250 days[253].

Cenya Beacons (© Cenya Imaging) are newly developed and commercially available polymer-entrapped perfluorocarbons designed to be loaded in cells. Cenya is compatible with many imaging modalities such as MRI, PET, and ultrasound, potentially allowing clinicians to benefit from the advantages of each modality. Paired with MRI, cell tracking

can yield spatial and quantitative in-vivo information. This chapter studies the imaging feasibility of macrophages and T-cells loaded with Cenya Beacons in both cell phantoms and in-vivo injected mice. Oxygenation correlation to T1 in MRI imaging with perfluror-15-crown-5-ether (PFCE) phantoms is also explored.

8.2 METHODS

8.2.1 HARDWARE

MRI scans were performed using the Bruker Biospin 9.4T small animal scanner. The coil was a custom made dual-tuned ($^{1}H/^{19}F$) Tx/Rx coil.

8.2.2 MRI PARAMETERS

^{1}H/anatomic scans were used for localization, anatomy identification, and shimming using a Bruker FLASH sequence (TE/TR: 3/291 ms, FA: 20°, FOV: 48X48 mm, matrix: 250X250X45, Slice thickness: 1 mm, averages: 3, acquisition duration: 2.74 minutes). ^{19}F images were taken using the Bruker Flash sequence (TE/TR: 1.86/100 ms, FA: 27°, FOV: 48X48 mm, matrix: 32X32X9, Slice thickness: 1 mm, averages: 300; acquisition duration: 16 minutes).

8.2.3 MACROPHAGES IN-VIVO MICE

Cenya Beacons loaded macrophages (loading concentration 2mg/ml) were injected in life mice, ^{1}H and ^{19}F images were taken at both brain and abdomen locations. Images were taken at multiple post-injection time frames. A loaded cell phantom of known number of cell concentration (3x10^6 cells/ml) was placed next to the mice at imaging for $^{1}H/^{19}F$ registration and quantification reference. A total of 6 mice were imaged at different times post injection. Each mouse was imaged for brain and abdomen scans resulting in a total

scanning and set-up time of 1 hour for each mouse. All mice survived the acquisition. Table 8.1 shows the mice ID, scan date, and hours post injection.

Table 8.1. Mice ID, Scan date, and post injection time

scan date	ID	post injection
8/31/2022	1_1	6 hrs
8/31/2022	1_2	6 hrs
8/31/2022	1_3	6 hrs
9/8/2022	1_1	198 hrs
9/9/2022	1_2	222 hrs
9/9/2022	1_3	222 hrs
9/14/2022	2_1	48 hrs
9/14/2022	2_2	48 hrs
9/14/2022	2_3	48 hrs
9/16/2022	2_1	96 hrs
9/16/2022	2_2	96 hrs
9/16/2022	2_3	96 hrs

The quantification of cell concentration was approximated using the cell phantom of known cell concentration (3x10^6 cells/ml) and matched to its average image intensity. Assuming a linear intensity/concentration relationship.

8.2.4 CAR-T CELLS

CD4 T-cells and CD8 T-cells were loaded with Cenya beacons at different loading concentrations. Control, 5mg/ml, 10mg/ml, and 20mg/ml for CD8 and control, 5mg/ml, and 10 mg/ml for CD4 T-cells. The phantoms were prepared with a cell concertation of 1x10^8 cells/ml. A water centrifuge tube was added to check scan orientation and sample identification.

8.2.5 OXYGEN SENSING

Two PFCE phantoms of 1 ml each was prepared in the scan day. One sample was left to equalize oxygen levels with room air (~21% O_2), the other sample was bubbled with 100% O_2 for 30 minutes. Scans were collected with flip angles 20, 25, and 30. Each flip angle was repeated three times for a total of 9 scans. T1 mapping was done with variable flip angle method[261,262]. The relationship between signal, TR, T1, and longitudinal magnetization can be expressed in matrix[263] form:

$$\begin{pmatrix} \frac{S_1}{\sin(\alpha_1)} \\ \frac{S_2}{\sin(\alpha_2)} \\ \vdots \\ \frac{S_n}{\sin(\alpha_n)} \end{pmatrix} = \begin{pmatrix} \frac{S_1}{\tan(\alpha_1)} & 1 \\ \frac{S_2}{\tan(\alpha_2)} & 1 \\ \vdots & \vdots \\ \frac{S_n}{\tan(\alpha_n)} & 1 \end{pmatrix} \cdot \begin{pmatrix} \exp(-\mathrm{TR}/T_1) \\ M_0 \cdot (1 - \exp(-\mathrm{TR}/T_1)) \end{pmatrix}, \tag{8.1}$$

Where n is the number of flip angles, S is the image signal, M_0 is the magnetization at thermal equilibrium, and α is the flip angle. Recognizing the M_0, TR, and T_1 are constants, equation (8.1) becomes:

$$\frac{S_n}{sin(\alpha_n)} = e^{-\frac{TR}{T_1}} \frac{S_n}{\tan(\alpha_n)} + C \tag{8.2}$$

Equation (8.2) has the form of a linear equation y = mx + b, where m is the exponential term. Then the slope m can be estimated from the slope of a linear regression with axis $\frac{S_n}{sin(\alpha_n)}$ and $\frac{S_n}{\tan(\alpha_n)}$, and T_1 is solved as:

$$T_1 = -\frac{TR}{\ln(slope)} \tag{8.3}$$

8.3 RESULTS

8.3.1 MACROPHAGES IN-VIVO MICE

Figures 8.1 and 8.1 show the anatomic and 19F brain scans fused and registered. Figures 8.3 and 8.4 show the anatomic and 19F abdomen scans fused and registered. Scan time after injection is shown on top of each image, mice ID is labeled on the left. The color bars indicate signal intensity. Each scan is shown with 3 orthogonal planes (from left to right, axial, coronal, sagittal).

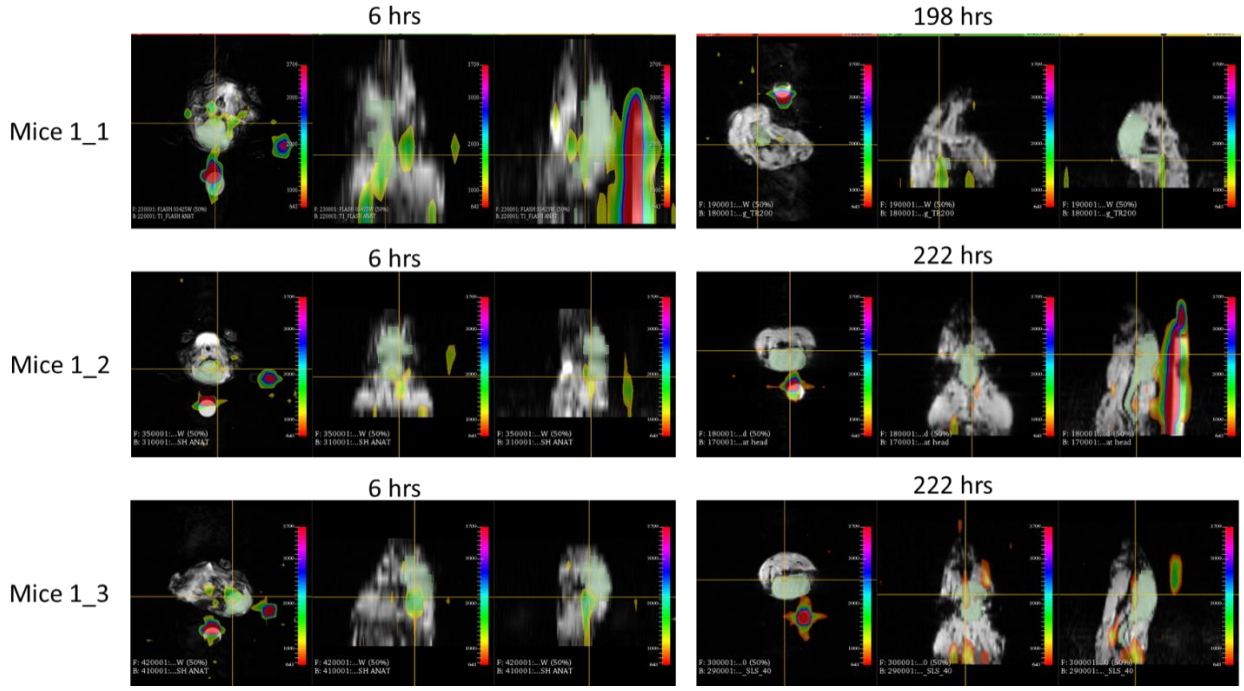

Figure 8.1. brain scans of mice in batch 1 at 6, 198, and 222 hours post injection, from left to right; transversal, coronal, and sagittal planes. The yellow horizontal and vertical lines indicate the location of the other two planes. The brain and brain stem are masked with transparent green

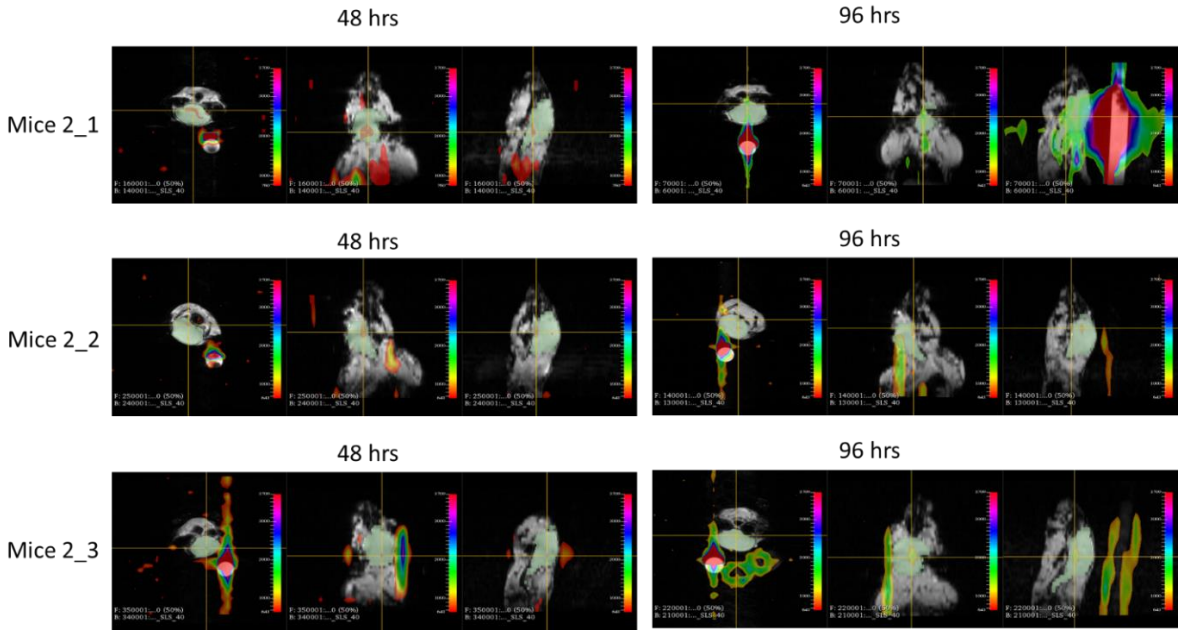

Figure 8.2. brain scans of mice in batch 2 at 48 and 96 hours post injection, from left to right; transversal, coronal, and sagittal planes. The yellow horizontal and vertical lines indicate the location of the other two planes. The brain and brain stem are masked with transparent green

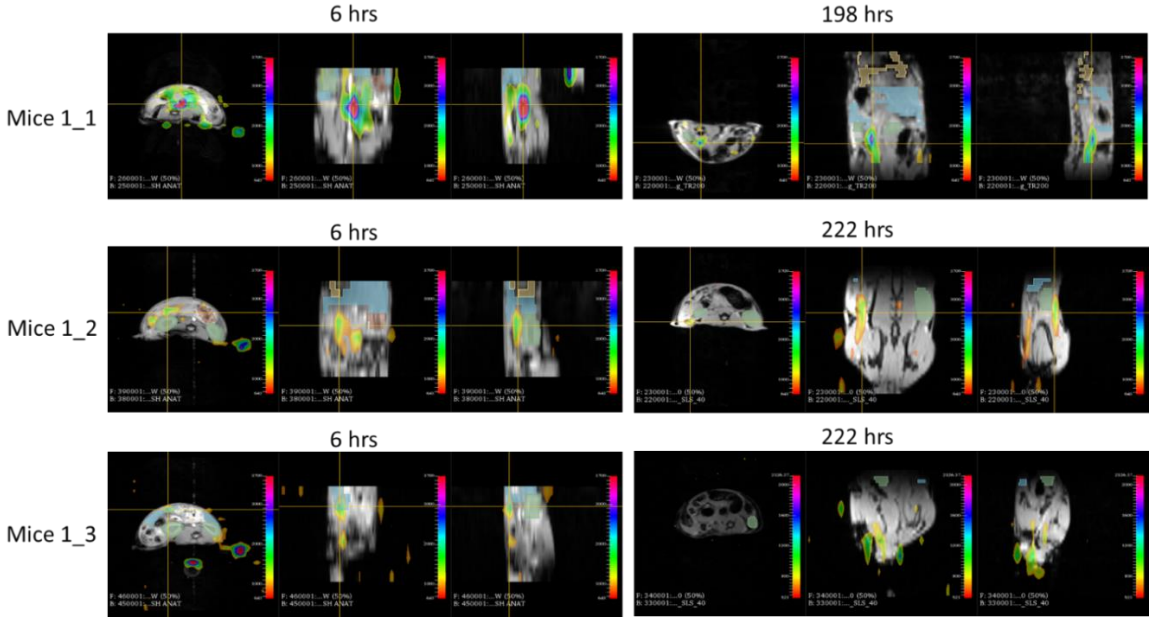

Figure 8.3. Abdomen scans of mice in batch 1 at 6, 198, and 222 hours post injection, from left to right; transversal, coronal, and sagittal planes. The yellow horizontal and vertical lines indicate the location of the other two planes. The kidneys, spleen, liver, and lungs (if visible) are masked with green, brown, blue, and yellow ROIs respectively

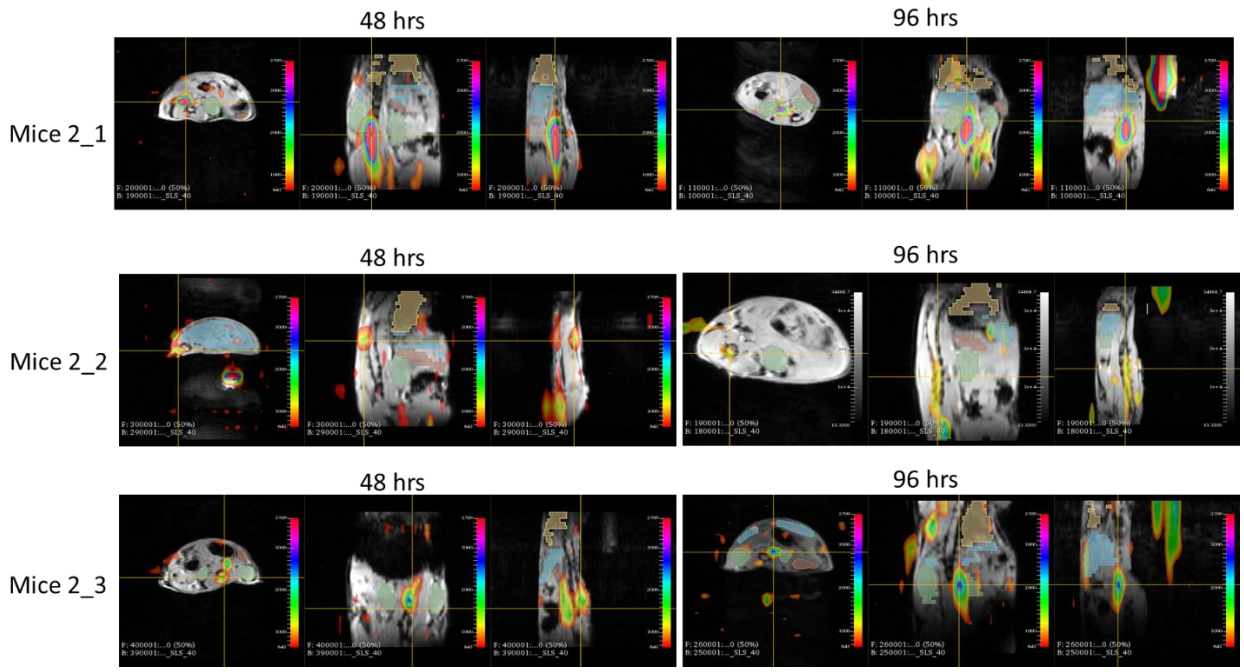

Figure 8.4. abdomen scans of mice in batch 2 at 48 and 96 hours post injection, from left to right; transversal, coronal, and sagittal planes. The yellow horizontal and vertical lines indicate the location of the other two planes. The kidneys, spleen, liver, and lungs (if visible) are masked with green, brown, blue, and yellow ROIs respectively

^{19}F signal was detected in the brain or brain stem at all imaged post-injection times. The loaded microphages can be observed in the abdomen at various sites. ^{19}F signal was detected in the brain or brain stem at all imaged post-injection times. Assuming a linear intensity/concentration relationship, the number of cells present at each voxel is 3.0971xS+0.443. Where S is the signal intensity.

8.3.2 CAR-T CELLS

All CAR-T cell samples were images in one scan. Figure 8.5 the ^{1}H localizer on the left and the ^{19}F scan on the right.

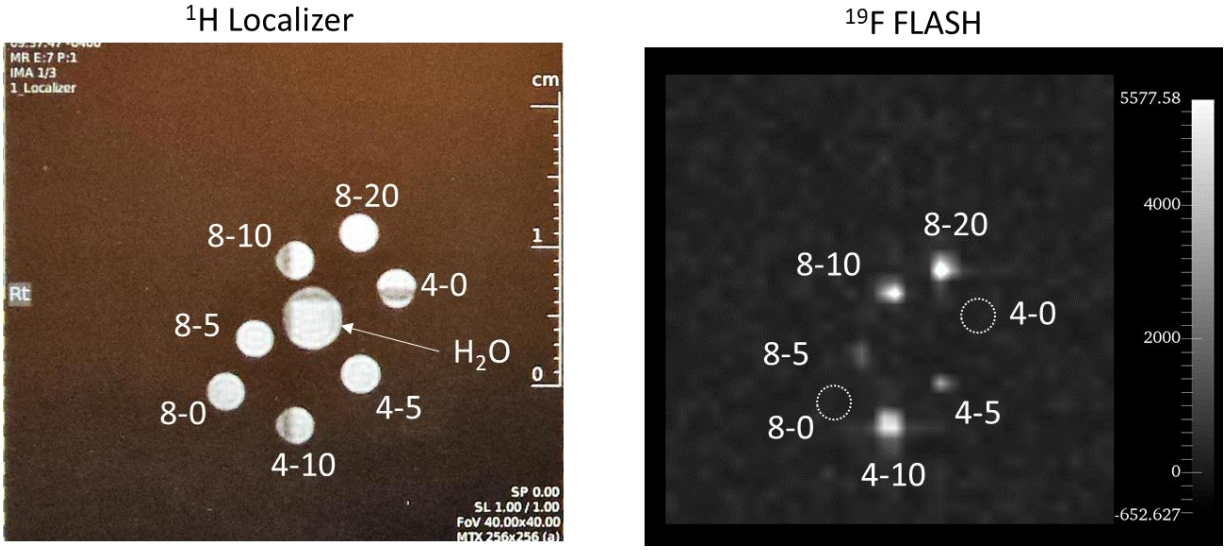

Figure 8.5. CAR-T cell scan, ^{1}H localizer (left), ^{19}F FLASH (right)

The resulting SNR changed based on Cenya loading concentrations as shown in Figure 8.6. Assuming a homogeneous mixing in the phantom, it is estimated that there are 100,000 cells per voxel. SNR is seen increasing with loading concentration and a potential plateauing near loading concentrations of 20mg/ml Cenya.

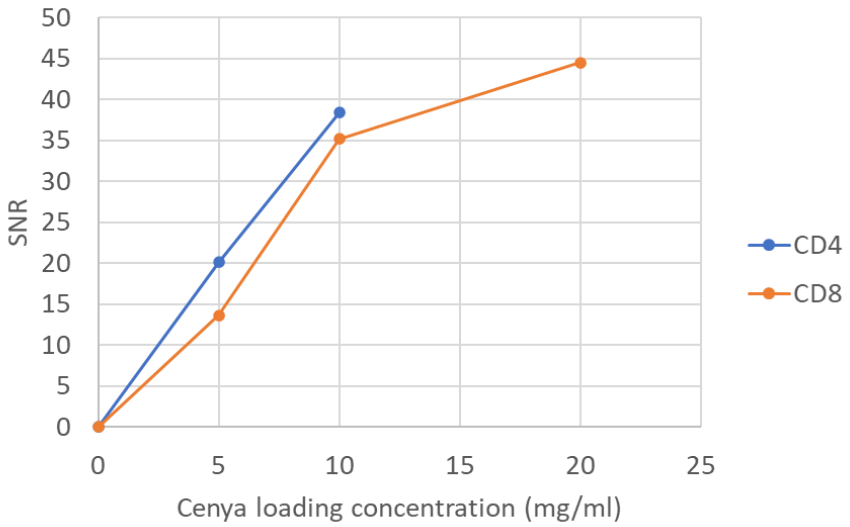

Figure 8.6. ^{19}F SNR for CD4 and CD8 cells and different loading concentrations

The SNR of CAR-T cells and macrophages (phantom) was calculated and normalized to 50,000 cells for comparison shown in Figure 7.

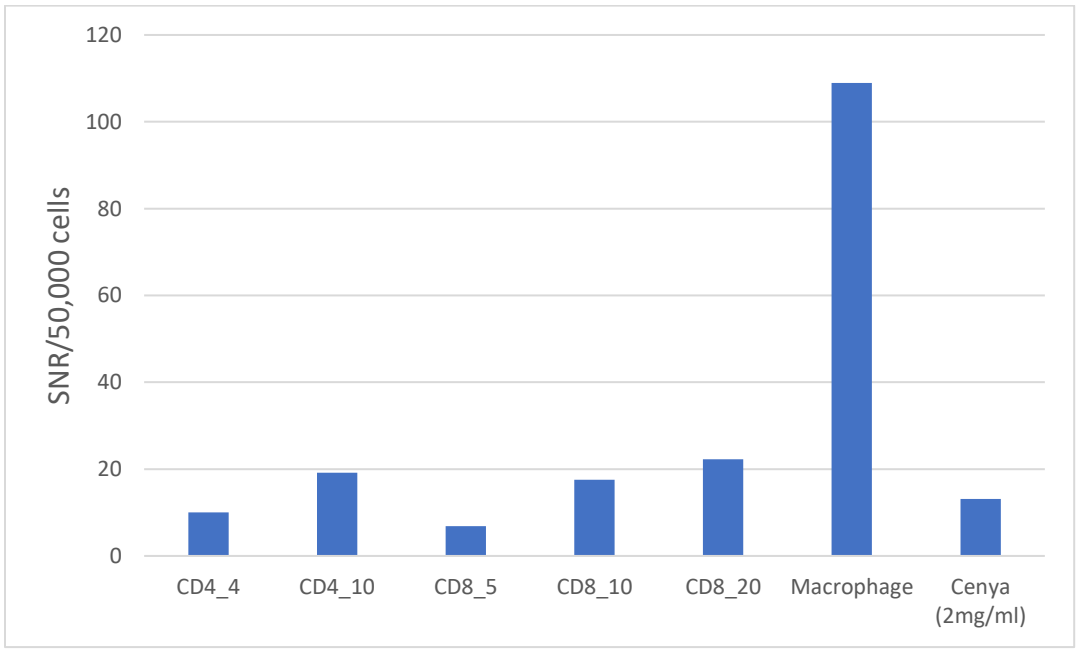

Figure 8.7. Comparison of SNR normalized to 50,000 cells between CD4, CD8 and macrophage (MP) cells. A Cenya/water mixture (2mg/ml) SNR is included for reference (not normalized)

8.3.3 OXYGEN SENSING

The signal changed with flip angle for both samples. The naming convention for the results is 'oxy' indicating oxygenated with 100% O_2 and numbering indicates repeat scan. Figure 8.8 shows the mean signal intensity over flip angle.

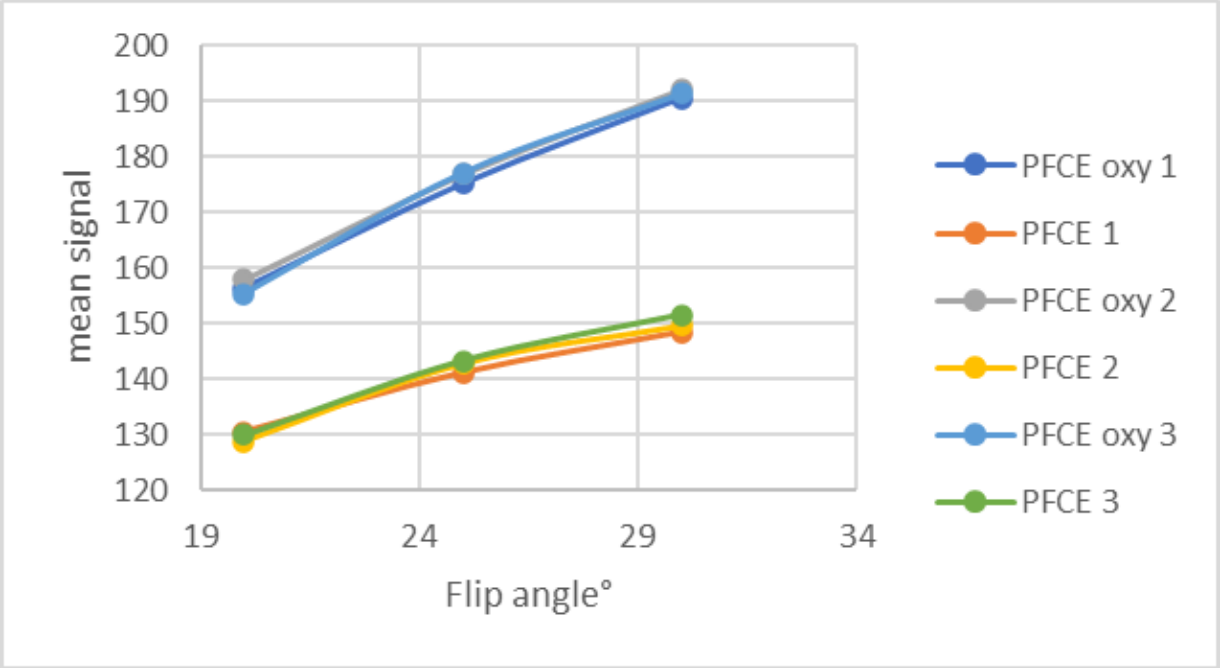

Figure 8.8. Mean signal intensity versus flip angle

Following the variable flip angle T_1 mapping method discussed in the methods section, the slopes were estimated with linear regression as shown in Figure 8.8. The estimated T_1 values are shown in Figure 8.9.

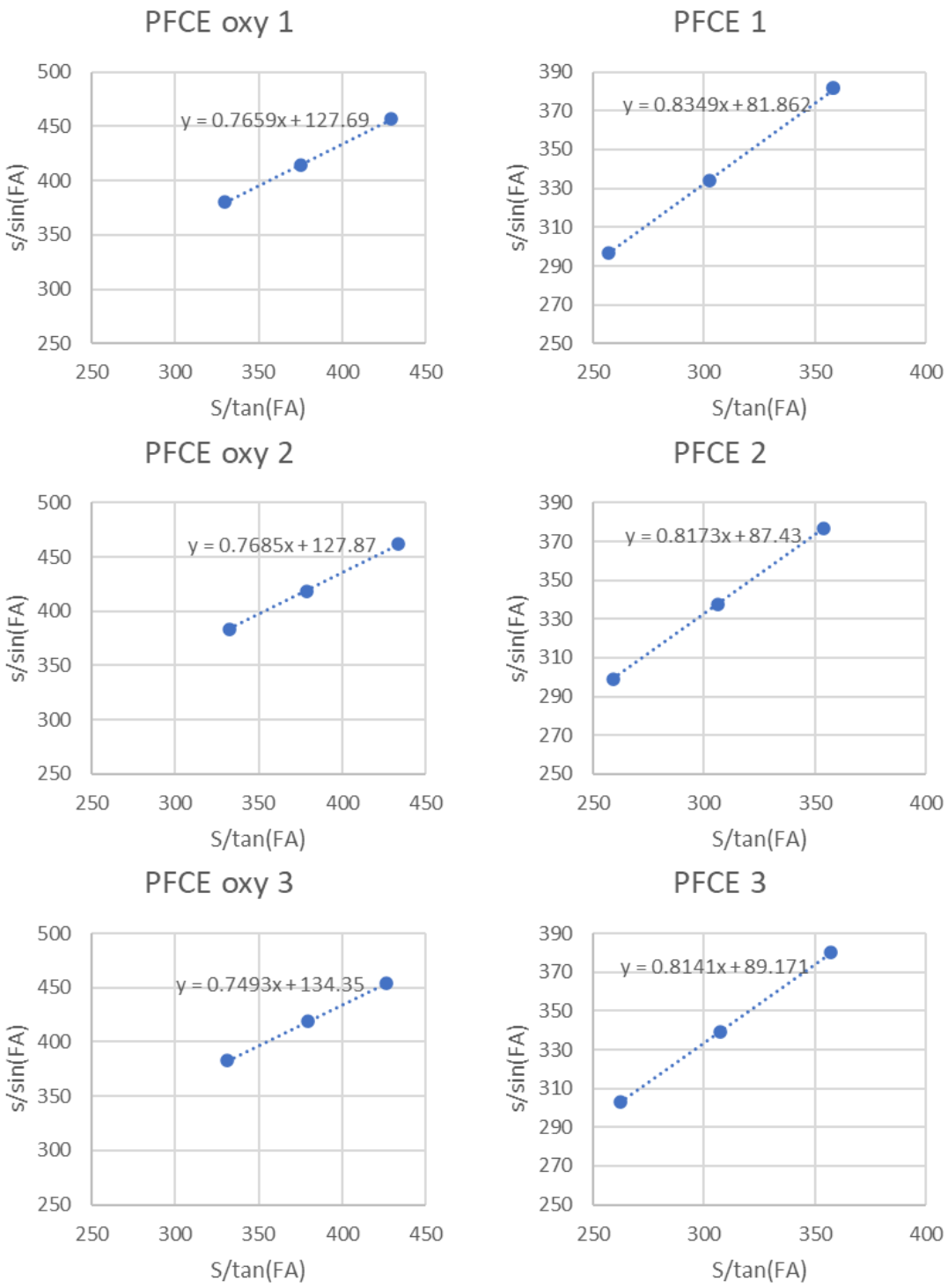

Figure 8.8. linear regression fits and resulting slope values. The left column shows the oxygenated sample, the right column shows the room oxygen sample. Numbering indicates repeat scans.

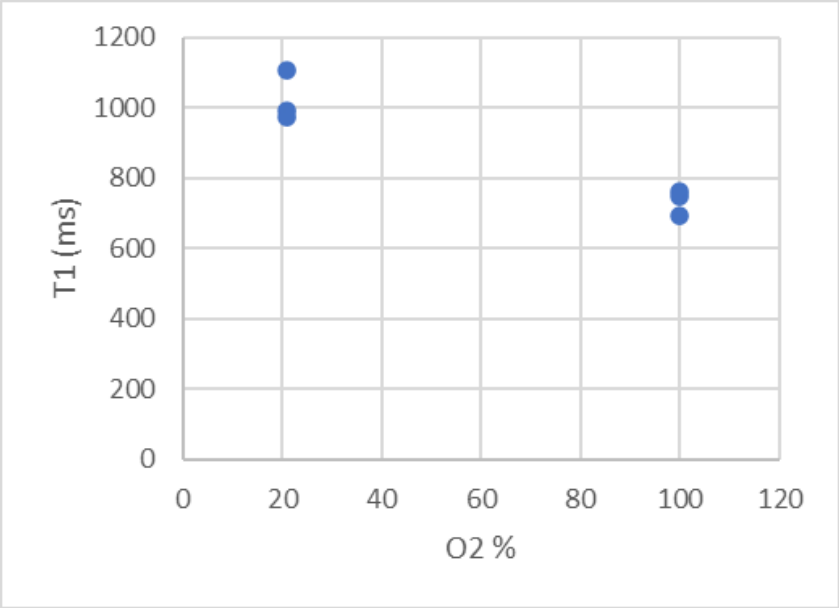

Figure 8.9. Estimated T_1 values versus O_2%

8.4 DISCUSSION AND CONCLUSION

This chapter showed the feasibility of cell tracking using Cenya Beacons on both macrophages and CAR-T (CD4 and CD8) cells. As expected, the SNR on CAR-T cells were lower than in macrophages. Macrophages imaging was shown in-vivo mice. The feasibility of Cenya loaded CAR-T cells for MRI imaging has to be verified with in-vivo studies.

The effect of oxygenation on PFCE's T_1 was also showed clearly. Verification should be done with in-vivo studies.

CHAPTER 9: DISCUSSION

9.1 SUMMARY

Chapter 1 presented an introduction on lung physiology and modern lung health measuring methods. The purpose of this chapter was to understand the current state on pulmonary care. It serves as an orientation of what needs are unmet and where ^{19}F fits in the overall scheme. Chapter 2 presented basic MR physics concepts needed to perform scans, understand sequence parameters, and short descriptions on widely used sequences including newer non-cartesian methods and the Ultra Short Echo time sequence.

Chapter 3 presents an introduction to the basic concepts used throughout chapters 4, 5, and 6. The main finding in chapter 3 was that ^{19}F lung MRI dynamic analysis provides measures more sensitive to disease than the current spirometry gold standard. This finding alone is a strong argument for the importance of ^{19}F lung MRI.

Chapters 4 to 6 present original work ordered chronologically depicting the evolution in our methodology. In chapter 4 we compared ^{19}F with hyperpolarized ^{129}Xe lung imaging. The initial aim was to test correlation between the two modalities. Analysis of the results gave us further insight into the intricacies of MRI lung imaging. In our comparison, we saw mismatched areas of signal and no signal in all 4 combinations ($^{129}Xe+$ $^{19}F+$, $^{129}Xe-$ $^{19}F+$, $^{129}Xe+$ $^{19}F-$, and $^{129}Xe-$ $^{19}F-$). The presence of all 4 mismatch areas hints that single breath analysis might be miscategorizing slow ventilation with ventilation defect,

which highlights the importance of multi-breath acquisitions.

Chapter 5 and 6 presents work on the development and testing of a sub 0.5 second ^{19}F acquisition. The main drive was to achieve ^{19}F full volumetric lung scans capable of acquisition during free-breathing. Forgoing the need for breath-holds not only increases patient comfort, but it may also open the door for 19F lung MRI on young children and infants. Furthermore, repeated breath-hold maneuvers can be exhausting, which in turn limits the total amount of gas that can be inhaled. In chapter 5, ventilation defect percentage (VDP) was found to be highly correlated between Spiral and VIBE scans, tenth breath (R=0.84) and 2nd breath (R=0.88). Chapter 6 showed good correlation between Spiral and VIBE fractional lung volume parameters and VDP with $r > 0.7$ for all parameters. The Spiral FLV τ_1 fast showed significant difference between healthy and cystic fibrosis (CF) patients with FEV1 % predicted $\geq$ 80%.

Chapter 7 shows preliminary work on ^{19}F lung diffusion imaging. A basic sequence was modified for testing purposes and explored the diffusion capabilities with the on-site 3T Siemens Prisma. Through simulation and known hardware limitations this chapter showed that our current on-site scanner and ^{19}F is constrained to the free diffusion and localized diffusion regimes.

Chapter 8 presents preliminary work on cell tacking with loaded macrophages and in-vivo mice. A Fast low angle shot (FLASH) sequence was optimized with resolution 1.5 X 1.5 X 1 mm and 16 min scan time for the 9.4 Bruker MRI scanner. In-vivo signal was detected in the mice even after 222 hours. This chapter shows successful imaging of ^{19}F loaded CAR-T cells in vials. The effect of loading concentration to MR signal was explored. Preliminary cell quantification in both in-vivo mice and in-vitro CART-T cells was

performed. Lastly, the ^{19}F sensitivity to surrounding oxygenation levels using Perfluoro-15-crown-5-Ether (PFP) was explored.

9.2 FUTURE WORK AND OUTLOOK

In ^{19}F lung imaging, minimizing sources of error should be a priority for eventual widespread clinical use. Differences in breath size between breaths in a single imaging session shifts lung regions making corresponding voxels hard to align in the temporal dimension. This creates error in the fitting process. Differences in breath size between scans may also introduce error due to it affecting the total amount of gas inhaled. Deformable registration is difficult due to relatively large voxel sizes, low sharpness, and high amount of partial volume signal present in ^{19}F lung scans. A possible solution to the problem of breath-size difference is to use grouped voxel averages with methods such as the moving window average or kernel filters. Another solution could be to control the amount of inhaled gas per breath to ensure breath size consistency.

Although chapters 5 and 6 showed good agreement between Spiral and VIBE scans, The real word application of Spiral ^{19}F imaging in free breathing remains to be validated. The acquisition protocol in the work presented in this dissertation was designed for the sole purpose of comparison. There are several points that need to be addressed in the current protocol. Since the ^{19}F scans would not be done at maximum inhalation breath-holds, but at free breathing, the anatomic scan used to draw the lung region of interest (ROI) needs to match the breath size of the ^{19}F scans. The ^{19}F scans would also need to be further processed to avoid using different inflation levels for dynamic fitting. This could be done by sorting the acquired images by breathing phase or using deformable registration to

normalize all the scans. Another possible solution is to collect external time synced lung inflation markers that can be later used to phase sort the ^{19}F scans.

In terms of translation to clinical use, 19F lung MRI needs further work in sequence, protocol, and processing standardization. Although 19F lung MRI is simpler than hyperpolarized lung MRI due to not needing hyperpolarization, sequence optimization and processing still requires knowledge in MR physics and coding that might not be available at all clinical imaging sites.

Despite the mentioned challenges the outlook for ^{19}F lung MRI is bright. The need of a sensitive and spatially localizable way to measure lung disease without ionizing radiation goes unfulfilled in the clinic, of which ^{19}F lung imaging is well positioned to fulfill. In CF, the introduction of novel cystic fibrosis transmembrane regulator (CFTR) modulators[25,34,196,264] has shifted the focus to younger children and infants where spirometry is difficult or not feasible. Spirometry feasibility studies in children is limited to ages 2 and up[265–267] with falling success rates the younger the study population[267]. The resulting increase in expected survivability has intensified the need for sensitive risk free longitudinal measures.

REFERENCES

1. SEER Training Modules, Lung Cancer, Anatomy. U. S. National Institutes of Health, National Cancer Institute. Accessed August 1, 2022. https://training.seer.cancer.gov/

2. Ball M, Hossain M, Padalia D. Anatomy, Airway. In: *StatPearls*. StatPearls Publishing; 2022.

3. Weibel ER. What makes a good lung? *Swiss Med Wkly*. 2009;139(27-28):375-386. doi:smw-12270

4. Bocci V. The potential toxicity of ozone: side effects and contraindications of ozonetherapy. In: *OZONE: A New Medical Drug*. Springer Netherlands; 2011:75-84. doi:10.1007/978-90-481-9234-2_7

5. Lenfant C. Discovery of endogenous surfactant and overview of its metabolism and actions. *Lung surfactants, basic science and clinical applications*. 2000;149.

6. Delgado BJ, Bajaj T. Physiology, Lung Capacity. In: *StatPearls*. StatPearls Publishing; 2023.

7. Powers KA, Dhamoon AS. Physiology, pulmonary ventilation and perfusion. In: *StatPearls*. StatPearls Publishing; 2022.

8. Lutfi MF. The physiological basis and clinical significance of lung volume measurements. *Multidiscip Respir Med*. 2017;12:3. doi:10.1186/s40248-017-0084-5

9. Mitzner WA. Leonardo and the physiology of respiration. *LUNG BIOLOGY IN HEALTH AND DISEASE*. 1995;83:37-37.

10. Pattle RE. Properties, function and origin of the alveolar lining layer. *Nature*. 1955;175(4469):1125-1126. doi:10.1038/1751125b0

11. Rohrer F. The correlation of respiratory forces and their dependence upon the state of expansion of the respiratory organs. *Translations in Respiratory*. 1975:67-88.

12. von Neergaard K. New interpretations of basic concepts of respiratory mechanics. Correlation of pulmonary recoil force with surface tension in the alveoli. *Translations in respiratory physiology Dowden, Hutchinson & Ross, Stroundsburg, PA*. 1975:270-290.

13. Martin HB. Respiratory bronchioles as the pathway for collateral ventilation. *J Appl Physiol*. 1966;21(5):1443-1447. doi:10.1152/jappl.1966.21.5.1443

14. Mitzner W. Mechanics of the lung in the 20th century. *Compr Physiol*. 2011;1(4):2009-2027. doi:10.1002/cphy.c100067

15. West JB. History of respiratory mechanics prior to World War II. *Compr Physiol*. 2012;2(1):609-619. doi:10.1002/cphy.c080112

16. Fry DL, Ebert RV, Stead WW, Brown CC. The mechanics of pulmonary ventilation in normal subjects and in patients with emphysema. *Am J Med*. 1954;16(1):80-97. doi:10.1016/0002-9343(54)90325-3

17. Otis AB, Mckerrow CB, Bartlett RA, et al. Mechanical factors in distribution of pulmonary ventilation. *J Appl Physiol*. 1956;8(4):427-443. doi:10.1152/jappl.1956.8.4.427

18. Mead J, Whittenberger JL. Evaluation of airway interruption technique as a method for measuring pulmonary airflow resistance. *J Appl Physiol*. 1954;6(7):408-416. doi:10.1152/jappl.1954.6.7.408

19. Mount LE. The ventilation flow-resistance and compliance of rat lungs. *J Physiol (Lond)*. 1955;127(1):157-167. doi:10.1113/jphysiol.1955.sp005246

20. Baswa S, Nazeran H, Nava P, Diong B, Goldman M. Evaluation of respiratory system models based on parameter estimates from impulse oscillometry data. *Conf Proc IEEE Eng Med Biol Soc*. 2005;2005:2958-2961. doi:10.1109/IEMBS.2005.1617094

21. Lutchen KR, Costa KD. Physiological interpretations based on lumped element models fit to respiratory impedance data: use of forward-inverse modeling. *IEEE Trans Biomed Eng*. 1990;37(11):1076-1086. doi:10.1109/10.61033

22. Dubois AB, Brody AW, Lewis DH, Burgess BF. Oscillation mechanics of lungs and chest in man. *J Appl Physiol*. 1956;8(6):587-594. doi:10.1152/jappl.1956.8.6.587

23. Mead J. Mechanical properties of lungs. *Physiol Rev*. 1961;41:281-330. doi:10.1152/physrev.1961.41.2.281

24. Woo T, Diong B, Mansfield L, Goldman M, Nava P, Nazeran H. A comparison of various respiratory system models based on parameter estimates from impulse oscillometry data. *Conf Proc IEEE Eng Med Biol Soc*. 2004;2004:3828-3831. doi:10.1109/IEMBS.2004.1404072

25. McBennett KA, Davis PB, Konstan MW. Increasing life expectancy in cystic fibrosis: Advances and challenges. *Pediatr Pulmonol*. 2022;57 Suppl 1(Suppl 1):S5-S12. doi:10.1002/ppul.25733

26. Andersen DH. Cystic fibrosis of the pancreas and its relation to celiac disease. *Am J Dis Child*. 1938;56(2):344. doi:10.1001/archpedi.1938.01980140114013

27. Farber S, Shwashman H, Maddock C. Pancreatic function and disease in early life. V. Pathologic changes associated with pancreatic insufficiency in early life. *Arch Pathol*. 1944;37:238-250.

28. Davis PB. Cystic fibrosis since 1938. *Am J Respir Crit Care Med*. 2006;173(5):475-482. doi:10.1164/rccm.200505-840OE

29. Di Sant'Agnese PA, Darling RC, Perera GA, Shea E. Abnormal electrolyte composition of sweat in cystic fibrosis of the pancreas; clinical significance and relationship to the disease. *Pediatrics*. 1953;12(5):549-563.

30. Riordan JR, Rommens JM, Kerem B, et al. Identification of the cystic fibrosis gene: cloning and characterization of complementary DNA. *Science*. 1989;245(4922):1066-1073. doi:10.1126/science.2475911

31. Rommens JM, Iannuzzi MC, Kerem B, et al. Identification of the cystic fibrosis gene: chromosome walking and jumping. *Science*. 1989;245(4922):1059-1065. doi:10.1126/science.2772657

32. Kerem B, Rommens JM, Buchanan JA, et al. Identification of the cystic fibrosis gene: genetic analysis. *Science*. 1989;245(4922):1073-1080. doi:10.1126/science.2570460

33. Veit G, Roldan A, Hancock MA, et al. Allosteric folding correction of F508del and rare CFTR mutants by elexacaftor-tezacaftor-ivacaftor (Trikafta) combination. *JCI Insight*. 2020;5(18). doi:10.1172/jci.insight.139983

34. Zaher A, ElSaygh J, Elsori D, ElSaygh H, Sanni A. A review of trikafta: triple cystic fibrosis transmembrane conductance regulator (CFTR) modulator therapy. *Cureus*. 2021;13(7):e16144. doi:10.7759/cureus.16144

35. Moore VC. Spirometry: step by step. *Breathe*. 2012;8(3):232-240. doi:10.1183/20734735.0021711

36. Beeckman-Wagner LA, Freeland D. Spirometry quality assurance; common errors and their impact on test results. 2012.

37. Welch L. A guide to spirometry best practice for community nurses. *Journal of Community Nursing*. 2016;30(1):58-64.

38. Criée CP, Sorichter S, Smith HJ, et al. Body plethysmography--its principles and clinical use. *Respir Med*. 2011;105(7):959-971. doi:10.1016/j.rmed.2011.02.006

39. Robinson PD, Latzin P, Verbanck S, et al. Consensus statement for inert gas washout measurement using multiple- and single- breath tests. *Eur Respir J*. 2013;41(3):507-522. doi:10.1183/09031936.00069712

40. Ramsey KA, Rosenow T, Turkovic L, et al. Lung clearance index and structural lung disease on computed tomography in early cystic fibrosis. *Am J Respir Crit Care Med*. 2016;193(1):60-67. doi:10.1164/rccm.201507-1409OC

41. Owens CM, Aurora P, Stanojevic S, et al. Lung Clearance Index and HRCT are complementary markers of lung abnormalities in young children with CF. *Thorax*. 2011;66(6):481-488. doi:10.1136/thx.2010.150375

42. Ramsey KA, Foong RE, Grdosic J, et al. Multiple-Breath Washout Outcomes Are Sensitive to Inflammation and Infection in Children with Cystic Fibrosis. *Ann Am Thorac Soc*. 2017;14(9):1436-1442. doi:10.1513/AnnalsATS.201611-935OC

43. Simpson SJ, Ranganathan S, Park J, et al. Progressive ventilation inhomogeneity in infants with cystic fibrosis after pulmonary infection. *Eur Respir J*. 2015;46(6):1680-1690. doi:10.1183/13993003.00622-2015

44. Beydon N, Davis SD, Lombardi E, et al. An official American Thoracic Society/European Respiratory Society statement: pulmonary function testing in preschool children. *Am J Respir Crit Care Med*. 2007;175(12):1304-1345. doi:10.1164/rccm.200605-642ST

45. Gustafsson PM. Inert gas washout in preschool children. *Paediatr Respir Rev*. 2005;6(4):239-245. doi:10.1016/j.prrv.2005.09.009

46. Taylor-Robinson D, Whitehead M, Diderichsen F, et al. Understanding the natural progression in %FEV1 decline in patients with cystic fibrosis: a longitudinal study. *Thorax*. 2012;67(10):860-866. doi:10.1136/thoraxjnl-2011-200953

47. Ellemunter H, Fuchs SI, Unsinn KM, et al. Sensitivity of Lung Clearance Index and chest computed tomography in early CF lung disease. *Respir Med*. 2010;104(12):1834-1842. doi:10.1016/j.rmed.2010.06.010

48. Gustafsson PM, De Jong PA, Tiddens HAWM, Lindblad A. Multiple-breath inert gas washout and spirometry versus structural lung disease in cystic fibrosis. *Thorax*. 2008;63(2):129-134. doi:10.1136/thx.2007.077784

49. Gangell CL, Hall GL, Stick SM, Sly PD, AREST CF. Lung function testing in preschool-aged children with cystic fibrosis in the clinical setting. *Pediatr Pulmonol*. 2010;45(5):419-433. doi:10.1002/ppul.21192

50. Hatziagorou E, Kampouras A, Avramidou V, et al. Toward the establishment of new clinical endpoints for cystic fibrosis: the role of lung clearance index and cardiopulmonary exercise testing. *Front Pediatr*. 2021;9:635719. doi:10.3389/fped.2021.635719

51. Crawford AB, Makowska M, Paiva M, Engel LA. Convection- and diffusion-dependent ventilation maldistribution in normal subjects. *J Appl Physiol*. 1985;59(3):838-846.

52. Verbanck S, Schuermans D, Van Muylem A, Paiva M, Noppen M, Vincken W. Ventilation distribution during histamine provocation. *J Appl Physiol*. 1997;83(6):1907-1916. doi:10.1152/jappl.1997.83.6.1907

53. Horsley AR, Gustafsson PM, Macleod KA, et al. Lung clearance index is a sensitive, repeatable and practical measure of airways disease in adults with cystic fibrosis. *Thorax*. 2008;63(2):135-140. doi:10.1136/thx.2007.082628

54. Stanojevic S, Bowerman C, Robinson P. Multiple breath washout: measuring early manifestations of lung pathology. *Breathe (Sheff)*. 2021;17(3):210016. doi:10.1183/20734735.0016-2021

55. Bouhuys A, van LENNEP H. Effect of body posture on gas distribution in the lungs. *J Appl Physiol*. 1962;17:38-42. doi:10.1152/jappl.1962.17.1.38

56. Robinson PD, Goldman MD, Gustafsson PM. Inert gas washout: theoretical background and clinical utility in respiratory disease. *Respiration*. 2009;78(3):339-355. doi:10.1159/000225373

57. Verbanck S, Schuermans D, Van Muylem A, et al. Conductive and acinar lung-zone contributions to ventilation inhomogeneity in COPD. *Am J Respir Crit Care Med*. 1998;157(5 Pt 1):1573-1577. doi:10.1164/ajrccm.157.5.9710042

58. Pabst R. Airway immune system: microanatomy. In: *Encyclopedia of Immunobiology*. Elsevier; 2016:453-465. doi:10.1016/B978-0-12-374279-7.07009-0

59. Röntgen WK. A new form of radiation. *Science*. 1896;3(72):726-729. doi:10.1126/science.3.72.726

60. Cho ZH, Jones JP, Singh M. Foundations of medical imaging. *Foundations of medical imaging*. 1993:71.

61. Ou X, Chen X, Xu X, et al. Recent Development in X-Ray Imaging Technology: Future and Challenges. *Research (Wash D C)*. 2021;2021:9892152. doi:10.34133/2021/9892152

62. Ryan JL. Ionizing radiation: the good, the bad, and the ugly. *J Invest Dermatol*. 2012;132(3 Pt 2):985-993. doi:10.1038/jid.2011.411

63. Ron E. Ionizing radiation and cancer risk: evidence from epidemiology. *Radiat Res*. 1998;150(5 Suppl):S30-41. doi:10.2307/3579806

64. Lynch DA, Oh AS. High-Spatial-Resolution CT Offers New Opportunities for Discovery in the Lung. *Radiology*. 2020;297(2):472-473. doi:10.1148/radiol.2020203473

65. Kakinuma R, Moriyama N, Muramatsu Y, et al. Ultra-High-Resolution Computed Tomography of the Lung: Image Quality of a Prototype Scanner. *PLoS ONE*. 2015;10(9):e0137165. doi:10.1371/journal.pone.0137165

66. Gargani L. Lung ultrasound: a new tool for the cardiologist. *Cardiovasc Ultrasound*. 2011;9:6. doi:10.1186/1476-7120-9-6

67. Lichtenstein D, Mézière G, Biderman P, Gepner A, Barré O. The comet-tail artifact. An ultrasound sign of alveolar-interstitial syndrome. *Am J Respir Crit Care Med*. 1997;156(5):1640-1646. doi:10.1164/ajrccm.156.5.96-07096

68. Ziskin MC, Thickman DI, Goldenberg NJ, Lapayowker MS, Becker JM. The comet tail artifact. *J Ultrasound Med*. 1982;1(1):1-7. doi:10.7863/jum.1982.1.1.1

69. Heidenreich JF, Weng AM, Metz C, et al. Three-dimensional Ultrashort Echo Time MRI for Functional Lung Imaging in Cystic Fibrosis. *Radiology*. 2020;296(1):191-199. doi:10.1148/radiol.2020192251

70. Ohno Y, Koyama H, Yoshikawa T, et al. Pulmonary high-resolution ultrashort TE MR imaging: Comparison with thin-section standard- and low-dose computed

tomography for the assessment of pulmonary parenchyma diseases. *J Magn Reson Imaging*. 2016;43(2):512-532. doi:10.1002/jmri.25008

71. Higano NS, Fleck RJ, Spielberg DR, et al. Quantification of neonatal lung parenchymal density via ultrashort echo time MRI with comparison to CT. *J Magn Reson Imaging*. 2017;46(4):992-1000. doi:10.1002/jmri.25643

72. Torres L, Kammerman J, Hahn AD, et al. "Structure-Function Imaging of Lung Disease Using Ultrashort Echo Time MRI". *Acad Radiol*. 2019;26(3):431-441. doi:10.1016/j.acra.2018.12.007

73. Bergin CJ, Pauly JM, Macovski A. Lung parenchyma: projection reconstruction MR imaging. *Radiology*. 1991;179(3):777-781. doi:10.1148/radiology.179.3.2027991

74. Tyler DJ, Robson MD, Henkelman RM, Young IR, Bydder GM. Magnetic resonance imaging with ultrashort TE (UTE) PULSE sequences: technical considerations. *J Magn Reson Imaging*. 2007;25(2):279-289. doi:10.1002/jmri.20851

75. Gurney PT, Hargreaves BA, Nishimura DG. Design and analysis of a practical 3D cones trajectory. *Magn Reson Med*. 2006;55(3):575-582. doi:10.1002/mrm.20796

76. Chassagnon G, Martin C, Ben Hassen W, et al. High-resolution lung MRI with Ultrashort-TE: 1.5 or 3 Tesla? *Magn Reson Imaging*. 2019;61:97-103. doi:10.1016/j.mri.2019.04.015

77. Anger HO. A new instrument for mapping gamma-ray emitters. *Biology and Medicine Quarterly Report UCRL*. 1957;3653.

78. Newman SP, Pitcairn GR, Hirst PH. A brief history of gamma scintigraphy. *Journal of Aerosol Medicine*. 2001;14(2):139-145. doi:10.1089/08942680152484072

79. Dolovich M, Ruffin RE, Roberts R, Newhouse MT. Optimal delivery of aerosols from metered dose inhalers. *Chest*. 1981;80(6 Suppl):911-915.

80. Newman SP, Pavia D, Clarke SW. Improving the bronchial deposition of pressurized aerosols. *Chest*. 1981;80(6 Suppl):909-911.

81. Short MD, Singh CA, Few JD, Studdy PR, Heaf PJ, Spiro SG. The labelling and monitoring of lung deposition of an inhaled synthetic anticholinergic bronchodilating agent. *Chest*. 1981;80(6 Suppl):918-921.

82. DE Kuhl, Hale J, Eaton WL. Transmission scanning: a useful adjunct to conventional emission scanning for accurately keying isotope deposition to radiographic anatomy. *Radiology*. 1966;87(2):278-284.

83. Conway J. Lung imaging - two dimensional gamma scintigraphy, SPECT, CT and PET. *Adv Drug Deliv Rev*. 2012;64(4):357-368. doi:10.1016/j.addr.2012.01.013

84. Parker JA, Coleman RE, Grady E, et al. SNM practice guideline for lung scintigraphy 4.0. *J Nucl Med Technol*. 2012;40(1):57-65. doi:10.2967/jnmt.111.101386

85. Burch WM, Sullivan PJ, McLaren CJ. Technegas--a new ventilation agent for lung scanning. *Nucl Med Commun*. 1986;7(12):865-871. doi:10.1097/00006231-198612000-00003

86. Zöphel K, Bacher-Stier C, Pinkert J, Kropp J. Ventilation/perfusion lung scintigraphy: what is still needed? A review considering technetium-99m-labeled macro-aggregates of albumin. *Ann Nucl Med*. 2009;23(1):1-16. doi:10.1007/s12149-008-0187-3

87. Fragaki M, Sifaki-Pistolla D, Samonakis DN, et al. Screening for Hepatopulmonary Syndrome in Cirrhotic Patients Using Technetium 99m-macroaggregated Albumin Perfusion Lung Scan (Tc-MAA): Diagnostic Approach and Clinical Correlations. *J Clin Gastroenterol*. 2018;52(9):828-834. doi:10.1097/MCG.0000000000000926

88. Bajc M, Schümichen C, Grüning T, et al. EANM guideline for ventilation/perfusion single-photon emission computed tomography (SPECT) for diagnosis of pulmonary embolism and beyond. *Eur J Nucl Med Mol Imaging*. 2019;46(12):2429-2451. doi:10.1007/s00259-019-04450-0

89. Wacholtz E, Ph. History and Development of PET.

90. Almuhaideb A, Papathanasiou N, Bomanji J. 18F-FDG PET/CT imaging in oncology. *Ann Saudi Med*. 2011;31(1):3-13. doi:10.4103/0256-4947.75771

91. de Prost N, Tucci MR, Melo MFV. Assessment of lung inflammation with 18F-FDG PET during acute lung injury. *AJR Am J Roentgenol*. 2010;195(2):292-300. doi:10.2214/AJR.10.4499

92. Dolovich MA. Influence of inspiratory flow rate, particle size, and airway caliber on aerosolized drug delivery to the lung. *Respir Care*. 2000;45(6):597-608.

93. Kim CS. Methods of calculating lung delivery and deposition of aerosol particles. *Respir Care*. 2000;45(6):695-711.

94. Vidal Melo MF, Layfield D, Harris RS, et al. Quantification of regional ventilation-perfusion ratios with PET. *J Nucl Med*. 2003;44(12):1982-1991.

95. Musch G, Layfield JDH, Harris RS, et al. Topographical distribution of pulmonary perfusion and ventilation, assessed by PET in supine and prone humans. *J Appl Physiol*. 2002;93(5):1841-1851. doi:10.1152/japplphysiol.00223.2002

96. Harris RK, Becker ED, Cabral de Menezes SM, Goodfellow R, Granger P. NMR nomenclature. Nuclear spin properties and conventions for chemical shifts(IUPAC Recommendations 2001). *Pure Appl Chem*. 2001;73(11). doi:10.1351/pac200173111795

97. Kauczor H, Surkau R, Roberts T. MRI using hyperpolarized noble gases. *Eur Radiol*. 1998;8(5):820-827. doi:10.1007/s003300050479

98. Fain SB, Korosec FR, Holmes JH, O'Halloran R, Sorkness RL, Grist TM. Functional lung imaging using hyperpolarized gas MRI. *J Magn Reson Imaging*. 2007;25(5):910-923. doi:10.1002/jmri.20876

99. Stewart NJ, Chan H-F, Hughes PJC, et al. Comparison of 3 He and 129 Xe MRI for evaluation of lung microstructure and ventilation at 1.5T. *J Magn Reson Imaging*. 2018;48(3):632-642. doi:10.1002/jmri.25992

100. Deninger AJ, Eberle B, Ebert M, et al. Quantification of regional intrapulmonary oxygen partial pressure evolution during apnea by (3)He MRI. *J Magn Reson*. 1999;141(2):207-216. doi:10.1006/jmre.1999.1902

101. Deninger AJ, Eberle B, Bermuth J, et al. Assessment of a single-acquisition imaging sequence for oxygen-sensitive (3)He-MRI. *Magn Reson Med*. 2002;47(1):105-114. doi:10.1002/mrm.10032

102. Fischer MC, Spector ZZ, Ishii M, et al. Single-acquisition sequence for the measurement of oxygen partial pressure by hyperpolarized gas MRI. *Magn Reson Med*. 2004;52(4):766-773. doi:10.1002/mrm.20239

103. Kern AL, Vogel-Claussen J. Hyperpolarized gas MRI in pulmonology. *Br J Radiol*. 2018;91(1084):20170647. doi:10.1259/bjr.20170647

104. Schreiber WG, Eberle B, Laukemper-Ostendorf S, et al. Dynamic 19F-MRI of pulmonary ventilation using sulfur hexafluoride (SF6) gas. *Magnetic Resonance in Medicine: An Official Journal of the International Society for Magnetic Resonance in Medicine*. 2001;45(4):605-613.

105. Wolf U, Scholz A, Heussel CP, Markstaller K, Schreiber WG. Subsecond fluorine-19 MRI of the lung. *Magn Reson Med*. 2006;55(4):948-951. doi:10.1002/mrm.20859

106. Halaweish AF, Moon RE, Foster WM, et al. Perfluoropropane gas as a magnetic resonance lung imaging contrast agent in humans. *Chest*. 2013;144(4):1300-1310. doi:10.1378/chest.12-2597

107. Holland GN, Bottomley PA, Hinshaw WS. 19F magnetic resonance imaging. *J Magn Reson*. 1977;28(1):133-136. doi:10.1016/0022-2364(77)90263-3

108. Couch MJ, Ball IK, Li T, Fox MS, Biman B, Albert MS. 19 F MRI of the lungs using inert fluorinated gases: challenges and new developments. *J Magn Reson Imaging*. 2019;49(2):343-354. doi:10.1002/jmri.26292

109. Halaweish AF, Foster WM, Moon RE, MacIntyre NR, MacFall JR, Charles HC. Dynamics of pulmonary ventilation distribution at steady state via 19fluorine-enhanced MRI: initial experiences and future developments. *Proc Intl Soc Mag Reson Med*. 2013;21:4111.

110. Gutberlet M, Kaireit TF, Voskrebenzev A, et al. Free-breathing Dynamic 19F Gas MR Imaging for Mapping of Regional Lung Ventilation in Patients with COPD. *Radiology*. 2018;286(3):1040-1051. doi:10.1148/radiol.2017170591

111. Gutberlet M, Kaireit T, Voskrebenzev A, et al. Real-time dynamic fluorinated gas MRI in free breathing for mapping of regional lung ventilation in patients with COPD and healthy volunteers using a 16 channel receive coil at 1.5 T. *Proceedings of the 24th Annual Meeting of ISMRM, Singapore*. 2016.

112. Couch MJ, Ball IK, Li T, et al. Pulmonary ultrashort echo time 19F MR imaging with inhaled fluorinated gas mixtures in healthy volunteers: feasibility. *Radiology*. 2013;269(3):903-909. doi:10.1148/radiol.13130609

113. Charles C, Moon RE, MacIntyre NR, et al. Cardio-respiratory tolerability of perfluoropropane-enhanced MRI of pulmonary ventilation. *B58 LUNG IMAGING I: PHYSIOLOGIC AND CLINICAL CORRELATES*. 2015.

114. Gutberlet M, Kaireit TF, Voskrebenzev A, et al. Repeatability of regional lung ventilation quantification using fluorinated (19F) gas magnetic resonance imaging. *Acad Radiol*. 2019;26(3):395-403. doi:10.1016/j.acra.2018.10.021

115. Klimeš F, Voskrebenzev A, Gutberlet M, et al. Free-breathing quantification of regional ventilation derived by phase-resolved functional lung (PREFUL) MRI. *NMR Biomed*. 2019;32(6):e4088. doi:10.1002/nbm.4088

116. Behrendt L, Voskrebenzev A, Klimeš F, et al. Validation of Automated Perfusion-Weighted Phase-Resolved Functional Lung (PREFUL)-MRI in Patients With Pulmonary Diseases. *J Magn Reson Imaging*. 2020;52(1):103-114. doi:10.1002/jmri.27027

117. Klimeš F, Voskrebenzev A, Gutberlet M, et al. Repeatability of dynamic 3D phase-resolved functional lung (PREFUL) ventilation MR Imaging in patients with chronic obstructive pulmonary disease and healthy volunteers. *J Magn Reson Imaging*. 2021;54(2):618-629. doi:10.1002/jmri.27543

118. Pöhler GH, Klimeš F, Behrendt L, et al. Repeatability of Phase-Resolved Functional Lung (PREFUL)-MRI Ventilation and Perfusion Parameters in Healthy Subjects and COPD Patients. *J Magn Reson Imaging*. 2021;53(3):915-927. doi:10.1002/jmri.27385

119. Klimeš F, Voskrebenzev A, Gutberlet M, et al. 3D phase-resolved functional lung ventilation MR imaging in healthy volunteers and patients with chronic pulmonary disease. *Magn Reson Med*. 2021;85(2):912-925. doi:10.1002/mrm.28482

120. Edelman RR, Hatabu H, Tadamura E, Li W, Prasad PV. Noninvasive assessment of regional ventilation in the human lung using oxygen-enhanced magnetic resonance imaging. *Nat Med*. 1996;2(11):1236-1239. doi:10.1038/nm1196-1236

121. Zhang W-J, Niven RM, Young SS, Liu Y-Z, Parker GJM, Naish JH. Dynamic oxygen-enhanced magnetic resonance imaging of the lung in asthma -- initial experience. *Eur J Radiol*. 2015;84(2):318-326. doi:10.1016/j.ejrad.2014.10.021

122. Chen Q, Jakob PM, Griswold MA, Levin DL, Hatabu H, Edelman RR. Oxygen enhanced MR ventilation imaging of the lung. *MAGMA*. 1998;7(3):153-161. doi:10.1007/BF02591332

123. Kruger SJ, Nagle SK, Couch MJ, Ohno Y, Albert M, Fain SB. Functional imaging of the lungs with gas agents. *J Magn Reson Imaging*. 2016;43(2):295-315. doi:10.1002/jmri.25002

124. Bloch F. Nuclear Induction. *Phys Rev*. 1946;70(7-8):460-474. doi:10.1103/PhysRev.70.460

125. Slichter CP. *Principles of Magnetic Resonance*. Vol 1. Springer Berlin Heidelberg; 1990. doi:10.1007/978-3-662-09441-9

126. Torrey HC. Bloch Equations with Diffusion Terms. *Phys Rev*. 1956;104(3):563-565. doi:10.1103/PhysRev.104.563

127. Fong W. *handbook of MRI pulse sequences*. *Med Phys*. 2005;32(5):1452-1452. doi:10.1118/1.1904597

128. Puiseux T, Sewonu A, Moreno R, Mendez S, Nicoud F. Numerical simulation of time-resolved 3D phase-contrast magnetic resonance imaging. *PLoS ONE*. 2021;16(3):e0248816. doi:10.1371/journal.pone.0248816

129. Schild HH. MRI made easy (... well almost). *MRI made easy (. well almost)*. 1992.

130. Elster AD. Gradient-echo MR imaging: techniques and acronyms. *Radiology*. 1993;186(1):1-8. doi:10.1148/radiology.186.1.8416546

131. Hahn EL. Spin Echoes. *Phys Rev*. 1950;80(4):580-594. doi:10.1103/PhysRev.80.580

132. Jo Y, Kim J, Park CH, et al. Guideline for Cardiovascular Magnetic Resonance Imaging from the Korean Society of Cardiovascular Imaging-Part 1: Standardized Protocol. *Korean J Radiol*. 2019;20(9):1313-1333. doi:10.3348/kjr.2019.0398

133. Levitt MH, Freeman R. NMR population inversion using a composite pulse. *J Magn Reson*. 1979;33(2):473-476. doi:10.1016/0022-2364(79)90265-8

134. Jung BA, Weigel M. Spin echo magnetic resonance imaging. *J Magn Reson Imaging*. 2013;37(4):805-817. doi:10.1002/jmri.24068

135. Paschal CB, Morris HD. K-space in the clinic. *J Magn Reson Imaging*. 2004;19(2):145-159. doi:10.1002/jmri.10451

136. Liang Z-P, Lauterbur PC. *Principles of Magnetic Resonance Imaging*. IEEE; 1999. doi:10.1109/9780470545652

137. Maier A, Steidl S, Christlein V, Hornegger J, eds. *Medical Imaging Systems: An Introductory Guide*. Springer; 2018. doi:10.1007/978-3-319-96520-8

138. Ma Y, Jang H, Jerban S, et al. Making the invisible visible-ultrashort echo time magnetic resonance imaging: Technical developments and applications. *Appl Phys Rev*. 2022;9(4):041303. doi:10.1063/5.0086459

139. Takahashi M, Togao O, Obara M, et al. Ultra-short echo time (UTE) MR imaging of the lung: comparison between normal and emphysematous lungs in mutant mice. *J Magn Reson Imaging*. 2010;32(2):326-333. doi:10.1002/jmri.22267

140. Sanchez F, Tyrrell PN, Cheung P, et al. Detection of solid and subsolid pulmonary nodules with lung MRI: performance of UTE, T1 gradient-echo, and single-shot T2 fast spin echo. *Cancer Imaging*. 2023;23(1):17. doi:10.1186/s40644-023-00531-4

141. Landini N, Orlandi M, Occhipinti M, et al. Ultrashort Echo-Time Magnetic Resonance Imaging Sequence in the Assessment of Systemic Sclerosis-Interstitial Lung Disease. *J Thorac Imaging*. 2023;38(2):97-103. doi:10.1097/RTI.0000000000000637

142. Renz DM, Herrmann K-H, Kraemer M, et al. Ultrashort echo time MRI of the lung in children and adolescents: comparison with non-enhanced computed tomography and standard post-contrast T1w MRI sequences. *Eur Radiol*. 2022;32(3):1833-1842. doi:10.1007/s00330-021-08236-7

143. Geiger J, Zeimpekis KG, Jung A, Moeller A, Kellenberger CJ. Clinical application of ultrashort echo-time MRI for lung pathologies in children. *Clin Radiol*. 2021;76(9):708.e9-708.e17. doi:10.1016/j.crad.2021.05.015

144. Afsahi AM, Ma Y, Jang H, et al. Ultrashort echo time magnetic resonance imaging techniques: met and unmet needs in musculoskeletal imaging. *J Magn Reson Imaging*. 2022;55(6):1597-1612. doi:10.1002/jmri.28032

145. Stemkens B, Paulson ES, Tijssen RHN. Nuts and bolts of 4D-MRI for radiotherapy. *Phys Med Biol*. 2018;63(21):21TR01. doi:10.1088/1361-6560/aae56d

146. Fourier JBJ. *Théorie Analytique de La Chaleur*. FIRMIN DIDOT , PÈRE ET FILS; 1822. doi:10.1017/CBO9780511693229

147. Cooley JW, Tukey JW. An algorithm for the machine calculation of complex Fourier series. *Math Comput*. 1965;19(90):297-297. doi:10.1090/S0025-5718-1965-0178586-1

148. Fessler JA, Sutton BP. Nonuniform fast fourier transforms using min-max interpolation. *IEEE Trans Signal Process*. 2003;51(2):560-574. doi:10.1109/TSP.2002.807005

149. Jackson JI, Meyer CH, Nishimura DG, Macovski A. Selection of a convolution function for Fourier inversion using gridding [computerised tomography application]. *IEEE Trans Med Imaging*. 1991;10(3):473-478. doi:10.1109/42.97598

150. Pauly J. Non-cartesian reconstruction. *URL: http://www stanford edu/class/ee369c/notes/non cart rec*. 2005;7.

151. Pauly JM. Gridding & the NUFFT for non-Cartesian image reconstruction. *ISMRM Educational Course on Image Reconstruction*. 2012;45.

152. Brown RW, Cheng YCN, Haacke EM, Thompson MR, Venkatesan R. *Magnetic Resonance Imaging: Physical Principles and Sequence Design*. (Brown RW, Cheng Y-

CN, Haacke EM, Thompson MR, Venkatesan R, eds.). John Wiley & Sons Ltd; 2014. doi:10.1002/9781118633953

153. Puderbach M, Eichinger M, Haeselbarth J, et al. Assessment of morphological MRI for pulmonary changes in cystic fibrosis (CF) patients: comparison to thin-section CT and chest x-ray. *Invest Radiol*. 2007;42(10):715-725. doi:10.1097/RLI.0b013e318074fd81

154. Altes TA, Eichinger M, Puderbach M. Magnetic resonance imaging of the lung in cystic fibrosis. *Proc Am Thorac Soc*. 2007;4(4):321-327. doi:10.1513/pats.200611-181HT

155. Couch MJ, Fox MS, Viel C, et al. Fractional ventilation mapping using inert fluorinated gas MRI in rat models of inflammation and fibrosis. *NMR Biomed*. 2016;29(5):545-552. doi:10.1002/nbm.3493

156. Ouriadov AV, Fox MS, Couch MJ, Li T, Ball IK, Albert MS. In vivo regional ventilation mapping using fluorinated gas MRI with an x-centric FGRE method. *Magn Reson Med*. 2015;74(2):550-557. doi:10.1002/mrm.25406

157. Soher BJ, Halaweish AF, Charles HC. Modeling of the spatio-temporal distribution of pulmonary ventilation via perfluoropropane gas enhanced MRI. *Proceedings of the 23rd Annual Meeting of ISMRM*. 2015;4006.

158. Kaireit TF, Gutberlet M, Voskrebenzev A, et al. Comparison of quantitative regional ventilation-weighted fourier decomposition MRI with dynamic fluorinated gas washout MRI and lung function testing in COPD patients. *J Magn Reson Imaging*. 2018;47(6):1534-1541. doi:10.1002/jmri.25902

159. Miller MR, Hankinson J, Brusasco V, et al. Standardisation of spirometry. *Eur Respir J*. 2005;26(2):319-338. doi:10.1183/09031936.05.00034805

160. Goralski JL, Akinnagbe E, Charles HC, Donaldson SH, Lee Y. PERFLUORINATED GAS MRI DETECTS REGIONAL VENTILATION HETEROGENEITY IN CF. *PEDIATRIC PULMONOLOGY*. 2016;51:275.

161. Mugler JP, Altes TA. Hyperpolarized 129Xe MRI of the human lung. *J Magn Reson Imaging*. 2013;37(2):313-331. doi:10.1002/jmri.23844

162. Ouriadov A, Farag A, Kirby M, McCormack DG, Parraga G, Santyr GE. Lung morphometry using hyperpolarized (129) Xe apparent diffusion coefficient anisotropy in chronic obstructive pulmonary disease. *Magn Reson Med*. 2013;70(6):1699-1706. doi:10.1002/mrm.24595

163. Kirby M, Svenningsen S, Owrangi A, et al. Hyperpolarized 3He and 129Xe MR imaging in healthy volunteers and patients with chronic obstructive pulmonary disease. *Radiology*. 2012;265(2):600-610. doi:10.1148/radiol.12120485

164. Kirby M, Svenningsen S, Kanhere N, et al. Pulmonary ventilation visualized using hyperpolarized helium-3 and xenon-129 magnetic resonance imaging: differences in

COPD and relationship to emphysema. *J Appl Physiol*. 2013;114(6):707-715. doi:10.1152/japplphysiol.01206.2012

165. Shukla Y, Wheatley A, Kirby M, et al. Hyperpolarized 129Xe magnetic resonance imaging: tolerability in healthy volunteers and subjects with pulmonary disease. *Acad Radiol*. 2012;19(8):941-951. doi:10.1016/j.acra.2012.03.018

166. Ebner L, Kammerman J, Driehuys B, Schiebler ML, Cadman RV, Fain SB. The role of hyperpolarized 129xenon in MR imaging of pulmonary function. *Eur J Radiol*. 2017;86:343-352. doi:10.1016/j.ejrad.2016.09.015

167. Couch MJ, Munidasa S, Rayment JH, et al. Comparison of Functional Free-Breathing Pulmonary 1H and Hyperpolarized 129Xe Magnetic Resonance Imaging in Pediatric Cystic Fibrosis. *Acad Radiol*. 2021;28(8):e209-e218. doi:10.1016/j.acra.2020.05.008

168. Couch MJ, Thomen R, Kanhere N, et al. A two-center analysis of hyperpolarized 129Xe lung MRI in stable pediatric cystic fibrosis: Potential as a biomarker for multi-site trials. *J Cyst Fibros*. 2019;18(5):728-733. doi:10.1016/j.jcf.2019.03.005

169. Thomen RP, Walkup LL, Roach DJ, Cleveland ZI, Clancy JP, Woods JC. Hyperpolarized 129Xe for investigation of mild cystic fibrosis lung disease in pediatric patients. *J Cyst Fibros*. 2017;16(2):275-282. doi:10.1016/j.jcf.2016.07.008

170. Patz S, Hersman FW, Muradian I, et al. Hyperpolarized (129)Xe MRI: a viable functional lung imaging modality? *Eur J Radiol*. 2007;64(3):335-344. doi:10.1016/j.ejrad.2007.08.008

171. Roos JE, McAdams HP, Kaushik SS, Driehuys B. Hyperpolarized gas MR imaging: technique and applications. *Magn Reson Imaging Clin N Am*. 2015;23(2):217-229. doi:10.1016/j.mric.2015.01.003

172. Kennedy RR, Stokes JW, Downing P. Anaesthesia and the "inert" gases with special reference to xenon. *Anaesth Intensive Care*. 1992;20(1):66-70.

173. Walkup LL, Thomen RP, Akinyi TG, et al. Feasibility, tolerability and safety of pediatric hyperpolarized 129Xe magnetic resonance imaging in healthy volunteers and children with cystic fibrosis. *Pediatr Radiol*. 2016;46(12):1651-1662. doi:10.1007/s00247-016-3672-1

174. Maunder A, Hughes PJ, Chan H, et al. Comparing 19 F C3F8 lung ventilation imaging with hyperpolarized 129 Xe: Similarities and limitations. *Proc Intl Soc Mag Reson Med*. 2018;26:1083.

175. Wild JM, Ajraoui S, Deppe MH, et al. Synchronous acquisition of hyperpolarised 3He and 1H MR images of the lungs - maximising mutual anatomical and functional information. *NMR Biomed*. 2011;24(2):130-134. doi:10.1002/nbm.1565

176. Wild JM, Marshall H, Xu X, et al. Simultaneous imaging of lung structure and function with triple-nuclear hybrid MR imaging. *Radiology*. 2013;267(1):251-255. doi:10.1148/radiol.12121153

177. Obert AJ, Gutberlet M, Kern AL, et al. 1 H-guided reconstruction of 19 F gas MRI in COPD patients. *Magn Reson Med*. 2020;84(3):1336-1346. doi:10.1002/mrm.28209

178. Neal MA, Pippard BJ, Hollingsworth KG, et al. Optimized and accelerated 19 F-MRI of inhaled perfluoropropane to assess regional pulmonary ventilation. *Magn Reson Med*. 2019;82(4):1301-1311. doi:10.1002/mrm.27805

179. He M, Kaushik SS, Robertson SH, et al. Extending semiautomatic ventilation defect analysis for hyperpolarized (129)Xe ventilation MRI. *Acad Radiol*. 2014;21(12):1530-1541. doi:10.1016/j.acra.2014.07.017

180. Li C, Gore JC, Davatzikos C. Multiplicative intrinsic component optimization (MICO) for MRI bias field estimation and tissue segmentation. *Magn Reson Imaging*. 2014;32(7):913-923. doi:10.1016/j.mri.2014.03.010

181. Obert AJ, Gutberlet M, Kern AL, et al. Examining lung microstructure using 19F MR diffusion imaging in COPD patients. *Magnetic Resonance in Medicine*. 2022.

182. Coxson HO, Leipsic J, Parraga G, Sin DD. Using pulmonary imaging to move chronic obstructive pulmonary disease beyond FEV1. *Am J Respir Crit Care Med*. 2014;190(2):135-144. doi:10.1164/rccm.201402-0256PP

183. Lee Y, Akinnagbe-Zusterzeel E, Goralski J, et al. 19F ventilation imaging of cystic fibrosis patients. *Proc Int Soc Magn Reson Med*. 2016;24:1607.

184. Goralski JL, Chung SH, Glass TM, et al. Dynamic perfluorinated gas MRI reveals abnormal ventilation despite normal FEV1 in cystic fibrosis. *JCI Insight*. 2020;5(2). doi:10.1172/jci.insight.133400

185. Kirby M, Mathew L, Heydarian M, Etemad-Rezai R, McCormack DG, Parraga G. Chronic obstructive pulmonary disease: quantification of bronchodilator effects by using hyperpolarized ^{3}He MR imaging. *Radiology*. 2011;261(1):283-292. doi:10.1148/radiol.11110403

186. Fain S, Schiebler ML, McCormack DG, Parraga G. Imaging of lung function using hyperpolarized helium-3 magnetic resonance imaging: Review of current and emerging translational methods and applications. *J Magn Reson Imaging*. 2010;32(6):1398-1408. doi:10.1002/jmri.22375

187. Stavngaard T, Søgaard LV, Mortensen J, et al. Hyperpolarized 3He MRI and 81mKr SPECT in chronic obstructive pulmonary disease. *Eur J Nucl Med Mol Imaging*. 2005;32(4):448-457. doi:10.1007/s00259-004-1691-x

188. Parraga G, Ouriadov A, Evans A, et al. Hyperpolarized 3He ventilation defects and apparent diffusion coefficients in chronic obstructive pulmonary disease: preliminary results at 3.0 Tesla. *Invest Radiol*. 2007;42(6):384-391. doi:10.1097/01.rli.0000262571.81771.66

189. Samee S, Altes T, Powers P, et al. Imaging the lungs in asthmatic patients by using hyperpolarized helium-3 magnetic resonance: assessment of response to

methacholine and exercise challenge. *J Allergy Clin Immunol*. 2003;111(6):1205-1211. doi:10.1067/mai.2003.1544

190. Hamedani H, Clapp JT, Kadlecek SJ, et al. Regional Fractional Ventilation by Using Multibreath Wash-in (3)He MR Imaging. *Radiology*. 2016;279(3):917-924. doi:10.1148/radiol.2015150495

191. McCallister A, Chung SH, Antonacci M, et al. Comparison of single breath hyperpolarized 129 Xe MRI with dynamic 19 F MRI in cystic fibrosis lung disease. *Magn Reson Med*. 2021;85(2):1028-1038. doi:10.1002/mrm.28457

192. Kanhere N, Couch MJ, Kowalik K, et al. Correlation of Lung Clearance Index with Hyperpolarized 129Xe Magnetic Resonance Imaging in Pediatric Subjects with Cystic Fibrosis. *Am J Respir Crit Care Med*. 2017;196(8):1073-1075. doi:10.1164/rccm.201611-2228LE

193. Charles HC, Jones RW, Halaweish AF, Ainslie MD. Parallel imaging for short breath hold times in perfluorinated gas imaging of the lung. *Proceedings of the 23rd Annual Meeting of ISMRM; Toronto, Canada*. 2015:3984.

194. McLeod C, Wood J, Schultz A, et al. Outcomes and endpoints reported in studies of pulmonary exacerbations in people with cystic fibrosis: A systematic review. *J Cyst Fibros*. 2020;19(6):858-867. doi:10.1016/j.jcf.2020.08.015

195. Nissenbaum C, Davies G, Horsley A, Davies JC. Monitoring early stage lung disease in cystic fibrosis. *Curr Opin Pulm Med*. 2020;26(6):671-678. doi:10.1097/MCP.0000000000000732

196. Dave K, Dobra R, Scott S, et al. Entering the era of highly effective modulator therapies. *Pediatr Pulmonol*. 2021;56 Suppl 1:S79-S89. doi:10.1002/ppul.24968

197. Loza LA, Kadlecek SJ, Pourfathi M, et al. Quantification of ventilation and gas uptake in free-breathing mice with hyperpolarized 129 Xe MRI. *IEEE transactions on medical imaging*. 2019;38(9):2081-2091.

198. Gutberlet M, Obert A, Voskrebenzev A, Klimes F, Wacker F, Vogel-Claussen J. Quantification of gas concentration and fractional ventilation using high temporal resolution MRI of pulmonary fluorinated (19F) gas washin dynamics in free breathing. *Proc 26th Annual Meeting ISMRM, Paris*. 2018.

199. Santyr G, Kanhere N, Morgado F, Rayment JH, Ratjen F, Couch MJ. Hyperpolarized gas magnetic resonance imaging of pediatric cystic fibrosis lung disease. *Acad Radiol*. 2019;26(3):344-354. doi:10.1016/j.acra.2018.04.024

200. Hedlund LW, Möller HE, Chen XJ, Chawla MS, Cofer GP, Johnson GA. Mixing oxygen with hyperpolarized 3He for small-animal lung studies. *NMR in Biomedicine: An International Journal Devoted to the Development and Application of Magnetic Resonance In Vivo*. 2000;13(4):202-206.

201. Huynh KM, Chang W-T, Chung SH, Chen Y, Lee Y, Yap P-T. Noise Mapping and Removal in Complex-Valued Multi-Channel MRI via Optimal Shrinkage of Singular

Values. In: de Bruijne M, Cattin PC, Cotin S, et al., eds. *Medical Image Computing and Computer Assisted Intervention – MICCAI 2021: 24th International Conference, Strasbourg, France, September 27–October 1, 2021, Proceedings, Part VI*. Vol 12906. Lecture notes in computer science. Springer International Publishing; 2021:191-200. doi:10.1007/978-3-030-87231-1_19

202. Charles HC, Soher BJ. Systems, methods, compositions and devices for in vivo magnetic resonance imaging of lungs using perfluorinated gas mixtures. 2017.

203. Halaweish AF, Charles HC. Physiorack: an integrated MRI safe/conditional, gas delivery, respiratory gating, and subject monitoring solution for structural and functional assessments of pulmonary function. *J Magn Reson Imaging*. 2014;39(3):735-741. doi:10.1002/jmri.24219

204. Fessler JA. Michigan image reconstruction toolbox. *Ann Arbor (MI): Jeffrey Fessler*. 2018.

205. Gavish M, Donoho DL. Optimal shrinkage of singular values. *IEEE Trans Inform Theory*. 2017;63(4):2137-2152. doi:10.1109/TIT.2017.2653801

206. Walsh DO, Gmitro AF, Marcellin MW. Adaptive reconstruction of phased array MR imagery. *Magn Reson Med*. 2000;43(5):682-690. doi:10.1002/(sici)1522-2594(200005)43:5<682::aid-mrm10>3.0.co;2-g

207. Chae EJ, Seo JB, Kim N, et al. Collateral ventilation in a canine model with bronchial obstruction: assessment with xenon-enhanced dual-energy CT. *Radiology*. 2010;255(3):790-798. doi:10.1148/radiol.10090947

208. Veraart J, Fieremans E, Novikov DS. Diffusion MRI noise mapping using random matrix theory. *Magn Reson Med*. 2016;76(5):1582-1593. doi:10.1002/mrm.26059

209. Veraart J, Novikov DS, Christiaens D, Ades-Aron B, Sijbers J, Fieremans E. Denoising of diffusion MRI using random matrix theory. *Neuroimage*. 2016;142:394-406. doi:10.1016/j.neuroimage.2016.08.016

210. Does MD, Olesen JL, Harkins KD, et al. Evaluation of principal component analysis image denoising on multi-exponential MRI relaxometry. *Magn Reson Med*. 2019;81(6):3503-3514. doi:10.1002/mrm.27658

211. Voskrebenzev A, Gutberlet M, Klimeš F, et al. Feasibility of quantitative regional ventilation and perfusion mapping with phase-resolved functional lung (PREFUL) MRI in healthy volunteers and COPD, CTEPH, and CF patients. *Magn Reson Med*. 2018;79(4):2306-2314. doi:10.1002/mrm.26893

212. Munidasa S, Couch MJ, Rayment JH, et al. Free-breathing MRI for monitoring ventilation changes following antibiotic treatment of pulmonary exacerbations in paediatric cystic fibrosis. *Eur Respir J*. 2021;57(4):2003104. doi:10.1183/13993003.03104-2020

213. Capaldi DPI, Guo F, Xing L, Parraga G. Pulmonary Ventilation Maps Generated with Free-breathing Proton MRI and a Deep Convolutional Neural Network. *Radiology*. 2021;298(2):427-438. doi:10.1148/radiol.2020202861

214. Campbell-Washburn AE, Xue H, Lederman RJ, Faranesh AZ, Hansen MS. Real-time distortion correction of spiral and echo planar images using the gradient system impulse response function. *Magn Reson Med*. 2016;75(6):2278-2285. doi:10.1002/mrm.25788

215. Duyn JH, Yang Y, Frank JA, van der Veen JW. Simple correction method for k-space trajectory deviations in MRI. *J Magn Reson*. 1998;132(1):150-153. doi:10.1006/jmre.1998.1396

216. Addy NO, Wu HH, Nishimura DG. Simple method for MR gradient system characterization and k-space trajectory estimation. *Magn Reson Med*. 2012;68(1):120-129. doi:10.1002/mrm.23217

217. Robison RK, Devaraj A, Pipe JG. Fast, simple gradient delay estimation for spiral MRI. *Magn Reson Med*. 2010;63(6):1683-1690. doi:10.1002/mrm.22327

218. Tan H, Meyer CH. Estimation of k-space trajectories in spiral MRI. *Magn Reson Med*. 2009;61(6):1396-1404. doi:10.1002/mrm.21813

219. Bhavsar PS, Zwart NR, Pipe JG. Fast, variable system delay correction for spiral MRI. *Magn Reson Med*. 2014;71(2):773-782. doi:10.1002/mrm.24730

220. Robson PM, Grant AK, Madhuranthakam AJ, Lattanzi R, Sodickson DK, McKenzie CA. Comprehensive quantification of signal-to-noise ratio and g-factor for image-based and k-space-based parallel imaging reconstructions. *Magn Reson Med*. 2008;60(4):895-907. doi:10.1002/mrm.21728

221. Constantinides CD, Atalar E, McVeigh ER. Signal-to-noise measurements in magnitude images from NMR phased arrays. *Magn Reson Med*. 1997;38(5):852-857. doi:10.1002/mrm.1910380524

222. Cordero-Grande L, Christiaens D, Hutter J, Price AN, Hajnal JV. Complex diffusion-weighted image estimation via matrix recovery under general noise models. *Neuroimage*. 2019;200:391-404. doi:10.1016/j.neuroimage.2019.06.039

223. Ma X, Uğurbil K, Wu X. Denoise magnitude diffusion magnetic resonance images via variance-stabilizing transformation and optimal singular-value manipulation. *Neuroimage*. 2020;215:116852. doi:10.1016/j.neuroimage.2020.116852

224. Coupe P, Yger P, Prima S, Hellier P, Kervrann C, Barillot C. An optimized blockwise nonlocal means denoising filter for 3-D magnetic resonance images. *IEEE Trans Med Imaging*. 2008;27(4):425-441. doi:10.1109/TMI.2007.906087

225. Chung SH, Huynh KM, Goralski JL, et al. Feasibility of free-breathing 19 F MRI image acquisition to characterize ventilation defects in CF and healthy volunteers at wash-in. *Magn Reson Med*. March 13, 2023. doi:10.1002/mrm.29630

226. Diaz S, Casselbrant I, Piitulainen E, et al. Hyperpolarized 3He apparent diffusion coefficient MRI of the lung: reproducibility and volume dependency in healthy volunteers and patients with emphysema. *Journal of Magnetic Resonance Imaging: An Official Journal of the International Society for Magnetic Resonance in Medicine*. 2008;27(4):763-770.

227. Chan H-F, Stewart NJ, Parra-Robles J, Collier GJ, Wild JM. Whole lung morphometry with 3D multiple b-value hyperpolarized gas MRI and compressed sensing. *Magn Reson Med*. 2017;77(5):1916-1925. doi:10.1002/mrm.26279

228. Yablonskiy DA, Sukstanskii AL, Leawoods JC, et al. Quantitative in vivo assessment of lung microstructure at the alveolar level with hyperpolarized 3He diffusion MRI. *Proc Natl Acad Sci USA*. 2002;99(5):3111-3116. doi:10.1073/pnas.052594699

229. Mata JF, Altes TA, Cai J, et al. Evaluation of emphysema severity and progression in a rabbit model: comparison of hyperpolarized 3He and 129Xe diffusion MRI with lung morphometry. *J Appl Physiol*. 2007;102(3):1273-1280. doi:10.1152/japplphysiol.00418.2006

230. Carrero-González L, Kaulisch T, Stiller D. In vivo diffusion-weighted MRI using perfluorinated gases: ADC comparison between healthy and elastase-treated rat lungs. *Magn Reson Med*. 2013;70(6):1761-1764. doi:10.1002/mrm.24627

231. Ruiz-Cabello J, Pérez-Sánchez JM, Pérez de Alejo R, et al. Diffusion-weighted 19F-MRI of lung periphery: Influence of pressure and air-SF6 composition on apparent diffusion coefficients. *Respir Physiol Neurobiol*. 2005;148(1-2):43-56. doi:10.1016/j.resp.2005.04.007

232. Jacob RE, Chang YV, Choong CK, et al. 19F MR imaging of ventilation and diffusion in excised lungs. *Magn Reson Med*. 2005;54(3):577-585. doi:10.1002/mrm.20632

233. Maunder A, Chan HF, Hughes PJ, et al. MR properties of 19F C3F8 gas in the lungs of healthy volunteers: and apparent diffusion coefficient at 1.5 T and at 3T. *Magnetic Resonance in Medicine*. 2021;85(3):1561-1570.

234. Yablonskiy DA, Sukstanskii AL, Woods JC, et al. Quantification of lung microstructure with hyperpolarized^3 He diffusion MRI. *J Appl Physiol*. 2009;107(4):1258-1265. doi:10.1152/japplphysiol.00386.2009

235. Mammarappallil JG, Rankine L, Wild JM, Driehuys B. New developments in imaging idiopathic pulmonary fibrosis with hyperpolarized xenon magnetic resonance imaging. *J Thorac Imaging*. 2019;34(2):136-150. doi:10.1097/RTI.0000000000000392

236. Chan H-F, Weatherley ND, Johns CS, et al. Airway Microstructure in Idiopathic Pulmonary Fibrosis: Assessment at Hyperpolarized 3He Diffusion-weighted MRI. *Radiology*. 2019;291(1):223-229. doi:10.1148/radiol.2019181714

237. Evans A, McCormack D, Ouriadov A, Etemad-Rezai R, Santyr G, Parraga G. Anatomical distribution of 3He apparent diffusion coefficients in severe chronic

obstructive pulmonary disease. *Journal of Magnetic Resonance Imaging: An Official Journal of the International Society for Magnetic Resonance in Medicine*. 2007;26(6):1537-1547.

238. Kaushik SS, Cleveland ZI, Cofer GP, et al. Diffusion-weighted hyperpolarized 129Xe MRI in healthy volunteers and subjects with chronic obstructive pulmonary disease. *Magn Reson Med*. 2011;65(4):1154-1165. doi:10.1002/mrm.22697

239. Stejskal EO, Tanner JE. Spin Diffusion Measurements: Spin Echoes in the Presence of a Time-Dependent Field Gradient. *J Chem Phys*. 1965;42(1):288. doi:10.1063/1.1695690

240. Le Bihan D, Breton E, Lallemand D, Grenier P, Cabanis E, Laval-Jeantet M. MR imaging of intravoxel incoherent motions: application to diffusion and perfusion in neurologic disorders. *Radiology*. 1986;161(2):401-407. doi:10.1148/radiology.161.2.3763909

241. de Figueiredo EHMSG, Borgonovi AFNG, Doring TM. Basic concepts of MR imaging, diffusion MR imaging, and diffusion tensor imaging. *Magn Reson Imaging Clin N Am*. 2011;19(1):1-22. doi:10.1016/j.mric.2010.10.005

242. Maunder A, Rao M, Robb F, Wild JM. Optimization of steady-state free precession MRI for lung ventilation imaging with 19 F C3 F8 at 1.5T and 3T. *Magn Reson Med*. 2019;81(2):1130-1142. doi:10.1002/mrm.27479

243. Le Bihan D, Breton E, Lallemand D, Aubin ML, Vignaud J, Laval-Jeantet M. Separation of diffusion and perfusion in intravoxel incoherent motion MR imaging. *Radiology*. 1988;168(2):497-505. doi:10.1148/radiology.168.2.3393671

244. Luciani A, Vignaud A, Cavet M, et al. Liver cirrhosis: intravoxel incoherent motion MR imaging--pilot study. *Radiology*. 2008;249(3):891-899. doi:10.1148/radiol.2493080080

245. Hurlimann MD, Helmer KG, Deswiet TM, Sen PN. Spin echoes in a constant gradient and in the presence of simple restriction. *Journal of Magnetic Resonance, Series A*. 1995;113(2):260-264. doi:10.1006/jmra.1995.1091

246. Hayden ME, Archibald G, Gilbert KM, Lei C. Restricted diffusion within a single pore. *J Magn Reson*. 2004;169(2):313-322. doi:10.1016/j.jmr.2004.05.002

247. Parra-Robles J, Ajraoui S, Deppe MH, Parnell SR, Wild JM. Experimental investigation and numerical simulation of 3He gas diffusion in simple geometries: implications for analytical models of 3He MR lung morphometry. *J Magn Reson*. 2010;204(2):228-238. doi:10.1016/j.jmr.2010.02.023

248. Staal AHJ, Becker K, Tagit O, et al. In vivo clearance of 19F MRI imaging nanocarriers is strongly influenced by nanoparticle ultrastructure. *Biomaterials*. 2020;261:120307. doi:10.1016/j.biomaterials.2020.120307

249. Srinivas M, Heerschap A, Ahrens ET, Figdor CG, de Vries IJM. (19)F MRI for quantitative in vivo cell tracking. *Trends Biotechnol*. 2010;28(7):363-370. doi:10.1016/j.tibtech.2010.04.002

250. Ahrens ET, Flores R, Xu H, Morel PA. In vivo imaging platform for tracking immunotherapeutic cells. *Nat Biotechnol*. 2005;23(8):983-987. doi:10.1038/nbt1121

251. Ahrens ET, Bulte JWM. Tracking immune cells in vivo using magnetic resonance imaging. *Nat Rev Immunol*. 2013;13(10):755-763. doi:10.1038/nri3531

252. Chapelin F, Capitini CM, Ahrens ET. Fluorine-19 MRI for detection and quantification of immune cell therapy for cancer. *J Immunother Cancer*. 2018;6(1):105. doi:10.1186/s40425-018-0416-9

253. Jacoby C, Temme S, Mayenfels F, et al. Probing different perfluorocarbons for in vivo inflammation imaging by 19F MRI: image reconstruction, biological half-lives and sensitivity. *NMR Biomed*. 2014;27(3):261-271. doi:10.1002/nbm.3059

254. Flögel U, Ding Z, Hardung H, et al. In vivo monitoring of inflammation after cardiac and cerebral ischemia by fluorine magnetic resonance imaging. *Circulation*. 2008;118(2):140-148. doi:10.1161/CIRCULATIONAHA.107.737890

255. Flögel U, Burghoff S, van Lent PLEM, et al. Selective activation of adenosine A2A receptors on immune cells by a CD73-dependent prodrug suppresses joint inflammation in experimental rheumatoid arthritis. *Sci Transl Med*. 2012;4(146):146ra108. doi:10.1126/scitranslmed.3003717

256. Mason RP, Rodbumrung W, Antich PP. Hexafluorobenzene: a sensitive 19F NMR indicator of tumor oxygenation. *NMR in Biomedicine: An International Journal Devoted to the Development and Application of Magnetic Resonance In Vivo*. 1996;9(3):125-134.

257. Zhao D, Jiang L, Hahn EW, Mason RP. Comparison of 1H blood oxygen level–dependent (BOLD) and 19F MRI to investigate tumor oxygenation. *Magnetic Resonance in Medicine: An Official Journal of the International Society for Magnetic Resonance in Medicine*. 2009;62(2):357-364.

258. Eidelberg D, Johnson G, Barnes D, et al. 19F NMR imaging of blood oxygenation in the brain. *Magn Reson Med*. 1988;6(3):344-352. doi:10.1002/mrm.1910060312

259. Mason RP, Nunnally RL, Antich PP. Tissue oxygenation: a novel determination using 19F surface coil NMR spectroscopy of sequestered perfluorocarbon emulsion. *Magn Reson Med*. 1991;18(1):71-79. doi:10.1002/mrm.1910180109

260. Baldwin NJ, Ng TC. Oxygenation and metabolic status of KHT tumors as measured simultaneously by 19F magnetic resonance imaging and 31P magnetic resonance spectroscopy. *Magn Reson Imaging*. 1996;14(5):541-551. doi:10.1016/0730-725x(96)00049-5

261. Blüml S, Schad LR, Stepanow B, Lorenz WJ. Spin-lattice relaxation time measurement by means of a TurboFLASH technique. *Magn Reson Med*. 1993;30(3):289-295. doi:10.1002/mrm.1910300304

262. Gupta RK. A new look at the method of variable nutation angle for the measurement of spin-lattice relaxation times using fourier transform NMR. *J Magn Reson*. 1977;25(1):231-235. doi:10.1016/0022-2364(77)90138-X

263. Liberman G, Louzoun Y, Ben Bashat D. T_1 mapping using variable flip angle SPGR data with flip angle correction. *J Magn Reson Imaging*. 2014;40(1):171-180. doi:10.1002/jmri.24373

264. Lopes-Pacheco M. CFTR modulators: the changing face of cystic fibrosis in the era of precision medicine. *Front Pharmacol*. 2019;10:1662. doi:10.3389/fphar.2019.01662

265. Crenesse D, Berlioz M, Bourrier T, Albertini M. Spirometry in children aged 3 to 5 years: reliability of forced expiratory maneuvers. *Pediatr Pulmonol*. 2001;32(1):56-61. doi:10.1002/ppul.1089

266. Jat KR. Spirometry in children. *Prim Care Respir J*. 2013;22(2):221-229. doi:10.4104/pcrj.2013.00042

267. Loeb JS, Blower WC, Feldstein JF, Koch BA, Munlin AL, Hardie WD. Acceptability and repeatability of spirometry in children using updated ATS/ERS criteria. *Pediatr Pulmonol*. 2008;43(10):1020-1024. doi:10.1002/ppul.20908